THE UNIVERSITY OF SHEFFIELD

ELECTROMAGNETIC PERFORMANCE OF FLUX-SWITCHING PERMANENT MAGNET BRUSHLESS MACHINES

By

Yong Pang

A thesis submitted for the degree of

Doctor of Philosophy in the

Department of Electronic and Electrical Engineering

University of Sheffield, UK

March 2008

ACKNOWLEDGEMENT

I would like to sincerely thank my supervisors Professor Zi Qiang Zhu and Professor David Howe, and my tutor Dr. Kais Atallah, for giving me this opportunity to be a PhD student in the Electrical Machines & Drives Research Group at the University of Sheffield. Without their continuous guidance and encouragement, it would not have been possible to complete my PhD studies in such a tight time schedule.

I would also like to take this opportunity to thank the following:

- IMRA UK Research Center, for sponsoring my PhD studies.

- All members of the Electrical Machines & Drives Research Group, for their advice and technical support during my theoretical and experimental work.

- Dr Y. Amara and his colleagues, for their generous help and providing a lot of very useful documents at the beginning of my PhD research.

- My friends, Dr. Somporn Ruangsinchaiwanich, Dr. Dahama Ishak, Dr. Pongpit Wipasuramonton, Dr. Yong Liu, Mr. Yu Chen, Mr. Yi Li, Mr. Xi Zhu and Mr. Xuan Chen, for their valuable discussions on various topics.

- My family, my parents, my wife and my son, for their precious support during my PhD from the beginning to the end.

- Also my company, Bosch Lawn and Garden Ltd, for its financial support so that I could complete the writing of my PhD thesis.

ABSTRACT

Flux-switching permanent magnet (PM) brushless machines have both the permanent magnets and the excitation coils in the stator. Compared with conventional PM brushless machines, they offer particular advantages, such as a simple and robust rotor topology, a high torque density, due to the bipolar flux-linkage, and a high magnetic loading, by utilizing magnet flux focusing, and generally, an essentially sinusoidal phase back-emf waveform, which make them good candidates for brushless AC drives. The magnets are in an environment in which there is greater scope to manage their thermal environment, since more precise and higher heat flux cooling methods can be applied to the stator than the rotor, and the influence of heat-soak from other components can be similarly more readily managed. In this thesis, the electromagnetic performance of 3-phase flux-switching PM brushless AC machines is investigated.

Systematic design optimization has been carried out for maximum torque density by finite element analysis, with due account for the influence of size (scaling) and 3-D end-effects. An analytical approach to predicting the performance of flux-switching PM machines is developed based on a non-linear adaptive lumped parameter magnetic circuit model, in order to enable the electromagnetic performance, e.g. airgap field distribution, phase flux-linkage and back-emf waveforms, stator winding inductance and torque, of flux-switching PM machines to be predicted both accurately and quickly.

The optimal split ratio for both conventional and flux-switching PM machines is derived analytically and validated by numerical analysis and experimentally. For conventional PM machines, the influence of brushless DC and AC operational modes, overlapping and non-overlapping winding dispositions, the tooth-tip height and the end-winding is investigated, while for flux-switching PM machines, the influence of the end-winding, and the magnetic and electrical loadings is studied.

The losses in flux-switching PM machines, viz. the copper loss, the iron loss, and the eddy current loss in the frame and the permanent magnets, are also investigated in detail. In addition, the influence of flux-weakening operation and methods for reducing the

losses are studied. All the predicted results are validated experimentally.

CONTENTS

SYMBOLS

Symbol	Unit	Definition
A_{cond}	m^2	Cross-sectional area of conductor
A_g	m^2	Area of airgap
A_m	m^2	Cross-sectional area of permanent magnet
A_s	m^2	Slot area
b_0	m	Width of stator slot openings
b_c	m	Thickness of current sheet
b_m	m	Thickness of permanent magnet in direction of magnetization
b_p	m	Width of rotor tooth
b_s	m	Width of stator slot
b_t	m	Width of stator tooth
B	T	Flux density
B_g	T	Airgap flux density
B_{gmax}	T	Maximum airgap flux density
B_{gr}	T	Radial component of airgap flux density
B_{gw}	T	Airgap flux density due to armature reaction
B_{leak}	T	Leakage flux density
B_{max}	T	Maximum flux density
B_r	T	Remanence of permanent magnet
d_{iron}	m	Thickness of lamination
D_{cond}	m	Diameter of conductor
D_o	m	Outer diameter of stator
D_s	m	Inner diameter of stator
e	V	Instantaneous back-emf
e_{ph}	V	Phase back-emf
f	Hz	Electrical frequency
F	A	Scalar magnetic potential
F_m	A	Scalar magnetic potential of permanent magnet

Symbol	Unit	Definition
F_w	A	Scalar magnetic potential of armature winding
g	m	Airgap length
h_0	m	Tooth tip height
h_m	m	Width of permanent magnets
h_c	m	Thickness of stator back-iron
H_c	kA/m	Magnet coercivity
i_a	A	Instantaneous current of phase A
i_b	A	Instantaneous current of phase B
i_c	A	Instantaneous current of phase C
I	A	RMS current
I_0	A	Zero-sequence current
I_a	A	RMS current of phase A
I_{apk}	A	Peak current of phase A
I_b	A	RMS current of phase B
I_c	A	RMS current of phase C
I_d	A	Current on d-axis
I_e	A	Current in excitation winding
I_{max}	A	Maximum current
I_q	A	Current on q-axis
J_a	A/m^2	Current density
J_c	A/m^2	Density of current sheet
K		Scaling factor
K_s		Slot packing factor
L	m	Length
L_a	m	Effective axial length
L_{aa}	H	Self-inductance of phase A
L_d	H	D-axis inductance
L_{da}	H	D-axis apparent inductance

Symbol	Unit	Definition
L_{di}	H	D-axis incremental inductance
L_e	m	End-winding length
L_q	H	Q-axis inductance
L_{qa}	H	Q-axis apparent inductance
L_{qi}	H	Q-axis incremental inductance
L_w	m	Length of winding per phase
m		Number of phases
m_v	kg/m^3	Mass density of lamination (7.65E+3 kg/m^3)
M	T	Magnetization
M_{ab}	H	Mutual-inductance between phase A and phase B
M_r	T	Radial magnetization
M_θ	T	Circumferential magnetization
n_{base}	rpm	Base speed
n_{max}	rpm	Maximum speed
n_N	rpm	Rated speed
N_{coil}		Number of turns per coil
N_e		Number of turns on excitation winding
N_w		Number of turns per phase
N_s		Number of stator slots
N_{seg}		Number of stator segments per phase
p		Number of electrical pole-pairs
P	H	Permeance
P_{a1}~P_{a5}	H	Airgap permeances
P_{class}	W/kg	Classical eddy current loss in lamination
P_{Cu}	W	Copper loss
P_{eddy}	W/kg	Eddy current loss in lamination
P_{excess}	W/kg	Excess loss in lamination
P_{hyst}	W/kg	Hysteresis loss in lamination

Symbol	Unit	Definition
P_{hyst_minor}	W	Hysteresis loss associated with minor loop in lamination
P_m	H	Permeance of permanent magnet
P_{mil}	H	Inner leakage permeance of permanent magnet
P_{mol}	H	Outer leakage permeance of permanent magnet
P_i	H	Permeance of stator lamination
P_{out}	W	Output power
P_{ri}	H	Permeance of rotor back- iron
P_{rp}	H	Permeance of rotor tooth
P_{st}	H	Permeance of stator tooth
P_{si}	H	Permeance of stator back-iron
Q	A/m	Electric loading
R_a	Ω	Phase resistance
R_{air}	m	Radius of outside airgap boundary
R_{ri}	m	Inner radius of rotor lamination
R_{rm}	m	Outer radius of rotor magnet
R_{ro}	m	Outer radius of rotor lamination
R_{sh}	m	Radius of rotor shaft
R_{si}	m	Inner radius of stator
R_{so}	m	Outer radius of stator
t	S	Time
T	Nm	Electromagnetic torque
T_m	Nm	Permanent magnet torque
T_N	Nm	Rated torque
T_r	Nm	Reluctance torque
U_0	V	Zero-sequence voltage
U_a	V	RMS voltage of phase A
U_{apk}	V	Peak voltage of phase A
U_b	V	RMS voltage of phase B

Symbol	Unit	Definition
U_c	V	RMS voltage of phase C
U_d	V	D-axis voltage
U_{max}	V	Maximum voltage
U_q	V	Q-axis voltage
U_{DC}	V	DC link voltage
V	m/s	Speed
V_m	m^3	Volume of motor
δ_{Al}	m	Skin depth in frame
Φ	Wb	Flux
Φ_m	Wb	Permanent magnet flux
Φ_{mol}	Wb	Permanent magnet outer leakage flux
Φ_{mil}	Wb	Permanent magnet inner leakage flux
Φ_{ri}	Wb	Flux in rotor back-iron
Φ_{rp}	Wb	Flux in rotor tooth
Φ_{sp}	Wb	Flux between stator tooth and rotor tooth
Φ_{si}	Wb	Flux in stator back-iron
Φ_{st}	Wb	Flux in stator tooth
β	degree	Current phase angle
μ_0	H/m	Permeability of free-space (4πE-7 H/m)
μ_r		Relative permeability
θ	Degree	Electrical angle of rotor displacement
θ_0	Degree	Tooth tip angle
θ_p	Degree	Rotor tooth mechanical angle
θ_r	Degree	Rotor tooth pitch mechanical angle
θ_s	Degree	Stator slot pitch mechanical angle
θ_t	Degree	Stator tooth mechanical angle
ρ_{Cu}	Ωm	Resistivity of copper
ρ_{Cu15C}	Ωm	Resistivity of copper at 15°C (0.0175E-6 Ωm)

Symbol	Unit	Definition
ρ_{iron}	Ωm	Resistivity of stator lamination (45E-8 Ωm)
σ_{Al}	$\Omega^{-1}m^{-1}$	Electrical conductivity of aluminium (3.76676E+7 $\Omega^{-1}m^{-1}$)
σ_m	$\Omega^{-1}m^{-1}$	Electrical conductivity of permanent magnet (6.25E+5 $\Omega^{-1}m^{-1}$)
ω	Rad/s	Angular velocity
ω_{elec}	Rad/s	Electrical angular velocity
ψ	Wb	Flux-linkage
ψ_0	Wb	Zero-sequence flux-linkage
ψ_{a_0}	Wb	Flux-linkage of phase A due to permanent magnets
ψ_{a_Ia}	Wb	Flux-linkage of phase A due to permanent magnets and phase A current I_a
ψ_{a_Ib}	Wb	Flux-linkage of phase A due to permanent magnets and phase B current I_b
ψ_a	Wb	Flux-linkage of phase A
ψ_b	Wb	Flux-linkage of phase B
ψ_c	Wb	Flux-linkage of phase C
ψ_m	Wb	Flux-linkage of permanent magnet on d-axis

Chapter 1 General Introduction

1.1. Introduction

With the emergence of high energy density permanent magnets (PM) (e.g. NdFeB), low cost power electronics and easy-to-implement control strategies [SLE94][JAH01] [JAH94], PM brushless machines have been widely adopted for industrial, commercial and domestic applications. They can offer a higher torque capability and power density than conventional brushed DC machines, induction machines and synchronous machines [VAG96]. Since they are electronically controlled, Fig. 1.1, PM brushless machines do not need brushes (or mechanical commutator) for commutation, while the speed and output power can easily be controlled to realize different control operational characteristics, e.g. maximum output torque, maximum output power, flux-weakening, etc [MOR90A][MOR90B].

From the control strategy point of view, there are two major types of PM brushless machine, viz. brushless DC machines which, ideally, have a trapezoidal back-emf waveform and are supplied by 120^{o} rectangular current waveforms, Fig. 1.2(a), and brushless AC machines which, ideally, have a sinusoidal back-emf waveform and are supplied by sinusoidal current waveforms, Fig. 1.2(b). A brushless DC machine needs only relatively low cost rotor position sensors (typically Hall effect or optical sensors) and also a simple control strategy, but its torque ripple can be relatively high. However, it is very suitable for cost-sensitive applications, such as domestic appliances. In contrast, a brushless AC machine requires relatively expensive rotor position sensors, such as an encoder or resolver, and also a relatively complicated control strategy, but can offer very high quality performance [JAH96]. Of course, significant developments have also occurred in sensorless control techniques, which enable operation without discrete sensors.

The investigation which is described in this thesis is focused on 3-phase flux-switching PM brushless machines – a relatively new topology of PM brushless AC machine,

although high-speed flux-switching permanent magnet generators are a relatively old concept [RAU55]. This chapter reviews PM brushless machine topologies, with particular emphasis on the flux-switching PM machine. The scope of the research which is reported in this thesis and its main contributions are presented at the end of this chapter.

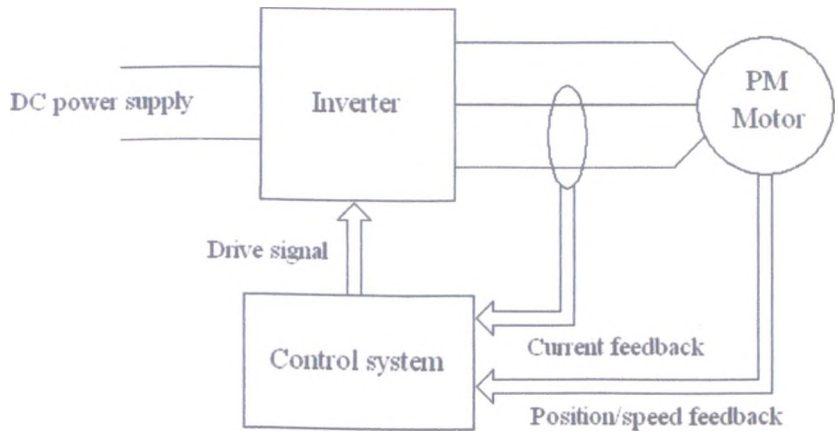

Fig.1.1. Schematic of PM brushless drive system

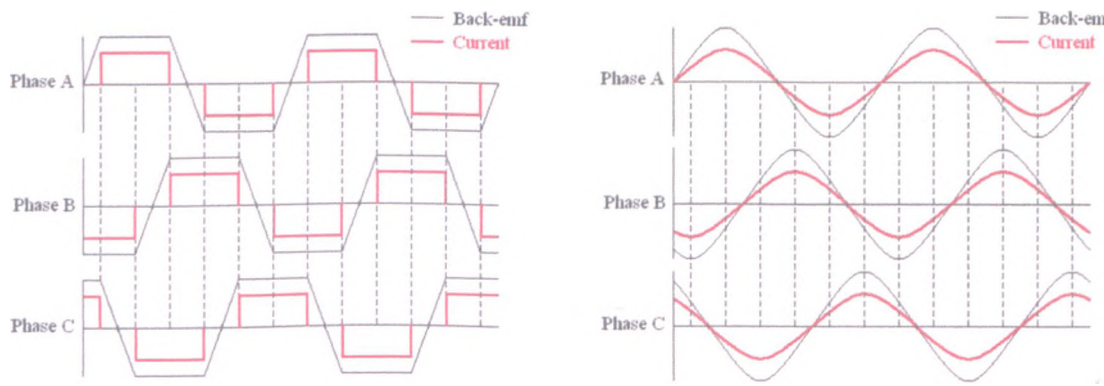

(a) PM brushless DC machine

(b) PM brushless AC machine

Fig. 1.2. 3-phase PM brushless DC and AC machines

1.2. Review of PM brushless machine topologies

The winding dispositions which are most commonly employed for radial-field PM brushless machines can be classified as:

- Overlapping winding, either distributed, Fig. 1.3(a), or concentrated, Fig. 1.3(b);
- Non-overlapping winding, either concentrated with all teeth wound, Fig. 1.3(c), or alternate teeth wound, Fig. 1.3(d).

A distributed overlapping winding generally results in a more sinusoidal MMF distribution and EMF waveform than produced by a non-overlapping winding. Therefore, it has been widely used in conventional induction machines, synchronous reluctance machines and synchronous PM machines [VAG96][CHA98][BIA02]. On the other hand, a non-overlapping winding results in significantly shorter end-windings, which is conducive to a low copper loss, a high efficiency, and a high torque density [ZHU02][MIW04][KEN85][MUR01][EL04]. Compared with machines in which all the teeth are wound, the phase flux-linkage in machines in which only alternate teeth are wound is essentially the same, while the phase self inductance is significantly increased, but the phase mutual inductance is reduced to almost zero. As a result, each phase is essentially magnetically isolated, which makes such machines eminently suitable for fault-tolerant, safety-critical applications [MEC96][CRO02][ISH05].

In general, the output torque of a PM brushless AC machine [JAH94] is given by:

$$T = T_m + T_r \tag{1.1}$$

where $$T_m = \frac{3}{2} p\left[\psi_m I_q\right] \tag{1.2}$$

$$T_r = \frac{3}{2} p\left[-\left(L_q - L_d\right) I_d I_q\right] \tag{1.3}$$

T_m being the PM excitation torque, T_r the reluctance torque, p the number of electrical pole-pairs, ψ_m the d-axis PM flux-linkage, L_q the q-axis inductance, L_d the d-axis inductance, I_q the q-axis current and I_d the d-axis current.

Clearly, in order to develop a reluctance torque component, a difference between L_d and L_q is essential. The machine should, therefore, be designed to have different permeances in the d- and q-axes. Further, it is necessary to employ a full-pitched, overlapping winding, since when a non-overlapping winding is employed the number of slots per

pole per phase is usually fractional. Consequently, the d- and q-axis winding inductances become similar and the reluctance torque will be small.

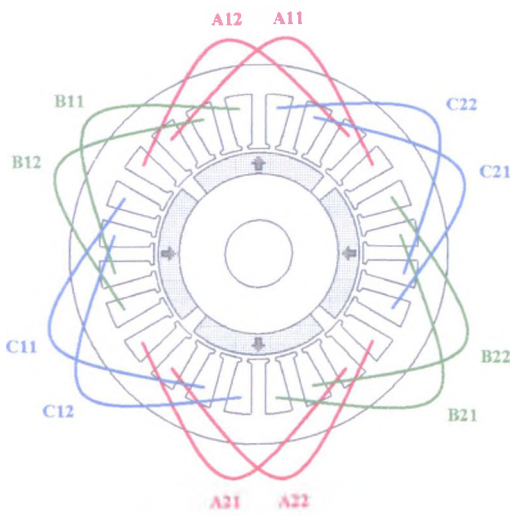

(a) 24-slot

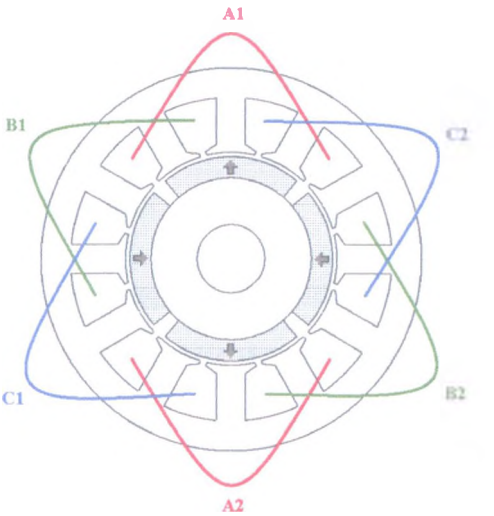

(b) 12-slot

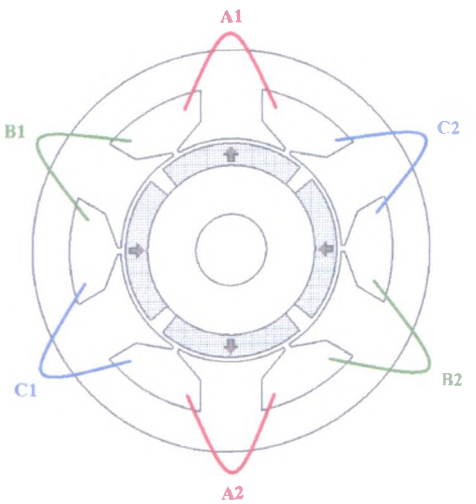

(c) 6-slot, all teeth wound

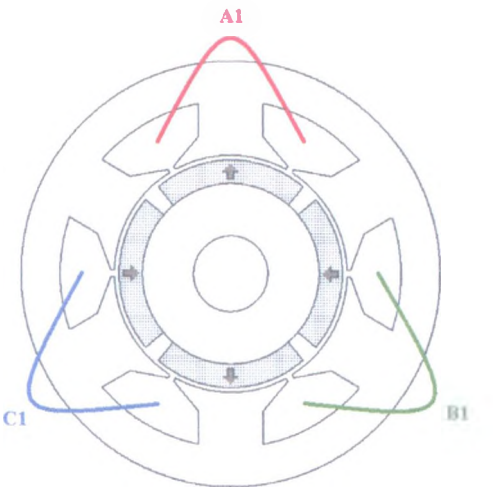

(d) 6-slot, alternate teeth wound

Fig. 1.3. Typical stator winding dispositions (4 poles)

1.2.1. PM brushless machine with magnets on rotor

(a) Surface-mounted PM (SPM) machines

This is the most widely used topology of PM brushless machine, Fig. 1.4(a). However, since the d-axis and q-axis stator winding inductances of such machines are the same,

they exhibit zero reluctance torque. Further, in general, the armature reaction field is relatively small and the stator windings have a low inductance, since the magnet has a relative permeability, which approximates to that of air, i.e. $\mu_r \approx 1$, and the effective airgap is, therefore, the sum of the actual airgap length and the radial thickness of the magnets. However, the magnets are exposed directly to the armature reaction field, and, hence, are susceptible to partial irreversible demagnetization.

Fig. 1.4(b) shows a schematic of a motor in which the magnets are inset into the rotor surface [LIN98][CHA99]. The magnet pole-arc is, therefore, less than a full pole-pitch. However, since the q-axis inductance is now greater than the d-axis inductance, a reluctance torque can be developed.

(b) Interior PM (IPM) machines

Figs. 1.4(c) and 1.4(d) show examples of PM brushless machines in which the magnets are accommodated within the rotor [JAH86][MIL91]. In Fig. 1.4(c) the magnets are radially magnetized, while in Fig. 1.4(d) they are circumferentially magnetized. Generally speaking, however, leakage flux from the magnets can be somewhat greater than that in SPM machines, unless carefully designed flux-barriers are employed. However, since the magnets are buried inside the rotor iron, the magnets are effectively shielded from the demagnetizing component of the armature reaction field. Further, since the d-axis inductance is smaller than the q-axis inductance, a reluctance torque exists, while the d-axis inductance is high compared with that of an equivalent surface-mounted magnet motor topology. Therefore, generally, such machine topologies are eminently appropriate for extended speed, constant power operation in the flux-weakening mode [JAH86][MIL91].

A virtue of the rotor topology shown in Fig. 1.4(d) is that, when the pole number is relatively high, flux focusing can be exploited and the air-gap flux density can be significantly higher than the magnet remanence. Hence, low cost, low energy product magnets, such as sintered ferrite, may be employed. Such a machine topology also

exhibits a higher d-axis inductance since the armature reaction flux only passes through a single magnet, rather than two magnets as in the other machine topologies, making it very suitable for extended constant power operation.

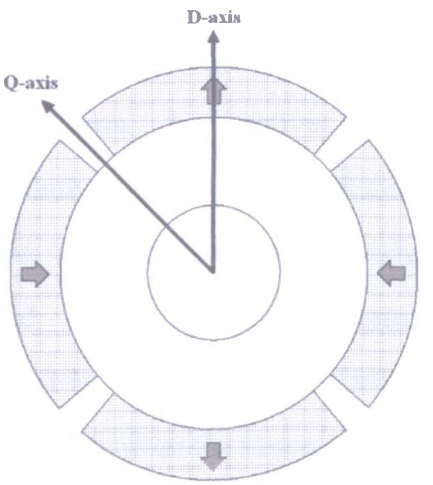

(a) Surface-mounted PM rotor

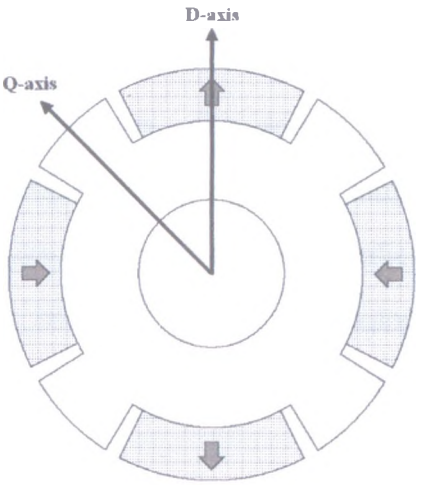

(b) Inset PM rotor

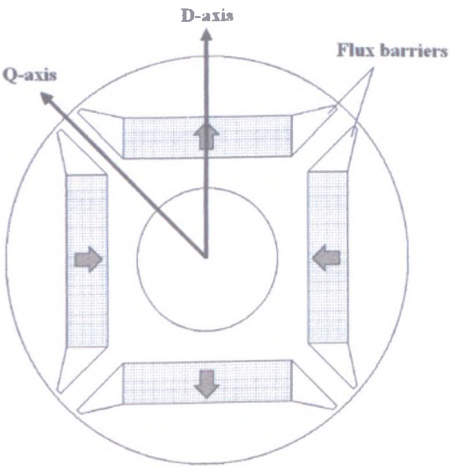

(c) Interior PM rotor with radial magnetization

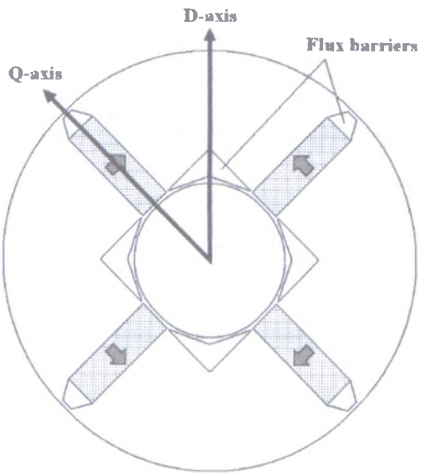

(d) Interior PM rotor with circumferential magnetization

Fig. 1.4 Typical PM brushless machines with magnets on rotor

1.2.2. PM brushless machine with magnets on stator

When the permanent magnets are located in the stator, the rotor must have a salient pole geometry, similar to that of an SR machine, which is simple and robust, and suitable for

relatively high-speed operation. However, for extremely high-speed operation, aerodynamic losses and rotor bending stiffness (which could cause rotor dynamic stability) need to be investigated. The stator carries a non-overlapping winding, with each tooth having a concentrated coil. The permanent magnets can be placed in the inner surface of the stator teeth, sandwiched within the stator teeth, or mounted in the stator back-iron. Irrespective of their location, however, the torque results predominantly from the permanent magnet excitation torque, i.e. the reluctance torque is negligible, although the torque production mechanism relies on the rotor saliency. Compared with conventional permanent magnet brushless machine topologies, generally, it is easier to limit the temperature rise of the magnets as heat is dissipated more effectively from the stator.

(a) Magnets in stator back-iron – doubly-salient PM machine

The machine topology, which is shown in Fig. 1.5(a), is referred to as a doubly-salient permanent magnet machine. For a 3-phase machine a magnet is required in the stator back-iron for every 3 teeth, while for a 4-phase machine a magnet is required for every 4 teeth. The flux-linkage in each coil as the rotor rotates is unipolar, while the back-emf waveform tends to be trapezoidal [LIA92][HUA05]. Thus, this topology is more suitable for brushless DC operation. However, the rotor may be skewed in order to obtain a more sinusoidal back-emf waveform to make it more appropriate for brushless AC operation. Further, it will be noted that the airgap reluctance as seen by the permanent magnets is essentially invariant with the rotor position. Therefore, the cogging torque is not significant. However, a major disadvantage is that, due to the unipolar flux-linkage, the torque density is relatively poor compared to that of other PM brushless machines [HUA05], although, as was reported in [CHE01], it can still be higher than that of an induction machine.

(b) Magnets on surface of stator teeth – flux-reversal permanent magnet machine

This machine topology is also commonly referred to as a flux-reversal PM machine, Fig. 1.5(b) [DEO96][WAN99][KIM04][KIM05]. Each stator tooth has a pair of magnets of

different polarity mounted on its surface. When a coil is excited, the field under one magnet is reduced while that under the other is increased, and the salient rotor tooth rotates towards the stronger magnetic field. The flux-linkage in each coil reverses polarity as the rotor rotates. Thus, the phase flux-linkage variation is bipolar, while the phase back-emf waveform is, again, essentially trapezoidal. Such a machine topology exhibits a low winding inductance, while the magnets are more vulnerable to partial irreversible demagnetization. In addition, significant induced eddy current loss may be induced in the magnets. Although in a magnetic circuit with two series airgaps, the net force on the magnet is, in the ideal case, zero. In reality, due to the edge leakage flux a relatively high radial magnetic force occurs. Further, since the airgap flux density is limited by the magnet remanence, the torque density may be compromised.

(c) Magnets in stator teeth – flux-switching PM machine

This machine topology is also referred to as a flux-switching permanent magnet machine, Fig. 1.5(c) [HOA97][HOA00][ZHU05]. The stator consists of "U"-shaped laminated segments between which circumferentially magnetized permanent magnets are sandwiched, the direction of magnetization being reversed from one magnet to the next. Each stator tooth comprises two adjacent laminated segments and a permanent magnet. Thus, flux-focusing may be readily incorporated, so that low cost ferrite magnets can be employed [HOA00]. Since the phase flux-linkage waveform is bipolar, the torque capability is significantly higher than that of a doubly-salient PM machine [HUA05]. The back-emf waveform of flux-switching PM machines is essentially sinusoidal, which makes them more appropriate for brushless AC operation. In addition, since a high per-unit winding inductance can readily be achieved, such machines are eminently suitable for constant power operation over a wide speed range. The investigation of the electromagnetic performance of 3-phase flux-switching PM machines is the subject of research which is described in this thesis. Therefore, it will be discussed further in the next section.

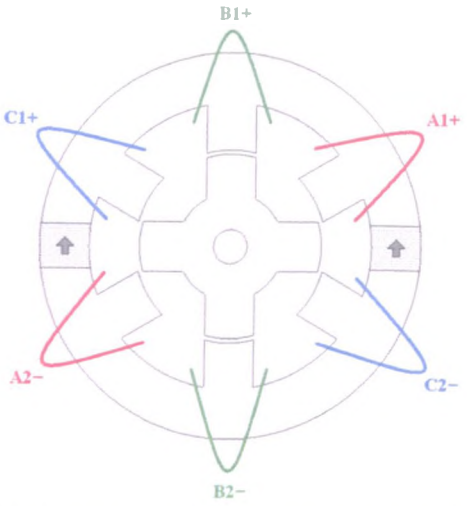

(a1) 3-phase doubly-salient PM machine

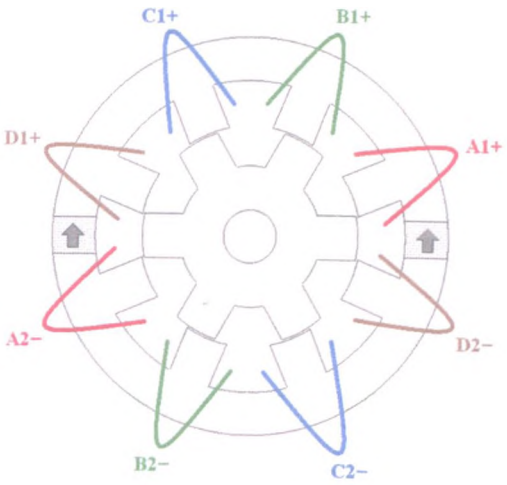

(a2) 4-phase doubly-salient PM machine

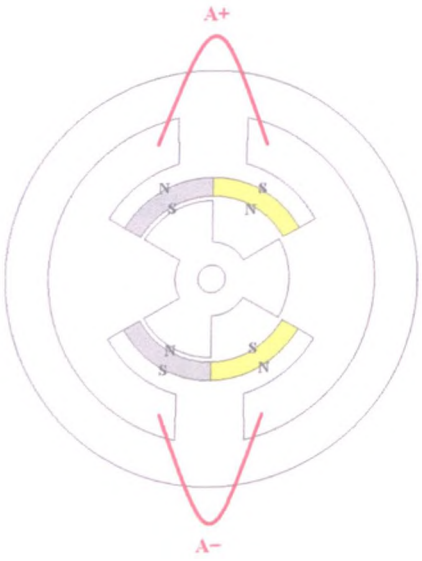

(b1) 1-phase flux-reversal PM machine

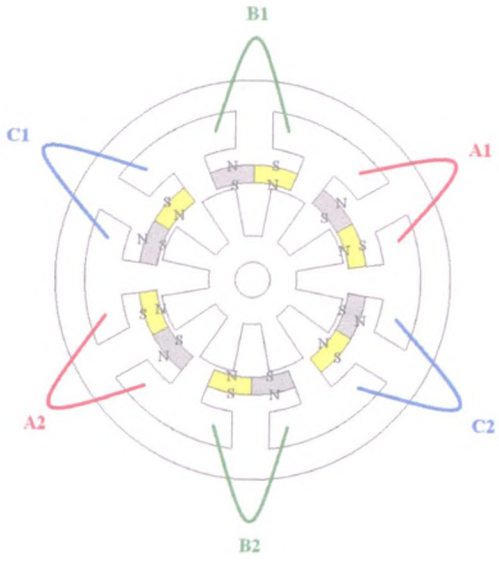

(b2) 3-phase flux-reversal PM machine

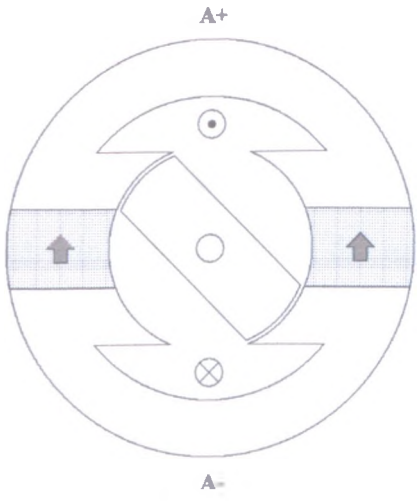

(c1) 1-phase flux-switching PM machine

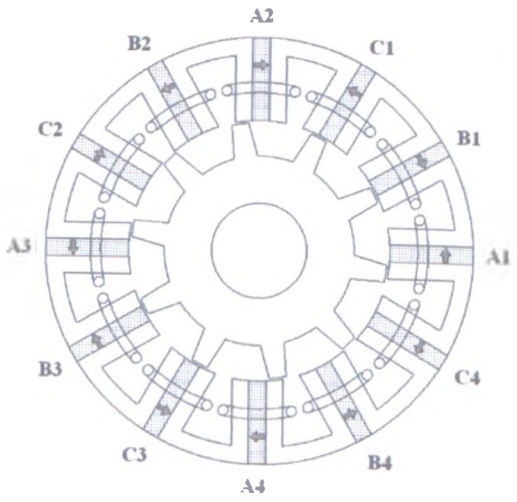

(c2) 3-phase flux-switching PM machine

Fig. 1.5 Typical PM brushless machines with magnets on stator

1.3. Alternative flux-switching PM machine topologies

1.3.1. Operating principle

Permanent magnet machines based on the principle of flux-switching have been studied for several decades. As mentioned earlier, such machines have a salient rotor tooth and the magnets are mounted in the stator. In 1955, a single-phase flux-switching alternator, Fig. 1.5(c1), was described in [RAU55] and was studied further in [SAR94], and three-phase flux-switching machines, Fig. 1.5(c2), have been described in [HOA97] [HOA00][AMA03], whilst the performance of a Law's relay (a flux-switching type of limited angle actuator) was studied in [BOL90]. Theoretically, such kinds of flux-switching machine can be excited by current-carrying coils [POL99][POL03a] [POL03b], permanent magnets [RAU55][SAR94][HOA97][HOA00][AMA03][ZHU05] [HUA05][CHE05], or a combination of the two [LI95][LEO96].

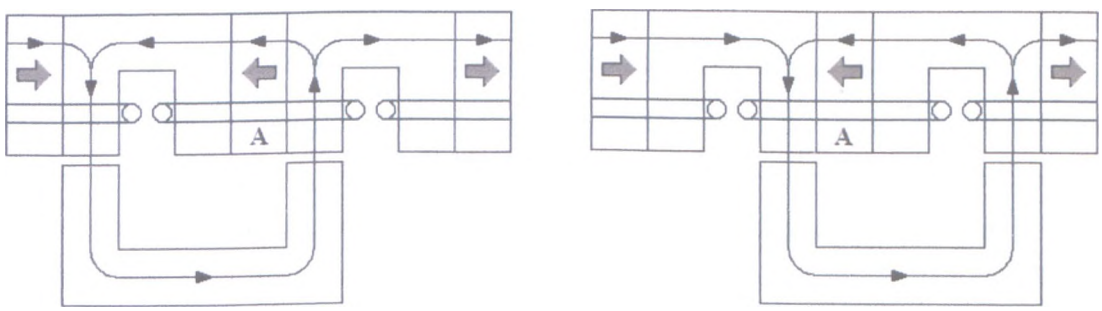

(a) Position 1 (b) Position 2

Fig. 1.6. Operating principle of flux-switching PM machine

The working principle of the flux-switching PM machine is very simple and is illustrated in Fig. 1.6. When the rotor tooth is at position 1, the direction of the flux which links coil A is from the rotor to the stator; whilst when the rotor tooth is moved to position 2, the direction of the flux which links coil A changes from the stator to the rotor. Therefore, the flux-linkage with coil A has been 'switched', i.e. the polarity of the flux-linkage of coil A changes when the rotor moves from position 1 to 2. This principle can be applied to a machine with any phase number. The resulting coil flux-linkage and back-emf waveforms are bipolar, idealized waveforms being shown in Fig. 1.7, while

finite element predicted waveforms are shown later in Figs. 1.11, 1.13, and 1.15. If alternating current is supplied to the coil(s), electromagnetic torque can be produced.

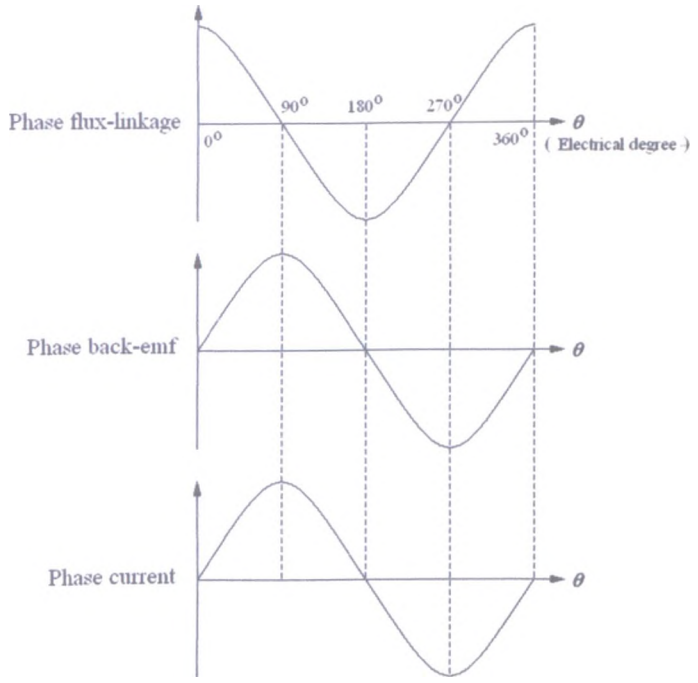

Fig.1.7. Ideal flux-linkage, back-emf, and phase current waveforms

1.3.2. Number of phases and stator and rotor tooth number combination

Based on the flux-switching principle, two main types of flux-switching PM brushless machines were proposed in [HOA97], as illustrated in Figs. 1.8 and 1.9.

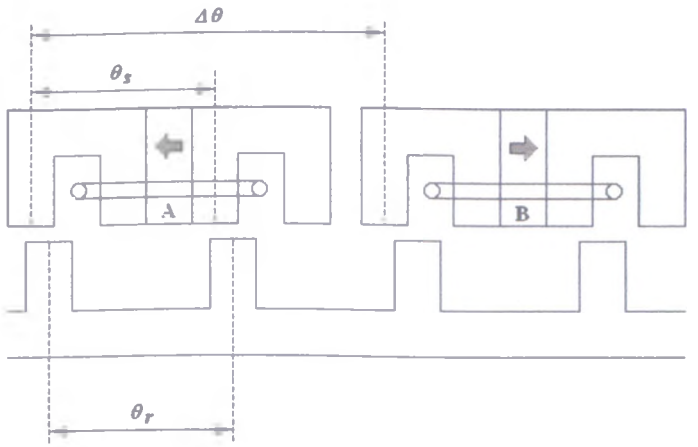

Fig. 1.8. Definition of angular dimensions in flux-switching PM machine

Type-A:

$$\Delta\theta = \frac{2\pi}{mN_{seg}} \tag{1.4}$$

$$\theta_s = \theta_r = \frac{\Delta\theta}{2 + \frac{\pm n}{m}} \tag{1.5}$$

Type-B:

$$\Delta\theta = \theta_s = \frac{2\pi}{mN_{seg}} \tag{1.6}$$

$$\theta_r = \frac{\Delta\theta}{2 + \frac{\pm n}{2m}} \tag{1.7}$$

where m is the number of phases, N_{seg} is the number of stator segments per phase, and $\pm n = \pm 1, \pm 2, \ldots$

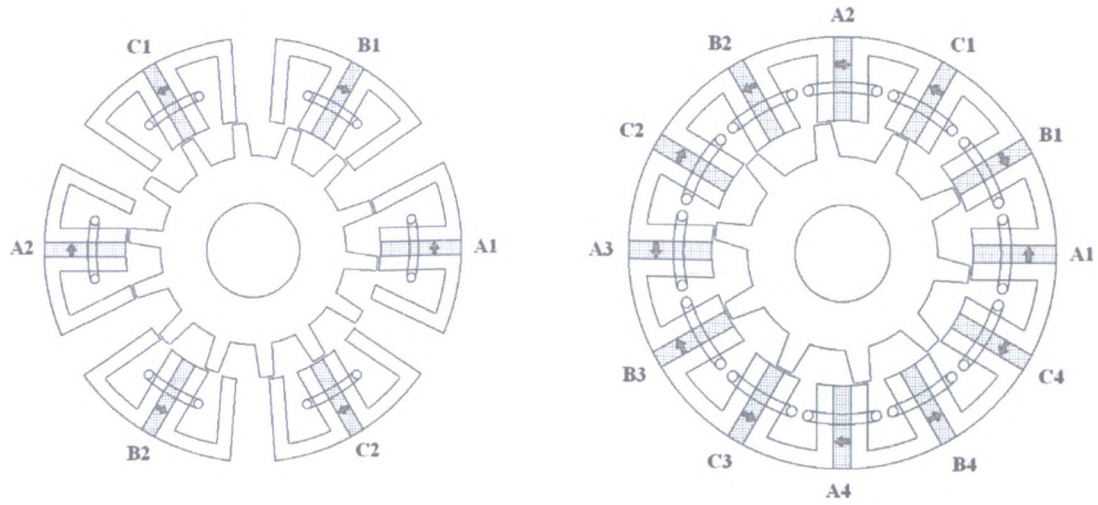

(a) Type-A (b) Type-B

Fig. 1.9. Typical 3-phase flux-switching PM machines (m=3, n=-7)

By using equations (1.4) to (1.7), two 3-phase flux-switching PM machines were derived in [HOA97], as shown in Fig. 1.9. It can be seen that for a Type-A flux-switching PM machine, the stator is modular and, hence, the machine is eminently suitable for fault-tolerant operation. However, a significant proportion of the stator

space is not effectively utilized. This results in a relatively low torque density compared to a Type-B flux-switching PM machine. Therefore, Type-B flux-switching PM machines are chosen for further investigation in this thesis.

(a) Single-phase flux-switching PM machine

For a single-phase flux-switching PM machine, $m=1$. If $N_{seg}=2$ and $\pm n=-2$, then from equation (1.4), $\Delta\theta=\theta_s=\theta_r=\pi$. Therefore, a single-phase flux-switching PM machine with the minimum stator slot number and rotor tooth number has two stator slots and two rotor teeth, as shown in Fig. 1.10.

Finite element predicted phase flux-linkage and phase back-emf waveforms are shown in Fig. 1.11. It can be seen that the resultant phase back-emf waveform is neither trapezoidal nor sinusoidal, which will result in large torque ripple in both brushless AC and DC drive modes. However, design optimization of the stator and rotor geometries shows that it is possible to achieve a trapezoidal back-emf waveform and also to obtain a starting torque, and this is currently being investigated by Mr. Yu Chen, a PhD student at the University of Sheffield [CHE06].

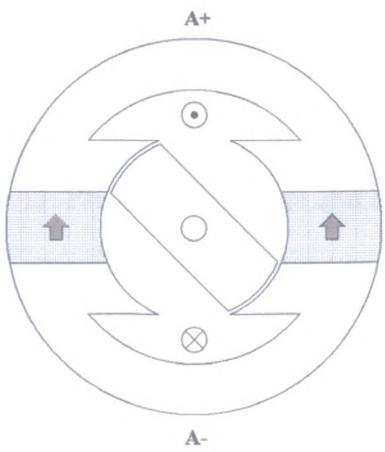

(a1) Cross-section (ψ_a=max.)

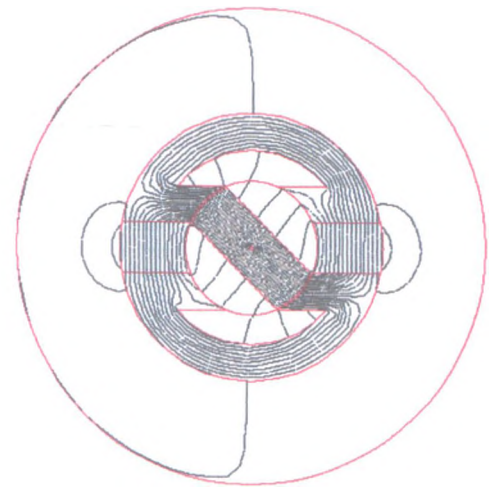

(b1) Open-circuit flux distribution (ψ_a=max.)

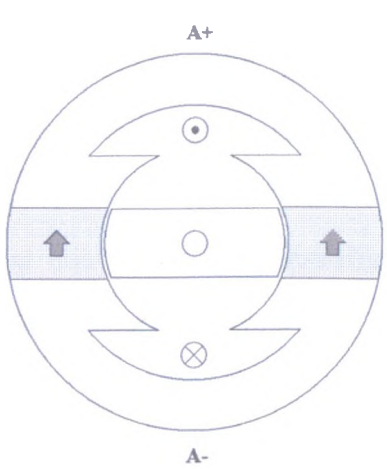

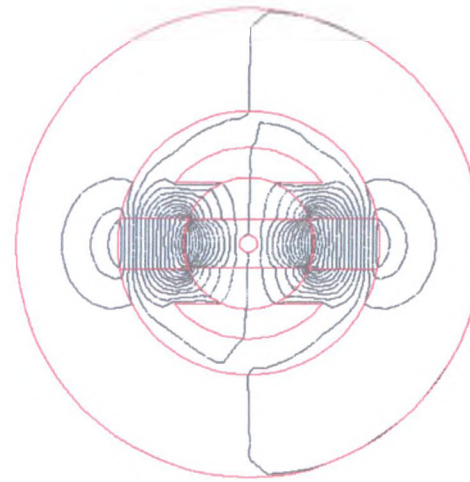

(a2) Cross-section (ψ_a=0) (b2) Open-circuit flux distribution (ψ_a=0)

Fig. 1.10. Single-phase flux-switching PM machine (2-rotor tooth, 2-stator slot)

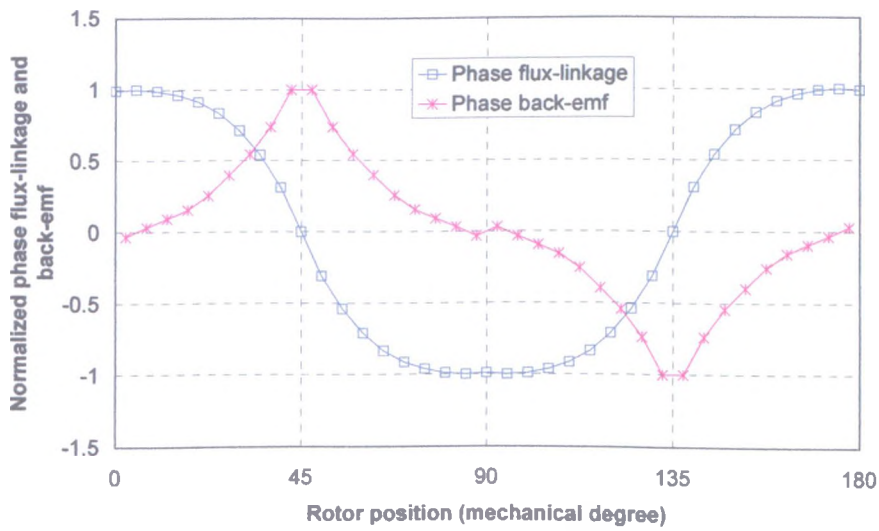

Fig. 1.11. Phase flux-linkage and back-emf waveforms of single-phase flux-switching PM machine

(b) 2-phase flux-switching PM machine

For a 2-phase flux-switching PM machine, $m = 2$. If $N_{seg} = 2$, then $\Delta\theta = \theta_s = \frac{\pi}{2}$ and $\theta_r = \frac{\frac{\pi}{2}}{2 + \frac{\pm n}{4}}$. The maximum value of θ_r, is given by $\theta_r = \frac{\frac{\pi}{2}}{2 + \frac{-5}{4}} = \frac{2\pi}{3}$, which is smaller than θ_s. Thus, the minimum stator slot number and rotor tooth number for a

2-phase flux-switching PM machine will be 4 and 3, respectively. However, it is well known that using an odd number of rotor teeth will result in a high unbalanced magnetic force. Therefore, the minimum stator slot number and rotor tooth number for a practical 2-phase flux-switching PM machine will be 8 and 6, respectively, Fig. 1.12. It can be seen that this 2-phase flux-switching PM machine is cyclically symmetric every 180° mech. Each phase consists of four coils which can be grouped into two sets, i.e. (A1, A3) and (A2, A4), the coils in each set having the same polarity, but the polarities of one set of coils A1 and A3 being opposite to that of the other set of coils A2 and A4, as can be seen from the predicted flux-linkage and back-emf waveforms, Fig. 1.13. This is due to the fact that the stator teeth for two sets of coils have different relative positions with the rotor teeth, e.g. when a rotor tooth is aligned with the right side magnet under coils A1 and A3, the rotor tooth is aligned with the left side magnet under coils A2 and A4, and when the centres of coils A1 and A3 align with the centre of the rotor tooth, the centres of coils A2 and A4 align with the centre of the rotor slot. Fig. 1.13 also shows that the resultant phase back-emf waveform is essentially trapezoidal with ~100° flat top, which is appropriate for brushless DC operation. However, if a sinusoidal back-emf waveform is desirable for brushless AC operation, the rotor tooth may be appropriately skewed. This flux-switching PM machine is being investigated by Mr. Wei Hua, a visiting PhD student at the University of Sheffield [HUA07].

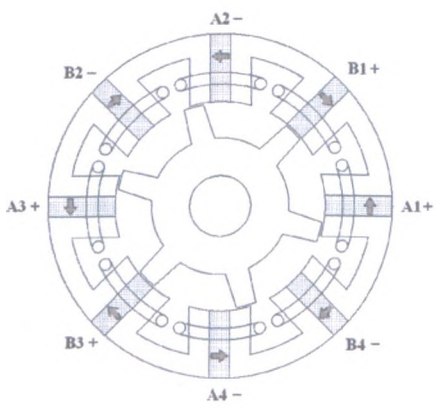

(a1) Cross-section (ψ_a=max.)

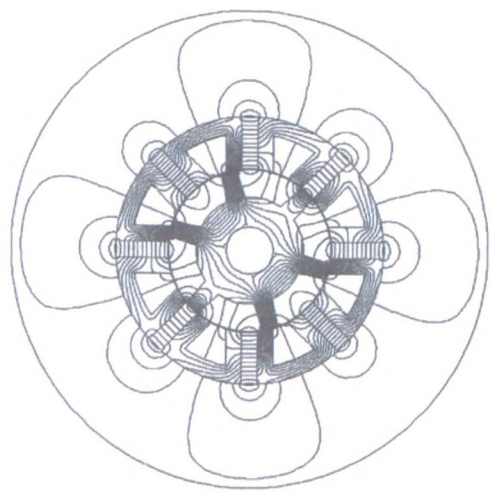

(b1) Open-circuit flux distribution (ψ_a=max.)

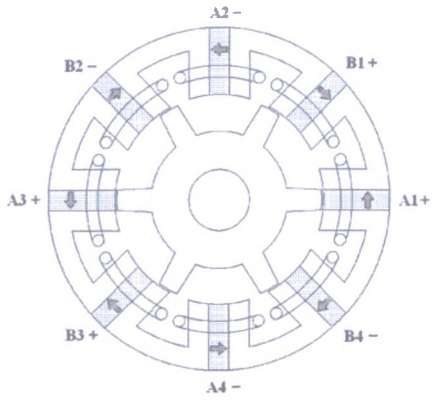

(a2) Cross-section (ψ_a=0)

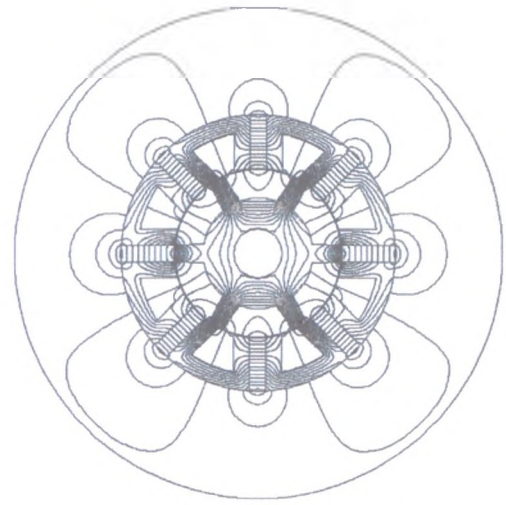

(b2) Open-circuit flux distribution (ψ_a=0)

Fig. 1.12. 2-phase flux-switching PM machine (6-rotor tooth, 8-stator slot)

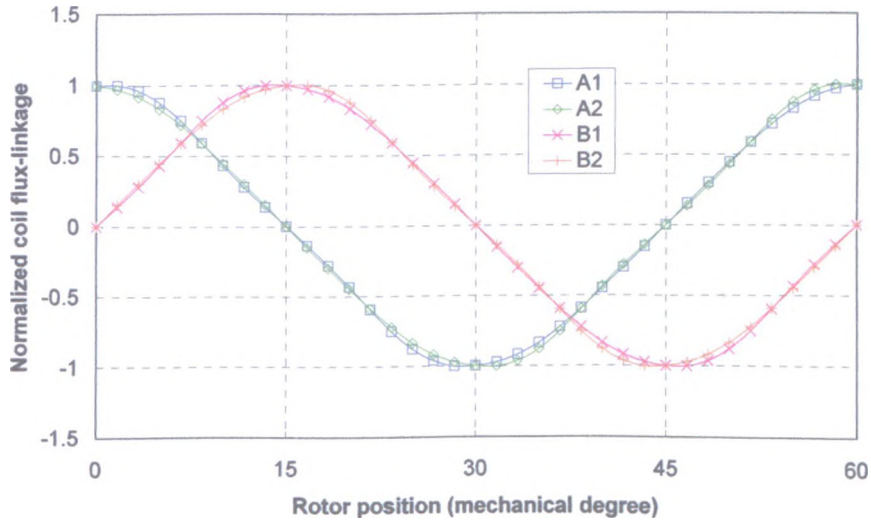

(a) Coil flux-linkage

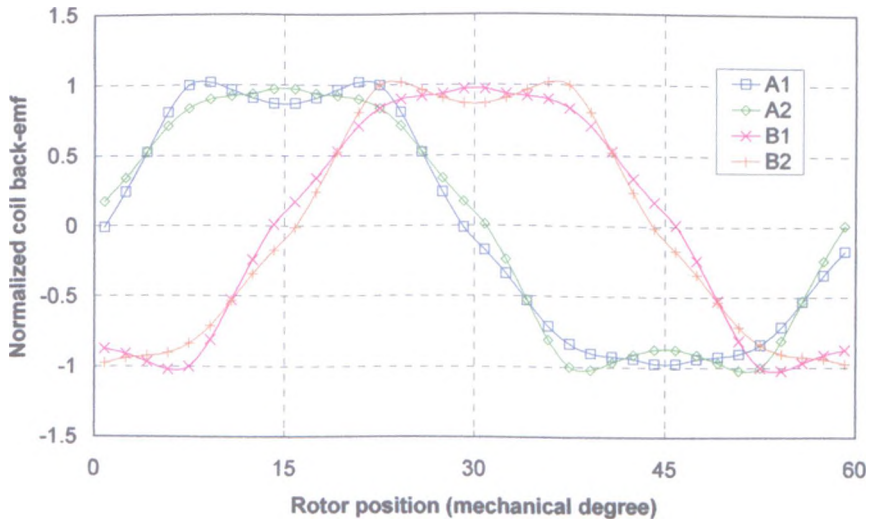

(b) Coil back-emf

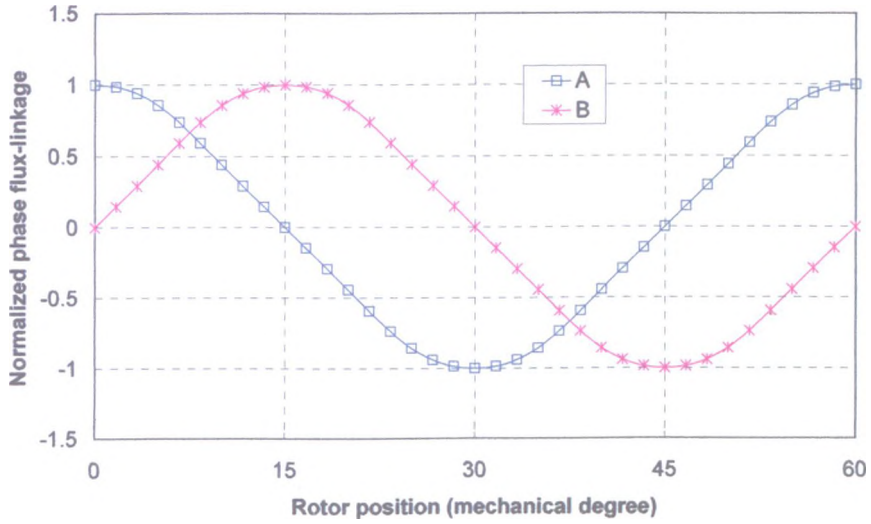

(c) Phase flux-linkage

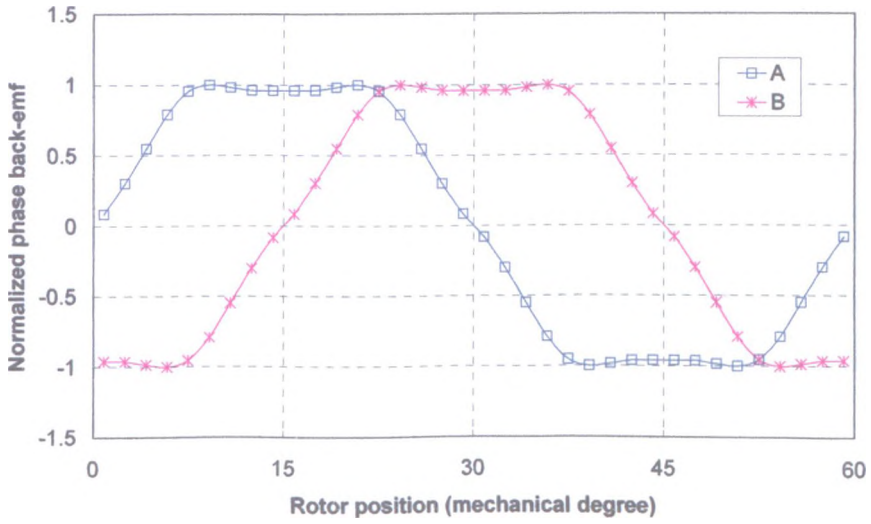

(d) Phase back-emf

Fig. 1.13. Performance of 2-phase flux-switching PM machine

(c) 3-phase flux-switching PM machine

For a 3-phase flux-switching PM machine, $m = 3$. If $N_{seg} = 2$, then $\Delta\theta = \theta_s = \frac{\pi}{3}$ and $\theta_r = \frac{\frac{\pi}{3}}{2 + \frac{\pm n}{6}}$. The maximum value of θ_r, is given by $\theta_r = \frac{\frac{\pi}{3}}{2 + \frac{-7}{6}} = \frac{2\pi}{5}$, which is smaller than θ_s. Thus, the minimum stator slot number and rotor tooth number for a 3-phase flux-switching PM machine will be 6 and 5, respectively. Similar to the 2-phase

flux-switching PM machine, however, using an odd number of rotor teeth will result in a high unbalanced magnetic force. Therefore, the minimum stator slot number and rotor tooth number for a practical 3-phase flux-switching PM machine will be 12 and 10, respectively, Fig. 1.14.

It can be seen that, similar to the 2-phase flux-switching PM machine, this 3-phase flux-switching PM machine is also cyclically symmetric every 180° mech. Each phase consists of four coils which can be grouped into two sets, i.e. (A1, A3) and (A2, A4), the coil flux-linkage and back-emf waveforms of each set are identical but have a small phase shift from those in the other set, but the polarities of all four coils are the same, as shown in Fig. 1.15. Fig. 1.15 also shows that although both the flux-linkage and back-emf waveforms in the different sets of coils are asymmetric; the resultant phase flux-linkage and phase back-emf waveforms are essentially sinusoidal, which makes it a good candidate for a brushless AC drive.

Based on the above principle, the combination of stator slot number and rotor tooth number for a higher number of phases can be similarly derived, and are summarized in Table 1.1. However, 3-phase flux-switching PM machines are the subject of the research which is reported in this thesis.

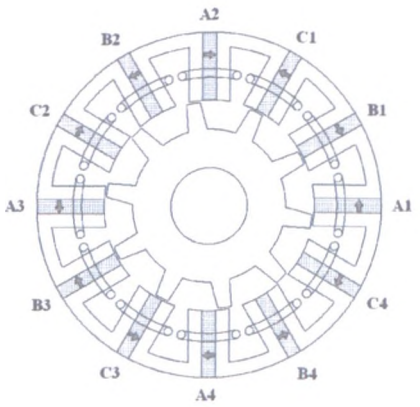

(a1) Cross-section (ψ_a=max.)

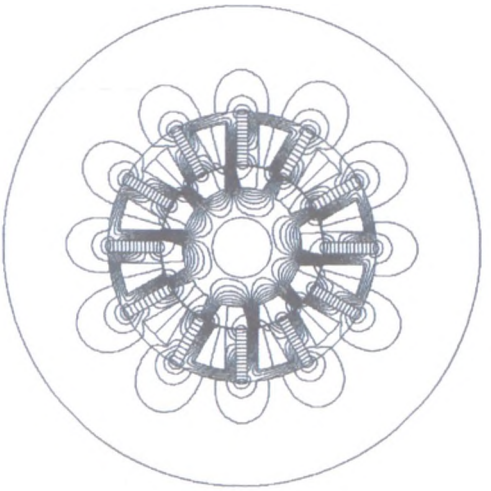

(b1) Open-circuit flux distribution (ψ_a=max.)

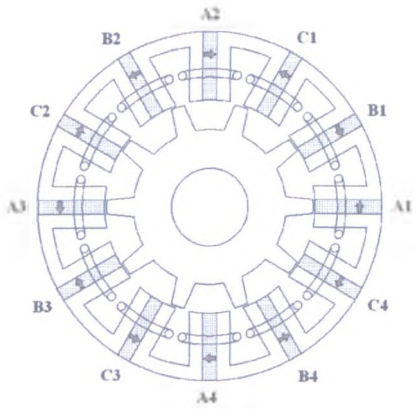

(a2) Cross-section (ψ_a=0)

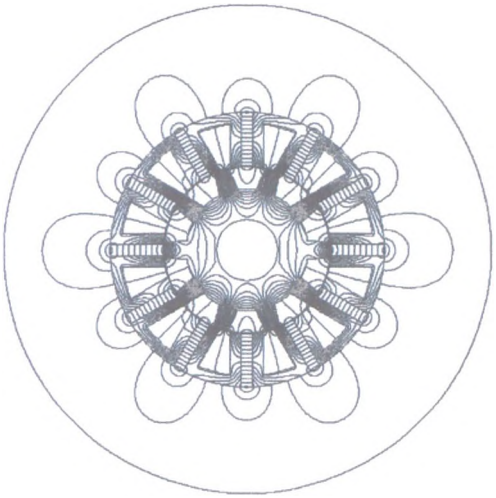

(b2) Open-circuit flux distribution (ψ_a=0)

Fig. 1.14. 3-phase flux-switching PM machine (10-rotor tooth 12-stator slot)

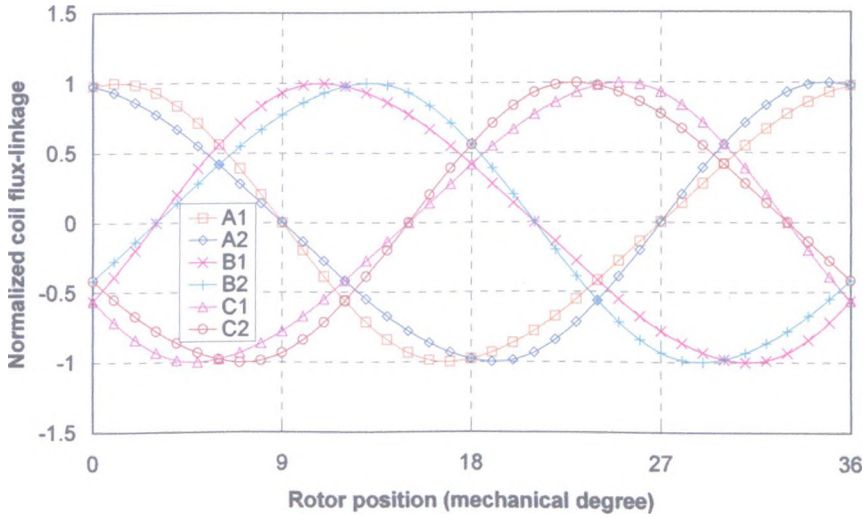

(a) Coil flux-linkage

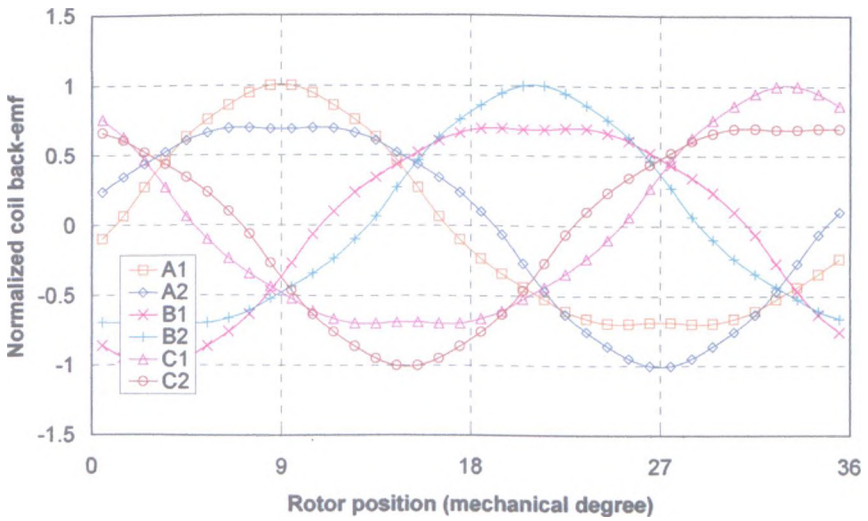

(b) Coil back-emf

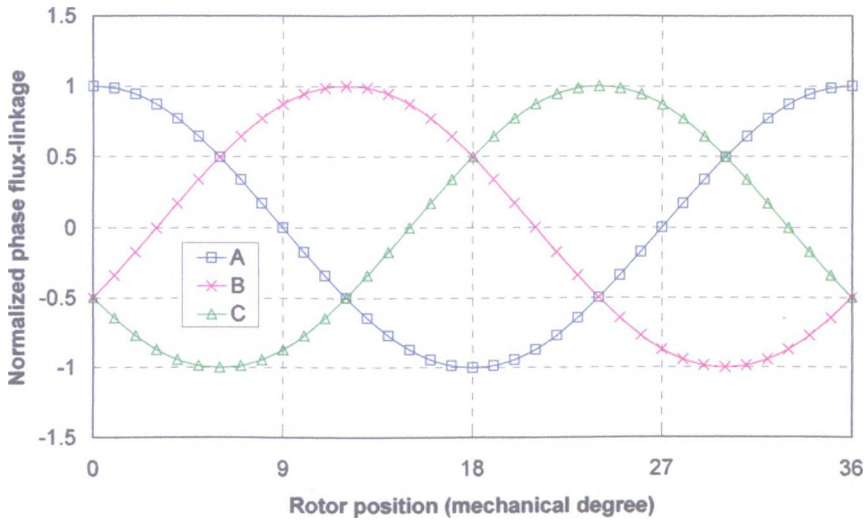

(c) Phase flux-linkage

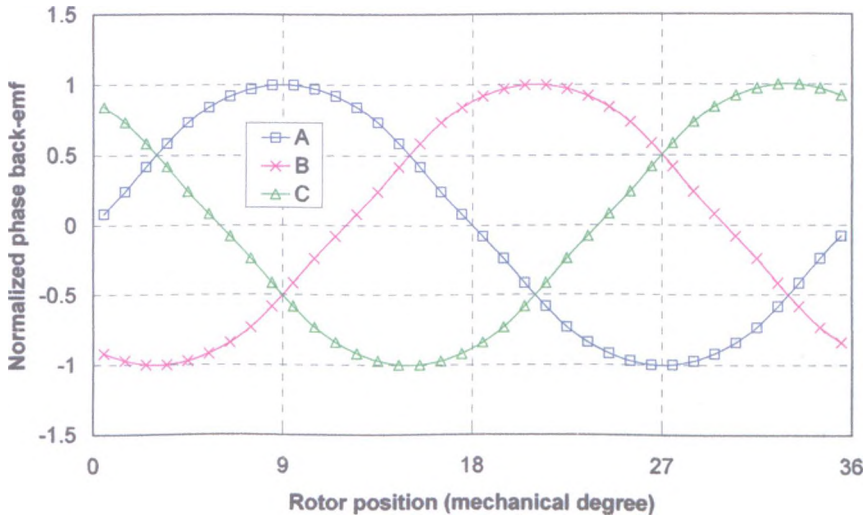

(d) Phase back-emf

Fig.1.15. Flux-linkage and back-emf of 3-phase flux-switching PM machine

Table 1.1. Practical minimum numbers of stator slots and rotor teeth

Number of phases	Number of stator slots	Number of rotor teeth
1	2	2
2	8	6
3	12	10
4	8	6
5	20	18
6	12	10

Note: The number of stator slots is defined as the same number of permanent magnets, each of which is encompassed by a coil (see Fig. 1.14).

1.3.3. Other flux-switching PM brushless machines

(a) External rotor flux-switching PM machine

External rotor PM machines are advantageous for some applications, such as direct-drives for electric vehicles [CRO98][WAN02]. Similar to conventional PM brushless machines, external rotor flux-switching PM machines are also possible, as shown in Fig. 1.16.

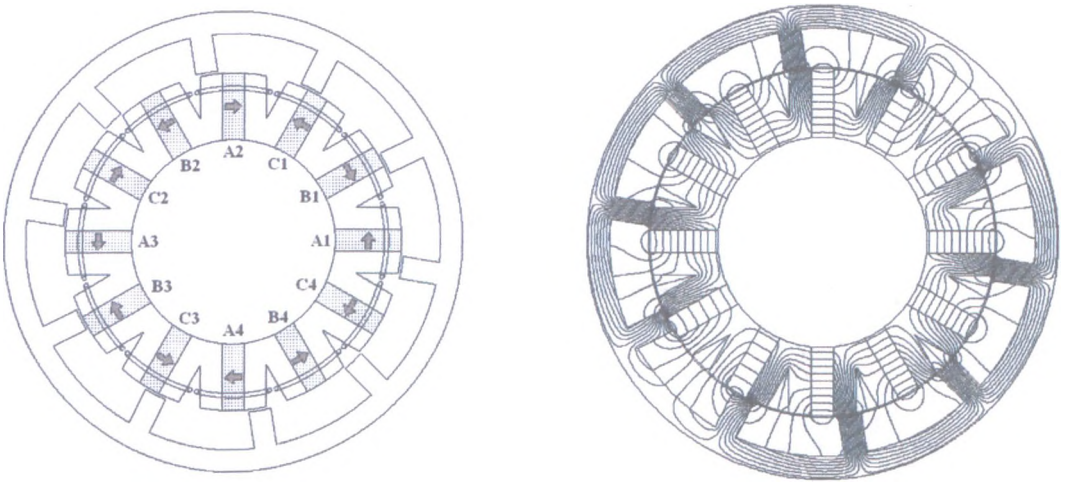

(a) Cross-section (b) Open-circuit flux distribution

Fig. 1.16. External rotor flux-switching PM machine

It can be seen that no external leakage flux exists in an external rotor flux-switching PM machine. This is a significant advantage over internal rotor flux-switching PM machines. However, the slot area of an external rotor flux-switching PM machine is significantly reduced, and finite element analysis has shown that its torque capability is much lower than that of an equivalent internal rotor flux-switching PM machine, which has an identical space envelope and the same stator copper loss. A given space envelope yields the same surface area for cooling and ultimately the same cooling capability. The torque capability of an external rotor flux-switching PM machine can be improved by either increasing the allowable temperature rise or using special cooling technology to

accommodate the large heat flux on the inner surface of the stator. Therefore, in this thesis, the research will focus on internal rotor flux-switching PM machines.

(b) Axial-field flux-switching PM machine

Similar to conventional axial-field PM machines [PLA89][SPO92], axial-field flux-switching PM machines are also possible.

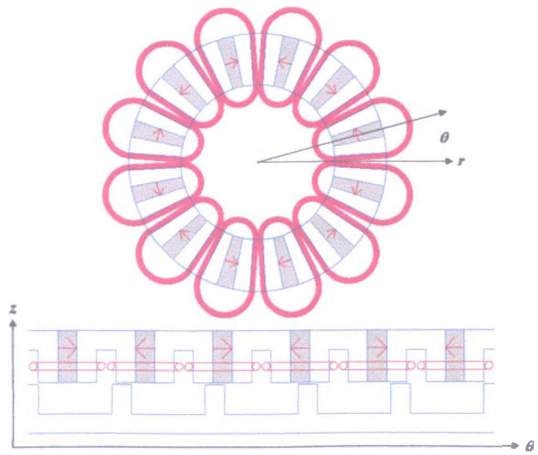

(a) Single-stator and single-rotor

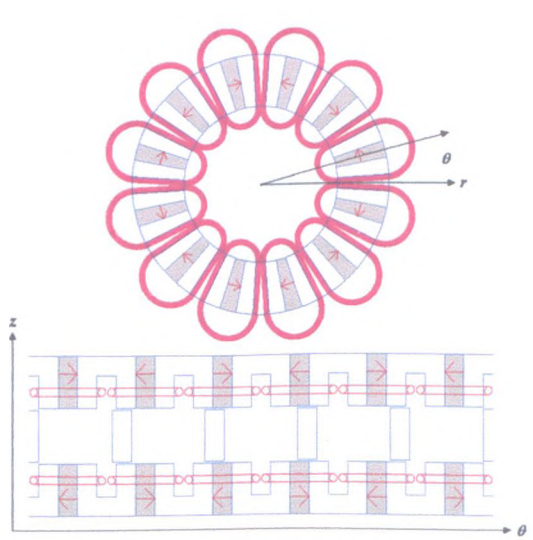

(b) Dual-stator and single-rotor

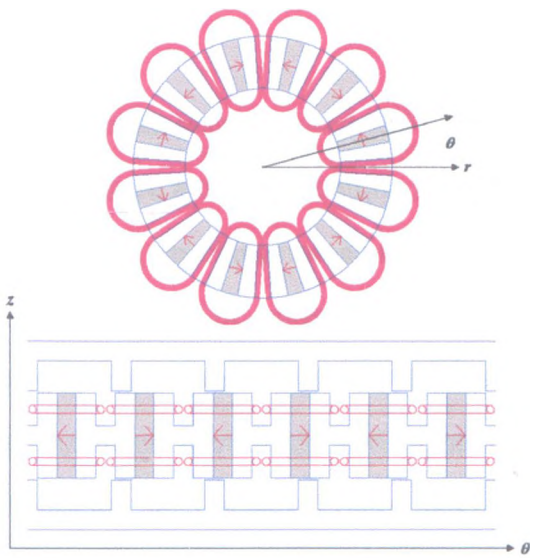

(c) Single-stator and dual-rotor

Fig. 1.17. Axial-field flux-switching PM machines

Fig. 1.17 shows typical single airgap and double airgap axial-field flux-switching PM

machines. It can be seen that for axial-field flux-switching PM machines, although the outer slot cross-sectional area is larger than the inner slot cross-sectional area, the effective slot area is limited by the inner radius.

(c) Linear flux-switching PM machines

From Figs. 1.9, 1.10, 1.12, 1.14 for radial-field flux-switching PM machines and Fig. 1.17 for axial-field flux-switching PM machines, it will be appreciated that these topologies are directly convertible to linear flux-switching PM machines.

1.4. Scope of research and contributions

As the foregoing has mentioned, flux-switching PM machines, because of their attractive characteristics, viz. high torque density and high power density due to the permanent magnet excitation, high speed capability due to the simple and robust rotor topology, the high electric load capability due to the permanent magnets being located in the stator, and their sinusoidal phase flux-linkage and phase back-emf waveforms, appear to be good candidates for brushless AC drives.

However, although the concept of flux-switching machines was proposed ~50 years ago [RAU55], it was not until relatively recently that they have attracted attention for further research. The research on single-phase flux-switching machines was pioneered by Professor Charles Pollock at the University of Leicester, UK, most notably on the development of a low-cost DC field winding excited version [POL99][POL03a] [POL03b], while 3-phase flux-switching PM machines have been investigated by LESiR/SATIE Laboratory, Ecole Normale Superieure de Cachan, France [HOA97] [HOA00][AMA03]. However, to date, the research is still rather limited and only the above major papers are available in the literature. In [HOA97], only the basic design principle for multi-phase flux-switching PM machines has been described, and their potential for constant power application has been demonstrated, and only finite element predicted results are presented in [HOA97][AMA03], while in [HOA00] only hysteresis

and classical eddy current losses were analyzed by the finite element method.

The purpose of this thesis is to systematically investigate the electromagnetic performance of 3-phase flux-switching PM machines.

In this chapter, the basic PM brushless machine topologies, having permanent magnets on either the rotor or the stator, have been briefly reviewed. Alternative flux-switching permanent magnet machines have been introduced, whilst the scope of the research and the major contributions of this thesis are summarized as follows:

In Chapter 2, the influence of design parameters, including the stator, rotor, and magnet geometries and dimensions, on the electromagnetic performance of a 3-phase, 10-rotor tooth, 12-stator slot, flux-switching PM machine is investigated by finite element analysis. 3-D end-effects and the effect of scaling are also studied.

In Chapter 3, an adaptive lumped parameter magnetic equivalent circuit model for flux-switching PM machines is established and validated by finite element calculations and measurements. It is then used to derive optimal key design parameters, including the stator tooth width, the rotor tooth width and the split ratio. The influence of magnetic saturation and 3-D end-effects are also studied.

The split ratio, i.e. the ratio of the stator bore diameter to the stator outer diameter ($\frac{D_s}{D_o}$), is one of the most important design parameters for permanent magnet brushless machines as it can significantly influence the torque capability and efficiency. Therefore, in Chapter 4, the optimal split ratio of surface-mounted and interior PM machines for maximum torque per volume is first systematically investigated for both brushless AC and DC operation of machines having overlapping and non-overlapping windings, and accounting for the influence of the airgap field distribution, back-emf waveform, the tooth-tips, and the end-windings. Analytical formulae for the optimal split ratio are obtained and validated by finite element analysis and measurements. The optimal split ratio for flux-switching PM machines is also investigated, with due account of the influence of magnetic saturation and the choice of permanent magnet material.

Chapter 5 systematically investigates the losses in flux-switching machines, including the stator copper loss, the eddy current loss in the frame due to the variation of the leakage flux external to the stator laminations, the eddy current loss in the permanent magnet as a result of the variation in the magnet working point on both no-load and loaded, and the stator and rotor iron loss with due account for the non-sinusoidal flux waveforms and the DC bias flux. An analytical model for the iron loss calculation is established to account for the flux density variation in flux-switching PM machines. The influence of the machine design parameters and machine operating mode on the losses is also investigated and validated experimentally.

Chapter 6 draws general conclusions.

The main contributions of this thesis include:

1. An adaptive lumped parameter magnetic equivalent circuit model for flux-switching PM machines is established to enable the optimal design parameters to be obtained, while the influence of the design parameters on the torque capability is investigated systematically.

2. Optimal split ratios for surface-mounted-magnet and interior-magnet PM machines and flux-switching PM machines are derived analytically and examined by finite element analyses and validated experimentally.

3. Various loss components, including the eddy current loss in the frame and the permanent magnets and the iron loss, in flux-switching PM machines are investigated systematically.

Chapter 2 Influence of Design Parameters on Electromagnetic Performance of Flux-Switching Permanent Magnet Machine

2.1. Introduction

Since a 3-phase, 10-rotor tooth, 12-stator slot, flux-switching PM machine, Fig. 2.1, has an essentially sinusoidal phase back-emf waveform, it was chosen for the investigation, which is described in this thesis. In this chapter, the influence of stator and rotor dimensions, such as the stator tooth width, the stator magnet thickness, the stator back-iron thickness, the rotor tooth width, and the rotor tooth length, etc., on the output torque will be investigated by finite element analysis. The investigation is based on the prototype machine whose design parameters are given in Appendix I. However, as finite element calculations are still relatively time-consuming, in order to simplify the investigation, it is assumed that all other design parameters remain unchanged while one design parameter is varied. Thus, the interdependence between different design parameters on the output torque is not considered, but will be investigated further by using an adaptive lumped parameter magnetic equivalent circuit model which is developed in Chapter 3.

The prototype flux-switching PM machine under investigation has stator outer diameter = 90mm, stator inner diameter = 45mm and airgap length = 0.5mm. The split ratio (ratio of stator inner diameter to stator outer diameter) will be optimized for maximum output torque at fixed copper loss as investigated in Chapter 4. The machine has rated output torque = 2.4Nm, rated current = 11Arms, rated current density = 10Arms/mm^2 and rated copper loss = 50W. The prototype flux-switching PM machine also has a relatively small aspect ratio (stator outer diameter = 90mm and stator axial length = 25mm), the measured output torque is found to be much lower than that obtained from 2-D finite element analysis due to significant 3-D end-effects. Thus, the 3-D end-effect in the flux-switching PM machine, together with that in surface-mounted magnet and interior

magnet machines, will be studied by 3-D finite element analysis. In addition, since the prototype flux-switching PM machine is a relatively small size machine, the influence of scaling will also be investigated analytically, with validation by finite element analyses.

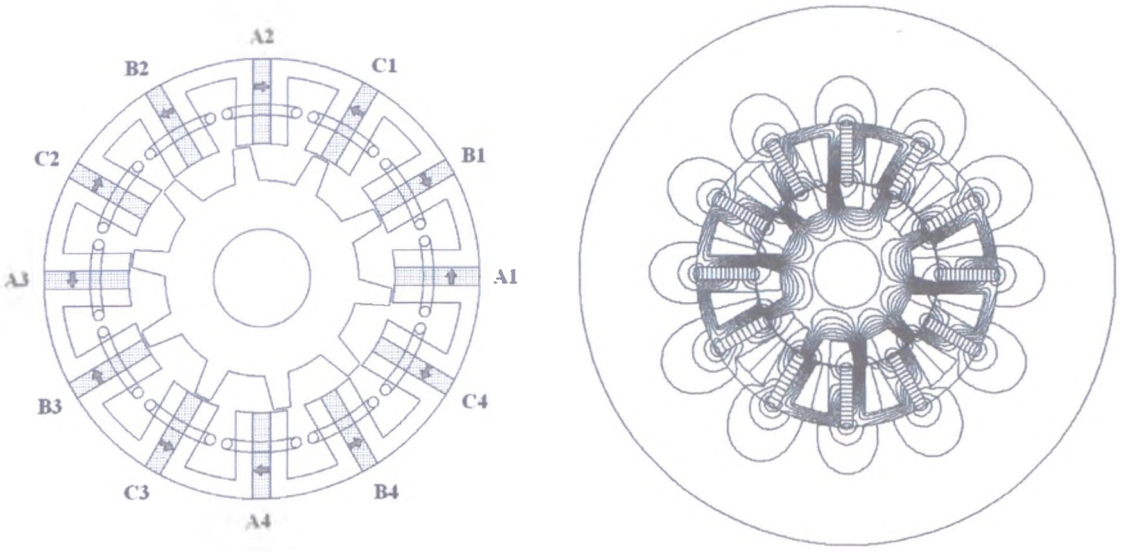

(a) Cross-section (b) Open-circuit flux distribution

Fig. 2.1. 3-phase, 10-rotor tooth, 12-stator slot flux-switching PM machine

2.2. Influence of design parameters

In [HOA97], which described the basic operating principle of flux-switching PM machines, the stator slot width b_s, the stator tooth width b_t and the stator magnet thickness b_m are assumed to be equal, i.e. $b_s = b_t = b_m$, as shown in Fig. 2.2.

However, no information has been published regarding the choice of the stator back-iron thickness, the rotor tooth width, the rotor back-iron thickness and the split ratio.

Therefore, in this chapter, the original design of a 3-phase, 10-rotor tooth, 12-stator slot flux-switching PM machine, which is shown in Fig. 2.1, will be initialized assuming:

$$b_s = b_t = b_m = b_t = b_p = \frac{T_s}{4} \tag{2.1}$$

$$Split\ ratio = 0.5 \sim 0.6 \tag{2.2}$$

where b_i is the stator and rotor back-iron thickness, b_p is the rotor tooth width, and T_s is the stator slot pitch.

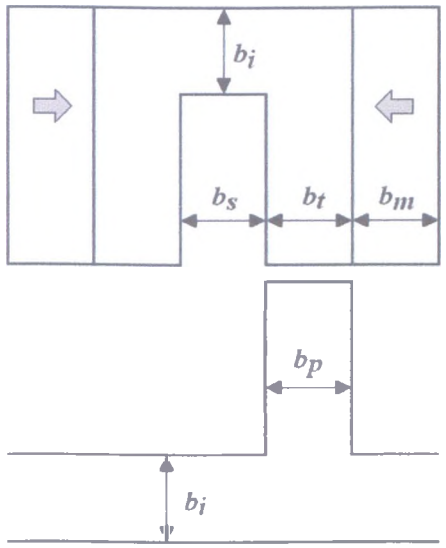

Fig. 2.2. Design parameters of flux-switching PM machine

The influence of all the design parameters will be investigated, except for the split ratio, which will be optimized later in subsequent chapters (Chapters 3 and 4) due to its complexity and importance. As mentioned earlier, in order to simplify the investigation, it is assumed that all other design parameters remain unchanged while one design parameter is varied.

Since the permanent magnets are located in the stator in flux-switching PM machines, the outer ends of the magnets are adjacent to the surrounding airspace and significant leakage flux exists, as will be evident from Fig. 2.1. Therefore, an appropriate outer boundary for the finite element analysis has to be determined. It was found that when the radius of the outer boundary is twice the outside radius of the stator its influence on the leakage flux distribution is negligible. Thus, this will be employed throughout the finite element analyses in this thesis.

2.2.1. Stator tooth width

The original flux-switching PM machine design has identical stator slot width b_s, stator tooth width b_t and stator magnet thickness b_m. The influence of varying the stator tooth width will be investigated in terms of its effect on the output torque, when the copper loss is fixed. In order to maintain the symmetry of the stator segments, the stator slot openings will be kept the same as the stator magnet thickness, i.e. $b_s = b_m$. Therefore, the equation $\frac{b_s}{2} + b_t + b_m + b_t + \frac{b_s}{2} = stator\ slot\ pitch$ is always satisfied.

Figs. 2.3(a) and (b) show flux-switching PM machines having 80% and 120% of the original stator tooth width, respectively. The calculated results, Fig. 2.2(c), show that the original design offers the highest output torque. Although the slot area is increased and the winding resistance is reduced by reducing the stator tooth width, thus permitting a higher current for a fixed copper loss, the phase flux-linkage, and, hence, the torque, is reduced significantly. Similarly, increasing the stator tooth width reduces the slot area, and, hence, the phase current has to be reduced for a fixed copper loss, which also leads to a reduction in the torque.

In summary, the original machine design, in which $b_s = b_t = b_m$, is the best choice for the maximum output torque.

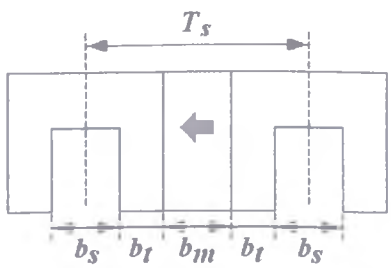

(a1) Tooth width=0.8×original width

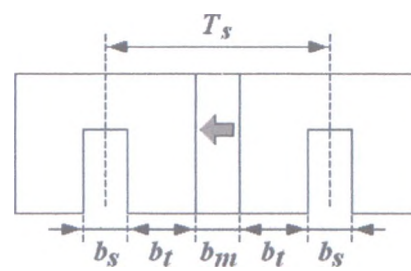

(b1) Tooth width=1.2×original width

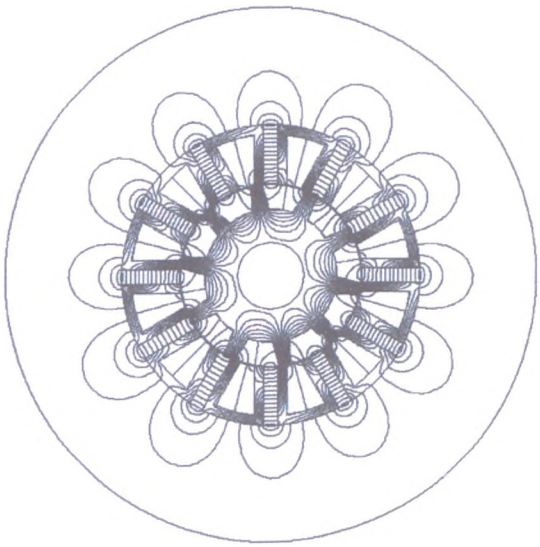

(a2) Tooth width=0.8×original width

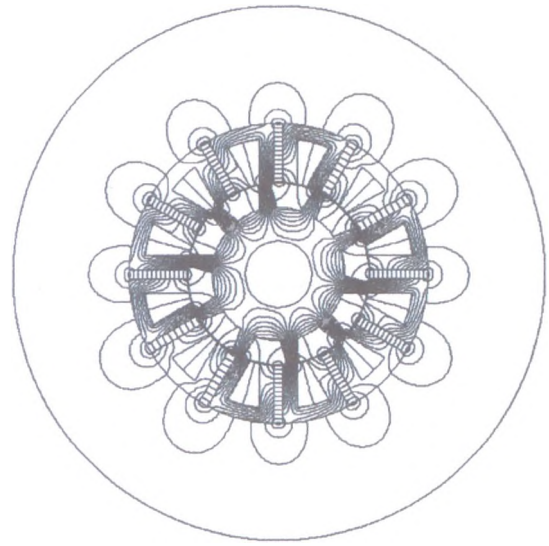

(b2) Tooth width=1.2×original width

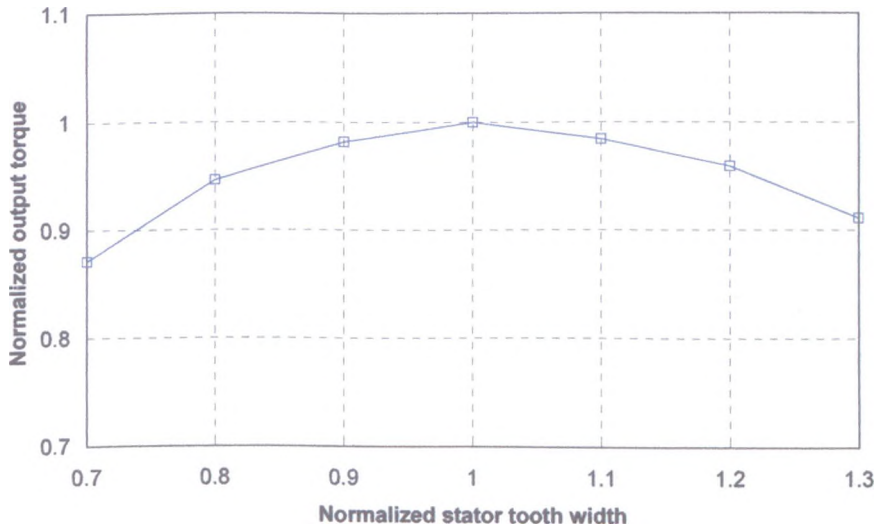

(c) Output torque vs. stator tooth width

Fig. 2.3. Variation of output torque with stator tooth width (fixed copper loss=50W)

2.2.2. Stator magnet volume

Section 2.2.1 showed that the original flux-switching PM machine offers a higher output torque than designs equipped with either thinner or thicker stator teeth. However, since the sintered NdFeB magnets which are employed in the prototype machine remain relatively expensive, it is desirable to minimize the magnet volume without sacrificing the machine performance.

The magnet volume can be reduced in the ways shown in Fig. 2.4(b), in which both the thickness and width of the magnets are reduced, and the angles of the tooth-tips are assumed to be 45°, while $b_s = b_t = b_m$, i.e. the stator tooth width and slot opening are not changed. As a result, when the magnet thickness is reduced, the slot area increases.

Fig.2.4(c) shows the variation of the output torque for a fixed copper loss. It can be seen that with a reduction in the magnet thickness, the output torque reduces. However, since the magnet volume reduces more quickly than the output torque, the ratio of the output torque to magnet volume increases. For example, if a 5% reduction in the output torque is acceptable, the volume of the magnet can be reduced by more than 20%, while if a 20% reduction in the output torque is acceptable, the volume of the magnet can be reduced by more than 50%.

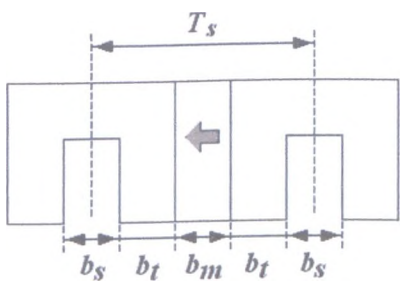

(a1) Original design

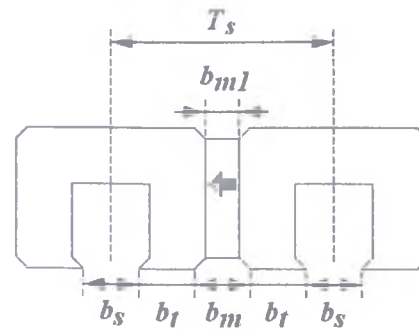

(b1) Reduced magnet thickness

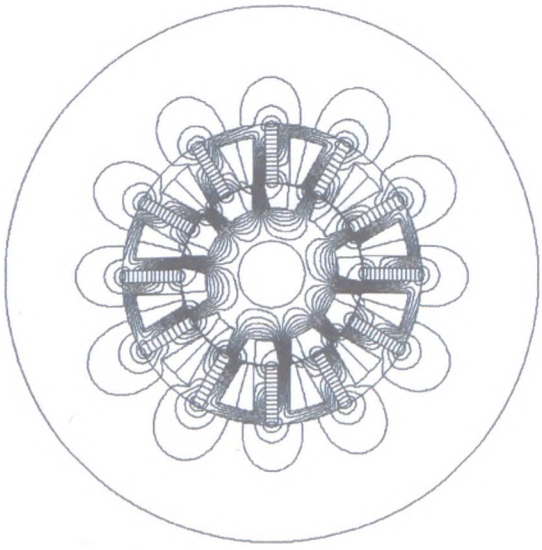

(a2) Original design

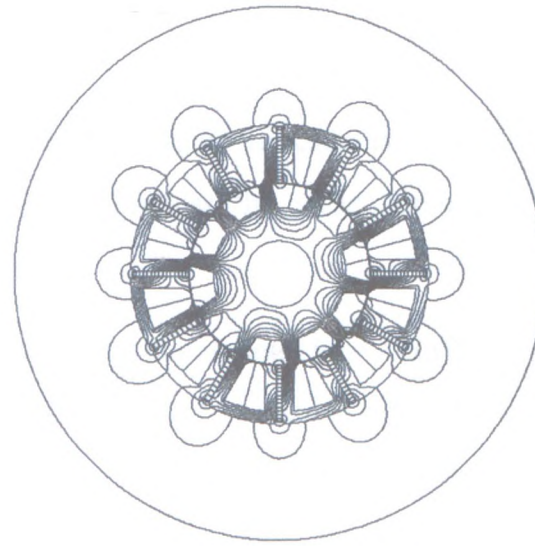

(b2) Reduced magnet thickness

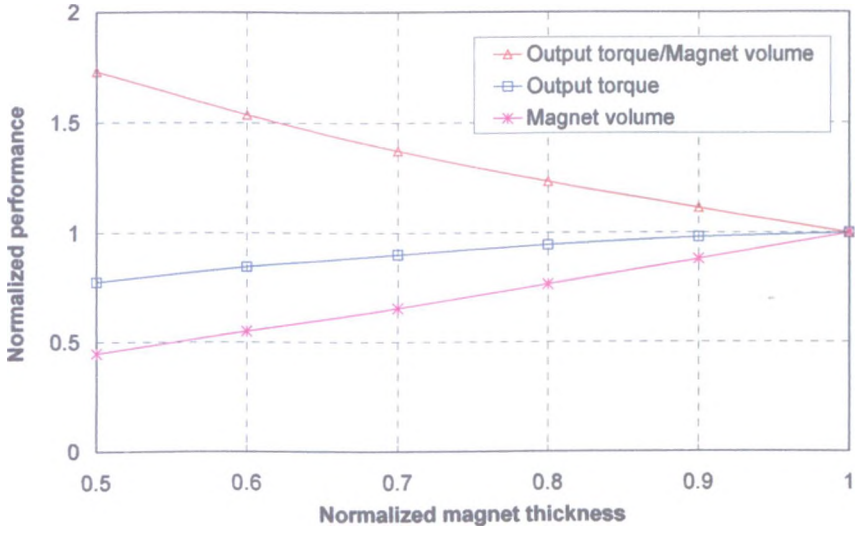

(c) Output torque and magnet volume vs. magnet thickness

Fig. 2.4. Variation of output torque with magnet thickness (fixed copper loss=50W)

2.2.3. Stator magnet shape

In section 2.2.2, the cross-section of the magnets was rectangular, and this remained unchanged when the magnet thickness was reduced. It was shown that reducing the magnet thickness decreases the output torque, but that the torque per magnet volume can be improved. Two different magnet shapes, viz. tapered and stepped, will be studied in this section, and the influence of the magnet volume on the output torque will be studied further.

Also, as was shown in the previous section, when the magnet thickness is reduced, the stator slot area is increased. Thus, for the same copper loss, the phase current can be increased.

Parallel stator slots, Fig. 2.5(b), instead of trapezoidal stator slots, Fig. 2.5(a), will be employed, as required by the sponsoring company in order to ease winding and also, potentially, to reduce the influence of magnetic saturation in the stator teeth. Although with parallel stator slots, the stator slot area generally becomes smaller, the phase flux-linkage is more or less unchanged, Fig. 2.5(c).

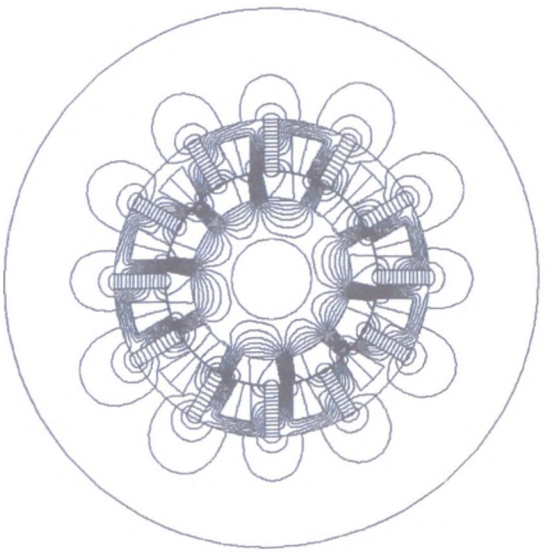

(a) Original design with parallel teeth

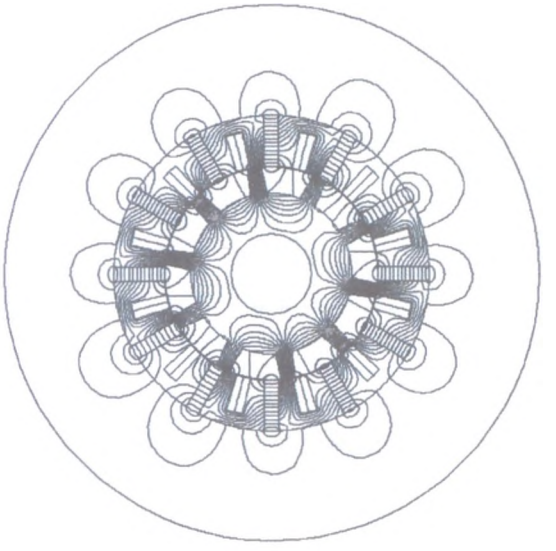

(b) Parallel slots

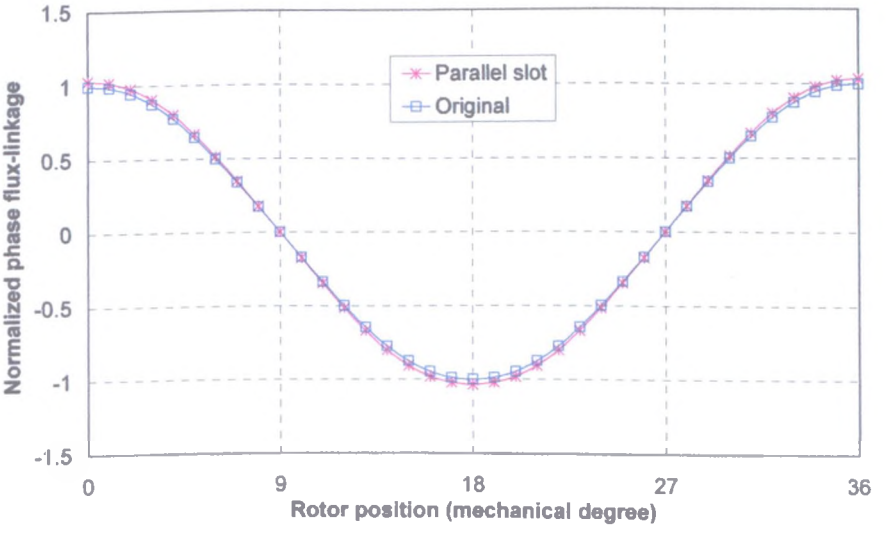

(c) Phase flux-linkage

Fig. 2.5. Flux-switching PM machine with different slot shapes

A. Tapered magnets

Fig. 2.6 shows the flux-switching PM machine equipped with tapered magnets, Fig. 2.6(a) having magnets which reduce in thickness and Fig. 2.6(b) having magnets which increase in thickness, from the inner to outer radius. The magnet thickness at the stator inner surface remains unchanged, while the stator tooth width, and the stator slot openings also remain identical.

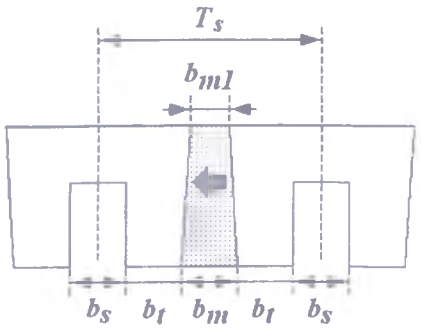

(a1) Reduced magnet

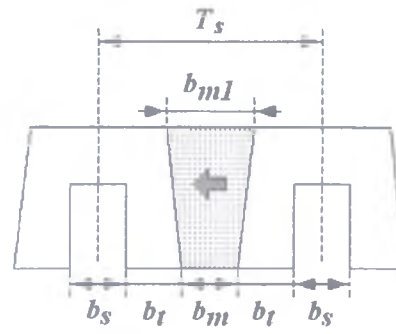

(b1) Increased magnet

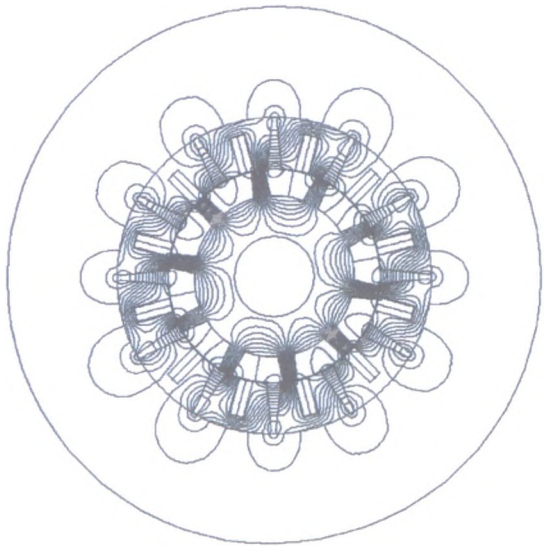

(a2) Reduced magnet

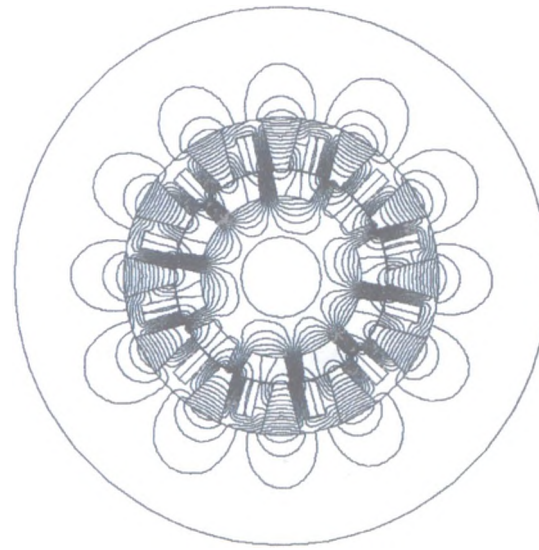

(b2) Increased magnet

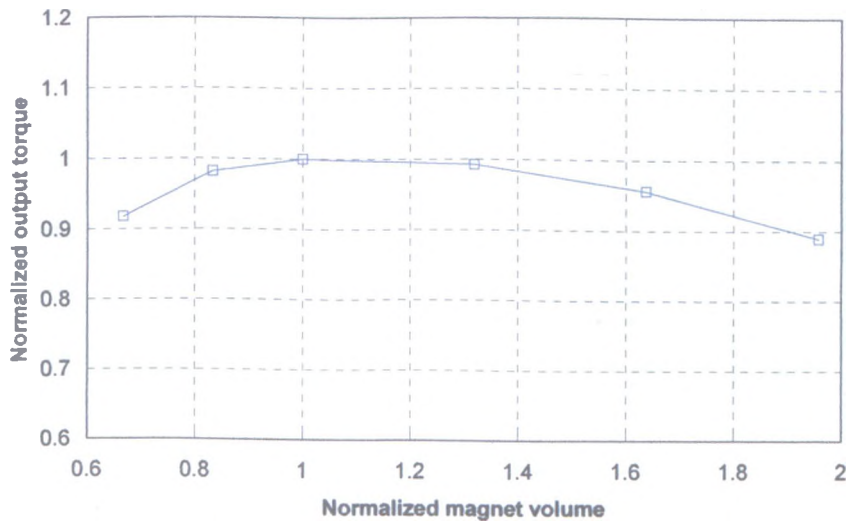

(c) Output torque vs. magnet volume

Fig. 2.6. Flux-switching PM machine with tapered magnets

The predicted output torque is shown in Fig. 2.6(d). It can be seen that no improvement in the torque is achieved, since reducing the magnet volume reduces the magnet flux, whilst increasing the magnet volume increases saturation in the stator teeth and flux leakage around the magnets.

B. Stepped magnets

With stepped magnets, each stator tooth is assumed to have two magnets of equal radial width. Only the thickness of the outer magnet is changed. Fig. 2.7 shows the flux-switching PM machine with reduced outer magnet thickness, Fig. 2.7(a), and with increased outer magnet thickness, Fig. 2.7(b).

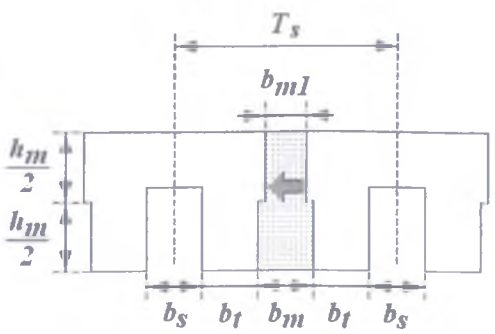

(a1) Reduced magnet

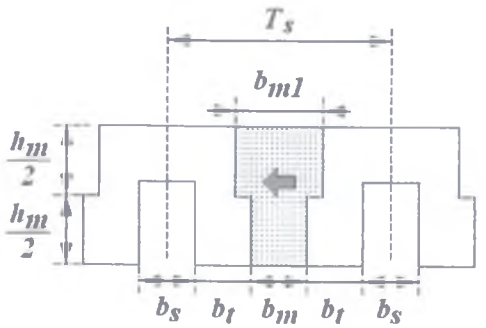

(b1) Increased magnet

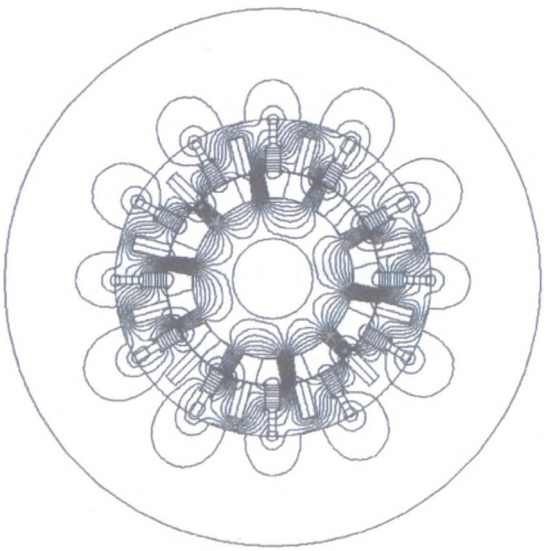

(a2) Reduced magnet

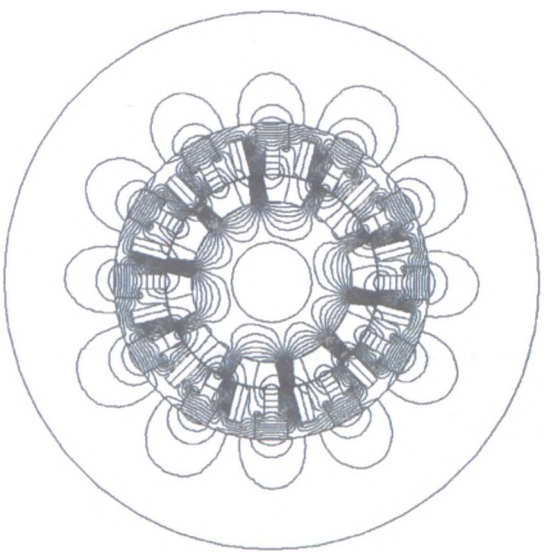

(b2) Increased magnet

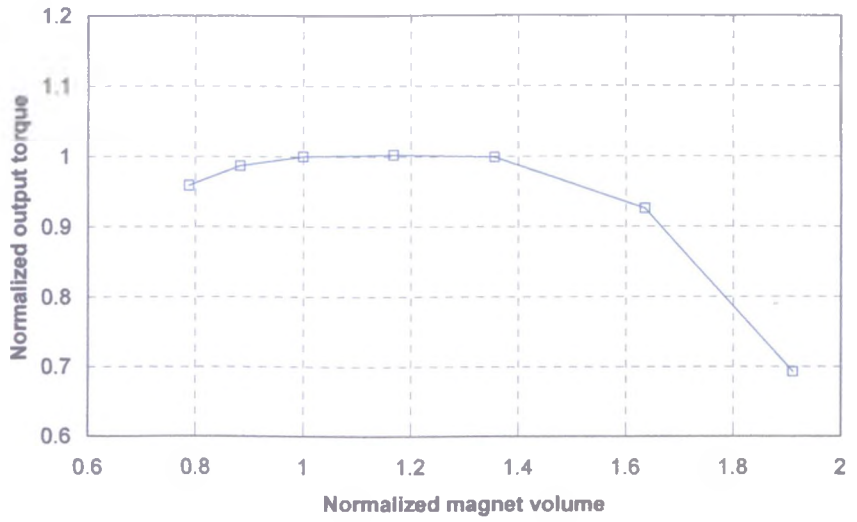

(c) Output torque vs. magnet volume

Fig. 2.7. Flux-switching PM machine with stepped magnets

The predicted output torque is shown in Fig. 2.7(c), from which it can be seen that, similar to the flux-switching PM machine with tapered magnets, the potential for improving the output torque by employing stepped magnets is very limited. Reducing the volume of the stepped magnets decreases the output torque due to the reduction of the magnet flux, while increasing the volume of the stepped magnets increases the output torque only slightly. A further increase in the volume of the stepped magnets reduces the output torque due to an increase in magnetic saturation in the stator teeth and flux leakage around the magnets.

2.2.4. Stator back-iron thickness

In the original flux-switching PM machine design the stator back-iron thickness was the same as the stator tooth width, as shown in Fig. 2.8(a). However, from the flux distribution, it can be seen that the flux density in the stator back-iron is much lower than that in the stator teeth. Therefore, in order to fully utilize the space envelope, the thickness of the stator back-iron can be reduced, as shown in Fig. 2.8(b), to bring the flux density in the back-iron to a similar level as that in the teeth. By doing so, the slot area is increased, and a higher phase current can be supplied for the same copper loss.

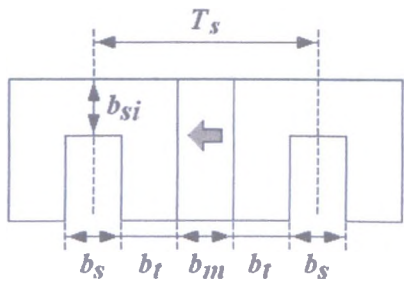

(a1) Original design

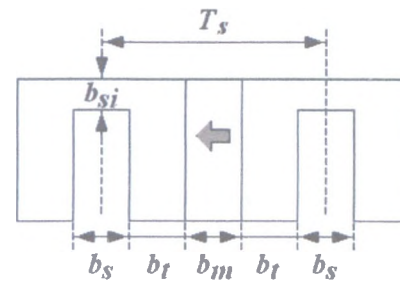

(b1) Reduced stator back-iron thickness

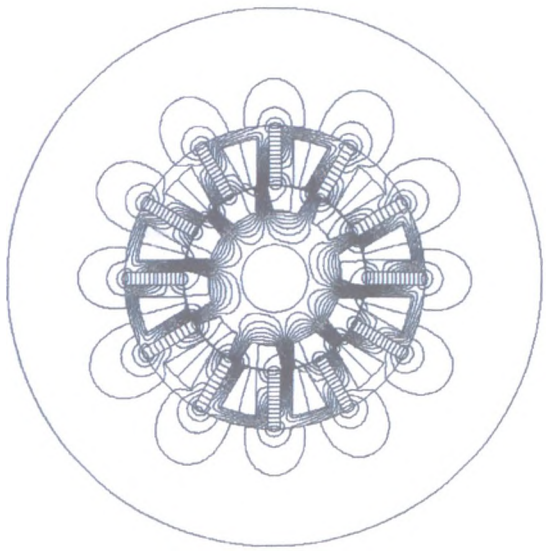

(a2) Original design

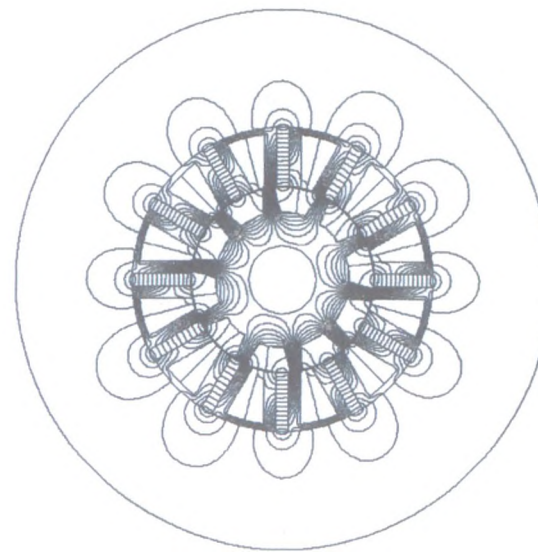

(b2) Reduced stator back-iron thickness

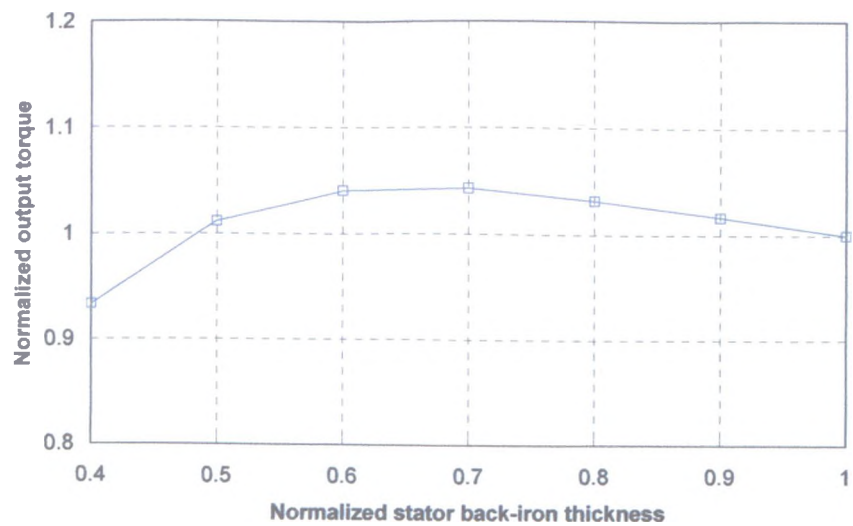

(c) Output torque vs. stator back-iron thickness

Fig. 2.8. Variation of output torque with stator back-iron thickness (fixed copper loss=50W)

Ultimately, the output torque can be enhanced. The calculated results in Fig. 2.8(c) show that when the thickness of the stator back-iron is reduced by around a third, the output torque is increased by ~5%.

2.2.5. Stator lamination bridge thickness

In the original flux-switching PM machine design, the stator lamination comprised of 12 separate 'U'-shaped laminated segments, as shown in Fig. 2.9(a). There were no bridges between the 'U'-shaped segments. The advantage of such a design is that the laminated modular stator segments can be manufactured by a small stamping machine. However, the disadvantage of this design is also very obvious, in that assembling 12 'U'-shaped stator segments with 12 permanent magnets is relatively difficult. In particular, to ensure the concentricity of a total of 24 components is very difficult to achieve, as experienced during prototyping.

If bridges between each pair of 'U'-shaped stator laminated segments can be added, as illustrated in Fig. 2.9(b), the stator lamination then can be made as a single unit. As a result, stator assembly can be significantly simplified, and each 'U'-shaped segment will be in exactly the right place. Of course, in this case, a relatively large stamping facility would be required, compared with that for the original design.

Clearly, however, such ferromagnetic bridges at the outer ends of the magnets will short-circuit part of the flux produced by each magnet, as shown in Figs. 2.9(c) and 2.9(d). Fig. 2.9(d) shows that if the bridges are too thick, much of the flux produced by the magnets will pass through the bridge rather than be directed to the airgap. Consequently, the phase flux-linkage is reduced significantly. Thus, the influence of the bridge thickness on the machine performance needs to be carefully investigated.

From the results shown in Fig. 2.9(e), it can be seen that from the machine performance point of view, the addition of a narrow bridge is likely to be acceptable, since the reduction in the magnet flux is very small. For example, a bridge which is 0.15 times the stator tooth width (i.e. 0.5mm for the prototype machine) reduces the torque by only

~1%. Even if the thickness of the bridge needs to be doubled, from a consideration of the mechanical stress and the feasibility of stamping the lamination, the reduction in the torque is still only ~5%, which, again, may be acceptable if the manufacture can be significantly simplified.

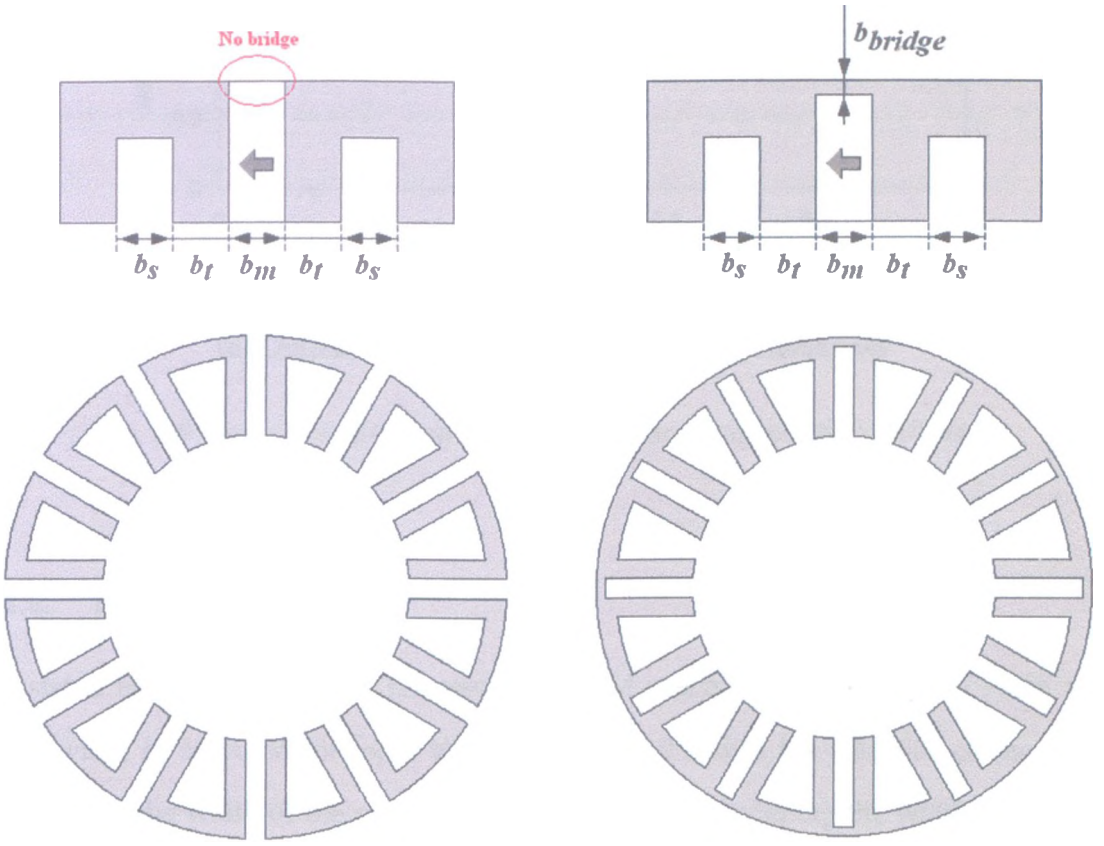

(a) Original design

(b) Bridge thickness=0.5mm

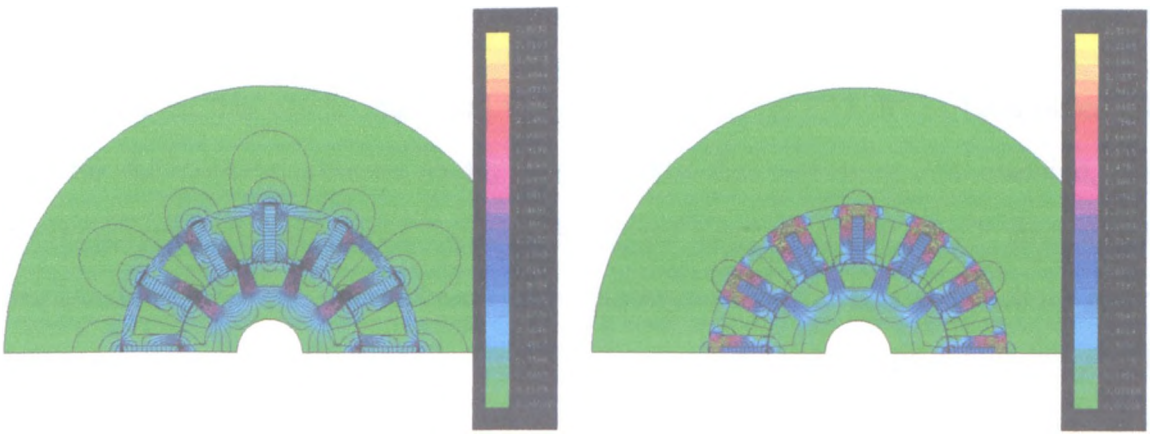

(c) Bridge thickness=0.15×tooth width

(d) Bridge thickness=1.0×tooth width

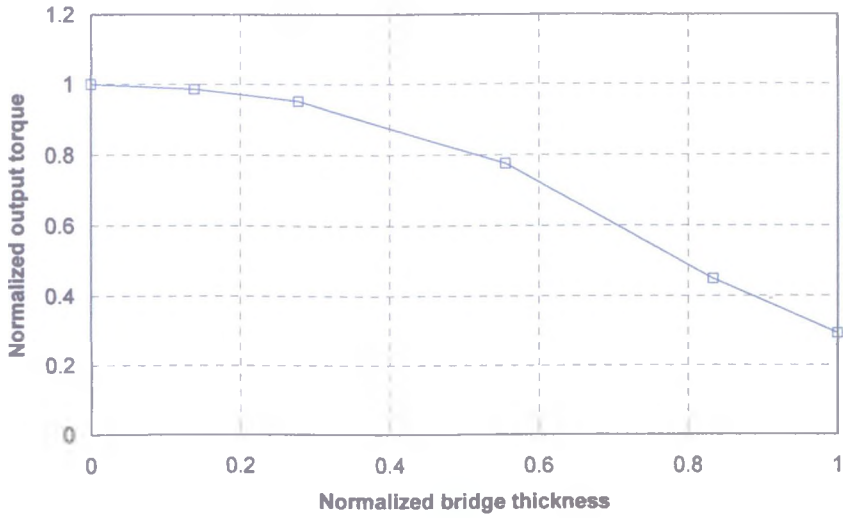

(e) Output torque vs. stator magnet bridge thickness

Fig. 2.9. Variation of output torque with stator magnet bridge thickness

2.2.6. Rotor tooth width

As stated earlier, the original flux-switching PM machine design had the same rotor tooth width b_p as the stator tooth width b_t. Fig. 2.10 shows the variation of the output torque with the width of the rotor tooth. As can be seen, reducing the width of the rotor tooth reduces the output torque. However, when the rotor tooth width is increased, the torque increases, and is a maximum when the tooth width is ~1.6 times the original value.

The reason for this can be explained with reference to Fig. 2.11. It has been observed that for the 3-phase, 10-rotor tooth, 12-stator slot flux-switching PM machine, the maximum phase A flux-linkage occurs when the centre of a rotor tooth is 9° mechanical displaced from the axis of the phase A coil, as shown in Fig. 2.11(a), in which the rotor tooth and stator tooth are not fully aligned. The phase A flux-linkage can be increased further if a greater proportion of the rotor tooth surface can be aligned with the stator tooth surface when the centre of the rotor tooth is still 9° mechanical displaced from the axis of the phase A coil, i.e. the phase A flux-linkage can be increased if a wider rotor tooth width is employed, which has its left edge aligned with the left edge of the stator

tooth, as illustrated in Fig. 2.11(b). The required rotor tooth-arc can be calculated as:

$$\theta_p = \left(9^o - \frac{7.5^o}{2}\right) \times 2 = 10.5^o \text{ mechanical} \tag{2.3}$$

This is 1.4 times that of the original rotor tooth-arc. Of course, in reality, when the influence of magnetic saturation and flux leakage are considered, the optimal rotor tooth-arc may not be exactly 1.4 times that of the original, Indeed, from the finite element calculations in this section it is ~1.6 times the original tooth-arc. Further increasing the tooth-arc causes an increase in flux leakage at the slot openings and the inner radius of the magnet, which reduces the phase flux-linkages and, hence, the torque.

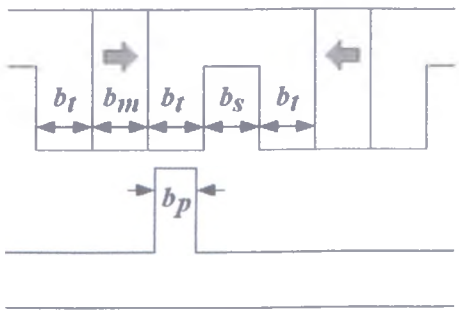

(a1) Rotor tooth width=0.6×original width

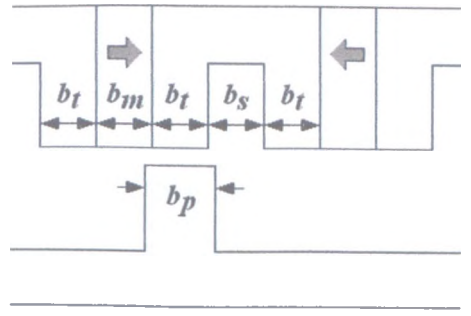

(b1) Rotor tooth width=1.4×original width

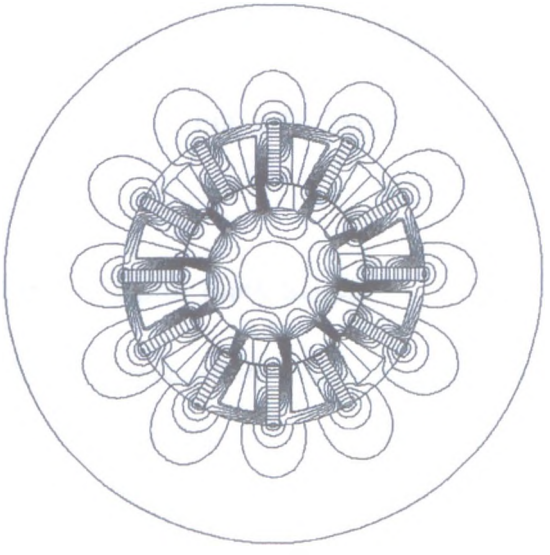

(a2) Rotor tooth width=0.6×original width

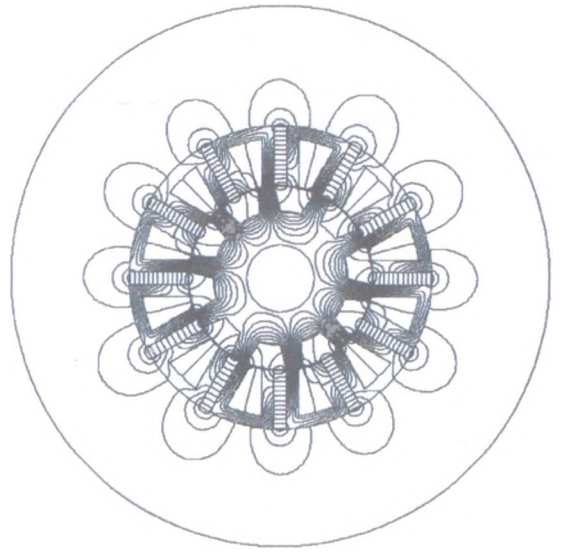

(b2) Rotor tooth width=1.4×original width

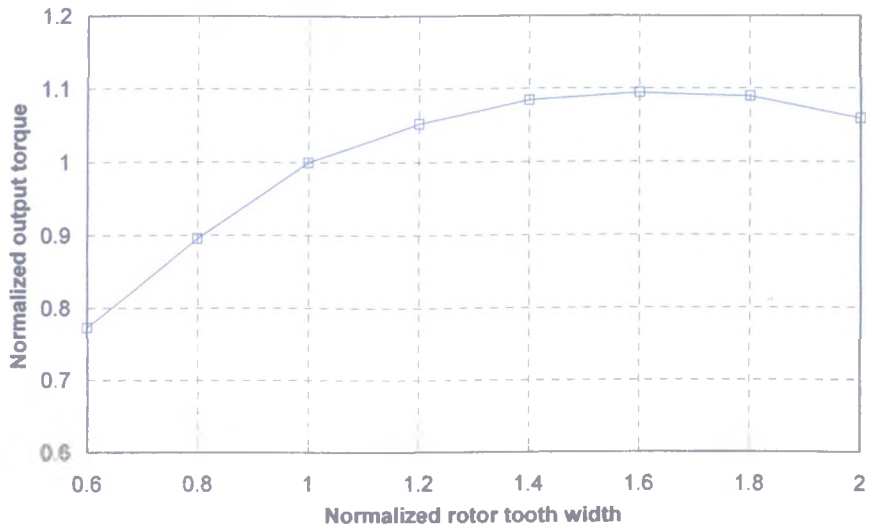

(c) Output torque vs. rotor tooth width/original width

Fig. 2.10. Variation of output torque with rotor tooth width

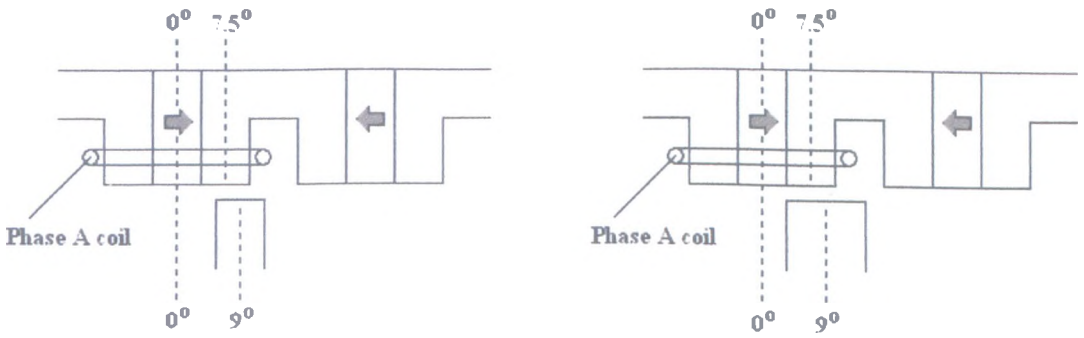

(a) Rotor tooth width=original width (b) Rotor tooth width=1.4×original width

Fig. 2.11. Variation of output torque with rotor tooth width

2.2.7. Rotor tooth height

The influence of the radial height of the rotor tooth is now investigated. As will be evident from Fig. 2.12(c), zero electromagnetic torque will be produced without rotor saliency, Fig. 2.12(a), although, as will be seen later, the reluctance torque is negligible in a flux-switching PM machine.

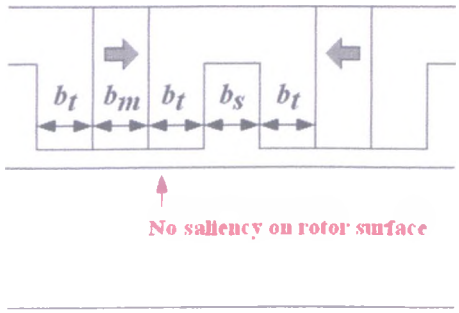

(a1) Rotor tooth height=0

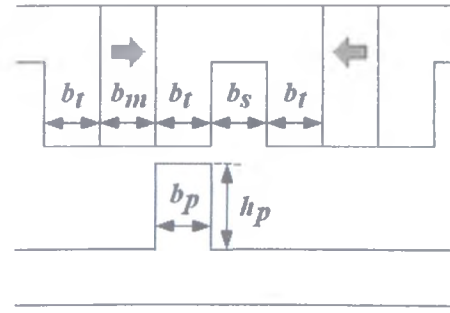

(b1) Rotor tooth height=2×stator tooth width

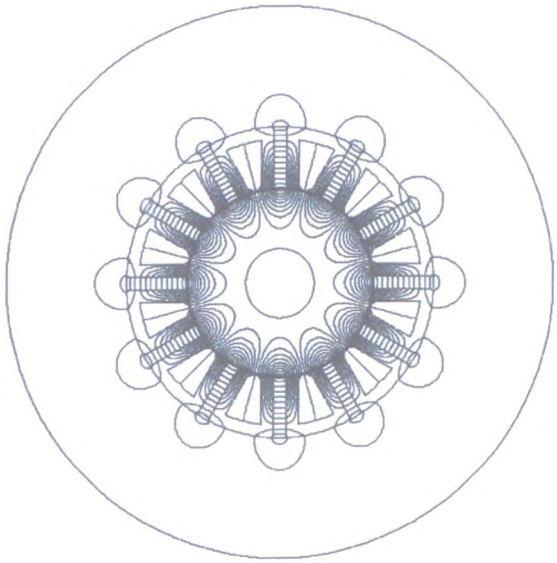

(a2) Rotor tooth height=0

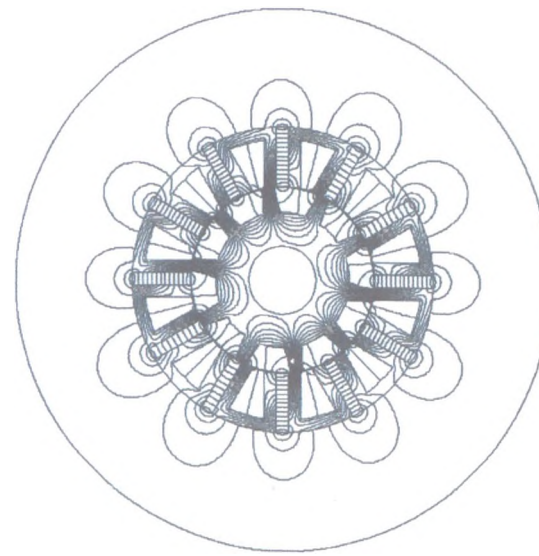

(b2) Rotor tooth height=2×stator tooth width

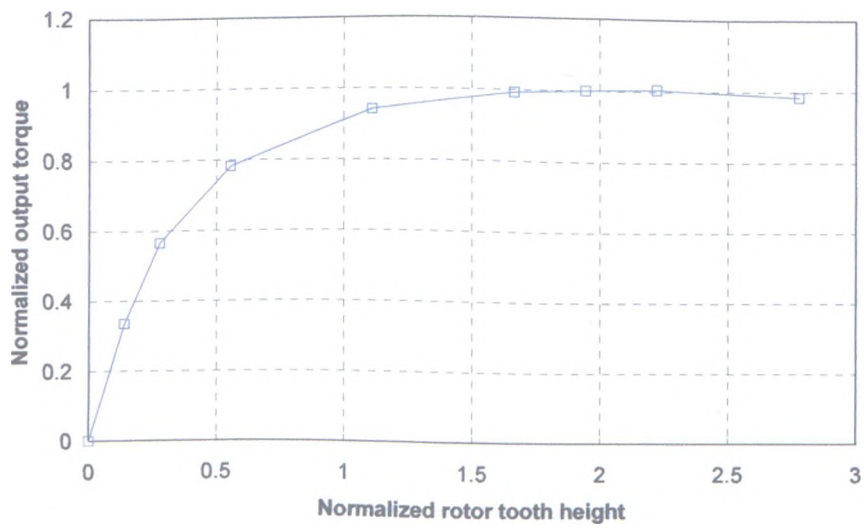

(c) Output torque vs. rotor tooth height

Fig. 2.12. Variation of output torque with rotor tooth height

As the radial height of the rotor tooth is increased, the torque increases, maximum torque being obtained when the radial height of the rotor tooth is around twice the stator tooth width. Further increasing the radial height of the rotor tooth reduces the torque, due to the increase in the magnetic potential drop in the rotor tooth body and an increase in flux leakage.

2.2.8. Rotor tooth shape

A. Trapezoidal shape

All the flux-switching PM machines, which have been considered in the foregoing investigations, have had square shaped rotor tooth. Two alternative rotor tooth shapes, viz. trapezoidal and curved, as illustrated in Figs. 2.13 and 2.14, are now considered. More specifically, the influence of the rotor tooth width b_{p1} of the trapezoidal rotor tooth and the slot depth h_p of the curved rotor tooth will be investigated.

Fig. 2.13(c) shows that if the rotor tooth width b_{p1} is smaller than the rotor tooth-arc, the magnetic potential drop in the rotor tooth will be increased, since the whole rotor tooth becomes highly saturated. By increasing the rotor tooth width b_{p1}, saturation can be reduced, and as a result, the magnetic potential drop is reduced and the torque is increased. The torque is a maximum when the rotor tooth width b_{p1} is ~2 times that of the original stator tooth width. There is no benefit in further increasing the rotor tooth width.

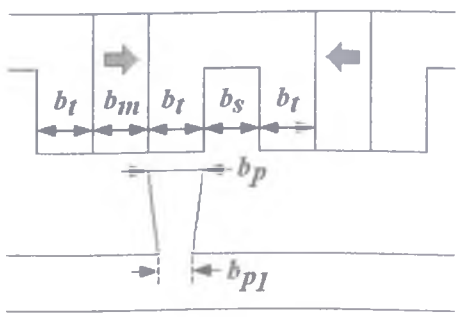

(a1) $b_{p1} < b_p$

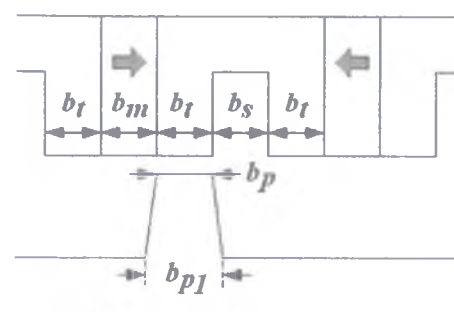

(b1) $b_{p1} > b_p$

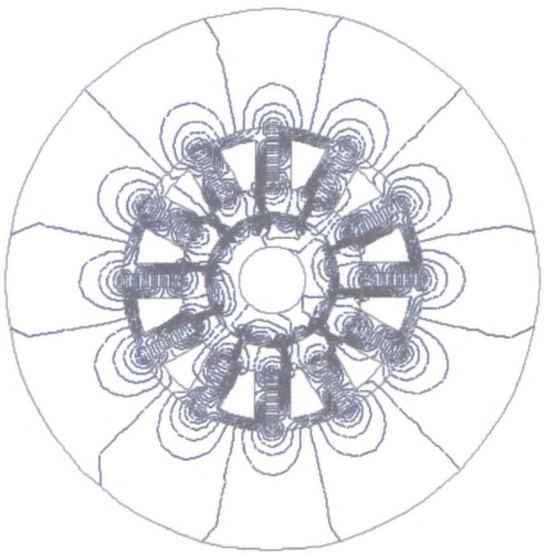

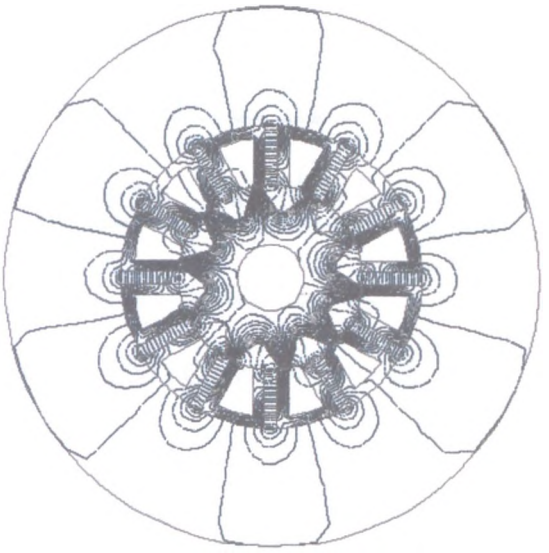

(a2) $b_{pl} < b_p$ (b2) $b_{pl} > b_p$

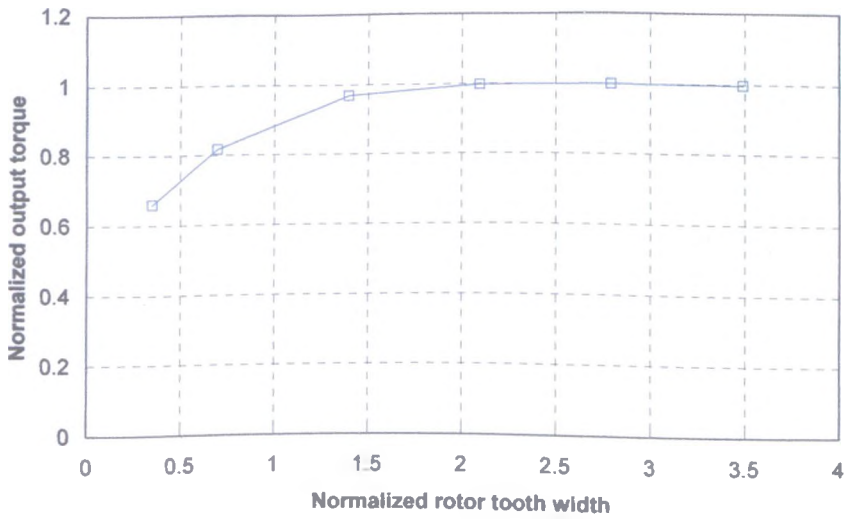

(c) Output torque vs. rotor tooth width

Fig. 2.13. Influence of rotor tooth shape (trapezoidal rotor tooth)

B. Curved shape

Fig. 2.14 shows the influence of varying the depth of the rotor teeth when they are curved. With an increase in the rotor tooth depth h_p, the torque increases, and is a maximum when h_p is equal to ~1.5 times the stator tooth width. Further increasing h_p decreases the torque due to an increase in the magnetic potential drop in the rotor tooth and an increase in flux leakage.

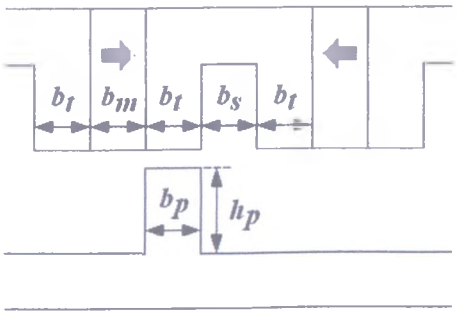

(a1) Square rotor tooth

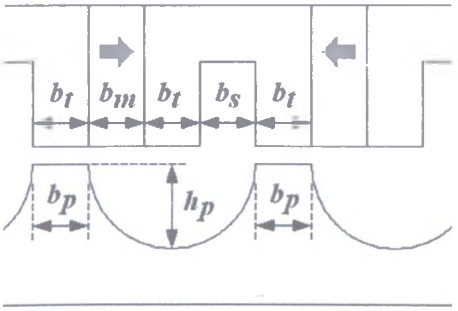

(b1) Curved rotor tooth

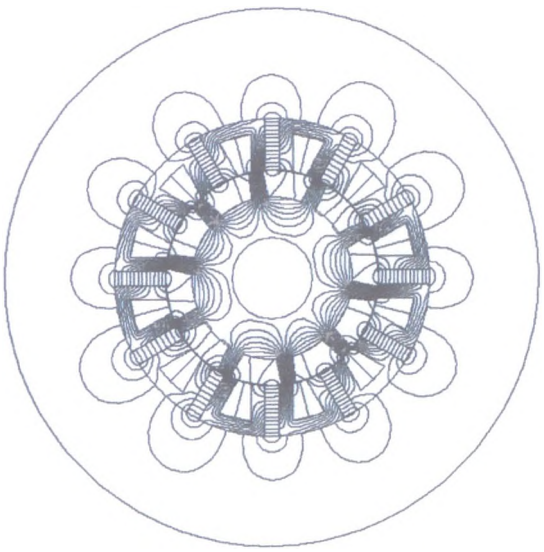

(a2) Square rotor tooth

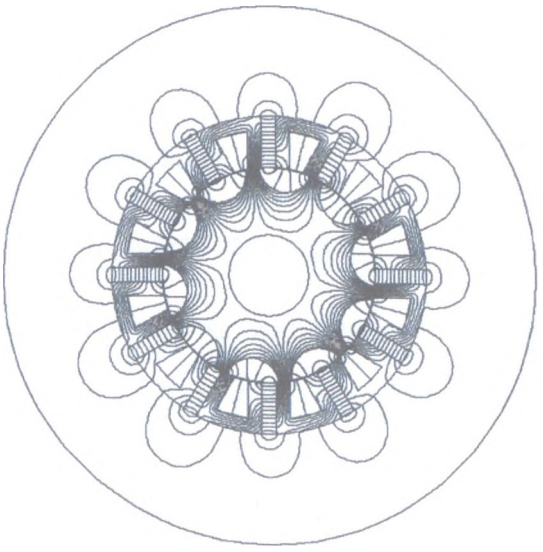

(b2) Curved rotor tooth

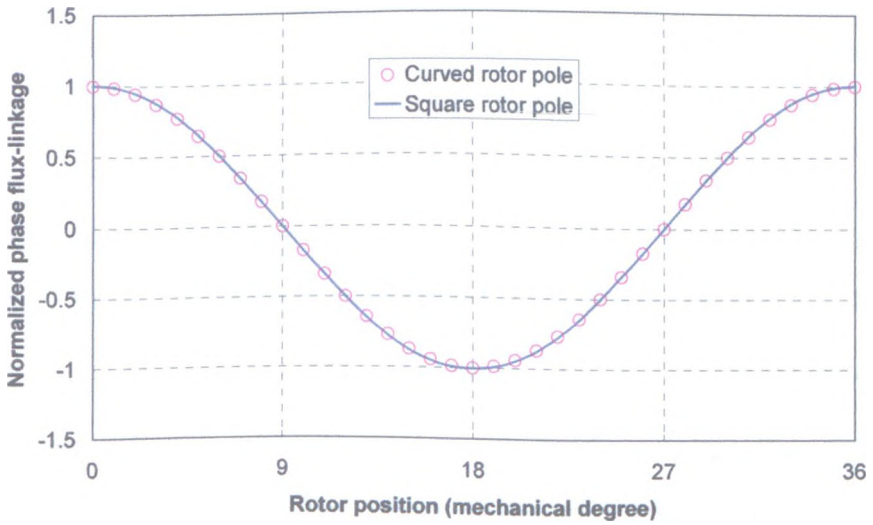

(c) Phase flux-linkage

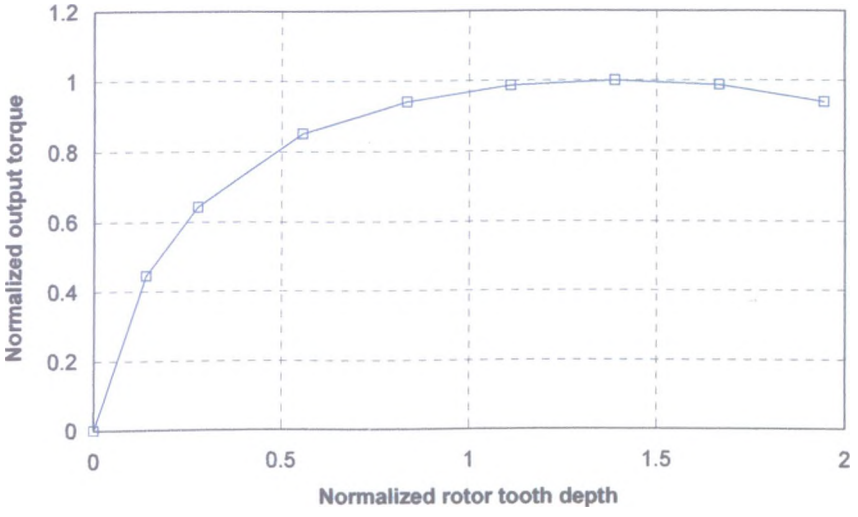

(d) Output torque vs. rotor tooth depth

Fig. 2.14. Influence of rotor tooth shape (curved rotor tooth)

Comparing the performance of flux-switching PM machines with optimized square rotor teeth and optimized curved rotor teeth, Fig. 2.14(c), their open-circuit phase flux-linkages are almost identical.

2.2.9. Rotor back-iron thickness

The influence of the thickness of the rotor back-iron has also been investigated. From Fig. 2.15(a), it can be seen that if the rotor back-iron thickness is too small, the saturation will be excessive, and this significantly reduces the output torque. In contrast, if the available cross-sectional area inside the rotor teeth is used for the back-iron, as shown in Fig. 2.15(b), saturation is reduced very significantly. From Fig. 2.15(c), it can be seen that when the rotor back-iron thickness is only $1/5$ of the stator tooth width, the torque capability is less than half the value for the original flux-switching PM machine. However, with an increase in the back-iron thickness, the torque initially increases, when the thickness is higher than the stator tooth width, the torque remains unchanged. Thus, the minimum rotor back-iron thickness is the same as the stator tooth width. Thicker rotor back-iron can be used, but will not enhance torque capability.

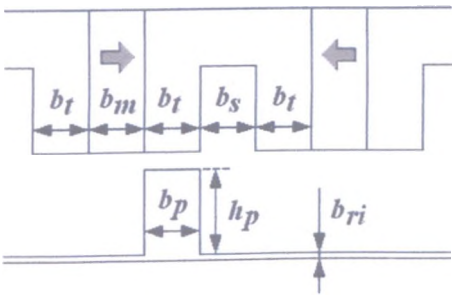

(a1) Rotor back-iron thickness=0.2×tooth width

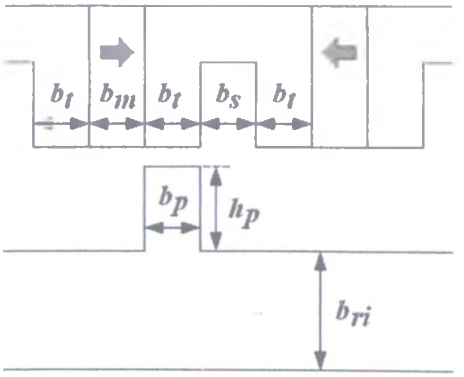

(b1) Rotor back-iron thickness=maximum

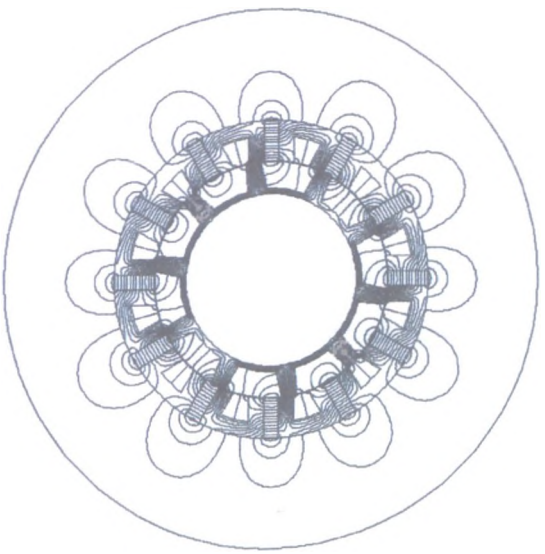

(a2) Rotor back-iron thickness=0.2×tooth width

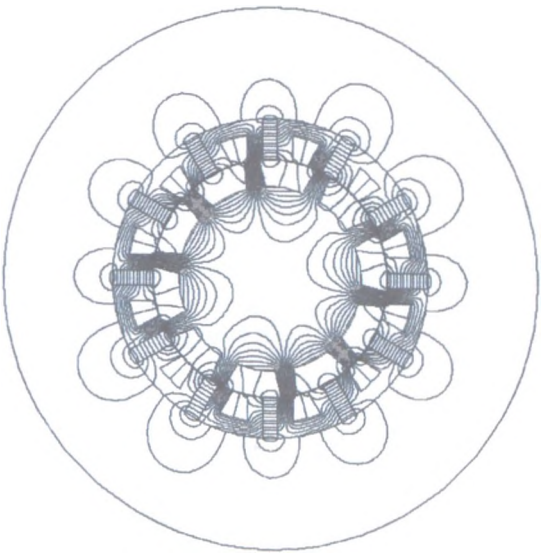

(b2) Rotor back-iron thickness=maximum

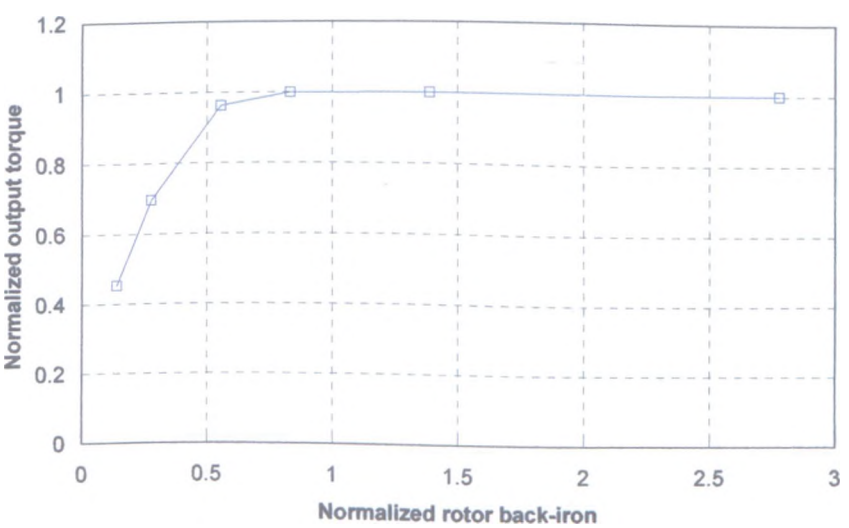

(c) Output torque vs. rotor back-iron thickness

Fig. 2.15. Influence of rotor back-iron thickness

2.3. Electromagnetic performance of flux-switching PM machine

In the preceding section, the influence of varying various design parameters on the torque capability has been investigated. In this section, the electromagnetic performance of the flux-switching PM machine will be studied systematically by 2-D finite element analysis. The specification of the prototype flux-switching PM machine under consideration is given in Appendix I.

The stator has the same tooth width as circumferential thickness of permanent magnet, which is the optimal value for the maximum output torque according to the foregoing investigation. The stator back-iron thickness is kept the same as the tooth width, since magnetic saturation in the stator back-iron will increase when the machine is loaded. Two rotors, one with the original rotor tooth-arc (equal to the stator tooth width) and another with the optimal rotor tooth-arc (equal to 1.4 times the stator tooth width), will be considered, so that the performance improvement can be quantified.

A. Open-circuit flux distribution

The open-circuit flux distributions of the two flux-switching PM machines are shown in Fig. 2.16. As can be seen the localized flux density can be extremely high, especially at the tooth-tips and in the rotor teeth.

B. Airgap field distribution

Due to the doubly salient topology, the airgap field distribution in a flux-switching PM machine is very non-sinusoidal and exhibits significant harmonics. The finite element calculated radial-component of the airgap flux density B_g is shown in Fig. 2.17. As will be seen, for the machines under consideration, the maximum airgap flux density exceeds 2T, while the average airgap flux density is ~0.69T. It also can be seen that by optimizing the rotor tooth-arc, the region of the airgap with a high flux density is increased slightly. As a result, the average airgap flux density is increased.

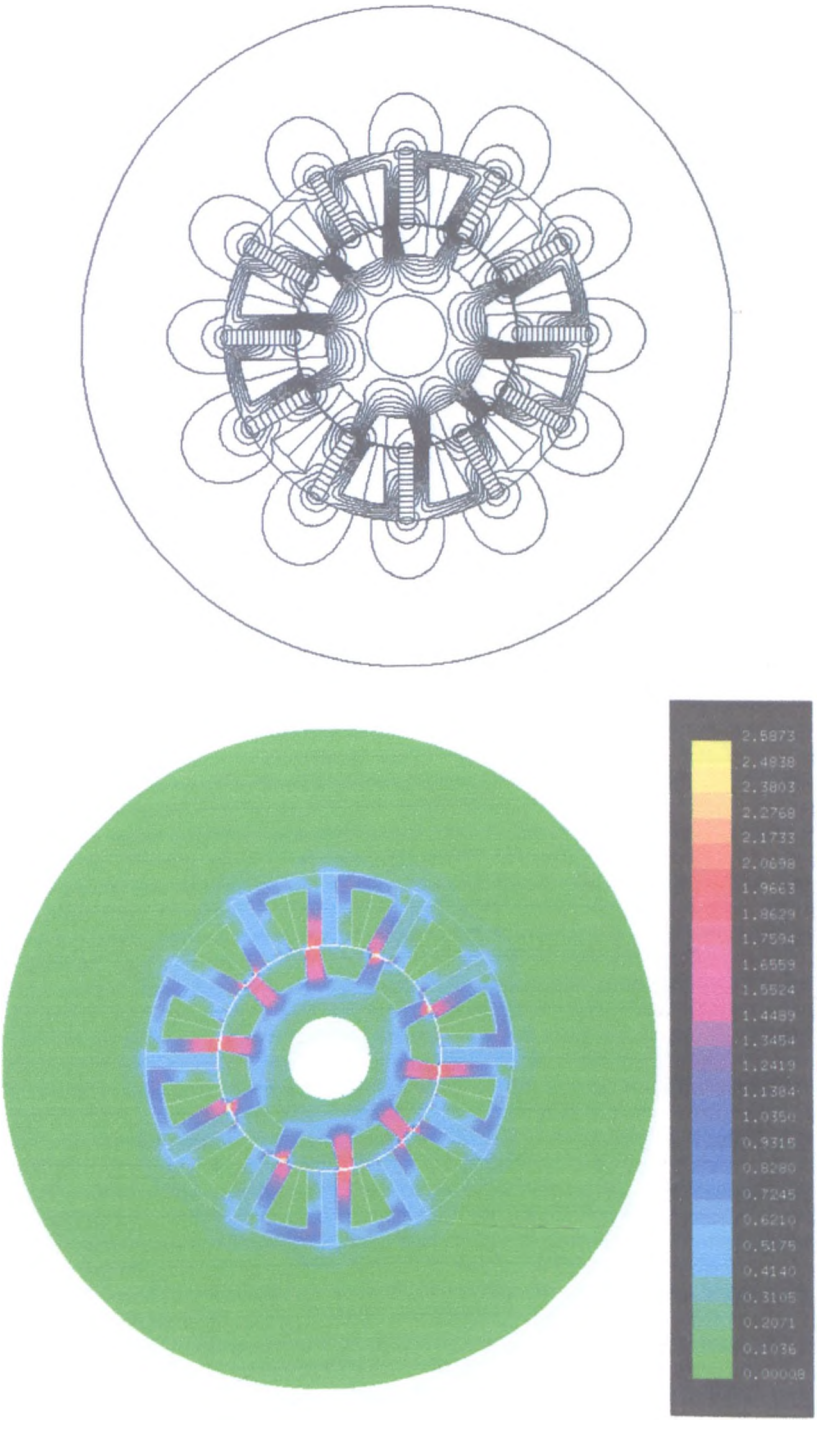

(a) Original rotor tooth width

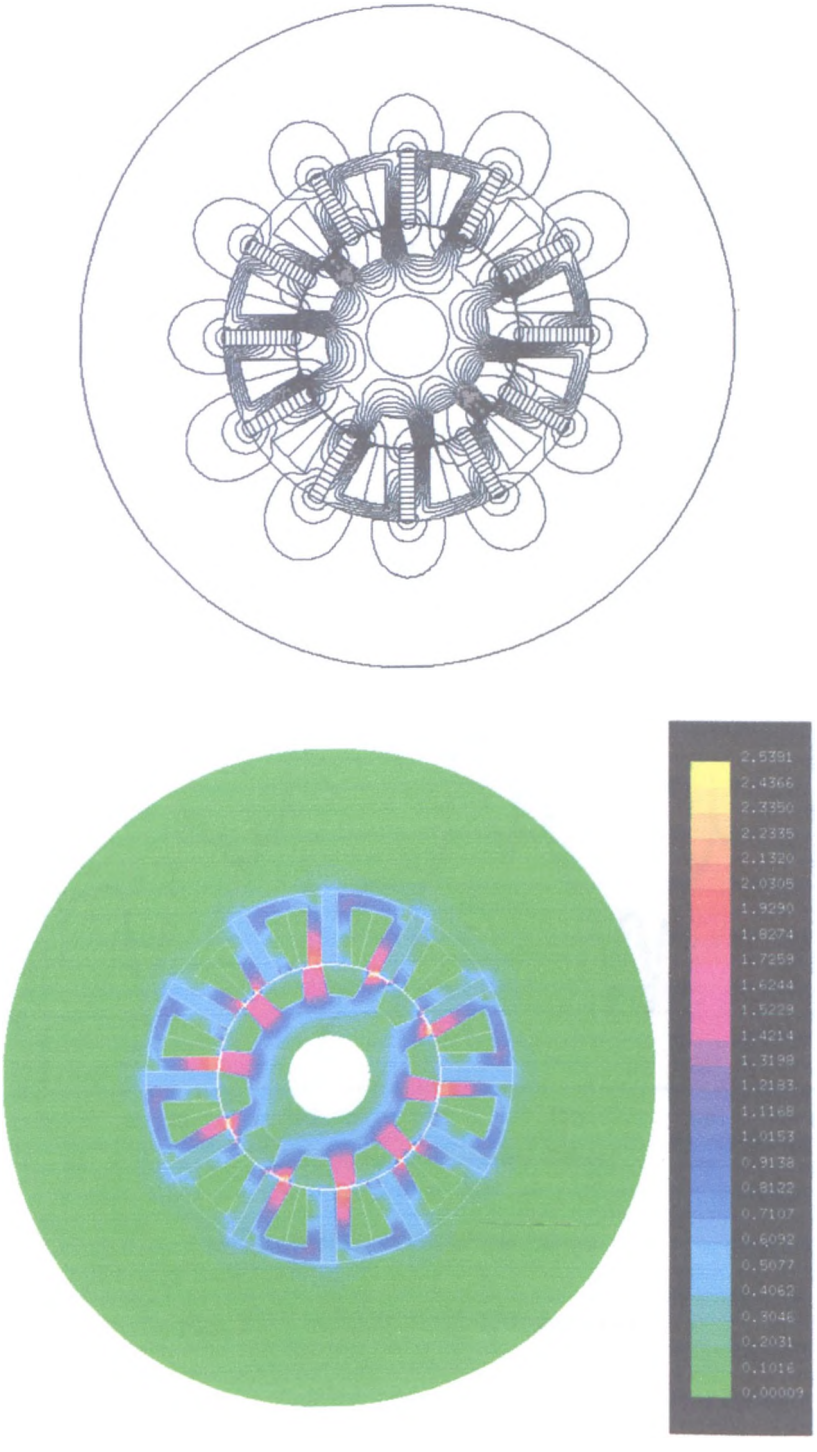

(b) Optimal rotor tooth width

Fig. 2.16. Open-circuit flux distributions

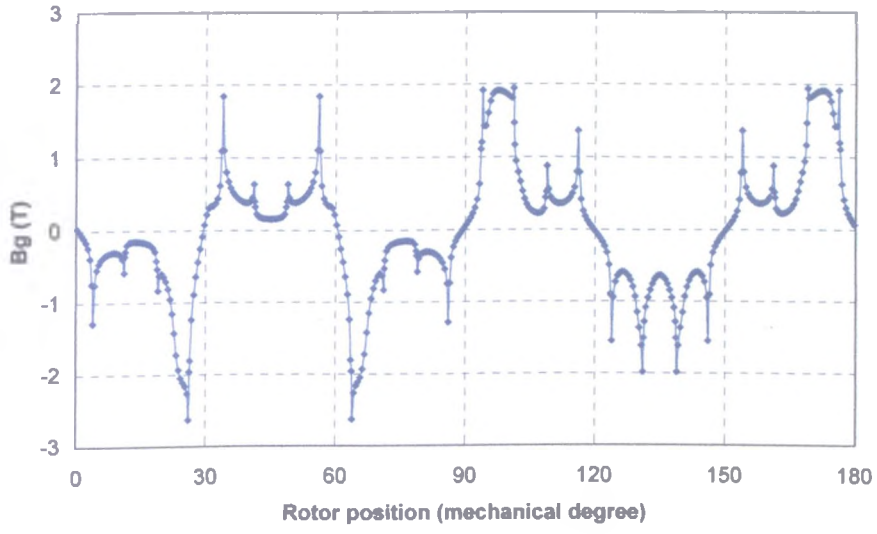

(a) Original rotor tooth width

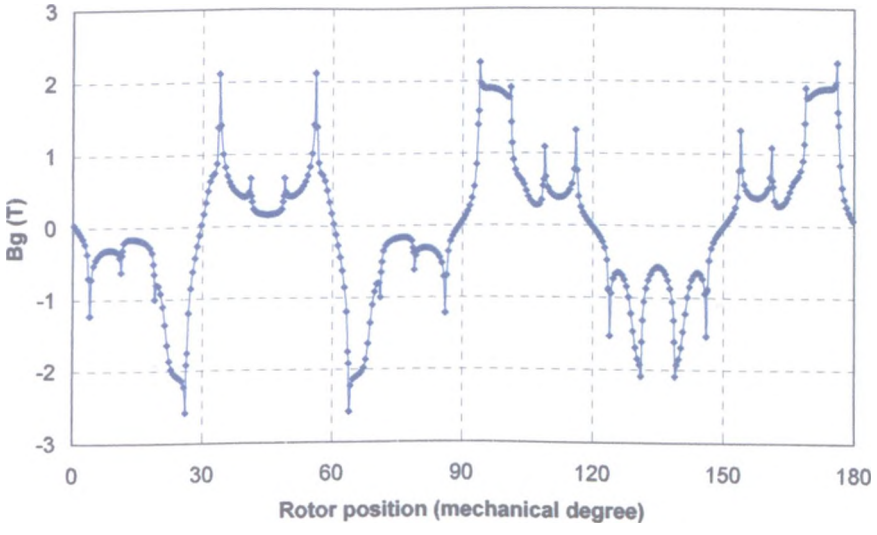

(b) Optimal rotor tooth width

Fig. 2.17. Airgap field distributions

C. Phase flux-linkage and phase back-emf

Although the airgap field distribution of a flux-switching PM machine is very non-sinusoidal, the phase flux-linkage and resultant phase back-emf waveforms are essentially sinusoidal, as shown in Fig. 2.18, since each of the two pairs of coils associated with a phase winding have slightly different flux-linkage and back-emf waveforms, as was mentioned in Chapter 1. By using the optimized rotor tooth-arc, the amplitude of both the phase flux-linkage and back-emf waveforms is increased slightly.

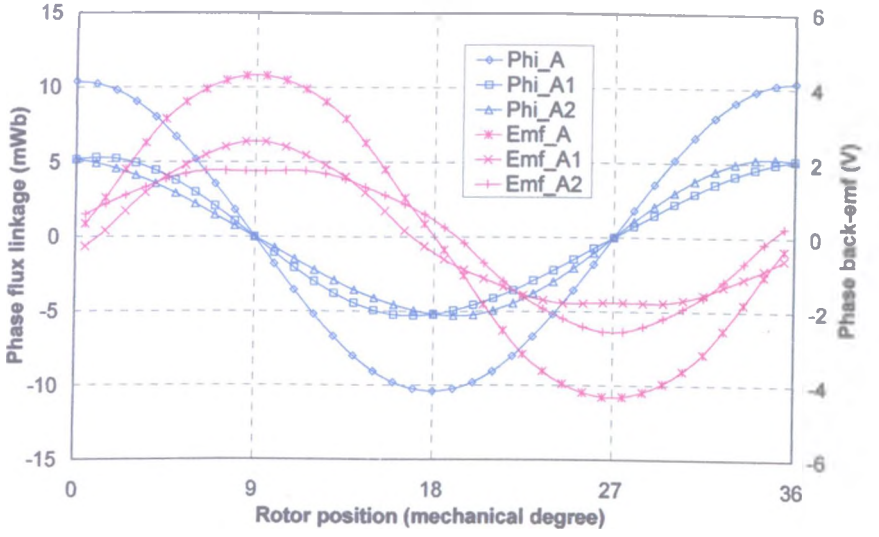

(a) Original rotor tooth-arc

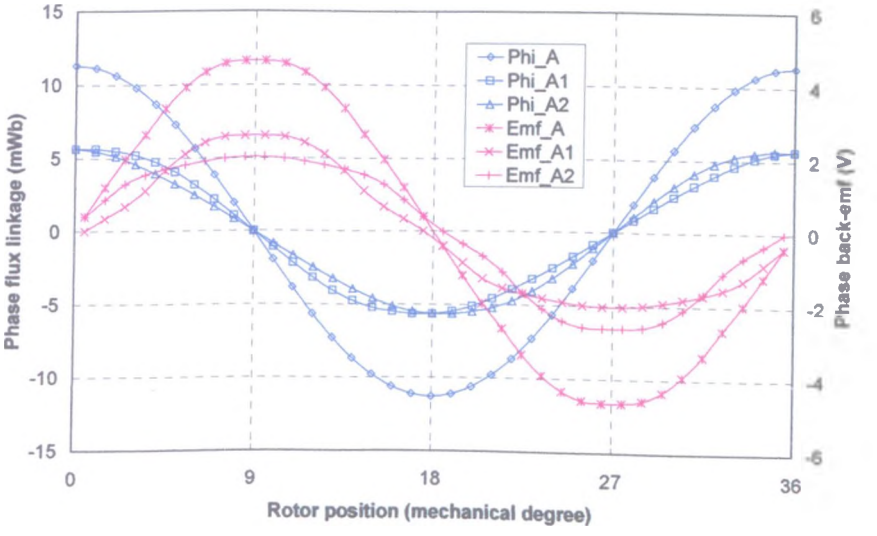

(b) Optimal rotor tooth-arc

Fig. 2.18. Phase flux-linkage and back-emf waveforms (N_w=72turns, n=400rpm)

D. Cogging torque

The cogging torque waveforms of the flux-switching PM machines under consideration are shown in Fig. 2.19. It can be seen that for the flux-switching PM machine with the original rotor tooth-arc, the peak-to-peak value of the cogging torque is ~10% of the rated output torque (2.4Nm), while with the optimal rotor tooth-arc, the cogging torque is increased by more than 60%.

E. Electromagnetic torque

The predicted electromagnetic torque waveforms of the flux-switching PM machines are shown in Fig. 2.20, assuming a current density J_a=10Arms/mm^2 and a slot packing factor K_s=0.4. Since the phase back-emf waveform of the flux-switching PM machine is essentially sinusoidal, 3-phase AC current is employed. D-axis current remains zero in a dq-coordination, according to the control strategy, which is described in Appendix IV. It can be seen that although the airgap field distributions exhibit extremely high harmonics, the electromagnetic torque ripple is only ~10% of rated torque T_N=2.4Nm, which is significantly lower than that of switched reluctance machines. By optimizing the rotor tooth-arc, the average electromagnetic torque can be increased by ~ 9%.

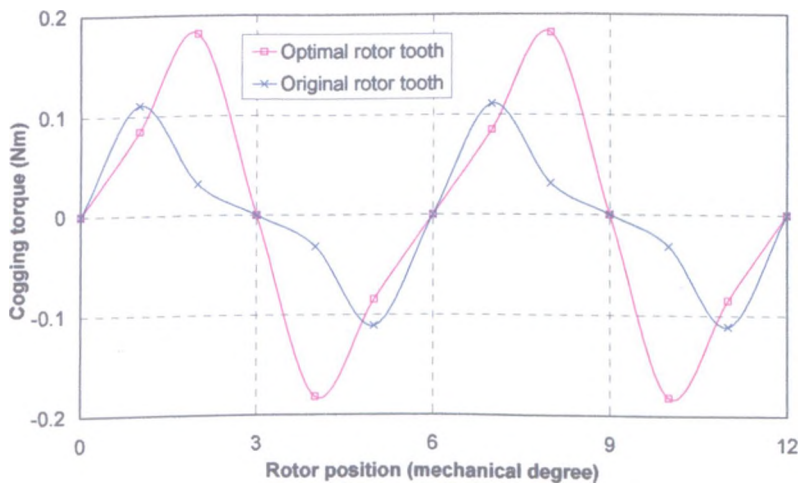

Fig. 2.19. Cogging torque waveforms

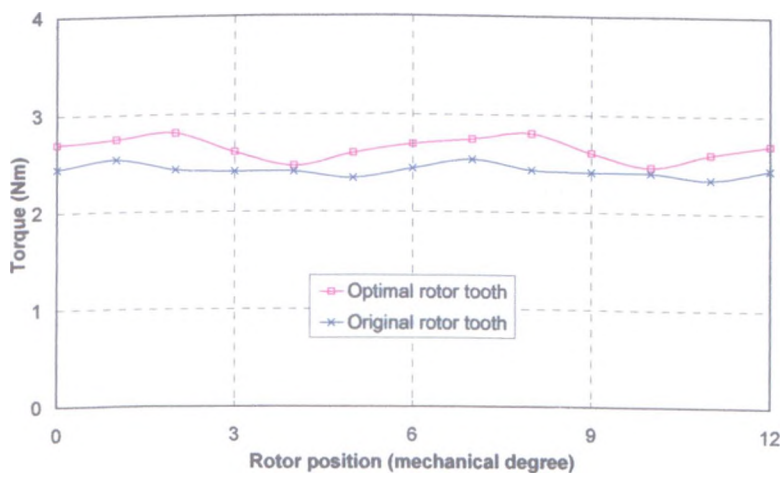

Fig. 2.20. Electromagnetic torque waveforms (J_a=10Arms/mm^2, K_s=0.4)

F. D-axis PM flux-linkage and d/q-axis inductances

By using the Park transformation given in Appendix IV, the d-axis PM flux-linkage and the d/q-axis inductances of a flux-switching PM machine can be obtained, as shown in Fig. 2.21. According to vector control strategy of PM brushless AC motor in Appendix IV, it is the apparent inductance, which is calculated and illustrated. The definition of d/q-axis inductances is shown in Fig. 2.22, e.g. for d-axis inductance, the d-axis flux linkage ψ_m is calculated when the d-axis current is zero, which is so-called d-axis PM flux linkage, then the d-axis flux linkage ψ_d is calculated when the d-axis current is I_d (15A rated), finally the d-axis inductance can be obtained by using the equation (2.4). While for the q-axis inductance, since the q-axis flux linkage equals zero when the q-axis current is zero, only q-axis flux linkage ψ_q is calculated when the q-axis current is I_q (15A rated), the q-axis inductance can then be obtained by using equation (2.5).

It shows that in dq-coordinates, the flux-linkage and inductance waveforms are almost constant. Fig. 2.21(b) shows that the q-axis inductance is only slightly higher than that for the d-axis, which, as a consequence, results in a very small reluctance torque.

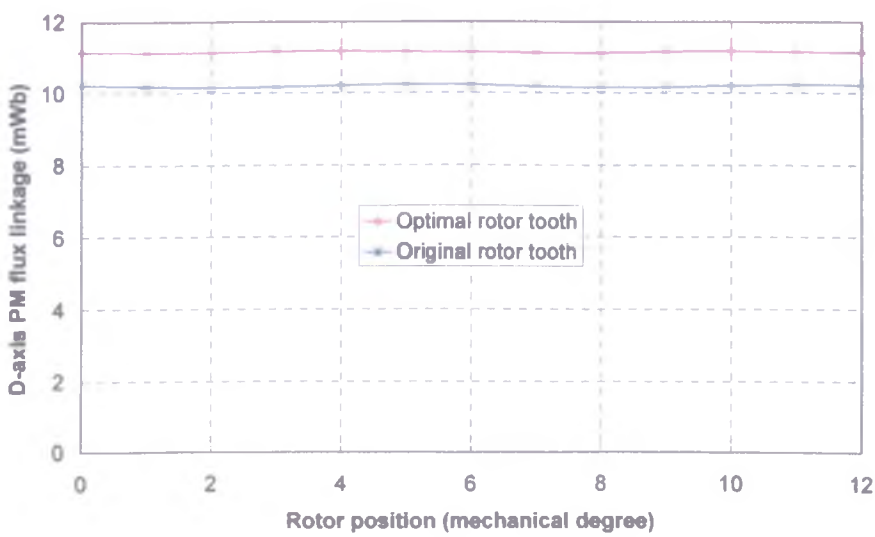

(a) D-axis PM flux-linkage

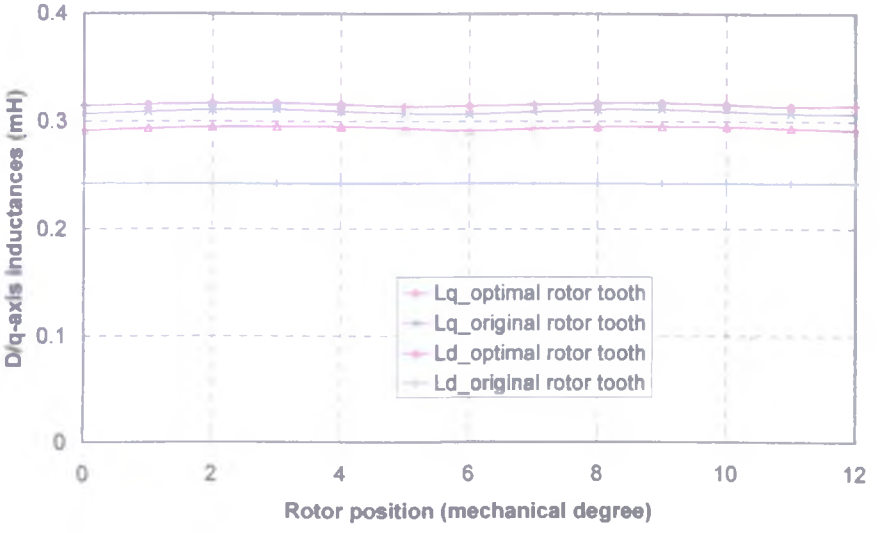

(b) D/q-axis inductances

Fig. 2.21. D-axis PM flux-linkage and d/q-axis inductances (J_a=10Arms/mm^2, K_s=0.4)

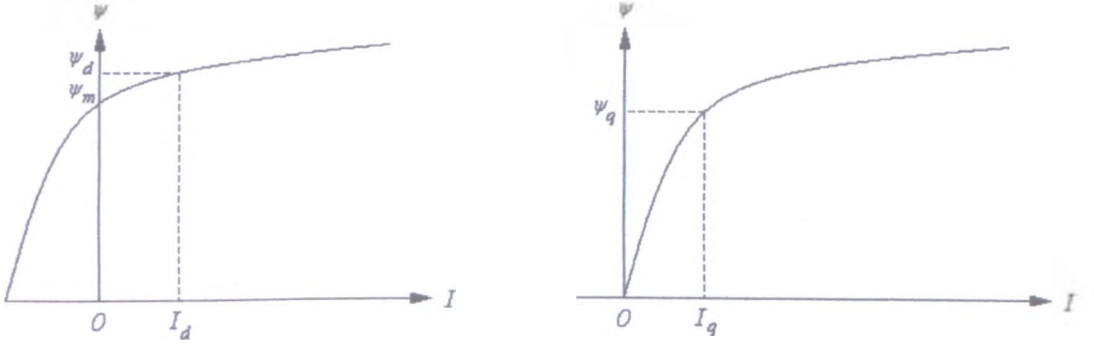

(a) D-axis inductance (b) Q-axis inductance

Fig. 2.22. D/q-axis inductance calculation

$$L_d = \frac{\psi_d - \psi_m}{I_d} \tag{2.4}$$

$$L_q = \frac{\psi_q}{I_q} \tag{2.5}$$

G. Flux-weakening capability

The predicted flux-weakening performance of the two flux-switching PM machines are shown in Fig. 2.22. It can be seen that although two desired working points, viz. 2.4Nm @ 400rpm and 0.4Nm @ 2400rpm are required by the sponsoring company, both can be

achieved by appropriate selection of the number of turns per phase and the phase current. However, overall flux-weakening capability can only be achieved over a speed range which is less than twice the base speed. Since the phase flux-linkage is increased by using the optimized rotor tooth-arc, the flux density can be reduced for the same maximum torque, and the base speed is increased from ~1400rpm to ~1500rpm. Since the q-axis inductance and d-axis inductance have only slightly different, the reluctance torque is almost negligible.

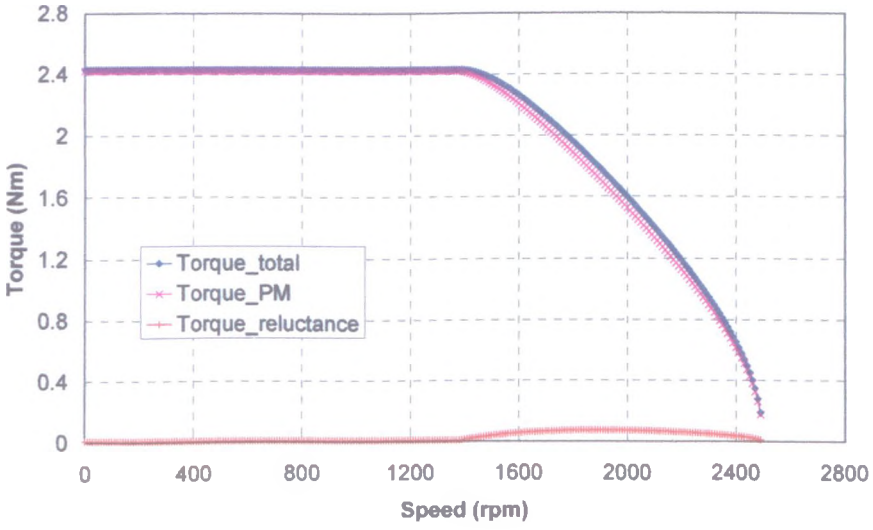

(a) Original rotor tooth width (N_w=72turns, I_a=11.1Arms, J_a=9.9Arms/mm^2)

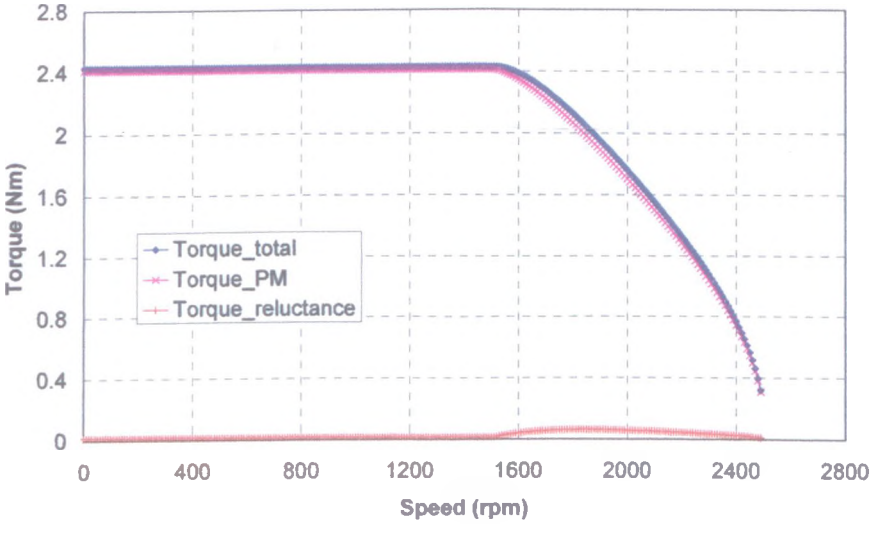

(b) Optimal rotor tooth width (N_w=64turns, I_a=11.5Arms, J_a=9.1Arms/mm^2)

Fig. 2.23. Flux-weakening performance

2.4. 3-D end-effect of flux-switching PM machine

All the foregoing investigations have been based on 2-D finite element analysis, which takes no account of 3-D end-effects. However, the flux-switching PM machines which have been studied in this chapter have a relatively small aspect ratio (stator outer diameter = 90mm and active axial length = 25mm), and the measured torque was found to be much lower than that predicted from 2-D finite element analyses due to significant 3-D end-effects. Hence, it was necessary to repeat the performance predictions by 3-D finite element analysis.

By using the ANSYS finite element software, a 3-D model of a flux-switching PM machine can be established, as shown in Fig. 2.24. The influence of 3-D end-effects on the maximum open-circuit airgap flux density distribution along the axial length of the machine is shown in Fig. 2.25, together with the results from 2-D finite element analysis. Clearly, the airgap flux density which is predicted from the 2-D analysis is constant in the axial direction, while predictions from the 3-D analyses show that towards the ends of the machine, the airgap flux density reduces significantly. As a result of the end-effects, the average airgap flux density (or resultant flux-linkage) in the prototype flux-switching PM machine is reduced by ~10% from that which was predicted by 2-D finite element analysis.

Clearly, the influence of 3-D end-effects can be reduced significantly by increasing the stator axial length, as will be evident in Fig. 2.25, where it can be seen that by increasing the axial length from 25mm to 90mm, which is the same as the stator outer diameter, the influence of end-effects is reduced to less than 5%.

Comparing 3-D finite element predictions for different PM brushless machines, viz. SPM and IPM machines, Fig. 2.26, and the flux-switching PM machine, whose design parameters are given in Table 2.1, it will be seen that the SPM machine exhibits the biggest reduction in airgap flux density at the end of the machine, but in the centre of the SPM machine the airgap flux density is almost the same as that which is predicted from the 2-D model, due to its relatively large effective airgap length, Fig. 2.27(b),

while for the IPM and flux-switching PM machines, the airgap flux density not only reduces at the ends, but the value at the centre of the machines as predicted from the 3-D analyses is lower than that predicted from the 2-D analyses, Figs. 2.25 and 2.27(c).

Fig. 2.24 3-D model of flux-switching PM machine (L_a=25mm)

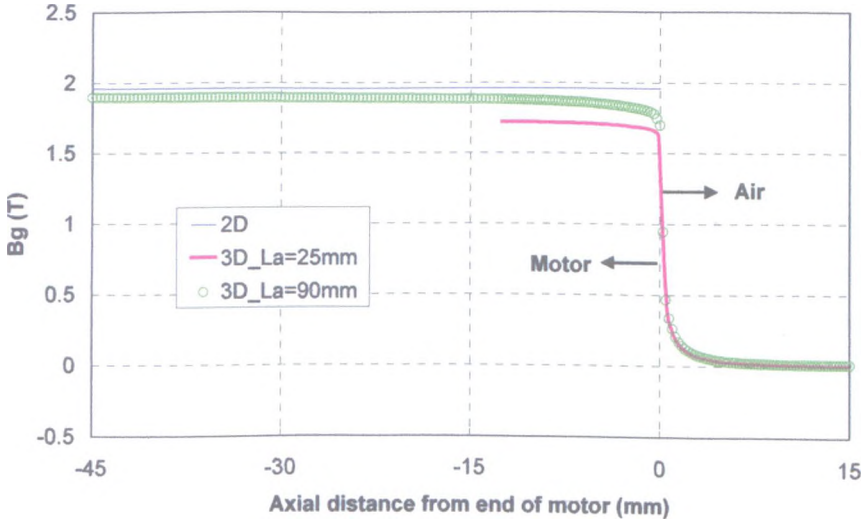

Fig. 2.25. Influence of 3-D end-effect on performance of flux-switching PM machine

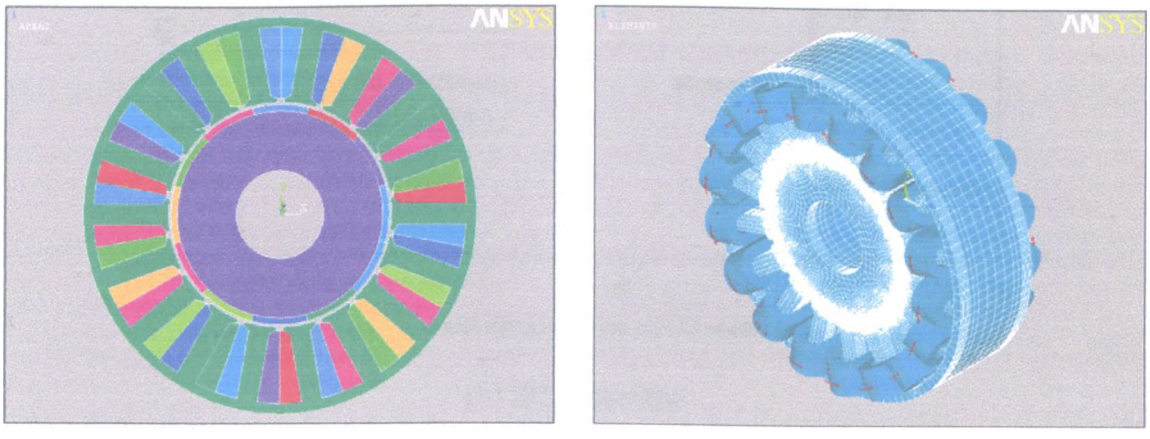

(a) SPM machine

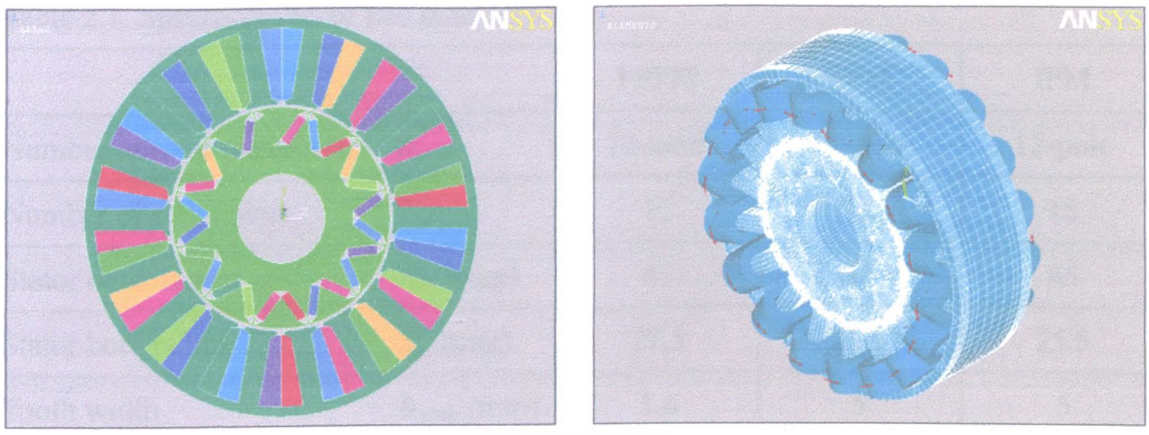

(b) IPM machine

Fig. 2.26. Conventional permanent magnet machines (L_a=25mm)

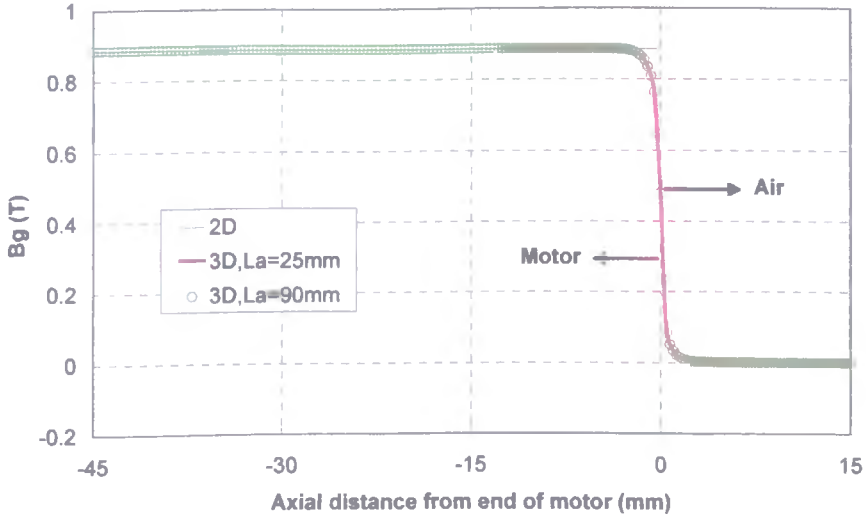

(a) SPM machine

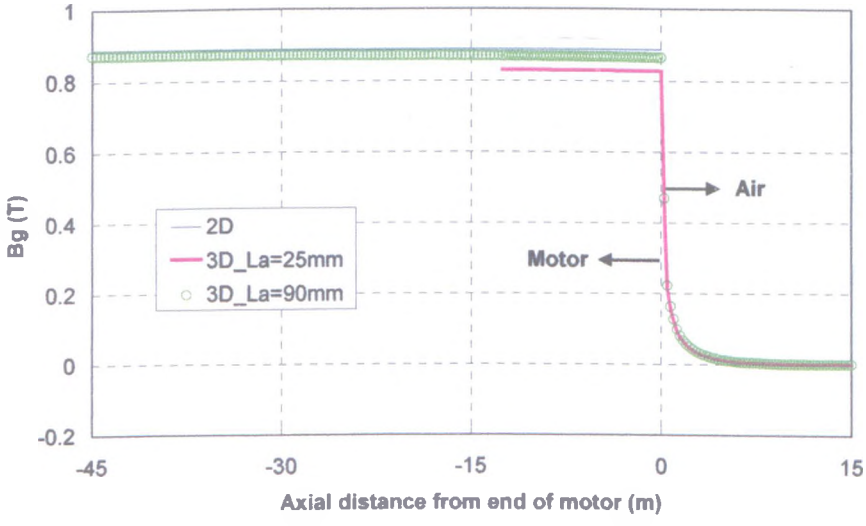

(b) IPM machine

Fig. 2.27. Maximum airgap flux density of PM machines

Table 2.1. Specifications of PM machines

		FSPM	SPM	IPM
Number of rotor teeth/poles	p	10-tooth	12-pole	12-pole
Number of stator slots	N_s	12	18	18
Stator outer radius	R_{so} (mm)	45	45	45
Stator bore radius	R_{si} (mm)	27.5	25.5	25.5
Tooth width	b_{tooth} (mm)	3.6	5	5
Back-iron thickness	h_c (mm)	3.6	2.5	2.5
Magnet thickness	b_m (mm)	3.6	2	2
Airgap length	g (mm)	0.5	0.5	0.5
Axial length	L_a (mm)	25	25	25

2.5. Scaling of flux-switching PM machine

The topic of machine scaling (or machine sizing) has been studied for decades in order to simplify electrical machine design and design comparison studies. The most common sizing equation, which appears frequently in the literature, is:

$$T \propto D_s^2 L_a \times BQ \tag{2.6}$$

where T is the output torque, D_s is the stator bore diameter, L_a is the active axial length, B is the magnetic loading, which is the average airgap flux density, and Q is the electric loading, which is the surface current density at the airgap.

The sizing equation has been improved in [HON87], by considering the stator and rotor geometries, and a modified equation is proposed as:

$$T \propto D_o^3 L_a \times BQ \tag{2.7}$$

in which the stator bore diameter D_s in the original equation is replaced by the stator outer diameter D_o, which makes it easier to compare machine power densities and

manufacturing costs, since the volume of the machine can easily be given as $D_o^2 L_a$.

Based on the machine sizing equation proposed in [HON87], further investigations have been carried out in [HUA98][HUA99]. General sizing equations have been derived so that comparisons can be made with machines having different phase back-emfs, e.g. sinusoidal, rectangular, trapezoidal and triangular, etc., and different machine technologies and topologies, e.g. induction machine and doubly-salient PM machine [HUA98], as well as radial-field machines and axial-field machines [HUA99].

Further investigations are reported in [BIN96], which shows that when the machine thermal behavior and armature reaction are taken into account, the coefficient in the sizing equation (2.5) is no longer 3 anymore, which can be re-written as:

$$T \propto D_o^{n+2} L_a \times BQ \tag{2.8}$$

where n is less than 1. After reviewing results from the published papers and performing numerical analyses on two particular machines, the value of $n = 0.5$ was proposed.

All the foregoing investigations which have been described in this chapter are based on a small prototype flux-switching PM machine. It was necessary, therefore, to investigate the influence of scaling, from the small prototype machine to a significantly larger machine.

An analytical approach will be employed first, and the results will be validated by numerical analysis. Two scenarios are considered: (a) all the dimensions are scaled up by the same factor, and (b) all the dimensions except for the airgap length are scaled up by the same factor.

2.5.1. Analytical equations

The investigation in this chapter will start from the most common torque equation in which the stator bore diameter D_s is used:

$$T \propto D_s^2 L_a \times BQ \tag{2.9}$$

where D_s is the stator bore diameter, L_a is the active axial length, B is the magnetic loading, and Q is the electric loading.

The torque density is then given by:

$$Torque\ density \propto \frac{D_s^2 L_a \times BQ}{D_o^2 L_a} \tag{2.10}$$

If the split ratio is fixed, the equation for the torque density can be simplified as:

$$Torque\ \ density \propto BQ \tag{2.11}$$

in which the magnetic loading B may be replaced by the average airgap flux density B_g. Therefore, the airgap flux density B_g and the electric loading Q are the two most important parameters in the study of the machine size scaling.

A. Scaling up all machine dimensions by factor K

The fundamental equation for the airgap flux density in a permanent magnet machine is:

$$B_g = \frac{B_r}{\frac{A_g}{A_m} + \mu_r \frac{g}{b_m}} \tag{2.12}$$

where B_r is the remanence of the permanent magnets, A_g is the cross-sectional area of the airgap, A_m is the cross-sectional area of the permanent magnets in the magnetization direction, g is the airgap length and b_m is the length of the permanent magnets in the magnetization direction. For sintered NdFeB permanent magnets the relative recoil permeability μ_r is approximately equal to 1.

If all the machine dimensions are scaled by K times, the resulting airgap flux density can be derived as:

$$B_{g\_scaled} = \frac{B_r}{\frac{A_g \times K^2}{A_m \times K^2} + \mu_r \frac{g \times K}{b_m \times K}} = \frac{B_r}{\frac{A_g}{A_m} + \mu_r \frac{g}{b_m}} = B_g \tag{2.13}$$

i.e. after scaling, the airgap flux density remains unchanged. As a result, from (2.13), if the electric loading of the machine is fixed, after scaling, the scaled machine has a similar torque density as original machine.

The electric loading has the following relationship with the conductor current density:

$$Q = \frac{mI_a \cdot 2N_w}{\pi D_s} = \frac{J_a A_s K_s N_s}{\pi D_s} \tag{2.14}$$

where m is the number of phases, I_a is the phase current, N_w is the number of turns per phase, D_s is the stator bore diameter, J_a is the current density, A_s is the slot area, K_s is the slot packing factor, and N_s is the number of slots.

Therefore, when the machine is scaled by a factor K, if the phase current is increased by K times, the electric loading Q is unchanged:

$$Q_{scaled} = \frac{mI_a \times K \cdot 2N_w}{\pi D_s \times K} = \frac{mI_a \cdot 2N_w}{\pi D_s} = Q \tag{2.15}$$

Hence, the torque density of the machine also remains unchanged.

However, if the phase current is increased by K^2 times, i.e. the current density is unchanged, the electric loading Q will be increased by K times:

$$Q_{scaled} = \frac{mI_a \times K^2 \cdot 2N_w}{\pi D_s \times K} = \frac{J_a A_s \times K^2 K_s N_s}{\pi D_s \times K} = \frac{mI_a \cdot 2N_w}{\pi D_s} \times K = \frac{J_a A_s K_s N_s}{\pi D_s} \times K = Q \times K \tag{2.16}$$

The torque density will then be increased by K times.

Alternatively, if the machine has a sinusoidal phase back-emf waveform, this K times increase can be explained by the following equations in d/q-axis co-ordinates:

For the original machine with I_d=0:

$$T = \frac{3}{2} p \psi_m I_q \tag{2.17}$$

$$V_m = \pi R_{so}^2 L_a \tag{2.18}$$

where p is the number of electrical pole-pairs, ψ_m is the PM flux-linkage, I_q is the q-axis current, R_{so} is the stator outer radius, and L_a is the active axial length.

When the machine is scaled by the factor K, the PM flux-linkage is increased by K^2:

$$\psi_{m\_scaled} = B_g \left(A_g \times K^2 \right) = \psi_m \times K^2 \tag{2.19}$$

If the phase current is increased by K times, i.e. the electric loading Q remains constant, the q-axis current will be increased by K times. Therefore,

$$T_{scaled} = \frac{3}{2} p \left(\psi_m \times K^2 \right) \left(I_q \times K \right) = T \times K^3 \tag{2.20}$$

and

$$\frac{T_{scaled}}{V_{m\_scaled}} = \frac{T \times K^3}{V_m \times K^3} = \frac{T}{V_m} \tag{2.21}$$

i.e. the torque density is unchanged.

If the phase current is increased by K^2 times, i.e. the current density is fixed, the q-axis current will be increased by K^2 times, and:

$$T_{scaled} = \frac{3}{2} p \left(\psi_m \times K^2 \right) \left(I_q \times K^2 \right) = T \times K^4 \tag{2.22}$$

and

$$\frac{T_{scaled}}{V_{m\_scaled}} = \frac{T \times K^4}{V_m \times K^3} = \frac{T}{V_m} \times K \tag{2.23}$$

i.e. the torque density is increased by K times.

The foregoing discussion has only considered the influence of scaling on the magnetic loading, i.e. the airgap flux density B_g, and on the electric loading separately. When the current density is very high, the influence of magnetic saturation on the airgap flux

density due to the electric loading (or the armature reaction) when the machine is scaled up also has to be accounted for.

The airgap flux density B_{gw}, which is produced by the armature reaction, can be approximated by (2.23), if the magnetic potential drops in the stator and rotor laminations are ignored:

$$\frac{B_{gw}}{\mu_0} \times g = N_{coil} I_a \tag{2.24}$$

where B_{gw} is the airgap flux density produced by the armature reaction, μ_0 is the permeability of free-space, g is the airgap length, and $N_{coil}I_a$ is the winding MMF.

If B_{gw} corresponds to the current in a single slot, then the equation can be re-written as:

$$B_{gw} = \mu_0 \frac{N_{coil} I_a}{g} \tag{2.25}$$

or the current density:

$$B_{gw} = \mu_0 \frac{J_a A_s K_s}{g} \tag{2.26}$$

where I_a is the phase current, J_a is the phase current density, A_s is the slot area, and K_s is the slot packing factor.

When the machine is scaled by K times, if the phase current is scaled by K times, i.e. the electric loading Q remains constant, the airgap flux density produced by the armature reaction is maintained unchanged:

$$B_{gw\_scaled} = \mu_0 \frac{N_{coil} I_a \times K}{g \times K} = \mu_0 \frac{N_{coil} I_a}{g} = B_{gw} \tag{2.27}$$

If the phase current is scaled by K^2 times, i.e. the phase current density is fixed, the airgap flux density produced by the armature reaction, then, will be increased by K times:

$$B_{gw\_scaled} = \mu_0 \frac{J_a A_s \times K^2 K_s}{g \times K} = \mu_0 \frac{J_a A_s K_s}{g} \times K = B_{gw} \times K \tag{2.28}$$

It can be seen from (2.13) that after scaling, the airgap flux density produced by the permanent magnets is unchanged. If the phase current is increased by K times, both the torque density and the magnetic saturation will remain unchanged. Alternatively, if the phase current is increased by K^2 times, i.e. the phase current density is fixed, both the torque density and the airgap flux density produced by the armature reaction will be increased by K times, which indicates that for the same current density, magnetic saturation will be increased. This may result in a torque reduction and a lower torque density.

B. Scaling up all machine dimensions by factor K, except for airgap length

In order to simplify the study of scaling with a fixed airgap length, two scenarios are considered, viz. scaling all the dimensions by K times, as has been studied in the foregoing, then reducing the airgap length by a factor $\frac{1}{K}$.

If the airgap length of a machine is reduced by $\frac{1}{K}$ times, the airgap flux density is increased to:

$$B_{g\_small\ airgap} = \frac{B_r}{\frac{A_g}{A_m} + \mu_r \frac{g \times \frac{1}{K}}{b_m}} = B_g \times K' \tag{2.29}$$

where $K' = \dfrac{\frac{A_g}{A_m} + \mu_r \frac{g}{b_m}}{\frac{A_g}{A_m} + \mu_r \frac{g \times \frac{1}{K}}{b_m}}$ (2.30)

Since the electric loading will not be affected by the airgap length, the torque density will be increased by K' times.

Alternatively, for a machine with I_d=0:

$$T = \frac{3}{2} p \psi_m I_q \tag{2.31}$$

$$V_m = \pi R_{so}^2 L_a \tag{2.32}$$

where p is the number of electrical pole-pairs, ψ_m is the PM flux-linkage, I_q is the q-axis current, R_{so} is the stator outer radius, and L_a is the active axial length.

If the airgap length is fixed during scaling, the airgap flux density will be increased by K' times, as will the PM flux-linkage, the output torque and the torque density:

$$\psi_{m\_small\ airgap} = \left(B_g \times K'\right) A_g = \psi_m \times K' \tag{2.33}$$

$$T_{small\ airgap} = \frac{3}{2} p \left(\psi_m \times K'\right) I_q = T \times K' \tag{2.34}$$

$$\frac{T_{small\ airgap}}{V_m} = \frac{T \times K'}{V_m} = \frac{T}{V_m} \times K' \tag{2.35}$$

The airgap flux density B_{gw} which is produced by the armature reaction will be influenced significantly by the airgap length:

$$B_{gw} = \mu_0 \frac{N_{coil} I_a}{g} \tag{2.36}$$

If the airgap length is fixed during scaling, the airgap flux density produced by armature reaction will be increased by K times:

$$B_{gw\_small\ airgap} = \mu_0 \frac{N_{coil} I_a}{g \times \frac{1}{K}} = \mu_0 \frac{N_{coil} I_a \times K}{g} = B_{gw} \times K \tag{2.37}$$

Thus, if the airgap length is fixed during scaling, the airgap flux density due to the permanent magnets is increased only slightly by the factor K', which will result in a further increase in the torque density; while the airgap flux density due to armature reaction is significantly increased by the factor K, which will cause heavy magnetic saturation.

2.5.2. Scaling of flux-switching PM machine

The flux-switching PM machine, which has been studied in Section 2.2 and which is shown in Fig. 2.1, is the subject of the scaling investigation.

The main dimensions of the original prototype flux-switching PM machine are given in Table 2.2, together with the dimensions of a machine scaled up by a factor 2.62, which was required by sponsoring company, i.e. the stator outer radius is increased from 45mm to 118mm, the airgap length is increased from 0.5mm to 1.31mm and the axial length is increased from 25mm to 65.56mm. Correspondingly, the slot area is increased by 6.87 times (2.62^2) and the machine volume by 18 times (2.62^3).

Table 2.2. Dimensions of original and scaled flux-switching PM machines

	Original FSPM	Scaled FSPM	Scaling factor
Stator outer radius (mm)	45	118	×2.62
Airgap length (mm)	0.5	1.31	×2.62
Axial length (mm)	25	65.56	×2.62
Stator inner radius (mm)	27.5	72.11	×2.62
Stator tooth width (mm)	3.6	9.44	×2.62
Stator slot area (m^2)	1.01E-4	6.94E-4	$\times 2.62^2$

A. Scaling up all machine dimensions by factor 2.62

According to (2.13), the open-circuit field distributions and the flux density distributions as well as the open-circuit airgap field distributions of the scaled flux-switching PM machine will be exactly the same as those for the small flux-switching PM machines. The phase flux-linkage is increased by 6.87 times (2.62^2), because the tooth width is scaled up by 2.62 times and the tooth axial length is scaled up by 2.62 times, as shown in the finite element predicted results in Figs. 2.28(a) and 2.28(b).

The finite element predicted electromagnetic torque density of both the original and scaled flux-switching PM machines are shown in Fig. 2.28(c). The comparison in Fig.

2.28(d) shows that for the same current density, the torque density of the scaled flux-switching PM machine is increased by 2.62 times when the current density is low, i.e. when magnetic saturation resulting from armature reaction can be neglected. With an increase in the current density, magnetic saturation in the scaled flux-switching PM machine is significantly higher than that in the original flux-switching PM machine. As a result, the advantage of the increased torque density in the large flux-switching PM machine will be diminished.

Fig. 2.28(e) shows the influence of the electric loading, in that the scaled flux-switching PM machine has the same torque density as before. With an increase of the electric loading, the influence of magnetic saturation due to armature reaction in both the scaled and original flux-switching PM machines is the same.

Comparing the torque density performance in Fig. 2.28(f), it can be seen that the torque density reduction due to magnetic saturation is identical, before and after scaling.

B. Scaling up all machine dimensions by factor 2.62, except for airgap length

The influence of linearly scaling all the dimensions by 2.62 times as has already been studied, so that effect of reducing the airgap length by $\frac{1}{2.62}$ times will now be considered. According to equation (2.28), the airgap flux density of the scaled up flux-switching PM machine will be increased by K' times:

$$K' = \frac{\frac{A_g}{A_m} + \mu_r \frac{g}{b_m}}{\frac{A_g}{A_m} + \mu_r \frac{g \times \frac{1}{K}}{b_m}} = \frac{0.21 + \frac{1.31}{9.43}}{0.21 + \frac{1.31 \times \frac{1}{2.62}}{9.43}} = 1.33 \qquad (2.38)$$

where μ_r is again assumed as 1.

Thus, theoretically, the maximum airgap flux density can be increased by 33%, but due to the highly saturated magnetic circuit of the scaled flux-switching PM machine, the maximum airgap flux density is only increased by ~13%, as confirmed by Fig. 2.28(a), as well as the phase flux-linkage shown in Fig. 2.28(b). Consequently, the torque

density of the scaled flux-switching PM machine with unchanged airgap length can only be ~13% higher than that of the scaled flux-switching PM machine with a scaled up airgap length. As a result, since the torque density of the scaled flux-switching PM machine with a scaled up airgap length is 2.62 times of that of original flux-switching PM machine, the torque density of the scaled flux-switching PM machine with unchanged airgap length is 2.97 times of the torque density of the original flux-switching PM machine, as shown in Figs. 2.28(c) and 2.28(d).

Equation (2.38) indicates that by using a smaller airgap length in the scaled flux-switching PM machine, the airgap flux density due to armature reaction will be increased very significantly. As a result, when a large current density is employed, magnetic saturation in the scaled up flux-switching PM machine with the unchanged airgap length will be much higher than that in the scaled up flux-switching PM machine with the larger airgap length, as confirmed in Figs. 2.28(e) and 2.28(f).

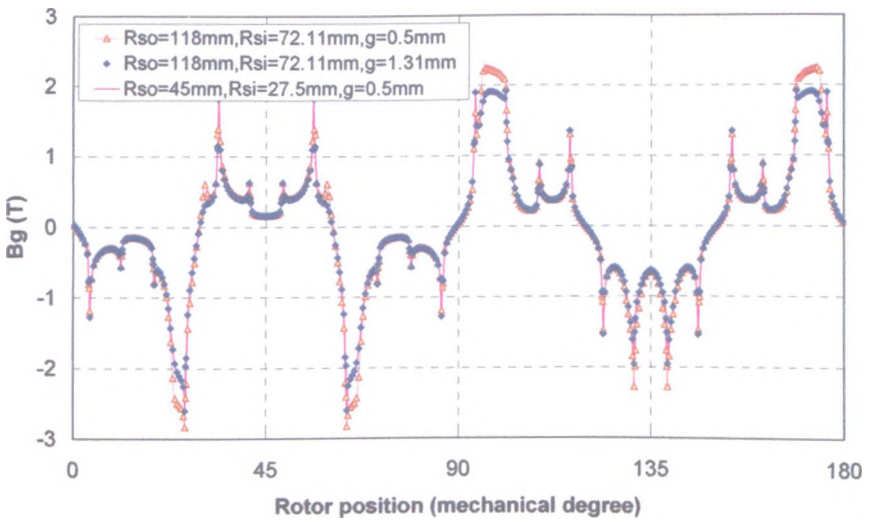

(a) Airgap field distribution

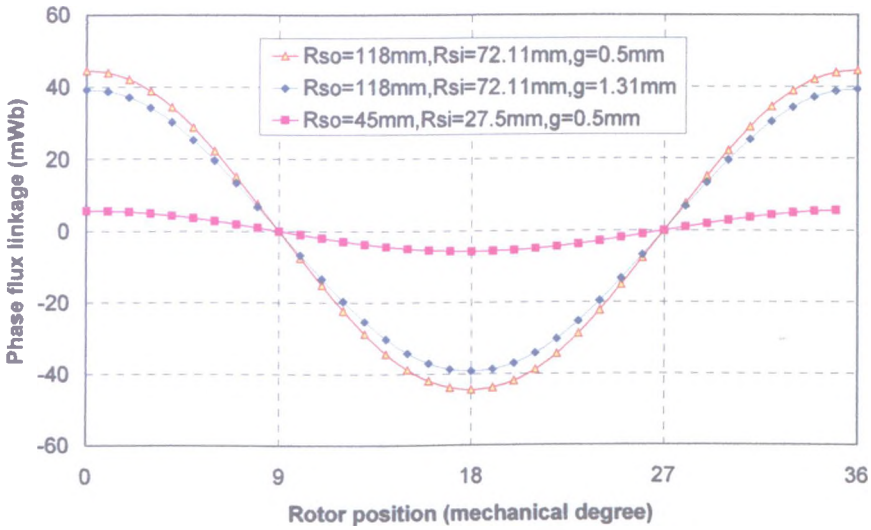

(b) Phase flux-linkage (N_w=40turn)

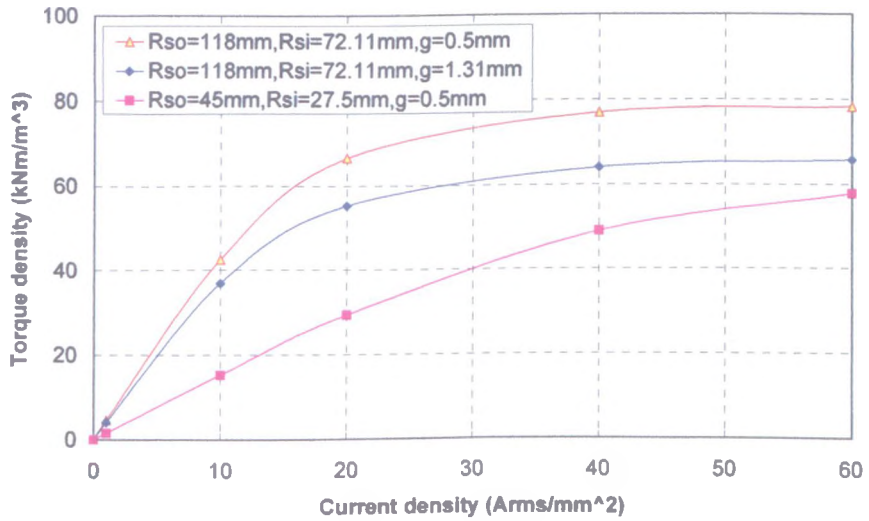

(c) Torque density vs. current density

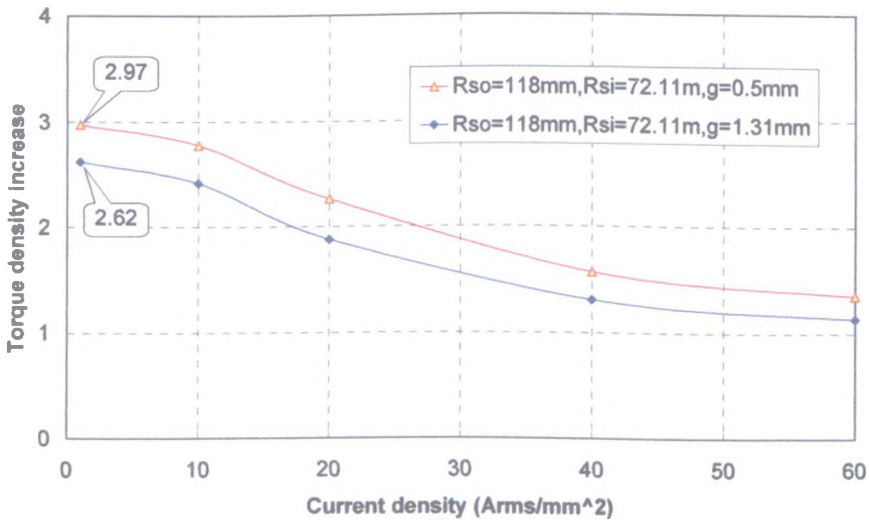

(d) Torque density increase vs. current density

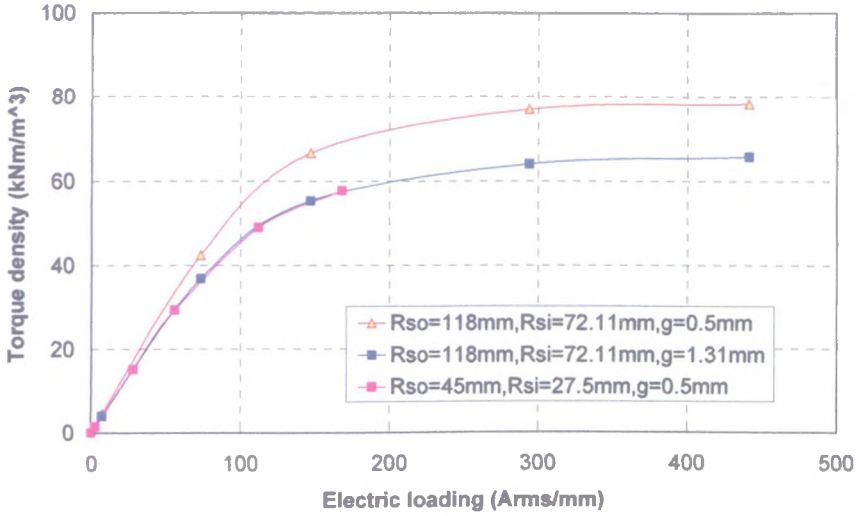

(e) Torque density vs. electric loading

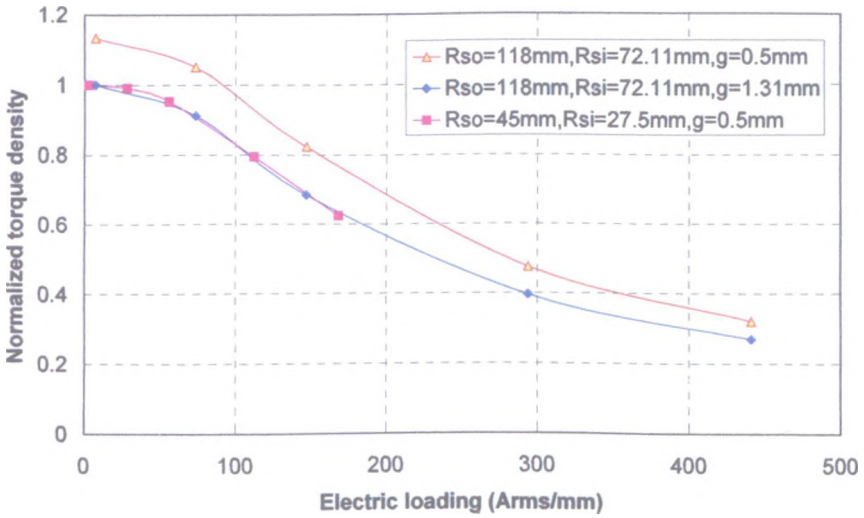

(f) Normalized torque density vs. electric loading

Fig. 2.28. Scaling of flux-switching PM machine

2.6. Summary

In this chapter, the main dimensions of a flux-switching PM machine for maximum output torque have been investigated. These are the stator tooth width, the stator magnet thickness, the stator back-iron thickness, the stator lamination bridge thickness, the rotor tooth width, the rotor tooth height, and the rotor back-iron thickness. In addition, the influence of the shape of the magnets and the rotor teeth has been investigated.

1. The flux-switching PM machine with the original stator tooth width, stator magnet thickness and magnet shape (i.e. stator tooth width = magnet thickness) offers the maximum output torque.

2. However, the torque can be increased if the stator back-iron thickness is reduced to ~70% of the original size, since the slot area can be increased.

3. Adding narrow bridges between the stator 'U'-shaped lamination modules compromises the output torque, but is worthy of consideration since it may simplify machine manufacture.

4. The output torque can be increased by ~8% if the rotor tooth-arc is increased by 40%~60%, since this increases the phase flux-linkage.

5. The minimum rotor tooth height and rotor back-iron thickness for maximum torque have been obtained.

The electromagnetic performance of the prototype flux-switching PM machine, which has been designed and built, has been predicted, including the open-circuit flux distribution, the airgap field distribution, the cogging torque, the electromagnetic torque, the d-axis PM flux-linkage, the d/q-axis inductances and the flux-weakening capability. It has been shown that, in a flux-switching PM machine, the airgap field distribution is highly complex, and the amplitude can be very high due to flux focusing. The d- and q-axis winding inductances are similar, and, hence, the reluctance torque is negligible, although without salient rotor teeth no electromagnetic torque would be developed.

A 3-D model of a flux-switching PM machine has been established using the ANSYS finite element software and the influence of end-effects has been investigated. Compared with predictions obtained from 2-D finite element analysis, the airgap flux density at the ends of the machine can be significantly reduced. Clearly, increasing the stator axial length will reduce the influence of 3-D end-effects.

The issue of scaling from a small prototype machine to a larger machine is important, and has been addressed. Analytical equations have been derived and validated by

numerical calculations. They show that, when magnetic saturation is neglected, scaling the dimensions by a factor K, with the phase current increased by K^2 times, i.e. the current density is constant, the maximum airgap flux density is unchanged, but the electric loading and torque density are increased by K times. If the phase current is increased by K times, i.e. the electric loading is fixed, the maximum airgap flux density is still unchanged, and the torque density remains unchanged. Taking account of magnet saturation, however, the torque densities of the scaled up flux-switching PM machines may decrease significantly.

The investigations carried out in this chapter are all based on finite element analyses, which remains a very time-consuming process. Thus, lumped parameter magnetic equivalent circuit model will be established in the next chapter in order to aid design optimization, so that more than two design parameters can be optimized simultaneously.

Chapter 3 Non-linear Adaptive Lumped Parameter Magnetic Circuit Model of Flux-switching Permanent Magnet Machine

3.1. Introduction

The finite element method is widely used for analyzing the electromagnetic performance of electrical machines [CHE01][HOA97]. In Chapter 2, it was used to analyze the influence of design parameters on the output torque of flux-switching PM machines. However, it remains relatively time consuming, and while the influence of one design parameter on the electromagnetic performance was investigated in Chapter 2, the other design parameters were fixed, which prevents globally optimized designs from being obtained. Lumped parameter magnetic circuit modelling is an alternative to finite element analysis, and is often preferred at the design stage, e.g. to calculate the back-emf waveform, the winding inductances and the static torque characteristic [CHE00] [LOV02].

Hence, in this chapter, a non-linear adaptive lumped parameter magnetic circuit model is developed to predict the electromagnetic performance of flux-switching PM machines, taking account of magnetic saturation and leakage flux. The predicted airgap field distribution, back-emf waveform, winding inductances and electromagnetic torque are validated by both 2-D and 3-D finite element analyses and measurements on a 3-phase, 10-rotor tooth, 12-stator slot, flux-switching PM machine. In addition, end-effects and optimal design parameters, i.e. the rotor tooth width, the stator segment tooth width and the split ratio (i.e. the ratio of the inner to outer stator diameter) are investigated, using the developed lumped parameter magnetic circuit model and more than two design parameters can be optimized at the same time.

3.2. Establishment of lumped parameter magnetic circuit model

3.2.1. Basic principle

The basic principle of lumped parameter magnetic circuit models can be illustrated by the simple model as shown in Fig. 3.1:

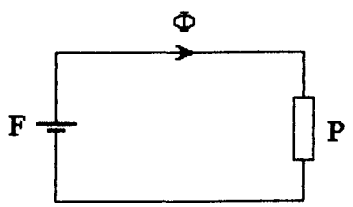

Fig. 3.1. Basic principle of lumped parameter magnetic circuit model

$$F = \frac{\Phi}{P} \tag{3.1}$$

where Φ is the magnetic flux, P is the permeance and F is the scalar magnetic potential (MMF).

The permeance of a region in a magnetic circuit can be calculated from:

$$P = \mu_r \mu_0 \frac{S}{L} \tag{3.2}$$

where μ_r is the relative permeability, μ_0 is the permeability of free-space, S is the cross-sectional area in the direction in which the flux flows, and L is the length in the direction of flux flow.

Thus, each region of a flux-switching PM machine can be modelled as follows.

3.2.2. Model of laminated region

Based on equation (3.2), the permeance of a laminated ferromagnetic region in either the stator or rotor is given as:

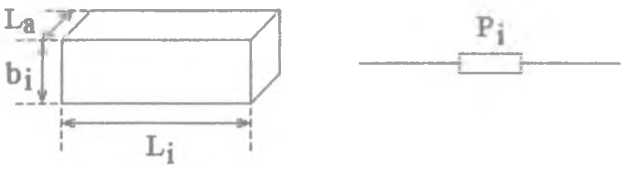

Fig. 3.2. Lumped parameter model of laminated region

$$P_i = \mu_r \mu_0 \frac{b_i L_a}{L_i} \tag{3.3}$$

where P_i is the permeance, b_i and L_i are the width and length of the laminated region, and L_a is the axial length of the machine.

When the laminations are highly saturated, e.g. stator tooth as illustrated in Fig.3.3, the relative permeability μ_r has to be deduced iteratively by using the B-H curve of the lamination material, while the effective length of the stator tooth needs to be corrected by finite element calculations.

Fig. 3.3. Saturated stator tooth

In Fig. 3.3, it shows that only the part of the stator tooth which is close to the airgap has a high flux density, other parts of the stator tooth having a relatively low flux density, while in the lumped parameter magnetic circuit model, the whole stator tooth is assumed to have the same maximum flux density. As a result, the permeance of the stator tooth will be underestimated by using (3.3), if the actual stator tooth length is used. In order to compensate for the underestimated permeance, an effective length is used, the value of which is determined by comparing with the results from finite element analysis. As a result, the effective length of stator tooth may be much less than its active length.

For example, for the prototype flux-switching PM machine shown in Appendix I, if the actual length of stator tooth is used in lumped parameter magnetic circuit model, since

the stator tooth permeance is underestimated, the total phase flux-linkage is ~40% less than the result from finite element calculation. The effective length of the stator tooth needs to be reduced to ~ $1/10$ of its actual length, then the proper machine performance can be predicted by using the lumped parameter magnetic circuit model.

Once the effective length is obtained, it then can be used for subsequent investigations. Alternatively, a more refined lumped parameter model, in which the stator teeth, and other ferromagnetic regions, are sub-divided into smaller regions, each represented by a separate permeance, could be employed.

3.2.3. Model of permanent magnet

Since the NdFeB permanent magnets, which are used in the flux-switching PM machine, have a linear demagnetization characteristic, as shown in Fig. 3.4(a), they can be modeled as shown in Fig. 3.4(b).

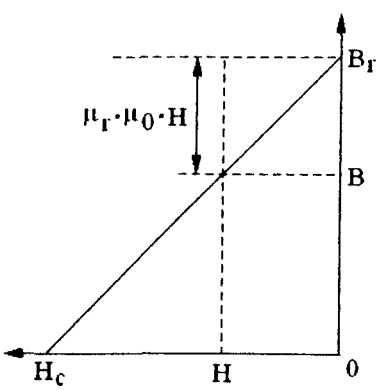

(a1) *B-H* demagnetization curve

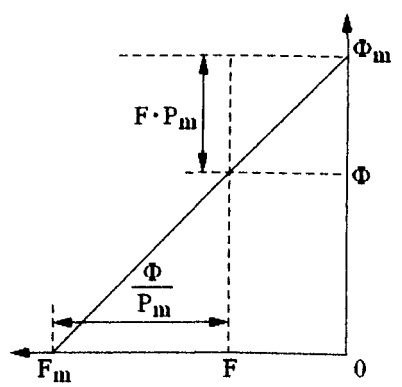

(a2) *Φ-F* demagnetization curve

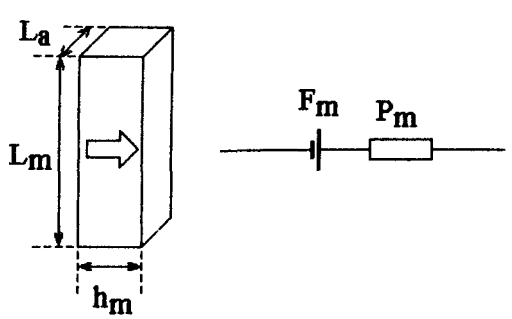

(b) Model of permanent magnet

Fig. 3.4. Lumped parameter model of permanent magnet

$$F = F_m - \frac{\Phi}{P_m} \tag{3.4}$$

where $$F_m = \frac{B_r}{\mu_r \mu_0} h_m \tag{3.5}$$

$$P_m = \mu_r \mu_0 \frac{L_m L_a}{h_m} \tag{3.6}$$

in which F_m is the magnetic potential of the permanent magnet, B_r is the remanence, h_m is the thickness in the direction of magnetization, L_m is the length and P_m is the permeance of the permanent magnet.

3.2.4. Model of stator winding

The lumped parameter magnetic circuit model of the stator winding is obtained by considering the net ampere-conductors in each slot, as shown in Fig. 3.5:

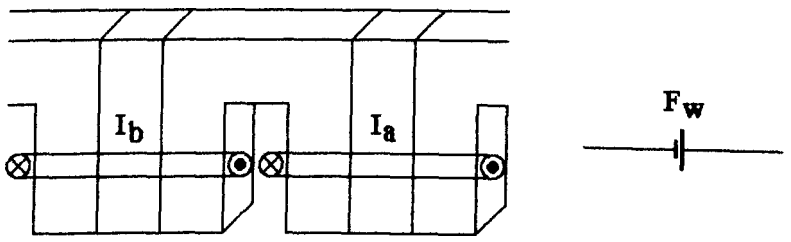

Fig. 3.5. Lumped parameter model of stator winding

$$F_w = (I_a - I_b) N_c \tag{3.7}$$

where F_w is the effective scalar magnetic potential due to the coil sides which occupy a slot, I_a and I_b are the currents in phases A and B, respectively, and N_c is the number of turns per coil.

3.2.5. Model of airgap/airspaces

The flux distribution in the airgap/airspaces between the stator and rotor is more complicated than that in the laminated stator and rotor cores. However, the permeances corresponding to five idealized flux patterns can be derived, as shown in Fig. 3.6, and these can subsequently be used to model the flux distribution in the airgap/airspace region.

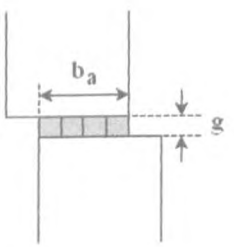

(a) $P_{a1} = \dfrac{\mu_0 L_a b_a}{g}$

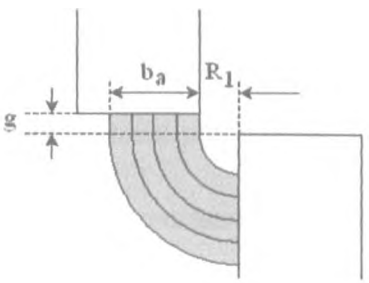

(b) $P_{a2} = \dfrac{2\mu_0 L_a}{\pi} ln\left(1 + \dfrac{\pi b_a}{\pi R_{a1} + 2g}\right)$

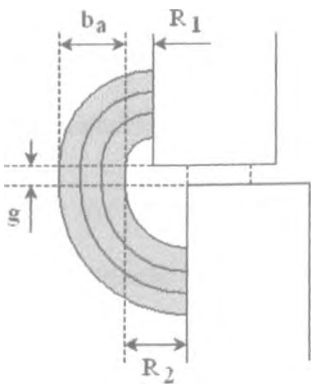

(c) $P_{a3} = \dfrac{\mu_0 L_a}{\pi} ln\left(1 + \dfrac{2\pi b_a}{\pi(R_{a1} + R_{a2}) + 2g}\right)$

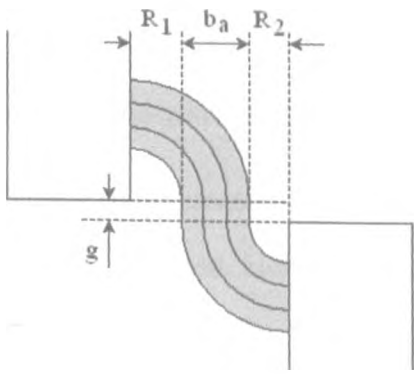

(d) $P_{a4} = \dfrac{2\mu_0 L_a b_a}{\pi(R_{a1} + R_{a2} + b_a) + 2g}$

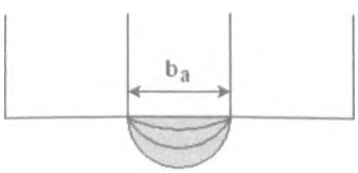

(e) $P_{a5} = 0.26\mu_0 L_a$

Fig. 3.6. Models of idealized flux paths

P_{a1}~P_{a5} are the associated permeances, where g is the actual airgap length, b_a is the

width of the idealized flux path, and R_{a1} and R_{a2} are radii associated with the flux paths.

3.2.6. Model of flux-switching PM machine

The 3-phase, 10-rotor tooth, 12-stator slot flux-switching PM machine shown in Fig. 3.7 is symmetrical about its diameter. Hence, only half the machine needs to be modelled. Further, due to the relatively high number of rotor teeth and stator slots, the machine can be modelled in rectangular co-ordinates, Fig. 3.8, without unduly compromising the accuracy, as will be shown later by comparison with finite element predictions.

Whilst the permeances of the ferromagnetic regions and the permanent magnets are relatively easy to determine, the permeances of the airgap region are more difficult to specify due to the relative complexity of the field distribution, as will be evident from the open-circuit field distribution shown in Fig. 3.12. The assumed flux paths in the airgap region between the stator and rotor and external to the stator outer surface are simplified, as illustrated in Fig. 3.9, and the stator and rotor surfaces are assumed to be equal-potential surfaces, expressions for the permeances being given in Fig. 3.6.

By combining the models of the various regions, a lumped parameter magnetic circuit model of the complete flux-switching PM machine can be obtained. However, since the airgap flux distribution varies as the rotor rotates, the model needs to be modified adaptively in accordance with the rotor position. It has been established that six different lumped parameter magnetic circuit models are required for each stator segment in order to account for the variation in airgap flux distribution as the rotor rotates. These are as shown in Fig. 3.10 for the 10-rotor tooth, 12-stator slot machine for the 6 different relative positions of the rotor teeth and stator teeth. Saturation is accounted for by solving the lumped parameter magnetic circuit model iteratively, the permeability of the stator and rotor regions being varied according to their flux density, using the B-H curve for the lamination material.

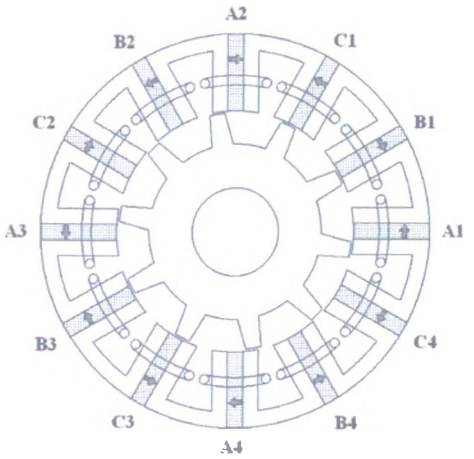

Fig. 3.7. 3-phase, 10-rotor tooth, 12-stator slot flux-switching PM machine

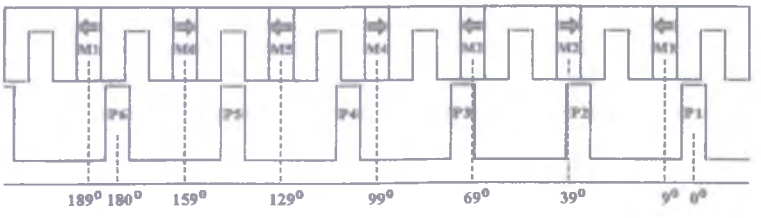

(a) Rotor at 0^{o} mechanical

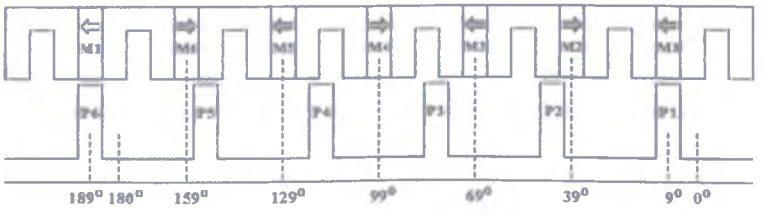

(b) Rotor at 9^{o} mechanical

Fig. 3.8. Flux-switching PM machine model in rectangular co-ordinates

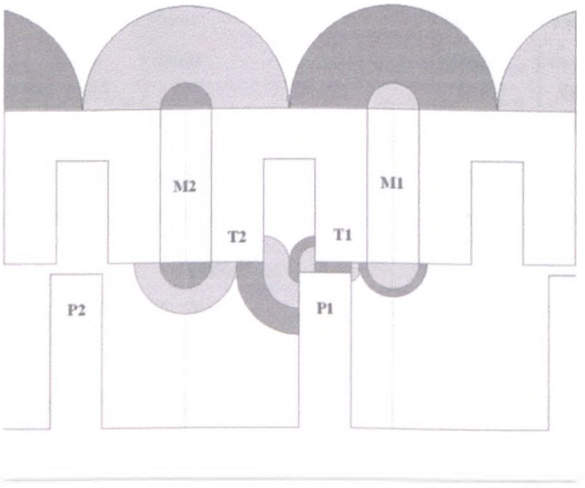

Fig. 3.9. Simplified flux paths of flux-switching PM machine

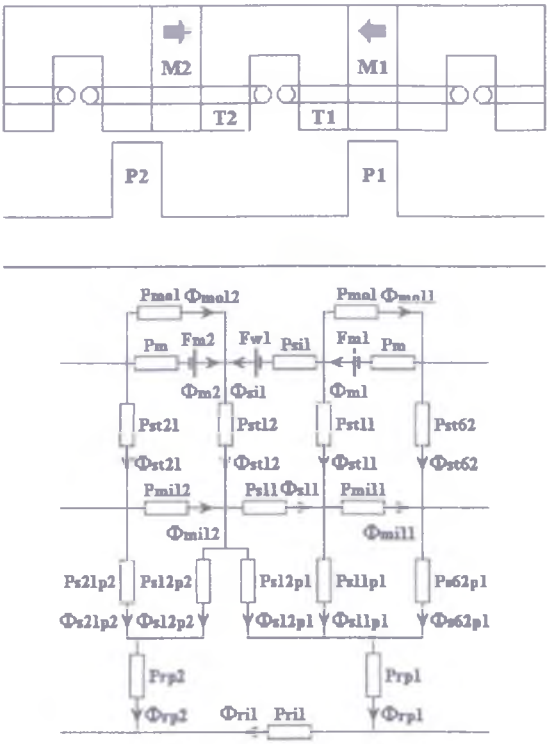

(a) Model 1 ($P_{T1\text{-}P2}$=0)

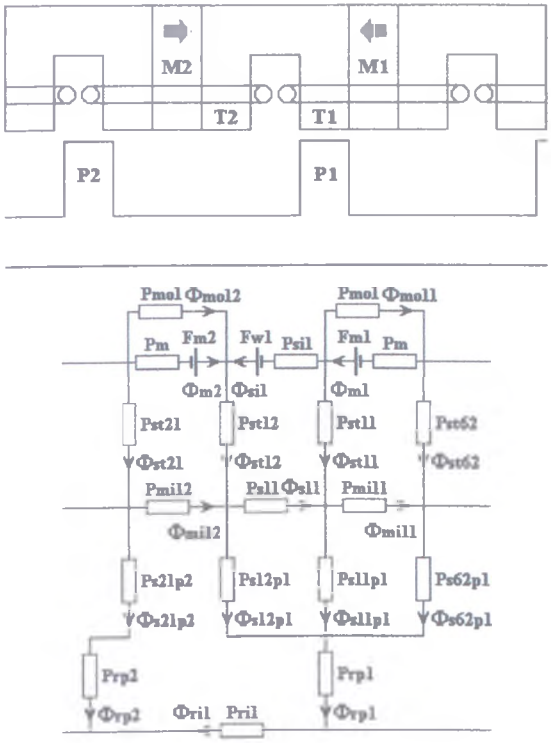

(b) Model 2 ($P_{T1\text{-}P2}$=0, $P_{T2\text{-}P2}$=0)

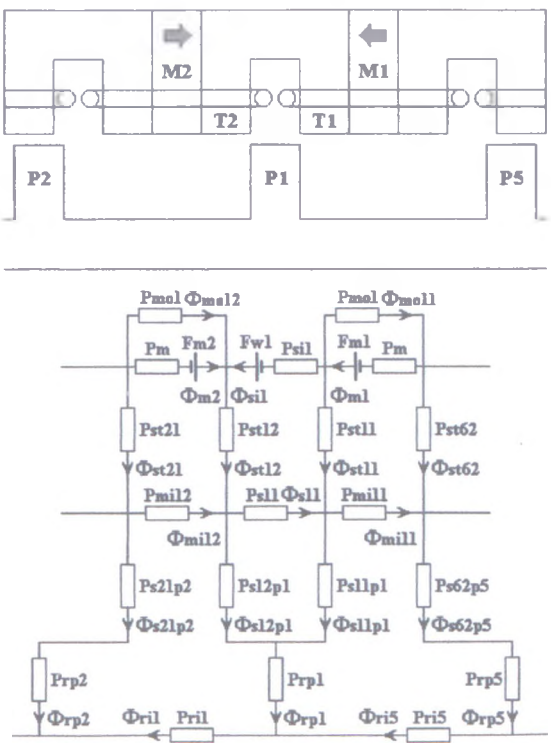

(c) Model 3 ($P_{T1\text{-}P5}$=0, $P_{T2\text{-}P2}$=0)

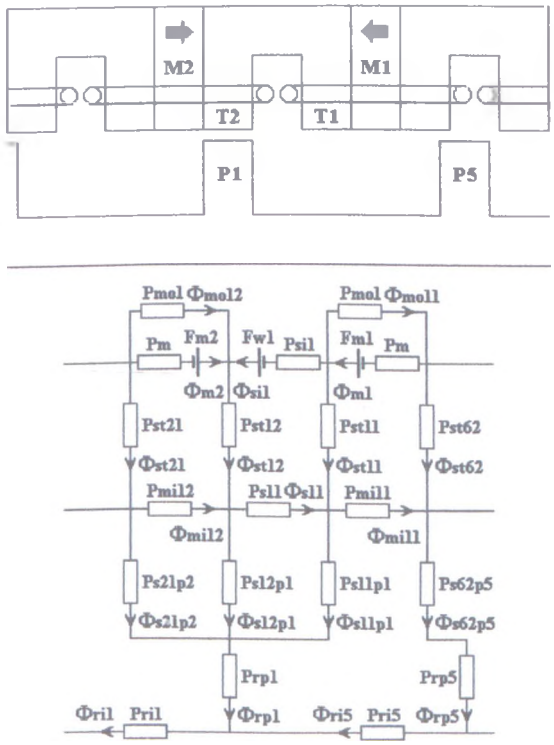

(d) Model 4 ($P_{T1\text{-}P5}$=0, $P_{T2\text{-}P5}$=0)

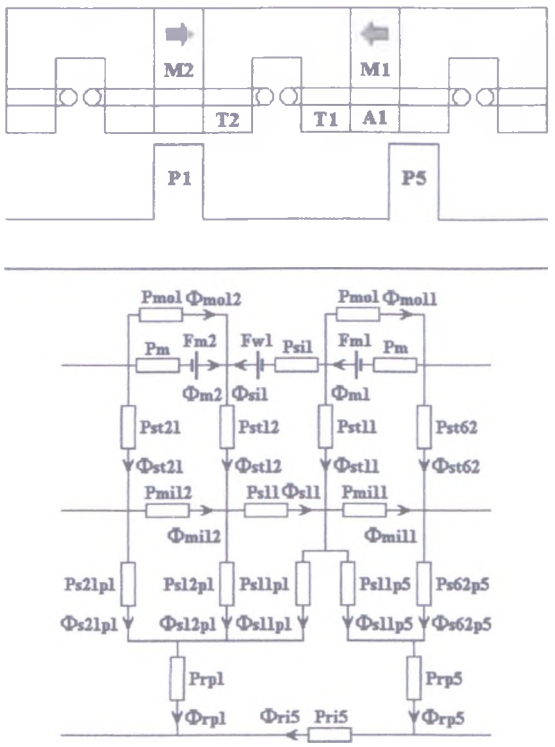

(e) Model 5 ($P_{T2\text{-}P5}$=0)

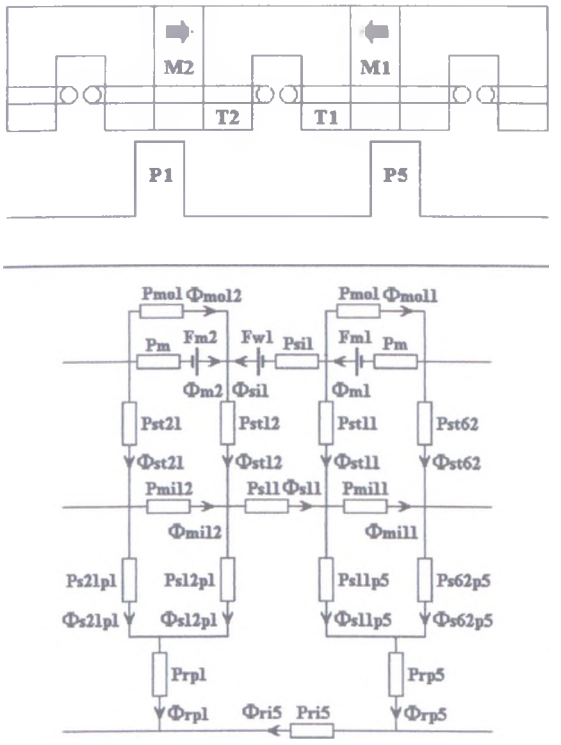

(f) Model 6 ($P_{T1\text{-}P1}$=0, $P_{T2\text{-}P5}$=0)

Fig. 3.10. Lumped parameter models of one stator segment for different rotor positions

The symbols in Fig. 3.10, in which the numerical subscripts relate to the corresponding stator tooth or rotor tooth, are as follows:

P_m Main permeance of permanent magnet

P_{mol} Outer leakage permeance of permanent magnet

P_{mil} Inner leakage permeance of permanent magnet

F_m Magnetic potential of permanent magnet

F_w Magnetic potential of stator winding

P_{st} Permeance of stator tooth

P_{si} Permeance of stator back-iron

P_{sp} Permeance between stator tooth and rotor tooth

P_{rp} Permeance of rotor tooth

P_{ri} Permeance of rotor back- iron

Φ_m Main flux of permanent magnet

Φ_{mol} Outer leakage flux of permanent magnet

Φ_{mil} Inner leakage flux of permanent magnet

Φ_{st} Flux in stator tooth

Φ_{si} Flux in stator back-iron

Φ_{sp} Flux passing between stator tooth and rotor tooth

Φ_{rp} Flux in rotor tooth

Φ_{ri} Flux in rotor back-iron

The subscripts on the symbols P_{mil}, F_m, Φ_m, Φ_{mol}, Φ_{mil}, P_{si}, Φ_{si}, F_w, P_{rp}, Φ_{rp}, P_{ri}, Φ_{ri} are associated with a specific magnet, stator segment, rotor tooth and the rotor back-iron. As regards the subscripts on P_{st} and Φ_{st}, the first digit is the stator segment number and the second is the tooth number to which the segment belongs. By way of example, the subscripts s12 and p1 in P_{s12p1} and Φ_{s12p1} are associated with stator segment number (s1), of tooth number (2), and rotor tooth number (p1).

In the next section, the electromagnetic performance of the 10-rotor tooth, 12-stator slot flux-switching PM machine will be predicted by using the foregoing lumped parameter magnetic circuit models, whilst the influence of end-effects and optimum machine dimensions will be investigated in subsequent sections.

3.3. Prediction of electromagnetic performance

The performance of the 3-phase, 10-rotor tooth, 12-stator slot flux-switching PM machine is predicted by using the lumped parameter magnetic circuit models and is compared with predictions from 2-D finite element analysis, with end-effects neglected. The main design parameters and the machine performance specification are given in Appendix I, whilst the B-H curve of the stator and rotor lamination material is given in Appendix III.

Although the permanent magnets are located in the stator and there is no flux source in the rotor, generalized machine theory using the dq-axis co-ordinate system can still be employed, based on the theory of abc→dq co-ordinate transformation. The d- and q-axis

currents, I_d and I_q, are related to the 3-phase currents, I_a, I_b and I_c, as shown in (3.6) [FIT92].

$$\begin{bmatrix} I_d \\ I_q \end{bmatrix} = \frac{2}{3}\begin{bmatrix} cos(\theta) & cos(\theta-120^o) & cos(\theta+120^o) \\ -sin(\theta) & -sin(\theta-120^o) & -sin(\theta+120^o) \end{bmatrix}\begin{bmatrix} I_a \\ I_b \\ I_c \end{bmatrix} \tag{3.6}$$

where θ is the rotor displacement angle. Fig. 3.11 shows the position of the d- and q-axes relative to the stator teeth and rotor teeth. As will be shown later, when rotor tooth P1 is displaced –9° mechanical from the centre of magnet M1 the phase-A flux-linkage attains its maximum value, which indicates that this rotor position corresponds to the d-axis, whilst the rotor position which coincides with the centre of magnet M1 is the q-axis.

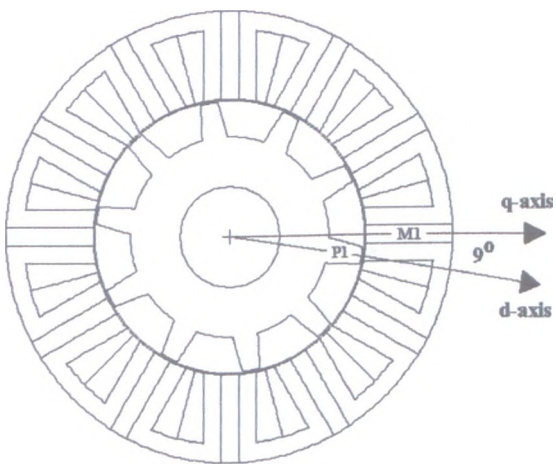

Fig. 3.11. Definition of dq-axis

3.3.1. Flux field distribution and magnet working point

The stator winding has been considered in the lumped parameter magnetic circuit model. As a result, the influence of the phase currents can be taken into account. It is noticed that although the results from finite element analysis shows that the field distribution changes slightly due to the influence of the phase currents, Fig. 3.12; in lumped the parameter magnetic circuit model, it is assumed that the simplified flux paths shown in Fig. 3.9 remain unchanged. This has been validated by further studies.

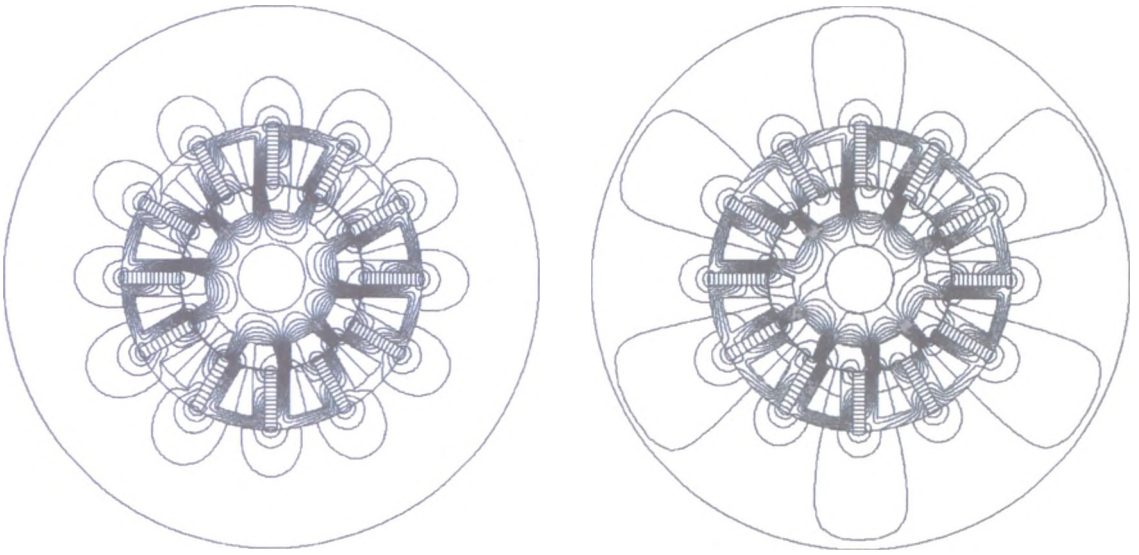

(a) No-load, I_d=0, I_q=0 (b) Full-load, I_d=0, I_q=15A

Fig. 3.12. Field distribution of flux-switching PM machine

The flux density variation in the permanent magnets of the flux switching PM machine is shown in Fig. 3.13(a). It will be seen that both no-load (I_d=0, I_q=0) and full-load (I_d=0, I_q=15A) conditions can be considered in the lumped parameter magnetic circuit model. Compared with results obtained from finite element analysis, it confirms that the predictions from the lumped parameter model are in very good agreement.

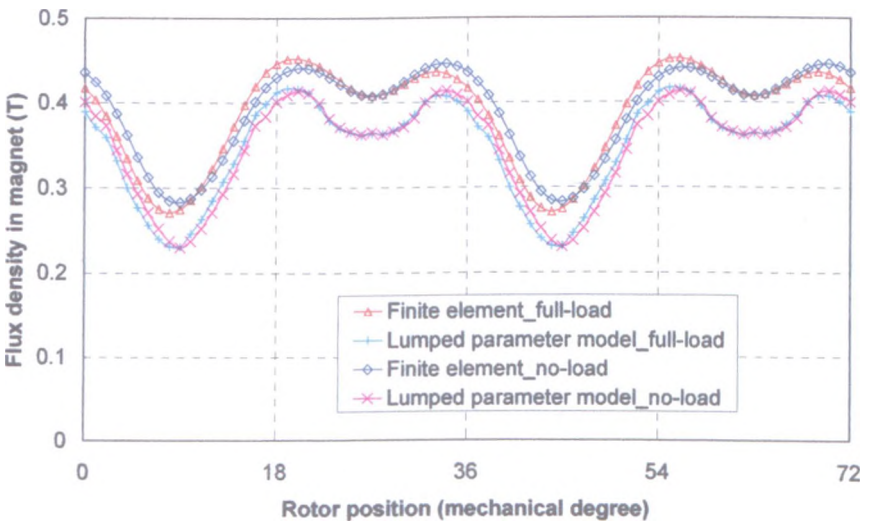

(a) Flux density waveform in magnet

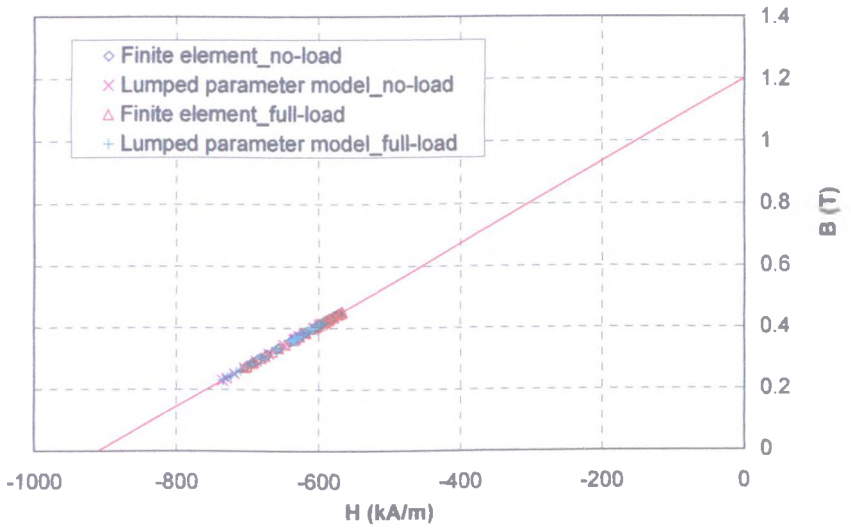

(b) Magnet working point on de-magnetization curve

Fig. 3.13. Magnet working point in flux-switching PM machine

Fig. 3.13(b) shows the variation of the magnet working point on the de-magnetization curve. It can be seen that although the sintered NdFeB magnet material has relatively high remanence (B_r=1.2T), the actual working point in the flux-switching PM motor is relatively low, only 0.2T~0.4T, due to the saturation which results from flux concentration.

3.3.2. Airgap field distribution

Fig. 3.14 compares airgap field distributions predicted from the lumped parameter magnetic circuit model and by finite element analysis. As can be seen, good agreement is achieved, both on no-load and at full-load when the d-axis current I_d=0, and the q-axis current is I_q=0 and I_q=15A, respectively. Due to the doubly salient machine topology, the airgap field distribution is very non-sinusoidal and exhibits significant harmonics, similar to a switched reluctance machine. However, due to the simplification of the airgap flux paths, the airgap field distributions obtained from the lumped parameter magnetic circuit model are much smoother than those obtained from finite element analysis, in which the flux density can locally exceed 2T, as a result of flux concentration around the corners of the stator teeth and rotor teeth.

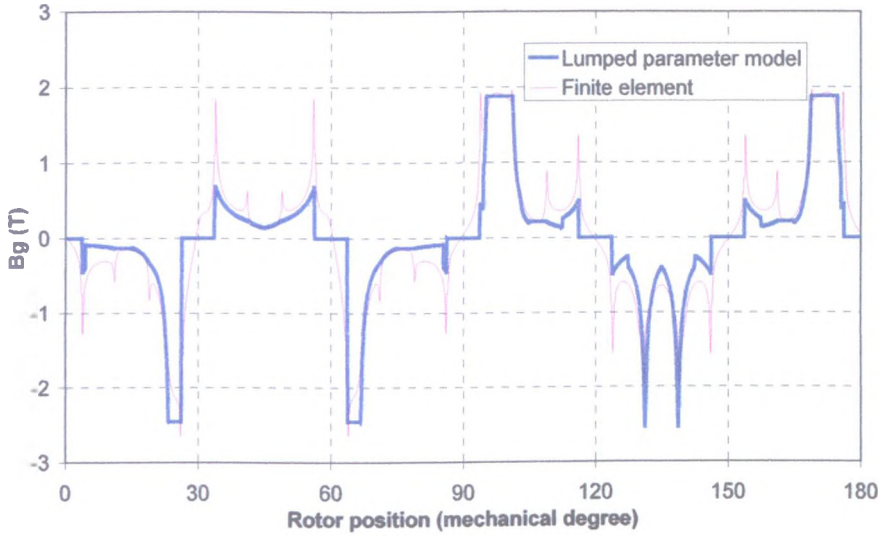

(a) I_d=0, I_q=0, rotor at 0° mechanical

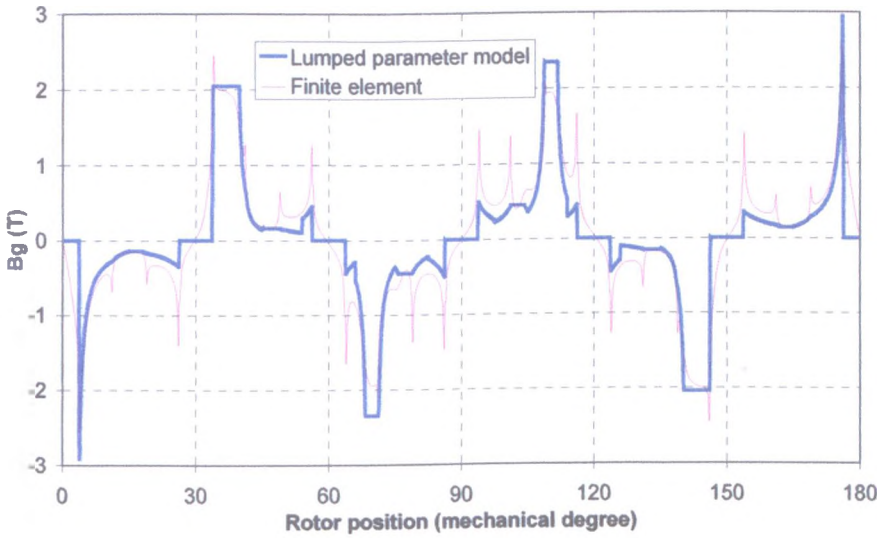

(b) I_d=0, I_q=0, rotor at 9° mechanical

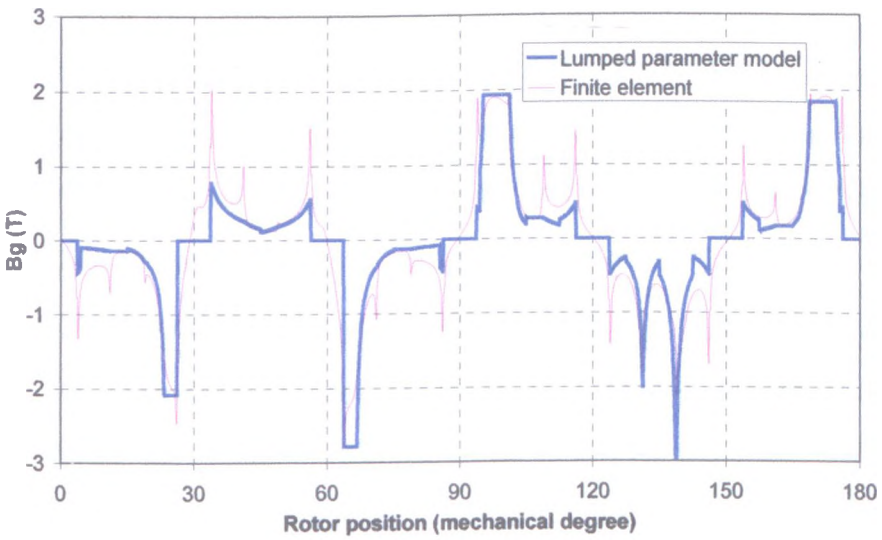

(c) I_d=0, I_q=15A, rotor at 0° mechanical

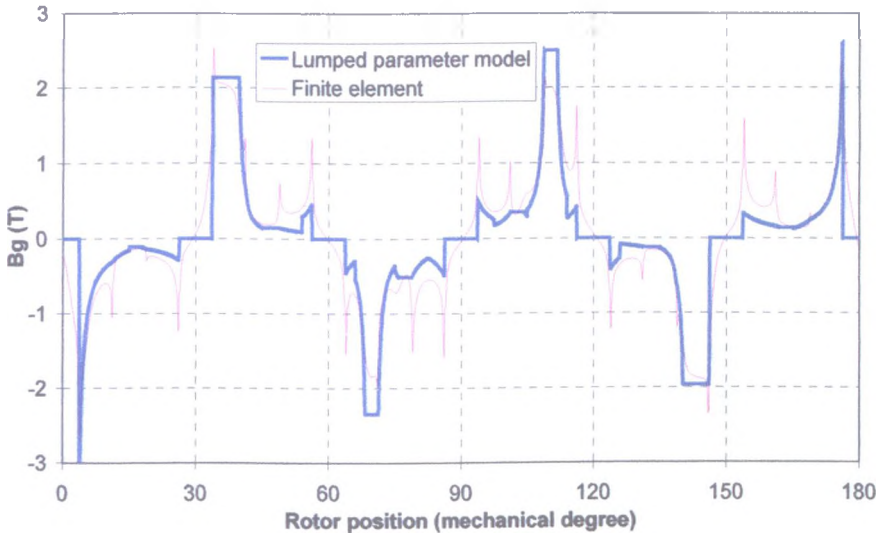

(d) I_d=0, I_q=15A, rotor at 9° mechanical

Fig. 3.14. Comparison of predicted airgap field distributions

3.3.3. Phase flux-linkage and back-emf waveforms

The phase flux-linkage ψ waveform can be predicted directly from the lumped parameter magnetic circuit model, and the back-emf can be determined from:

$$e = -\frac{d\psi}{dt} \tag{3.7}$$

As will be evident from Fig. 3.16, the flux-linkage and back-emf waveforms for coils A1 and A2 of phase A differ slightly, due to the difference in the relative position between the associated stator and rotor teeth. It will be seen from Fig. 3.15(a) that when the flux-linkage in phase A is a maximum, the axis of the rotor tooth under coil A1 is displaced by –9° mechanical from the axis of coil A1, while the axis of the rotor tooth under coil A2 is displaced by +9° mechanical from the axis of coil A2. An anti-clockwise rotation of 9° mechanical results in the flux-linkage of phase A becoming zero, Fig. 3.15(b), when the rotor tooth under coil A1 is aligned with the axis of the coil, and the axis of coil A2 is aligned with the centre of a rotor slot. Fig. 3.16 also shows that since localized magnetic saturation is accounted for more precisely in the finite element analysis, the finite element predicted back-emf waveforms have a lower harmonic content than those derived from the non-linear lumped parameter magnetic

circuit model. Further, although the flux-linkage and back-emf waveforms for coils A1 and A2 are non-sinusoidal, the resultant phase flux-linkage and phase back-emf waveforms are essentially sinusoidal.

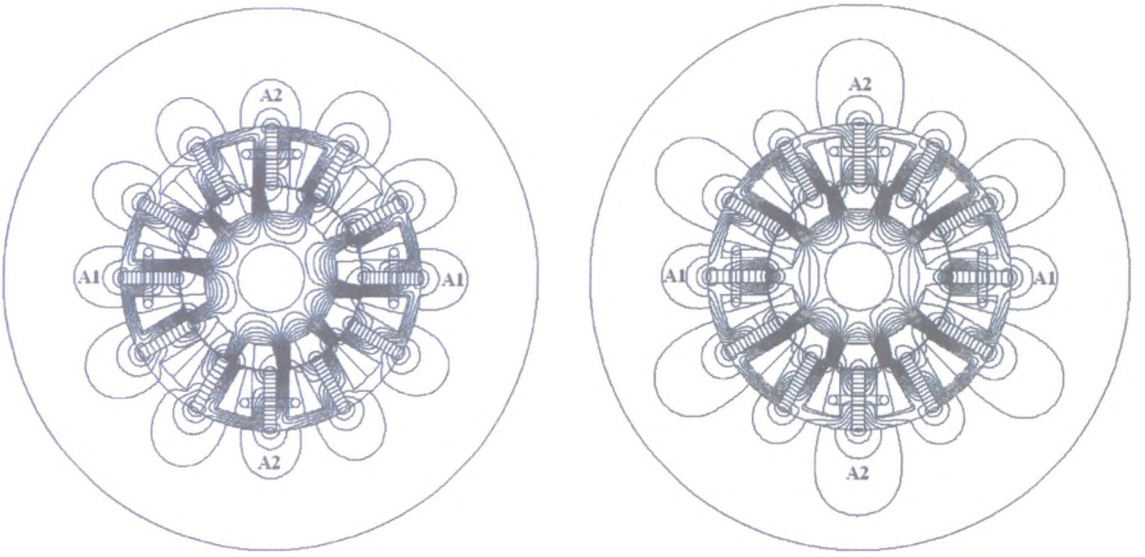

(a) Flux-linkage of phase A = max. (b) Flux-linkage of phase A = 0

Fig. 3.15. Open-circuit flux distributions

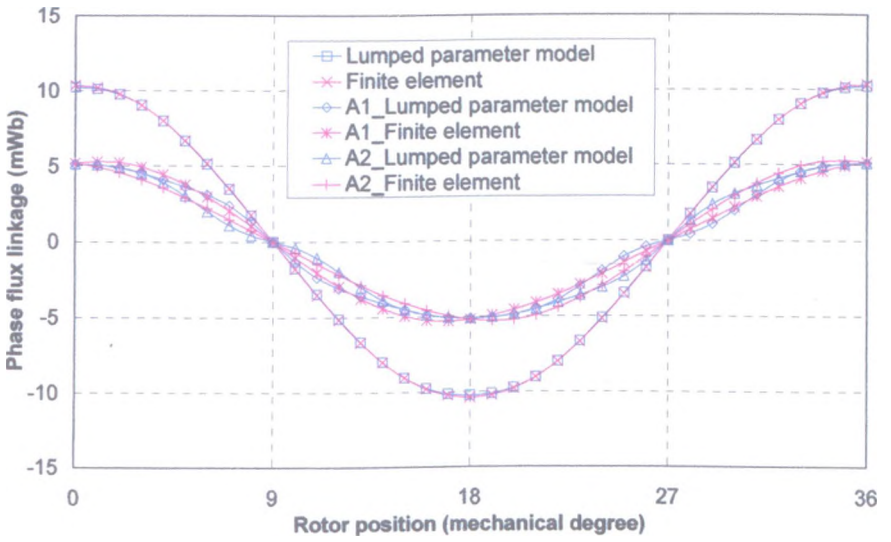

(a) Phase flux-linkage

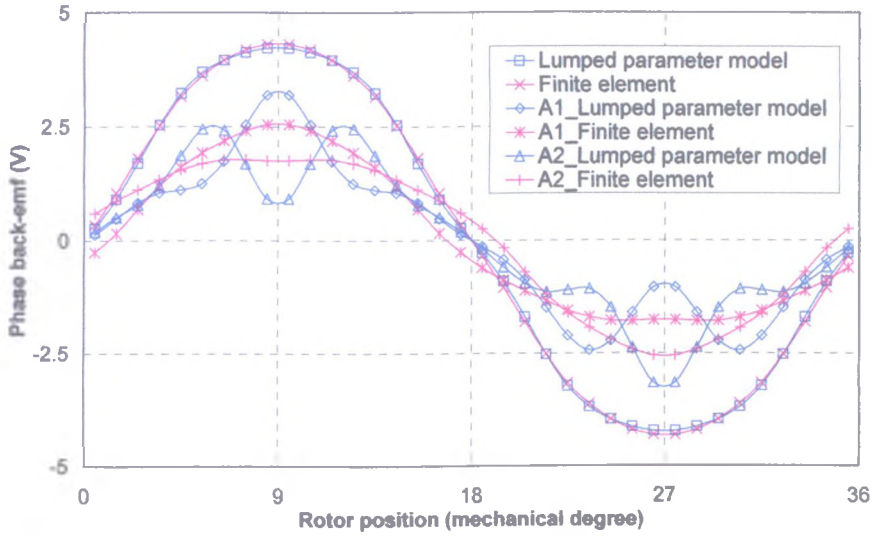

(b) Phase back-emf

Fig. 3.16. Phase flux-linkage and back-emf waveforms

3.3.4. Phase self-inductance and mutual-inductance

The phase self-inductance and mutual-inductance are obtained from the phase flux-linkage variation with current, i.e.:

$$L_{aa} = \frac{\psi_{a\_I_a} - \psi_{a\_0}}{I_a} \tag{3.8}$$

$$M_{ab} = \frac{\psi_{a\_I_b} - \psi_{a\_0}}{I_b} \tag{3.9}$$

where

L_{aa} Self-inductance of phase A

M_{ab} Mutual-inductance between phase A and phase B

ψ_{a_0} Flux-linkage of phase A due to permanent magnets

ψ_{a_Ia} Flux-linkage of phase A due to permanent magnets and phase A current I_a

ψ_{a_Ib} Flux-linkage of phase A due to permanent magnets and phase B current I_b

I_a Phase A current

I_b Phase B current

Fig. 3.17 compares the self-inductance and mutual-inductance predicted from the lumped parameter magnetic circuit model and by finite element analysis. As will be seen, due to the different relative positions between the stator teeth and rotor teeth, the self-inductance and mutual-inductance of coils A1 and A2 differ slightly. In general, good agreement is achieved, although the finite element predicted inductances vary less with rotor position since localized magnetic saturation effects are not accounted for in the non-linear lumped magnetic circuit model. Due to the "U"-shaped stator segments, the mutual-inductance between phases is, on average, approximately half the phase self-inductance, as in conventional PM brushless machines, as illustrated in Fig. 3.18.

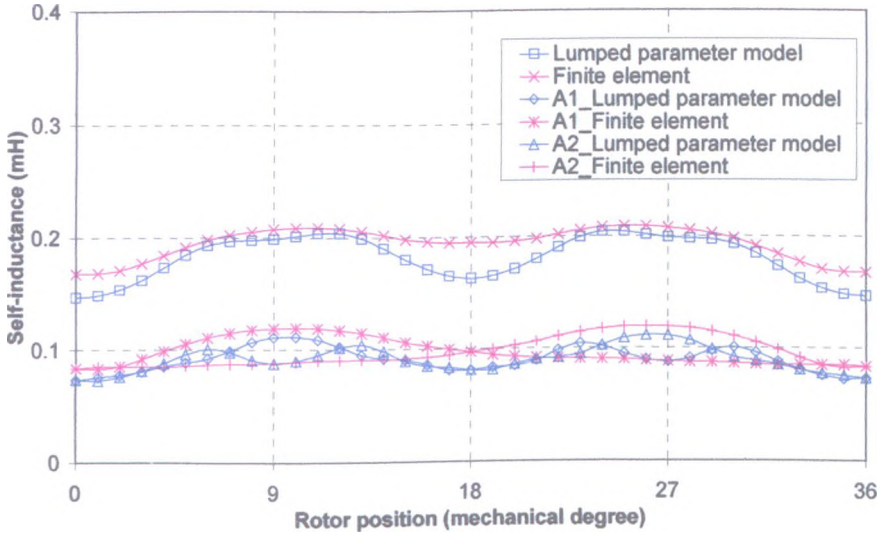

(a) Self-inductance

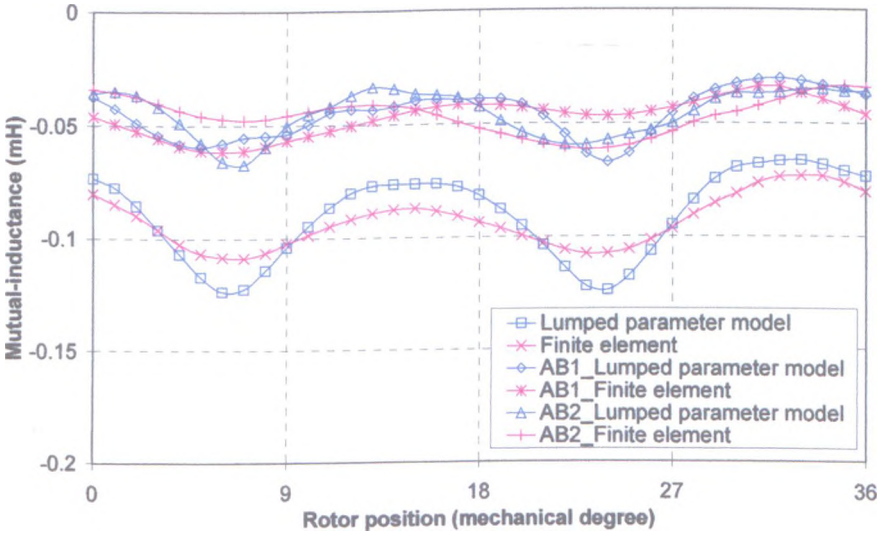

(b) Mutual-inductance

Fig.3.17. Self-inductance and mutual-inductance

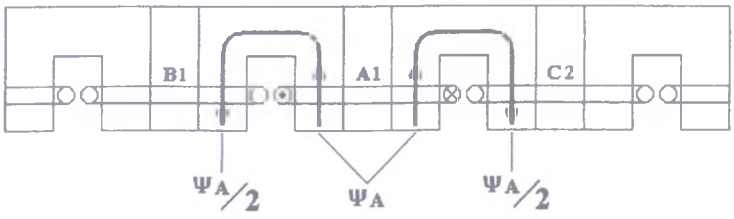

Fig.3.18. Phase-A flux paths

3.3.5. Open-circuit PM flux-linkage and dq-axis inductances

The d-axis PM flux-linkage, ψ_m, and the d- and q-axis inductances, L_d and L_q, can be calculated from the abc→dq transformation, and are shown in Fig. 3.19.

As will be seen, the d-axis PM flux-linkage is almost constant with rotor position, while L_d and L_q are similar in magnitude. As a result, although flux-switching PM machines have a salient tooth rotor topology, the reluctance torque is relatively small.

3.3.6. Electromagnetic torque

Since the reluctance torque in a flux-switching PM machine can usually be neglected, the electromagnetic torque can simply be calculated from:

$$T = \frac{3}{2} p \psi_m I_q \tag{3.10}$$

Fig. 3.20 shows the variation of the torque with rotor position, predicted from the lumped parameter magnetic circuit model, along with results from finite element analysis which is based on Maxwell stress model. As will be seen, the machine exhibits very little torque ripple, despite the fact that it has a doubly salient topology.

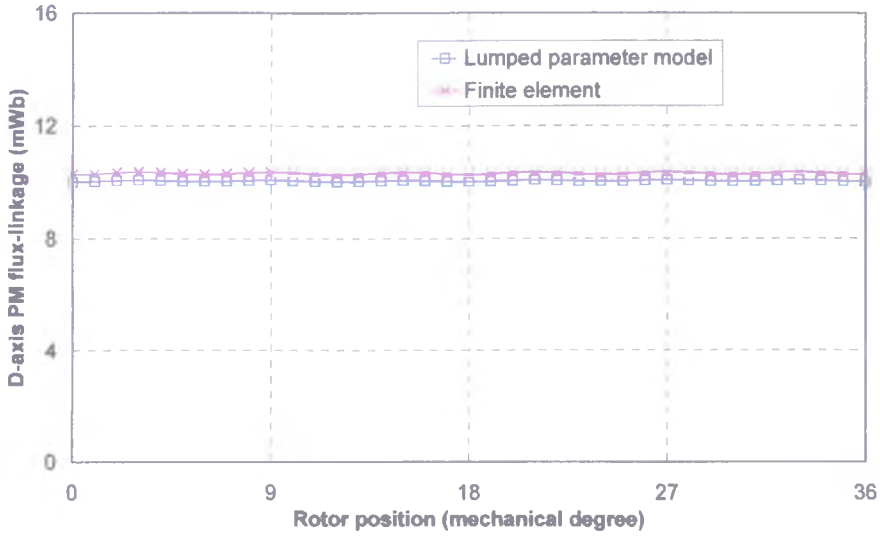

(a) D-axis PM flux-linkage

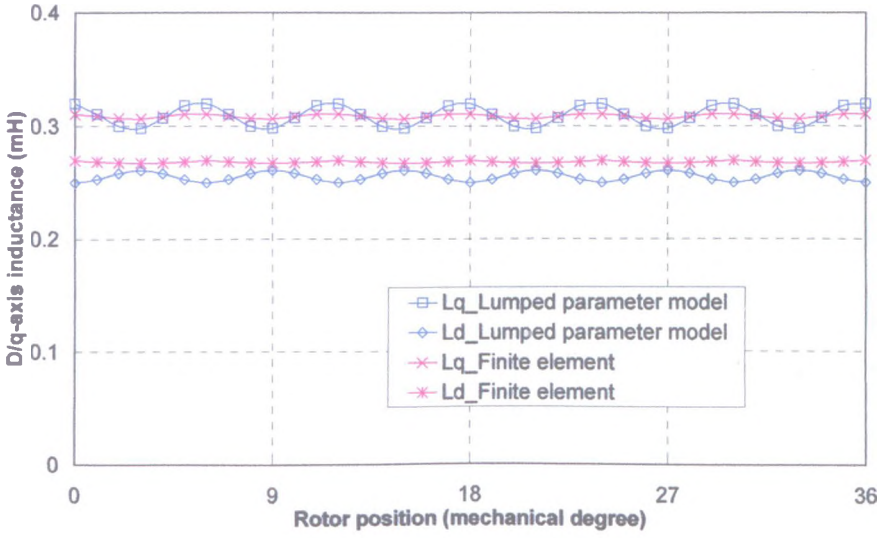

(b) D/q-axis inductances

Fig.3.19. D-axis PM flux-linkage and dq-axis inductances

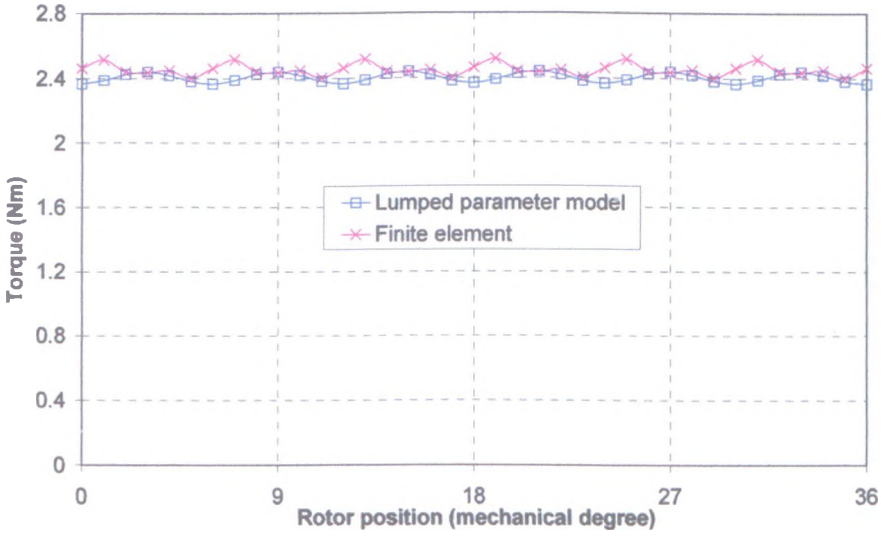

Fig.3.20. Variation of torque with rotor position (I_d=0 and I_q=15A)

3.4. 2-D and 3-D analyses

In the previous section, magnetic saturation in the laminations and leakage flux external to the outer surface of a flux-switching PM machine were taken into account in the non-linear adaptive lumped parameter magnetic circuit model. In this section, the influence of these aspects will be considered further, as well as the influence of leakage flux at the end-surfaces of the machine, which can also be considered in the lumped parameter magnetic circuit model. Predictions from the lumped parameter magnetic circuit model will be validated by 2-D and 3-D finite element analyses. All the analyses assume that the flux-switching PM machine is on open-circuit.

3.4.1. Influence of magnetic saturation

Fig. 3.21 shows that no matter what the position the rotor is with respect to the stator, the stator tooth tips and the rotor tooth tips are highly saturated, e.g. the local maximum flux density can be higher than 2.5T, while the knee point of the magnetization characteristic of the lamination material is only ~1.6T. As a result, magnetic saturation in the stator and rotor laminations will have a significant influence on the performance.

In the lumped parameter model, magnetic saturation of the stator and rotor laminations is accounted for by using the appropriate non-linear B-H characteristic. The working points of different parts of stator and rotor laminations need to be determined iteratively from the B-H curve, the higher the magnetic saturation, the more iterations are needed. It can be seen from Fig. 3.22 that when saturation is considered, i.e. the magnetization characteristics of stator and rotor laminations are non-linear, the maximum phase flux-linkage is 10.3mWb; which compares with a maximum phase flux-linkage of 14.0mWb when saturation is neglected and the relative permeability of the stator and rotor is assumed to be 2000.

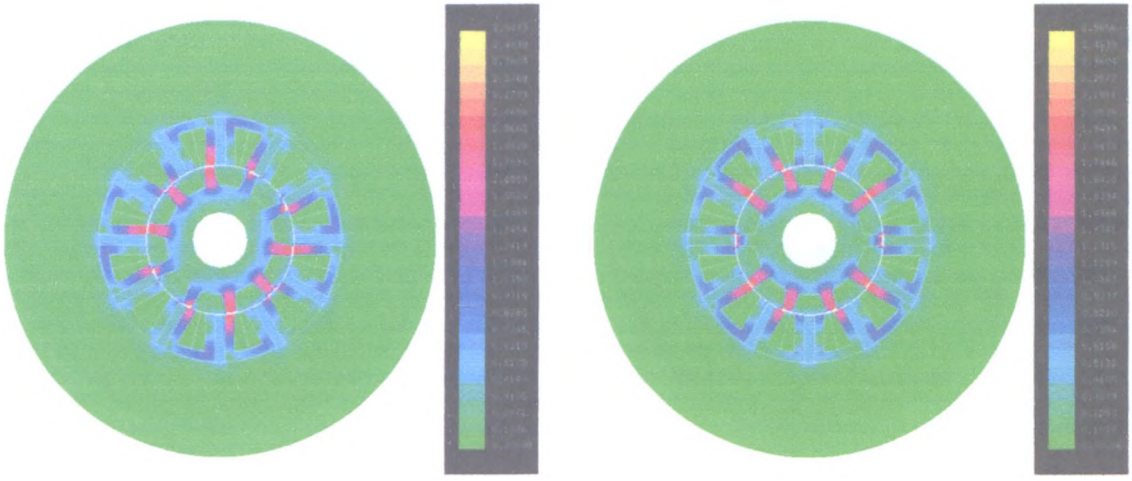

(a) Rotor=0° mechanical (B_{max}=2.58T) (b) Rotor=9° mechanical (B_{max}=2.56T)

Fig. 3.21. Flux density distribution (B_r=1.2T)

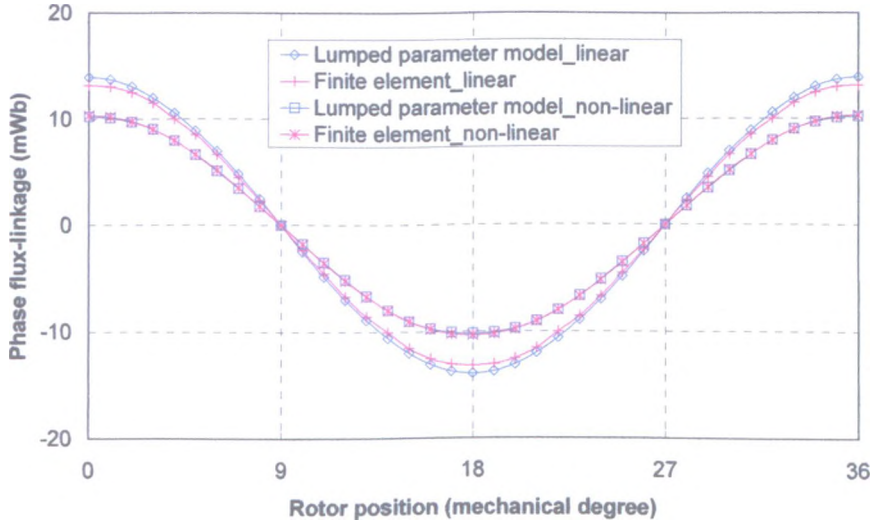

Fig. 3.22. Influence of magnetic saturation on phase flux-linkage

3.4.2. Influence of magnet remanence

Although sintered NdFeB magnets offer the highest remanence of the various permanent magnet materials, and can result in a very high power density, their cost is still relatively high. Therefore, bonded NdFeB magnets with B_r≈0.8T or sintered ferrite magnets with B_r≈0.4T may be preferred for many cost-sensitive commercial applications.

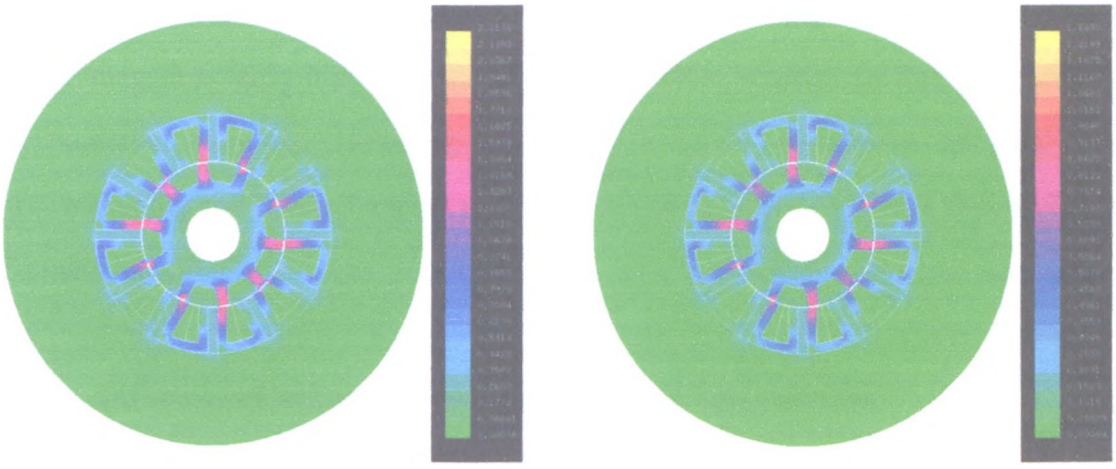

(a) B_r=0.8T (B_{max}=2.21T) (b) B_r=0.4T (B_{max}=1.26T)

Fig. 3.23. Flux density distribution (Rotor=0°)

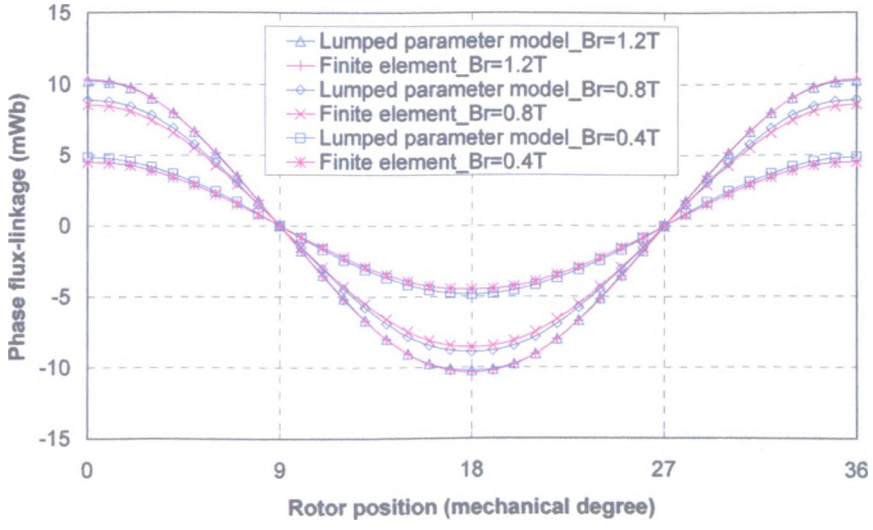

Fig. 3.24. Influence of magnet remanence on phase flux-linkage

The influence of changing the magnet remanence can be readily assessed. By way of example, it can be seen from Fig.3.24 that reducing the remanence from 1.2T to 0.8T, Fig. 3.24(a), i.e. by 33%, reduces the phase flux-linkage by only 17%; whilst reducing the remanence from 1.2T to 0.4T, Fig. 3.24(b), i.e. by 67%, the phase flux-linkage is reduced by just over 50%, all the other parameters of the original machine design being fixed. However, subsequent investigations will show that a high remanence permanent magnet is not always the best choice for a flux-switching PM machine, and that for some applications, a low remanence magnet may be more appropriate. For example, for

a hybrid excited machine, since the original flux-switching PM machine equipped with NdFeB magnet is fairly highly saturated, it is difficult to weaken the flux by employing an excitation winding. However, by using a lower remanence magnet, good flux-weakening and flux-enhancing performance can be achieved from a flux-switching PM machine.

3.4.3. Influence of leakage flux external to stator outer surface

Since the magnets in a flux-switching PM machine are sandwiched between two 'U'-shaped stator lamination segments, the outer ends of the magnets give rise to leakage flux external to the stator core, as shown in Fig. 3.12.

Similar to the internal airgap flux paths, the external leakage flux paths can be simplified, as shown in Fig. 3.25, to enable a lumped parameter magnetic circuit model to be employed. However, the comparison shown in Fig. 3.26 indicates that due to the highly saturated magnetic circuit of the flux-switching PM machine, the influence of the external leakage flux on the performance is very small, and indeed is almost negligible.

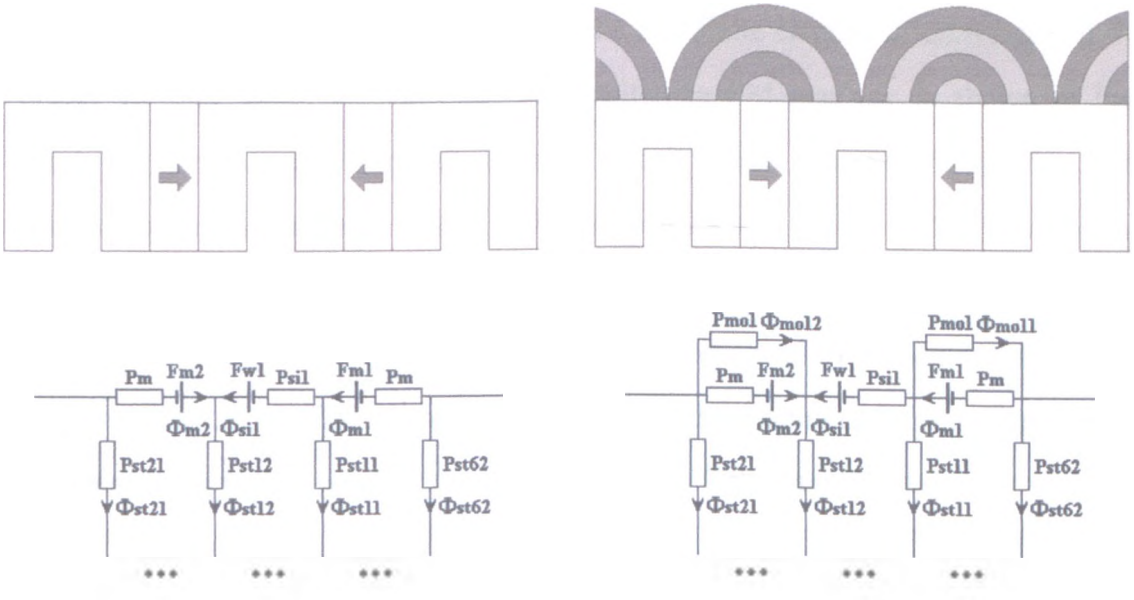

(a) Without leakage (b) With leakage

Fig. 3.25. Modeling of leakage flux path external to stator core

(Permeance equation reference to Fig. 3.6(c))

where P_{mol} is the permeance of the leakage external to stator core, and Φ_{mol} is the leakage flux external to stator core.

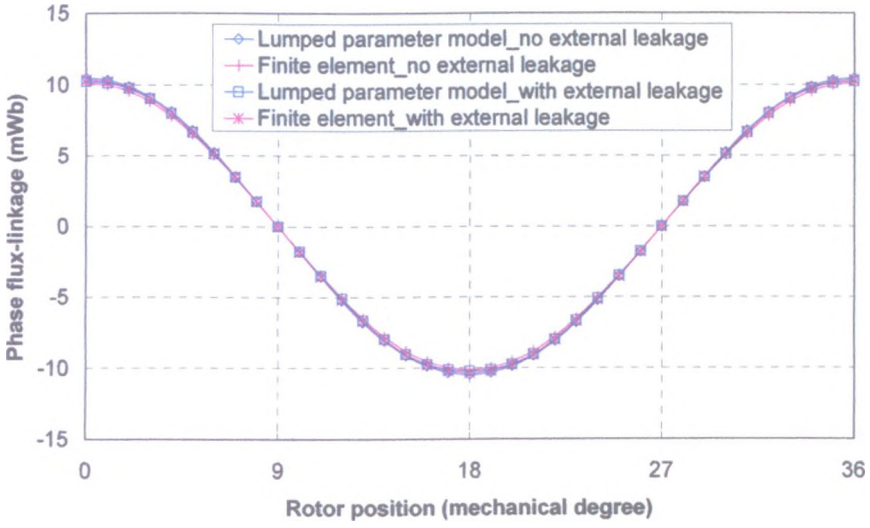

Fig.3.26. Influence of external leakage flux on phase flux-linkage

3.4.4. Influence of end-leakage flux

The influence of end-leakage flux, i.e. the 3-D effect due to the finite axial length, is generally an issue for all types of machines. The 3-D finite element discretisation of the 3-phase, 10-rotor tooth, 12-stator slot flux-switching PM machine is shown in Fig. 3.27(a). For the lumped parameter magnetic circuit model, the end-leakage flux path can be simplified as shown in Fig. 3.27(b). As will be seen in Fig. 3.28(a), neglecting end-effects in the machine under consideration (i.e. a 2-D calculation) results in ~10% overestimate in the phase flux-linkage, as has been confirmed by performing 3-D finite element analysis. Fig. 3.28(b) shows the 3-D predicted variation of the maximum airgap flux density along the axis of the flux-switching PM machine, together with the predicted variation from a 2-D finite element analysis. It can be seen that, due to end-effects, the average airgap flux density in the active machine region is reduced by ~10%, which is consistent with the reduction in the phase flux-linkage.

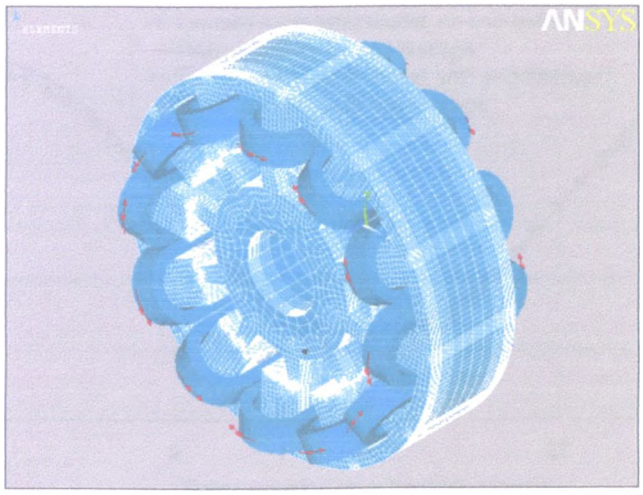

(a) 3-D model in ANSYS

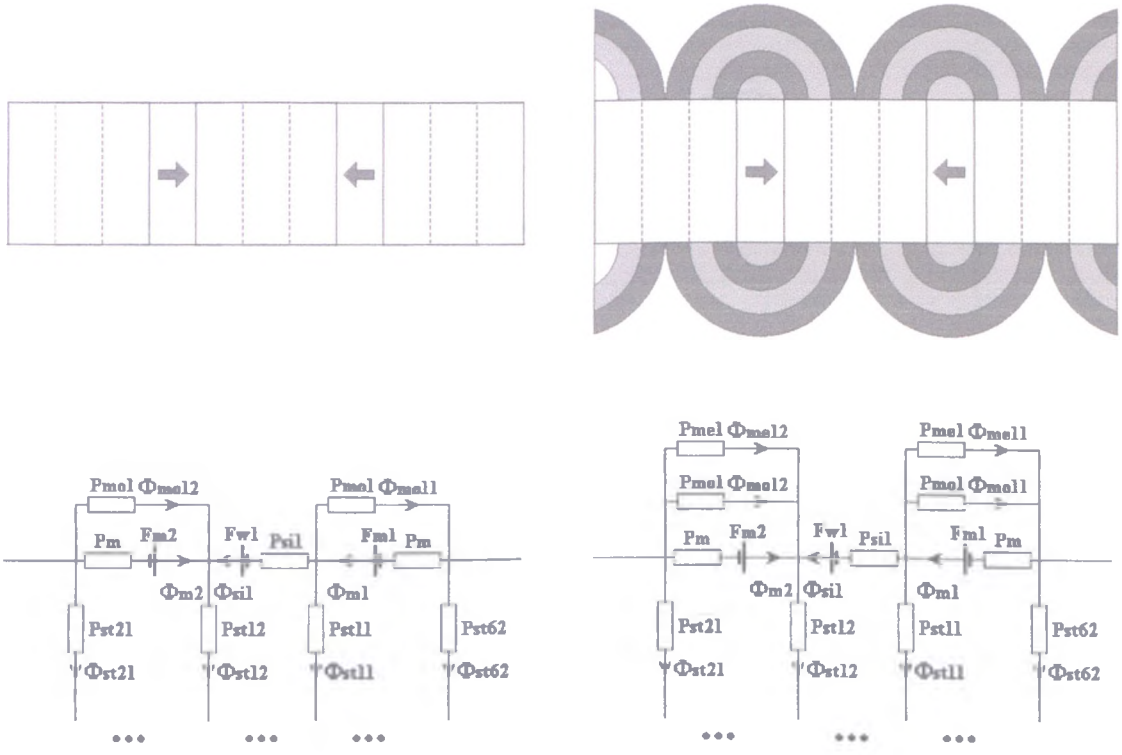

(b) Without end-leakage flux

(c) With end-leakage flux

Fig. 3.27. Modelling of end-leakage flux

(Permeance equation reference to Fig.3.6(c))

where P_{mel} is the permeance of the end-leakage flux, and Φ_{mel} is the end-leakage flux.

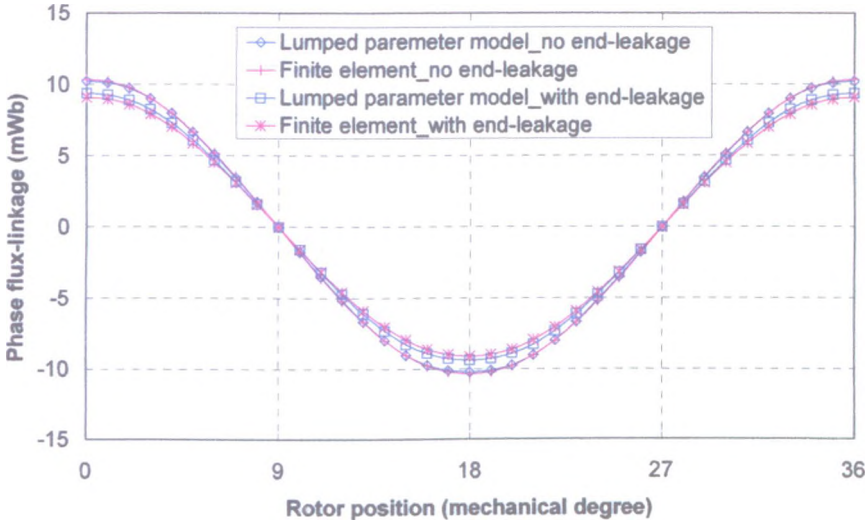

(a) Phase flux-linkage

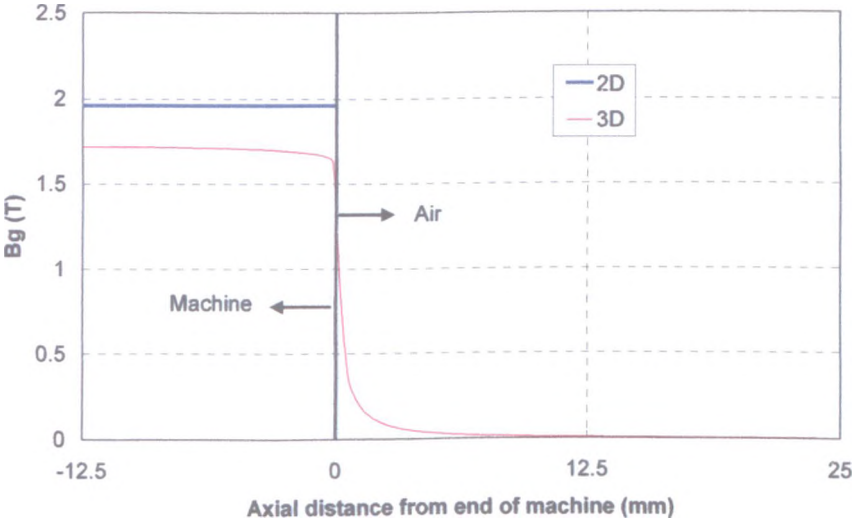

(b) Airgap flux density

Fig.3.28. Influence of 3-D end-leakage flux

3.5. Design optimization

In this section, by using the developed adaptive lumped parameter magnetic circuit model of the flux-switching PM machine, the optimal stator tooth width, rotor tooth width, and ratio of the inner to outer stator diameter (i.e. the split ratio) will be investigated, with reference to the original machine design, i.e. in which the stator teeth, the slot openings, and rotor teeth have identical widths.

3.5.1. Stator tooth width

Fig. 3.29 shows the influence of the stator tooth width on the torque, predicted from both the lumped parameter magnetic circuit model and finite element analysis, when the copper loss is limited to 50W and all the other dimensions are maintained fixed. It shows that the torque is a maximum when the stator tooth width is equal to the width of the slot openings. Although the slot area for accommodating the coils could be increased by reducing the tooth width, the teeth would become more heavily saturated and the phase flux-linkage would be reduced, Fig. 3.30. In contrast, an increase in the stator tooth width relieves saturation, but the electromagnetic torque would be reduced, since the slot area is reduced for a fixed copper loss.

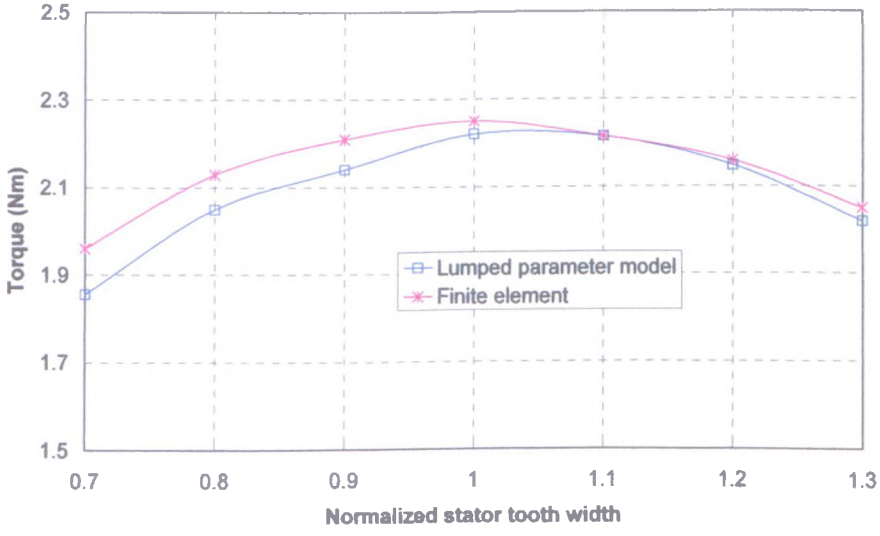

Fig.3.29. Influence of stator tooth width on torque

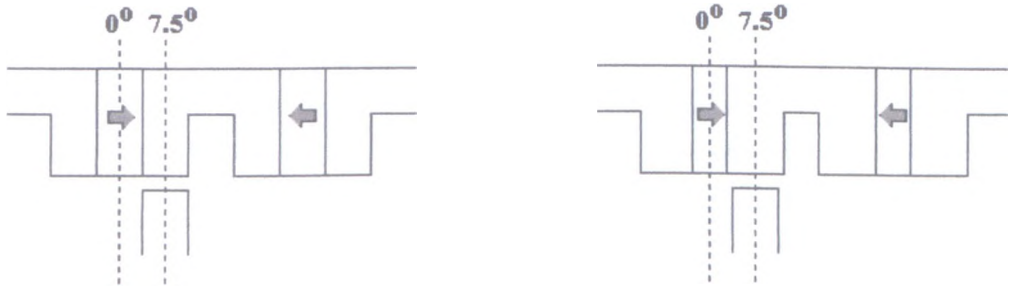

(a) Stator tooth width = rotor tooth width (b) Stator tooth width > rotor tooth width

Fig.3.30. Optimization of stator tooth width

3.5.2. Rotor tooth width

When the phase current is maintained constant, the electromagnetic torque varies with the rotor tooth width as shown in Fig. 3.31. As will be seen, maximum torque is achieved when the rotor tooth width is ~1.4-1.6 times the original value (which was equal to the stator tooth width and the width of the slot opening). This can be explained by referring to Fig. 3.32. Fig. 3.32(a) shows the relative position of a rotor tooth and a stator tooth for maximum phase flux-linkage, when the rotor tooth and stator tooth are displaced by 9° mech., with the rotor tooth width equal to the stator tooth width. However, by making the rotor tooth width wider than the stator tooth width such that one edge of the tooth is aligned with the edge of the stator tooth, as shown in Fig. 3.32(b), the maximum phase flux-linkage is increased.

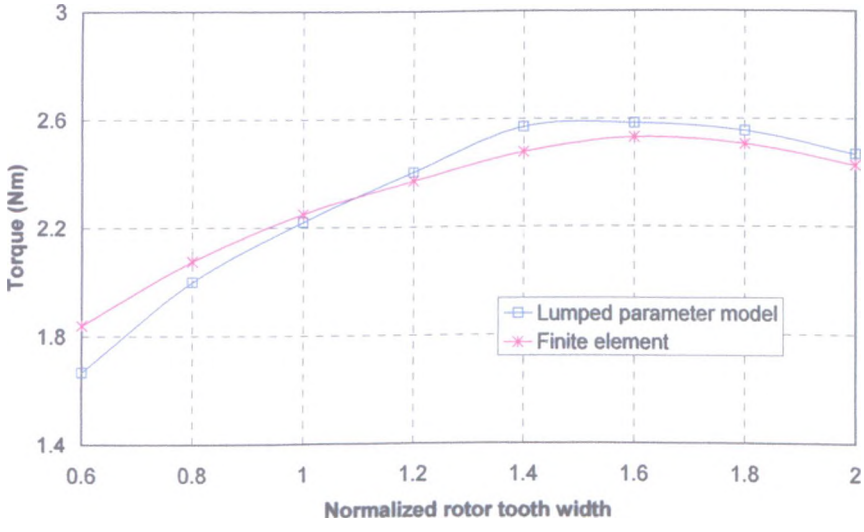

Fig. 3.31. Influence of rotor tooth width on torque

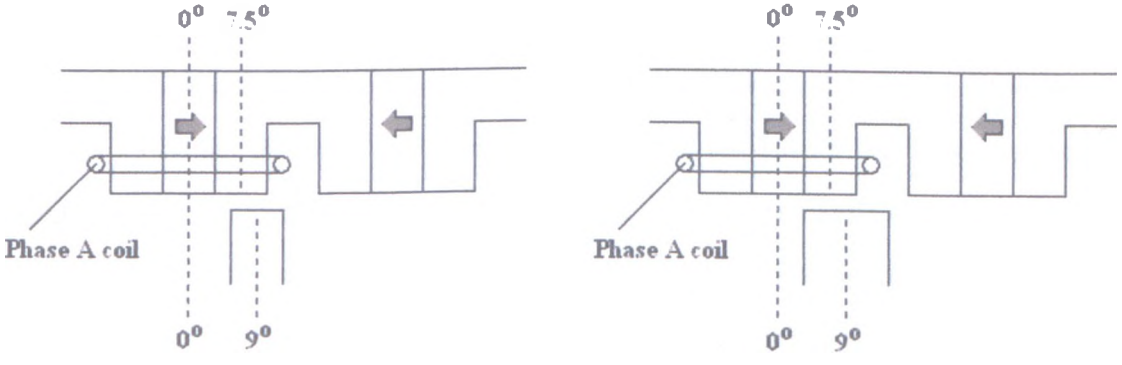

(a) Rotor tooth width = stator tooth width (b) Optimized rotor tooth width

Fig. 3.32. Optimization of rotor tooth width

3.5.3. Split ratio

The optimal split ratio, i.e. the ratio of the inner to outer diameter of the stator, is one of the most important design parameters since the torque is usually proportional to the square of the rotor diameter, while the stator slot area reduces as the rotor diameter is increased. Fig. 3.33 shows the variation of torque with the split ratio, again for a fixed copper loss of 50W, maximum electromagnetic torque being achieved when the split ratio is 0.55~0.6.

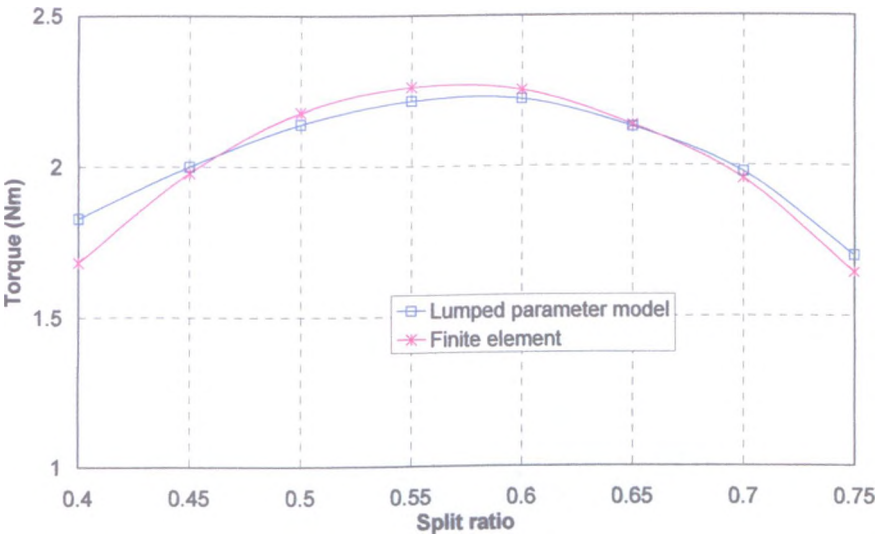

Fig. 3.33. Optimization of split ratio

3.5.4. Discussions

In the foregoing, the rotor tooth width, the stator tooth width and the split ratio of a flux-switching PM machine have been optimized individually by using the developed lumped parameter magnetic circuit model, the findings being validated by finite element analyses. Although the optimal design parameters obtained from the lumped parameter magnetic circuit model differ slightly from those deduced from finite element analysis, in general, the difference is relatively small. Hence, the lumped parameter magnetic circuit model may be used to identify an optimum machine design which may be refined further by finite element analysis.

The variation of the torque with the rotor tooth width, stator tooth width, and split ratio,

as calculated by the lumped parameter magnetic circuit model, is shown in Fig. 3.34. It will be seen that the optimal split ratio for maximum torque is ~0.6, at which the variation of torque with the rotor tooth width and stator tooth width is illustrated in Fig. 3.34(b). This multi-parameter optimization suggests that the optimal stator tooth width is ~1.1 times the original value, i.e. the optimal stator tooth width is approximately equal to the width of the stator slot opening, the optimal rotor tooth width is around 1.4~1.6 times the original stator tooth width, which is approximately equal to the stator slot opening, while the optimal split ratio is ~0.6. This confirms that the optimal rotor tooth width, stator tooth width, and split ratio can be deduced independently for a flux-switching PM machine.

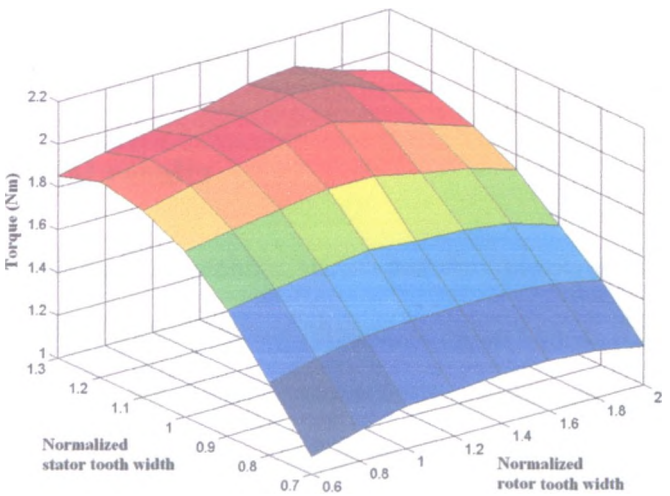

(a) Split ratio=0.4

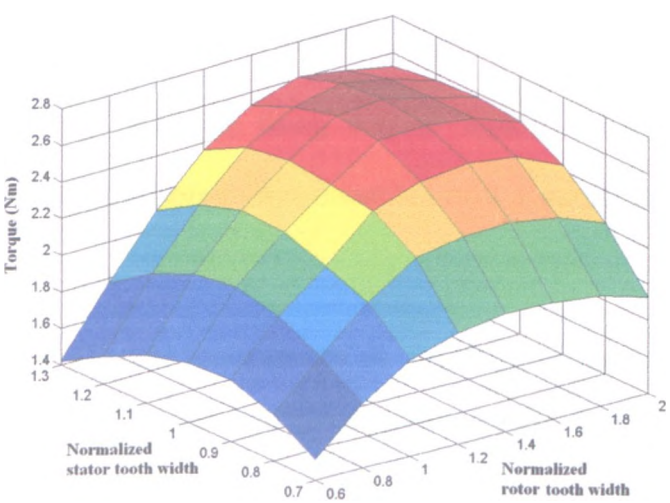

(b) Split ratio=0.6

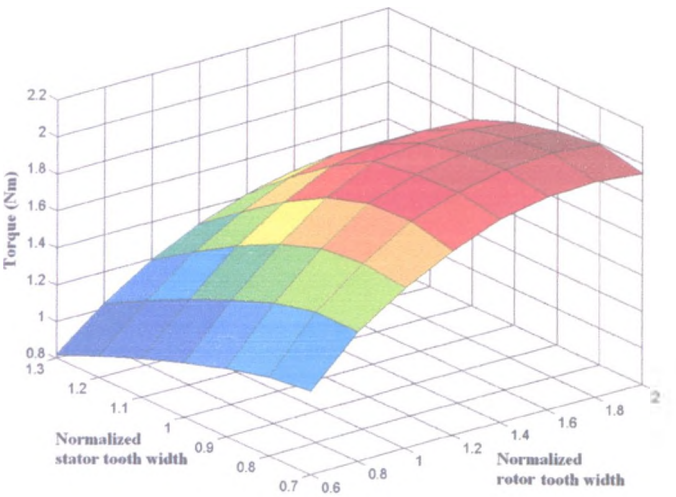

(c) Split ratio=0.75

Fig. 3.34. Optimization of rotor tooth width and stator tooth width

3.6. Experimental results

A prototype flux-switching PM machine, which has the optimized stator tooth width and optimized split ratio, has been built, as shown in Appendix I. Two rotors have been manufactured, one having the original rotor tooth width, and the other having the optimized rotor tooth width. The main design parameters of this prototype machine are listed in Appendix I.

The sponsoring company, IMRA UK Research Center, performed all the experiment testing on prototype flux-switching PM machine.

By driving the prototype machine using another motor, the phase back-emf was obtained. The electromagnetic torque was measured on a dynamometer with the $I_d = 0$ control.

The measurement of d/q-axis inductances is relatively complicated. The method proposed in [FIT92] is used, where the instantaneous stator phase self-inductances are assumed as:

$$L_{aa} = L_{aa0} + L_{al} + L_{g2}\cos(2\theta) \tag{3.11}$$

$$L_{bb} = L_{aa0} + L_{al} + L_{g2}\cos(2\theta + 120^o) \tag{3.12}$$

$$L_{cc} = L_{aa0} + L_{al} + L_{g2}\cos(2\theta - 120^o) \tag{3.13}$$

then, d/q-axis inductances are derived as:

$$L_d = L_{al} + \frac{3}{2}(L_{aa0} + L_{g2}) \tag{3.14}$$

$$L_q = L_{al} + \frac{3}{2}(L_{aa0} - L_{g2}) \tag{3.15}$$

$$L_0 = L_{al} \tag{3.16}$$

where, L_{aa0} is the average phase self-inductance, L_{al} is the phase leakage inductance and L_{g2} is the second-order harmonic component of the self-inductance waveform.

In practice, the phase self-inductance is measured by a pulse inductance meter with bias current at different rotor position, then the d/q-axis inductances can be derived. Although this method is not exactly the same as the method used in the finite element calculation, it should yield comparable results, with due consideration of the influence of phase current

Fig.3.35 compares the measured phase back-emf waveform, torque vs. current characteristic and dq-axis inductances vs. current characteristic with predictions from the lumped parameter magnetic circuit model. Clearly, end-effects can significantly reduce the phase back-emf and electromagnetic torque. The neglect of end-effects in the flux-switching PM machine under consideration (i.e. a 2-D calculation) results in ~10% overestimate of the phase flux-linkage and the phase back-emf, as has been confirmed by performing 3-D finite element analysis.

The electromagnetic torque of the flux-switching PM machine can be improved by optimizing the rotor tooth width, as shown in Fig. 3.36. It can be seen that, by optimizing the rotor tooth width, the electromagnetic torque can be improved by ~10%.

In general, the predicted and measured performance of the flux-switching PM machine agree very well, despite the fact that significant simplifying assumptions have to be

made for the airgap flux paths in the lumped parameter magnetic circuit model.

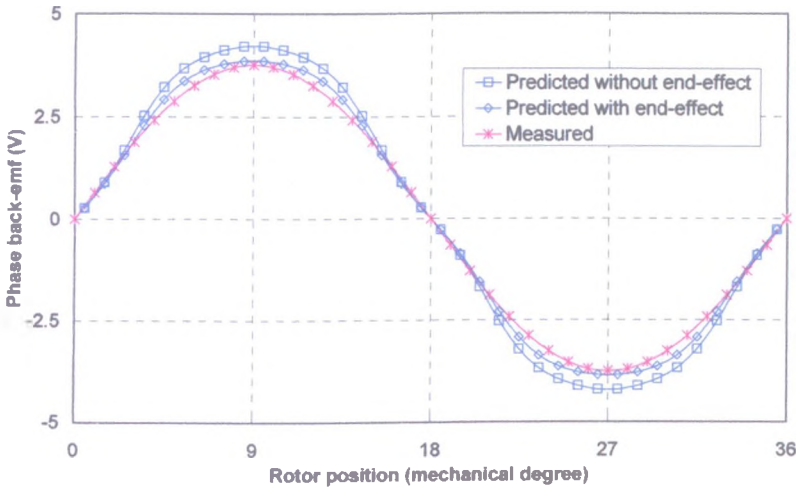

(a) Phase back-emf

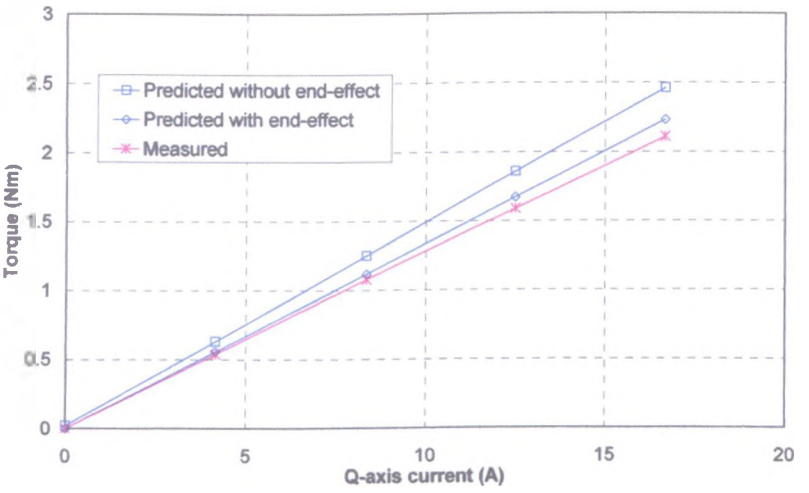

(b) Electromagnetic torque

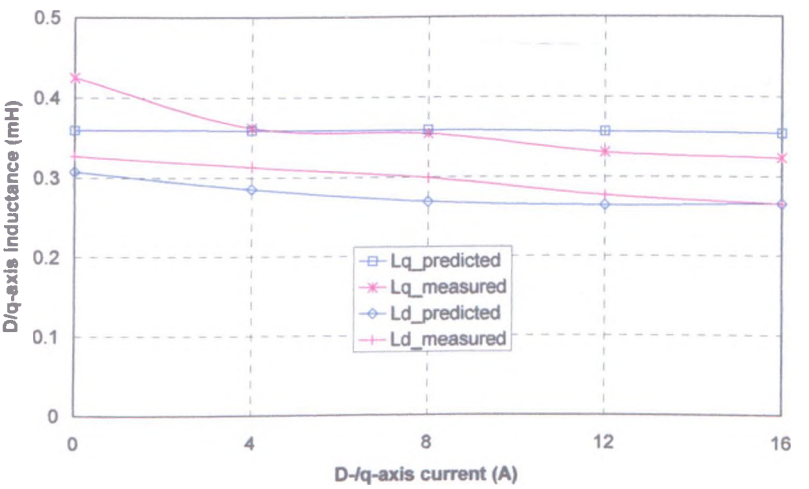

(c) D/q-axis inductances

Fig. 3.35. Comparison of predicted and measured performance (original rotor)

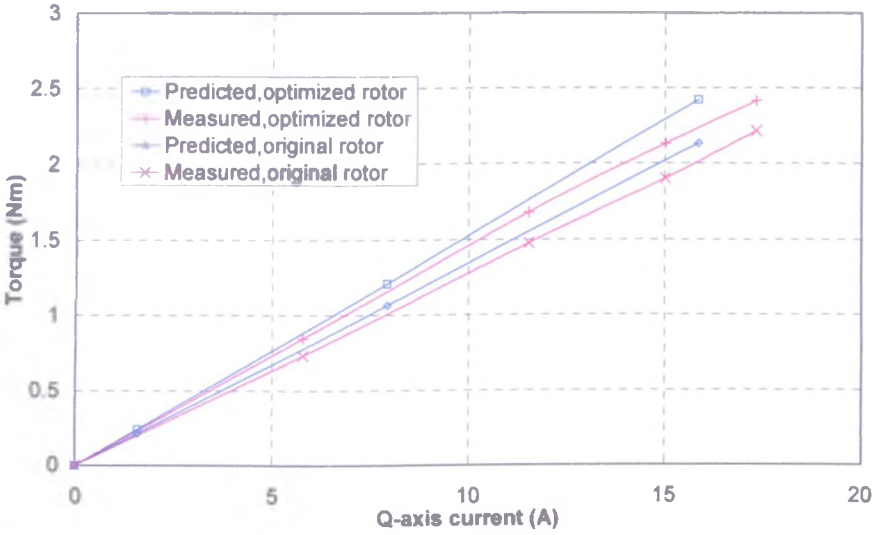

Fig. 3.36. Comparison of predicted and measured torque (optimized rotor)

3.7. Summary

A non-linear adaptive lumped parameter magnetic circuit model has been developed to predict the electromagnetic performance, i.e. the airgap field distribution, the phase flux-linkage and back-emf waveform, the self- and mutual-inductances, the d- and q-axis inductances and the electromagnetic torque, the predictions being validated by finite element calculations and measurements. End-effects have been investigated, and their influence, for the particular flux-switching PM machine under consideration, has been to reduce the phase flux-linkage, the phase back-emf and the electromagnetic torque by ~10%. An optimal rotor tooth width, stator tooth width and split ratio have been established, and it has been shown that these can be derived independently. It has been shown that for maximum torque capability, for a fixed copper loss, the optimal split ratio is ~0.55-0.6, whilst the optimal stator tooth width should be approximately equal to the width of the stator slot opening, and the optimal rotor tooth width should be ~1.4-1.6 times that of the stator tooth width.

A prototype flux-switching PM machine has been built, equipped with both a non-optimal tooth width rotor and an optimized tooth width rotor. Comparisons between the predicted machine performance and measured results confirm that a ~10% torque

reduction occurs due to end-effects, since the prototype has a relatively short axial length, and a ~10% torque increase is obtained when the optimized rotor tooth width is used.

Chapter 4 Optimal Split Ratio of Permanent Magnet Brushless Machines

4.1. Introduction

The split ratio, i.e. the ratio of the stator bore diameter to the stator outer diameter ($\frac{D_s}{D_o}$), is an important design parameter for permanent magnet brushless machines since it has a significant influence on the torque capability and efficiency, and also the cost. Previous work [HES87] has shown that an optimal split ratio exists for minimum copper loss, and that it has a significant influence on the magnetic circuit and winding design. A simple analytical expression for the optimal split ratio for maximum torque per volume was derived in [CHA94]. It depended on the pole number and the ratio of the maximum airgap flux density to the maximum flux density in the stator iron, and was applicable to both surface-mounted permanent magnet and interior-permanent magnet rotor topologies. In addition, the influence of the split ratio on the demagnetization withstand capability of the permanent magnets was discussed, since a low split ratio leads to a larger slot area and a higher electric loading, which, in turn, increases the likelihood of partial irreversible demagnetization of the magnets. However, the investigation was restricted to permanent magnet brushless machines having overlapping stator windings and neglected the influence of the tooth-tips, the end-windings and stator iron loss. The influence of the split ratio on the overall cost of a machine was discussed in [CHA00], assuming that the cost was dominated by the permanent magnets. Previous investigations on the split ratio had only been applied to brushless DC machines with a trapezoidal back-emf waveform and 120° electrical rectangular current waveforms. However, in [ZHU97], the analysis was extended to cater for brushless DC machines having non-overlapping stator windings and a sinusoidal back-emf waveform. Since the stator iron loss may be the dominant loss component in high-speed and/or high pole number PM machines with a high fundamental electrical frequency, a CAD design package was used in [EDE01] to investigate its influence on the optimal split ratio. It

was shown that the iron loss not only compromises the efficiency, but is relatively insensitive to the split ratio, while, generally, the optimal split ratio is reduced only slightly when the iron loss is taken into account [EDE01]. Of course, the sensitivity of the optimal split ratio to the iron loss depends on the fundamental frequency and the harmonic content in the stator flux waveforms.

However, all of the foregoing investigations make specific assumptions, and are usually only appropriate for a particular machine topology. For example, the optimal split ratio which was derived in [CHA94][CHA00] is only applicable to machines having overlapping stator windings, while that derived in [ZHU97] applies to machines having non-overlapping windings, both analyses neglecting the influence of the tooth-tips and the end-windings.

In this thesis, the optimal split ratio for maximum torque per volume is investigated for permanent magnet brushless machines having either overlapping or non-overlapping windings, and accounts for the influence of the airgap field distribution, the back-emf waveform, and the influence of the tooth-tips and end-windings. The analytical models, which are developed, are validated by both finite element analyses and measurements. Finally, the method is extended to flux-switching PM machines, for which the optimal split ratio is derived analytically and validated by finite element analysis, while the influence of the end-windings, and the magnetic and electric loadings is also investigated.

4.2. Optimal split ratio of conventional PM brushless machines

As mentioned in the introduction, it has been shown that, in general, the iron loss has a relatively small influence on the optimal split ratio. Thus, in order to make the ensuing analyses tractable, the iron loss will be neglected. In this section, the basic procedure for deriving an analytical expression for the optimal split ratio, which is similar to that reported in [CHA94], is described. The relationship between the electromagnetic torque and the machine dimensions, including the stator slot dimensions, is established, and the

optimal split ratio for maximum torque per volume is obtained analytically for a fixed machine outside diameter and temperature rise.

Two winding dispositions are considered, i.e. non-overlapping and overlapping. A non-overlapping winding has a coil wound around each stator tooth, the winding being short-pitched, i.e. ~120° electrical coil span, with the ratio of pole number to stator slot number typically being 2:3, while for an overlapping winding the coils are usually full-pitched, i.e. 180° electrical coil span, and the ratio of pole number to stator slot number is typically 2:6. However, an overlapping winding may also be short-pitched if a distributed winding is employed. Figs. 4.1(a) and (b) show schematics of 3-phase, 4-pole machines having 6 stator slots and 12 stator slots, and carrying non-overlapping windings and overlapping windings, respectively.

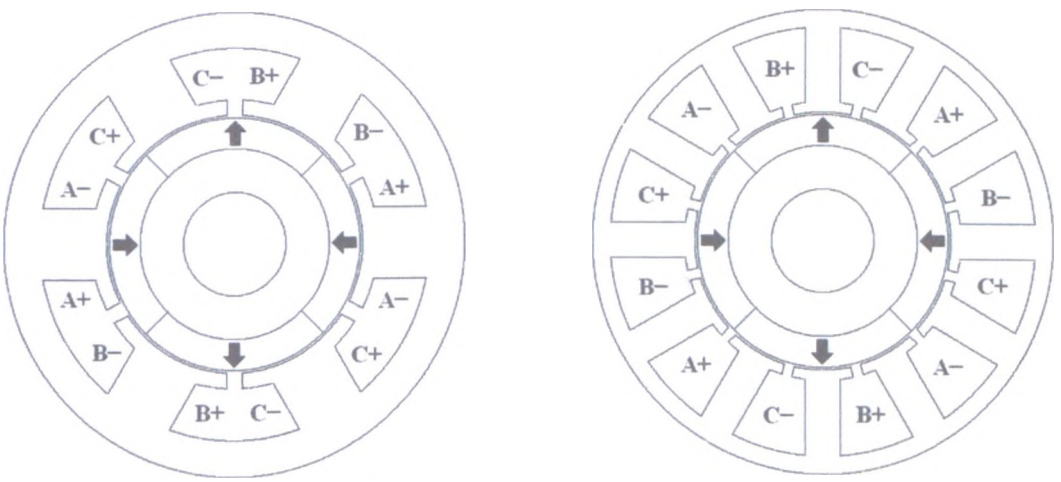

(a) 6-slot, non-overlapping winding (b) 12-slot, overlapping winding

Fig. 4.1. 3-phase, 4-pole permanent magnet machines

Two types of conventional permanent magnet brushless machine, viz. a surface-mounted permanent magnet (SPM) machine and an interior-permanent magnet (IPM) machine, are considered. It has been shown that both a trapezoidal airgap field distribution and a sinusoidal airgap field distribution can be obtained in either a SPM machine or an IPM machine. Hence, although the rotor topologies of SPM and IPM machines are different, the same stator can be employed for both, if the airgap field distributions are designed to be similar. Therefore, the equation for the optimal split

ratio of a SPM machine can be used for an IPM machine, if both machines have similar airgap field distributions and the same stators.

By way of example of the influence of the split ratio on the specific torque capability, Fig. 4.2 shows the variation of the torque with the split ratio and maximum airgap flux density, B_g, for a 4-pole brushless AC machine equipped with a non-overlapping winding when its stator outer diameter and copper loss are fixed, i.e. for the same thermal performance, where p is the number of pole-pairs, N_s is the number of stator slots, B_{max} is the maximum flux density in the stator iron, and D_o, D_s and L_a are the stator outer diameter, stator bore diameter and active axial length, respectively. It can be seen that for a certain value of airgap flux density B_g, an optimal split ratio exists for the maximum output torque, since the smaller split ratio results in less flux linkage while the larger split ratio results in less slot area.

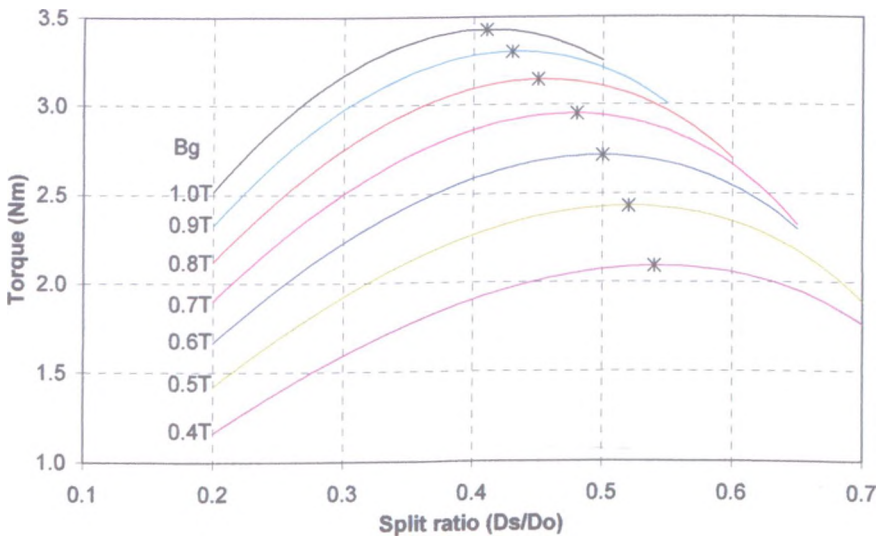

Fig. 4.2. Variation of torque with split ratio (p=2, N_s=6, B_{max}=1.5T, D_o=90mm, L_a=50mm, P_{Cu}=50W)

Since the investigation here is started from the airgap field distribution, different rotor topologies can be employed in order to achieve the same airgap field, e.g. the same airgap flux density can be achieved by either varying the magnet remanence or changing the magnet thickness. Clearly, the stator needs to be carefully designed, as will be considered later. Although Fig. 4.2 neglects the end-windings and the influence of the stator tooth-tips in the slot area calculation, it clearly indicates that an optimal split ratio

exists for maximum torque, and the airgap flux density has a significant influence on the optimum value. The analytical derivation of the optimum is the subject of this chapter. It should be noted that, since the stator iron loss is neglected, the derivation of the optimal split ratio for maximum torque per volume is equivalent to that for minimum copper loss, i.e. maximum efficiency.

4.2.1. PM brushless machine with a trapezoidal airgap field distribution

Initially, the optimal split ratio for a 3-phase brushless DC machine equipped with a non-overlapping stator winding will be derived, assuming (a) a trapezoidal airgap flux density distribution; (b) 120° electrical conduction, and (c) parallel-sided stator teeth, without tooth-tips, as illustrated in Fig. 4.3(c); and (d) neglecting the end-windings.

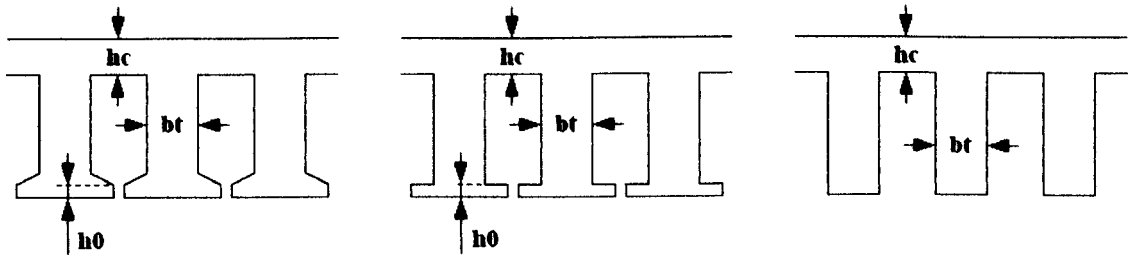

(a) Actual tooth shape (b) Idealized tooth shape (c) Simplified tooth shape

Fig.4.3. Alternative stator tooth shapes

The derived equations can be easily adopted for a brushless AC machine with a sinusoidal airgap field distribution, whilst the influence of the tooth-tips and end-windings will be investigated in subsequent sections.

When the winding pitch is 120° electrical, the phase back-emf is given by:

$$e_{ph} = BLV = B_g \cdot 2N_w L_a \cdot \frac{\omega_{elec}}{p} \frac{D_s}{2} \tag{4.1}$$

and the electromagnetic torque is obtained as:

$$T = IBLR = 2I_a \cdot B_g \cdot 2N_w L_a \cdot \frac{D_s}{2} \tag{4.2}$$

while the copper loss is given by:

$$P_{Cu} = 2I_a^2 R_a = 2I_a^2 \rho_{Cu} \frac{2N_w L_a}{A_{cond}} = 24 N_w^2 I_a^2 \rho_{Cu} \frac{L_a}{A_s K_s N_s} \tag{4.3}$$

where the cross-sectional area of the conductors is:

$$A_{cond} = \frac{\frac{A_s}{2} K_s}{\frac{3N_w}{N_s}} \tag{4.4}$$

where B_g is the airgap flux density, ω_{elec} is the electrical angular velocity; A_s is the slot area; A_{cond} is the conductor area; I_a is the rms phase current; ρ_{Cu} is the resistivity of copper; K_s is the slot packing factor; N_s is the number of slots; and N_w is the number of turns per phase.

If the copper loss is fixed, so that the temperature rise within a given stator frame diameter is also fixed, (4.3) can be rewritten as $I_a = f(P_{Cu})$:

$$I_a = \sqrt{\frac{P_{Cu} A_s K_s N_s}{24 N_w^2 \rho_{Cu} L_a}} \tag{4.5}$$

Substituting (4.5) into (4.2), the electromagnetic torque per machine volume can be derived as:

$$\frac{T}{V_m} = \frac{2I_a \cdot B_g \cdot 2N_w L_a \cdot \frac{D_o}{2}}{\pi \left(\frac{D_o}{2}\right)^2} = \sqrt{\frac{P_{Cu} K_s N_s}{24 N_w^2 \rho_{Cu} L_a}} \frac{B_g 2N_w L_a}{\frac{\pi}{4} D_o} \sqrt{\left(\frac{D_s}{D_o}\right)^2 A_s}$$

$$\frac{T}{V_m} \propto \sqrt{\left(\frac{D_s}{D_o}\right)^2 A_s} \tag{4.6}$$

It can be seen from (4.6) that the specific torque capability of a permanent magnet brushless DC machine with a trapezoidal airgap flux distribution depends only on the slot area A_s, which is determined mainly by the required stator tooth-body width and back-iron thickness.

Fig. 4.4(a) shows that for machines having a slot number to pole number ratio of 3/2, the tooth-pitch is equal to 2/3 of the pole-pitch and the maximum flux in the stator back-iron is half of that in a stator tooth.

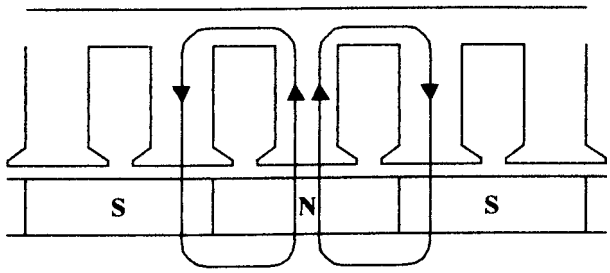

(a) N_s:2p = 3:2

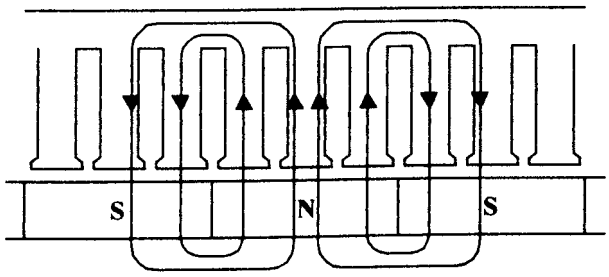

(b) N_s:2p = 6:2

Fig. 4.4. Idealized open-circuit flux distributions

The stator tooth width is given as:

$$b_t = \frac{\pi D_s}{N_s} \cdot \frac{B_g}{B_{max}} \tag{4.7}$$

and the stator back-iron thickness is:

$$h_c = \frac{b_t}{2} = \frac{1}{2} \cdot \frac{\pi D_s}{N_s} \cdot \frac{B_g}{B_{max}} \tag{4.8}$$

Therefore, the slot area is expressed as:

$$A_s = \frac{1}{N_s}\left[\pi\left(\frac{D_o - 2h_c}{2}\right)^2 - \pi\left(\frac{D_s}{2}\right)^2\right] - b_t\left[\frac{D_o - D_s}{2} - h_c\right]$$

$$A_s = \frac{\pi D_o^2}{4N_s}\left\{\begin{array}{l}\left(\frac{D_s}{D_o}\right)^2\left[\frac{\pi}{3p}\left(\frac{\pi}{3p}+2\right)\left(\frac{B_g}{B_{\max}}\right)^2+2\frac{B_g}{B_{\max}}-1\right] \\ -\left(\frac{D_s}{D_o}\right)\cdot 2\left(\frac{\pi}{3p}+1\right)\left(\frac{B_g}{B_{\max}}\right)+1\end{array}\right\} \tag{4.9}$$

where B_{max} is the maximum flux density in a stator tooth and the stator back-iron (T).

In contrast, for machines having a slot number to pole number ratio of 6/2, as shown in Fig. 4.4(b), the tooth-pitch is equal to 1/3 of the pole-pitch, and the maximum flux in the stator back-iron is half of the maximum flux per pole. Hence, the available slot area is different from that given in (4.8), as will be discussed in the next section.

Substituting (4.9) into (4.6), the relationship between $\frac{T}{V_m}$ and $\frac{D_o}{D_s}$ can be obtained, and the optimal split ratio for maximum torque per machine volume can be obtained by differentiating $\frac{T}{V_m}$ with respect to $\frac{D_o}{D_s}$, and equating to zero. The optimal ratio of $\frac{D_o}{D_s}$ is given by:

$$\left(\frac{D_s}{D_o}\right) = \frac{-b-\sqrt{b^2-4a}}{2a} \tag{4.10}$$

where

$$a = 2\left[\frac{k\pi}{p}\left(\frac{k\pi}{p}+2\right)\left(\frac{B_g}{B_{\max}}\right)^2+2\frac{B_g}{B_{\max}}-1\right] \tag{4.11}$$

$$b = -3\left(\frac{k\pi}{p}+1\right)\left(\frac{B_g}{B_{\max}}\right) \tag{4.12}$$

$$k = \frac{1}{3} \quad \text{for machines equipped with a non-overlapping winding} \tag{4.13}$$

It will be noted that this simple expression is similar to that given in [CHA94], but in which several typographical errors exist in the expression for the optimal split ratio, as was pointed out in [EDE01].

From (4.10)-(4.13), it can be seen that the optimal split ratio is influenced by the ratio of $\frac{B_g}{B_{max}}$ and the number of pole-pairs, p, the variation of the optimal split ratio with $\frac{B_g}{B_{max}}$ for different numbers of pole-pairs being shown in Fig. 4.5, assuming that the other machine parameters are identical to those cited in Fig. 4.2. It can be seen that the optimal split ratio reduces as $\frac{B_g}{B_{max}}$ is increased, since the higher the ratio of $\frac{B_g}{B_{max}}$, the wider the stator teeth and the thicker the back-iron which is needed in order to maintain the same level of saturation. Consequently, the slot area reduces and, in order to maintain the copper loss constant, the stator bore diameter must be reduced.

It can also be seen from Fig. 4.5 that, for a given ratio of $\frac{B_g}{B_{max}}$, the optimal split ratio increases as the number of pole-pairs is increased, since the thickness of the stator back-iron reduces and the slot area increases. Thus, the stator bore diameter for constant copper loss increases. Fig. 4.5 also shows that the influence of the pole number becomes more significant as the number of pole-pairs is reduced.

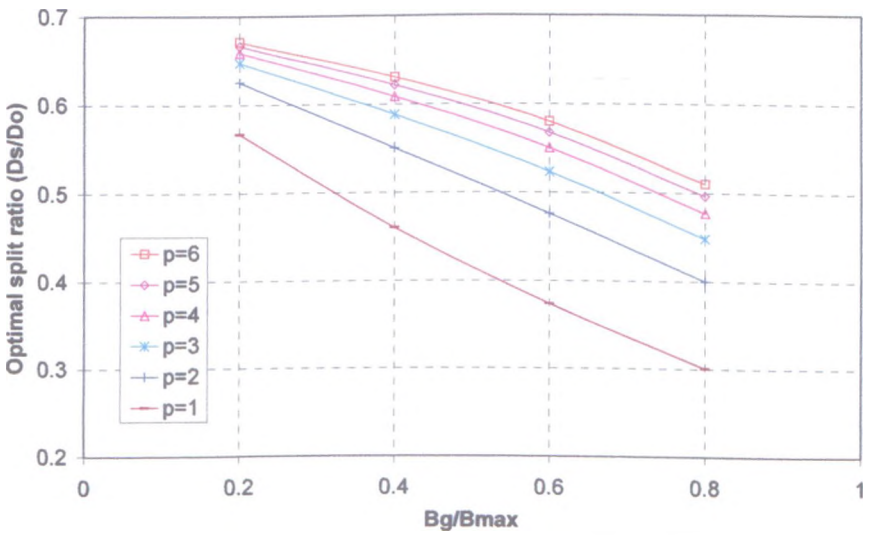

Fig. 4.5. Variation of optimal split ratio with ratio of $\frac{B_g}{B_{max}}$ for machine with non-overlapping winding

4.2.2. PM brushless machine with a sinusoidal airgap flux distribution

In the previous section, an analytical expression for the optimal split ratio was derived for a specific permanent magnet machine having a non-overlapping stator winding, assuming a trapezoidal airgap flux density distribution and 120° electrical brushless DC operation. In this section, the analysis is extended to cater for a permanent magnet brushless machine with a sinusoidal airgap flux density distribution and 180° electrical brushless AC operation.

When the winding pitch is 120° electrical, the phase back-emf is given by:

$$e_{ph} = BLV = \frac{\sqrt{3}}{2} B_{gm} \sin(\omega_{elec} t) \cdot 2N_w L_a \cdot \frac{\omega_{elec}}{p} \frac{D_s}{2} \tag{4.14}$$

and the electromagnetic torque is obtained as:

$$T = IBLR = 3I_a \cdot \frac{\sqrt{3}}{2\pi} B_{gm} \cdot 2N_w L_a \cdot \frac{D_s}{2} \cdot \frac{\pi}{\sqrt{2}} \tag{4.15}$$

while the copper loss is given by:

$$P_{Cu} = 3I_a^2 R_a = 3I_a^2 \rho_{Cu} \frac{2N_w L_a}{A_{cond}} = 36N_w^2 I_a^2 \rho_{Cu} \frac{L_a}{A_s K_s N_s} \tag{4.16}$$

where the cross-sectional area of the conductors is:

$$A_{cond} = \frac{\frac{A_s}{2} K_s}{\frac{3N_w}{N_s}} \tag{4.17}$$

where B_{gm} is the maximum airgap flux density, ω_{elec} is the electrical angular velocity; A_s is the slot area; A_{cond} is the conductor area; I_a is the rms phase current; ρ_{Cu} is the resistivity of copper; K_s is the slot packing factor; N_s is the number of slots; and N_w is the number of turns per phase.

If the copper loss is fixed, so that the temperature rise within a given stator frame diameter is also fixed, (4.16) can be rewritten as $I_a = f(P_{Cu})$:

$$I_a = \sqrt{\frac{P_{Cu} A_s K_s N_s}{36 N_w^2 \rho_{Cu} L_a}} \tag{4.18}$$

Substituting (4.17) into (4.15), the electromagnetic torque per machine volume can be derived as:

$$\frac{T}{V_m} = \frac{3 I_a \cdot \frac{\sqrt{3}}{2\pi} B_{gm} \cdot 2 N_w L_a \cdot \frac{D_s}{2} \cdot \frac{\pi}{2}}{\pi \left(\frac{D_o}{2}\right)^2} = 3 \sqrt{\frac{P_{Cu} K_s N_s}{36 N_w^2 \rho_{Cu} L_a}} \frac{\frac{\sqrt{3}}{2\pi} B_{gm} 2 N_w L_a \frac{\pi}{2}}{\frac{\pi}{4} D_o} \sqrt{\left(\frac{D_s}{D_o}\right)^2 A_s}$$

$$\frac{T}{V_m} \propto \sqrt{\left(\frac{D_s}{D_o}\right)^2 A_s} \tag{4.19}$$

It can be seen from (4.19) that the specific torque capability of a permanent magnet brushless AC machine with a sinusoidal airgap flux distribution also depends only on the slot area A_s, which is determined mainly by the required stator tooth-body width and back-iron thickness. Since the stator tooth-body width and back-iron thickness are determined by the airgap field distribution, e.g. trapezoidal or sinusoidal, and the winding topology, e.g. the ratio of stator slot number to rotor pole number, similar equations for the torque capability can be used for both brushless DC machines and brushless AC machines, i.e. equation (4.19) for a brushless AC machine is almost the same as equation (4.6) for brushless DC machine, although the expressions for the slot area A_s could be different.

The slot area of a permanent magnet brushless AC machine with a sinusoidal airgap flux distribution can be derived as follows:

The stator tooth width is given as:

$$b_t = \frac{\pi D_s}{N_s} \cdot \frac{\frac{3\sqrt{3}}{2\pi} B_{gm}}{B_{max}} = \frac{\pi D_s}{N_s} \cdot \frac{B_g}{B_{max}} \tag{4.20}$$

where $B_g = \frac{3\sqrt{3}}{2\pi} B_{gm}$ (4.21)

and stator back-iron thickness is:

$$h_c = \frac{b_t}{2} = \frac{1}{2} \cdot \frac{\pi D_s}{N_s} \cdot \frac{B_g}{B_{max}} \tag{4.22}$$

Therefore, the slot area can be expressed as:

$$A_s = \frac{1}{N_s}\left[\pi\left(\frac{D_o - 2h_c}{2}\right)^2 - \pi\left(\frac{D_s}{2}\right)^2\right] - b_t\left[\frac{D_o - D_s}{2} - h_c\right]$$

$$A_s = \frac{\pi D_o^2}{4N_s}\left\{\begin{array}{l}\left(\frac{D_s}{D_o}\right)^2\left[\frac{\pi}{3p}\left(\frac{\pi}{3p}+2\right)\left(\frac{B_g}{B_{\max}}\right)^2 + 2\frac{B_g}{B_{\max}} - 1\right] \\ -\left(\frac{D_s}{D_o}\right)\cdot 2\left(\frac{\pi}{3p}+1\right)\left(\frac{B_g}{B_{\max}}\right)+1\end{array}\right\} \tag{4.23}$$

where B_{max} is the maximum flux density in a stator tooth and the stator back-iron (T).

Substituting (4.23) into (4.19), the relationship between $\frac{T}{V_m}$ and $\frac{D_o}{D_s}$ can be obtained, and the optimal split ratio for maximum torque per machine volume can be obtained by differentiating $\frac{T}{V_m}$ with respect to $\frac{D_o}{D_s}$, and equating to zero. The optimal ratio of $\frac{D_o}{D_s}$ is given by:

$$\left(\frac{D_s}{D_o}\right) = \frac{-b - \sqrt{b^2 - 4a}}{2a} \tag{4.24}$$

where

$$a = 2\left[\frac{k\pi}{p}\left(\frac{k\pi}{p}+2\right)\left(\frac{B_g}{B_{\max}}\right)^2 + 2\frac{B_g}{B_{\max}} - 1\right] \tag{4.25}$$

$$b = -3\left(\frac{k\pi}{p}+1\right)\left(\frac{B_g}{B_{\max}}\right) \tag{4.26}$$

$k = \frac{1}{3}$ for machines equipped with a non-overlapping winding (4.27)

$$B_g = \frac{3\sqrt{3}}{2\pi} B_{gm} \tag{4.28}$$

Comparing the equations for the optimal split ratio for permanent magnet brushless machines with a sinusoidal airgap field distribution, i.e. (4.24)-(4.28), with the equations for permanent magnet brushless machine with a trapezoidal airgap field distribution, i.e. (4.10)-(4.13), it can be seen that if the effective airgap flux density is $B_g = \frac{3\sqrt{3}}{2\pi} B_{gm}$ for a permanent magnet machine with a sinusoidal airgap field distribution, then, irrespective of whether the permanent magnet machine has a trapezoidal airgap field distribution or a sinusoidal airgap field distribution, the same optimal split ratio equation can be utilized.

4.2.3. Influence of machine design parameters

In this section, the analysis is extended to consider the influence of the winding disposition, and the influence of the tooth-tip height and the end-windings.

A. Winding disposition

For a permanent magnet brushless machine having an overlapping winding (either concentrated or distributed), in which the flux in the stator back-iron is equal to half the airgap flux per pole, the slot area can be derived as follows:

The stator tooth width is given by:

$$b_t = \frac{\pi D_s}{N_s} \cdot \frac{B_g}{B_{max}} \tag{4.29}$$

and the stator back-iron thickness is:

$$h_c = \frac{\pi D_s}{2p} \cdot \frac{B_g}{B_{max}} \tag{4.30}$$

Therefore, the slot area can be expressed as:

$$A_s = \frac{1}{N_s}\left[\pi\left(\frac{D_o - 2h_c}{2}\right)^2 - \pi\left(\frac{D_s}{2}\right)^2\right] - b_t\left[\frac{D_o - D_s}{2} - h_c\right]$$

$$A_s = \frac{\pi D_o^2}{4N_s}\left\{\left(\frac{D_s}{D_o}\right)^2\left[\frac{\pi}{2p}\left(\frac{\pi}{2p}+2\right)\left(\frac{B_g}{B_{max}}\right)^2 + 2\frac{B_g}{B_{max}} - 1\right]\right\} \quad (4.31)$$
$$\left\{-\left(\frac{D_s}{D_o}\right)\cdot 2\left(\frac{\pi}{2p}+1\right)\left(\frac{B_g}{B_{max}}\right)+1\right\}$$

Following the same procedure as that given in the previous section, the optimal split ratio can again be given by equations (4.10)-(4.13), except that the coefficient k is now given by:

$$k = \frac{1}{2} \quad \text{for machines equipped with an overlapping winding} \quad (4.32)$$

Fig. 4.6 compares optimal split ratios for machines having overlapping and non-overlapping windings, assuming the same machine parameters which are cited in Fig. 4.2, from which it can be seen that the optimal split ratio for a machine with an overlapping winding is slightly smaller than that for a machine with a non-overlapping winding. This is due to the increased flux in the stator back-iron, and the corresponding increase in the thickness of the back-iron, in order to maintain the same flux density. As a result, the optimal split ratio is reduced so as to obtain a slot area, which is commensurate with the specified copper loss.

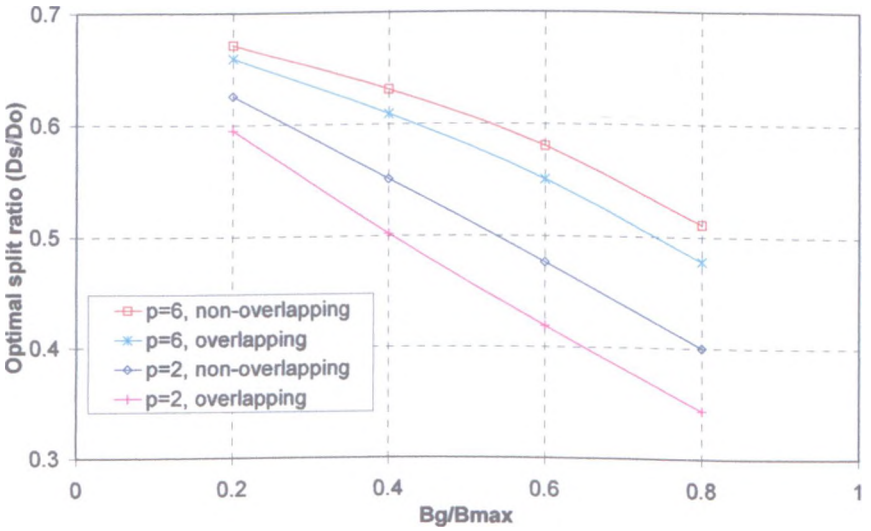

Fig. 4.6. Influence of winding disposition on optimal split ratio

B. Tooth-tip height

In the foregoing, the influence of both the stator tooth-tip and the end-windings have been neglected, in order to simplify the derivation of the analytical expressions. However, a stator tooth-tip is usually required, not only to maximize the coil flux-linkage but also to achieve a high phase inductance. Assuming a rectangular shaped tooth-tip, as illustrated in Fig.4.3(b), the stator slot area in (4.9) can be rewritten as:

$$A_s = \frac{1}{N_s}\left[\pi\left(\frac{D_o - 2h_c}{2}\right)^2 - \pi\left(\frac{D_s + 2h_0}{2}\right)^2\right] - b_t\left[\frac{D_o - D_s}{2} - h_c - h_0\right]$$

$$A_s = \frac{\pi D_o^2}{4N_s}\left\{\begin{aligned}&\left(\frac{D_s}{D_o}\right)^2\left[\frac{\pi}{3p}\left(\frac{\pi}{3p}+2\right)\left(\frac{B_g}{B_{max}}\right)^2 + 2\frac{B_g}{B_{max}} - 1\right]\\ &-\left(\frac{D_s}{D_o}\right)\left[2\left(\frac{\pi}{3p}+1-2\frac{h_t}{D_o}\right)\left(\frac{B_g}{B_{max}}\right)+4\frac{h_0}{D_o}\right]\\ &+1-4\left(\frac{h_0}{D_o}\right)^2\end{aligned}\right\} \tag{4.33}$$

where h_0 is the height of tooth-tip.

Following the same procedure as that given in the previous section, the optimal split ratio, which accounts for the tooth-tip height, can be derived as:

$$\left(\frac{D_s}{D_o}\right) = \frac{-b - \sqrt{b^2 - 4ac}}{2a} \tag{4.34}$$

where

$$a = 2\left[\frac{k\pi}{p}\left(\frac{k\pi}{p}+2\right)\left(\frac{B_g}{B_{max}}\right)^2 + 2\frac{B_g}{B_{max}} - 1\right] \tag{4.35}$$

$$b = \frac{3}{2}\left[-2\left(\frac{k\pi}{p}+1-2\frac{h_t}{D_o}\right)\left(\frac{B_g}{B_{max}}\right) - 4\frac{h_0}{D_o}\right] \tag{4.36}$$

$$c = 1 - 4\left(\frac{h_0}{D_o}\right)^2 \tag{4.37}$$

and

$k = \frac{1}{3}$ for machines equipped with a non-overlapping winding (4.38a)

$k = \frac{1}{2}$ for machines equipped with an overlapping winding (4.38b)

The influence of the tooth-tips on the optimal split ratio for a 4-pole machine equipped with a non-overlapping winding, and having the parameters cited in Fig. 4.2 is shown in Fig. 4.7. As can be seen, a tooth-tip height of 4mm reduces the optimal split ratio by ~10%.

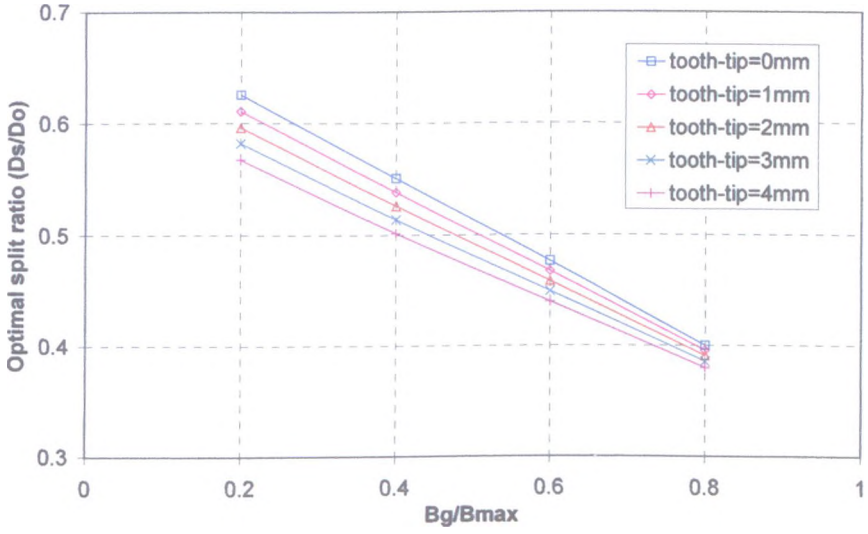

Fig. 4.7. Influence of tooth-tip height on optimal split ratio

C. End-windings

In order to account for the influence of the end-windings, the active length of the coils, L_a, in the derived expression is replaced by (L_a+L_e), where L_e is the average total length of the end-windings, which are assumed to be semicircular in shape for both non-overlapping and overlapping windings. Consequently, equation (4.3) for the copper loss can be re-written as:

$$P_{Cu} = 24 N_w^2 I_a^2 \rho_{Cu} \frac{(L_a + L_e)}{A_s K_s N_s} \tag{4.39}$$

while L_e can be derived as:

$$L_e = d\frac{D_s}{D_o} + e \tag{4.40}$$

where

$$d = \frac{\pi^2 D_o}{4N_s}\left[\frac{1}{2} + \left(1 - \frac{\pi}{2N_s}\right)\frac{B_g}{B_{\max}}\right] \quad \text{for a non-overlapping winding} \tag{4.41a}$$

$$e = \frac{\pi^2 D_o}{4N_s}\left[\frac{1}{2} + \frac{h_0}{D_o}\right] \quad \text{for a non-overlapping winding} \tag{4.41b}$$

and

$$d = \frac{3\pi^2 D_o}{2N_s}\left[\frac{1}{2} - \frac{3\pi}{2N_s}\frac{B_g}{B_{max}}\right] \quad \text{for an overlapping winding} \tag{4.42a}$$

$$e = \frac{3\pi^2 D_o}{2N_s}\left[\frac{1}{2} + \frac{h_0}{D_o}\right] \quad \text{for an overlapping winding} \tag{4.42b}$$

The electromagnetic torque per volume for a given copper loss, equation (4.6), then can be obtained as:

$$\frac{T}{V_m} \propto \sqrt{\left(\frac{D_s}{D_o}\right)^2 \frac{A_s}{L_a + L_e}} = \sqrt{\frac{a\left(\frac{D_s}{D_o}\right)^4 + b\left(\frac{D_s}{D_o}\right)^3 + c\left(\frac{D_s}{D_o}\right)^2}{d\left(\frac{D_s}{D_o}\right) + e + L_a}} \tag{4.43}$$

Therefore, the optimal split ratio for a fixed copper loss, can be derived as:

$$\left(\frac{D_s}{D_o}\right) = y_i - \frac{2bd + 4ae}{9ad}, \text{ where } i=1, 2, 3 \tag{4.44}$$

$$y_1 = \sqrt[3]{-\frac{q_1}{2} + \sqrt{\left(\frac{q_1}{2}\right)^2 + \left(\frac{p_1}{3}\right)^3}} + \sqrt[3]{-\frac{q_1}{2} - \sqrt{\left(\frac{q_1}{2}\right)^2 + \left(\frac{p_1}{3}\right)^3}} \tag{4.45}$$

$$y_2 = s \cdot \sqrt[3]{-\frac{q_1}{2} + \sqrt{\left(\frac{q_1}{2}\right)^2 + \left(\frac{p_1}{3}\right)^3}} + s^2 \cdot \sqrt[3]{-\frac{q_1}{2} - \sqrt{\left(\frac{q_1}{2}\right)^2 + \left(\frac{p_1}{3}\right)^3}} \tag{4.46}$$

$$y_3 = s^2 \cdot \sqrt[3]{-\frac{q_1}{2} + \sqrt{\left(\frac{q_1}{2}\right)^2 + \left(\frac{p_1}{3}\right)^3}} + s \cdot \sqrt[3]{-\frac{q_1}{2} - \sqrt{\left(\frac{q_1}{2}\right)^2 + \left(\frac{p_1}{3}\right)^3}} \tag{4.47}$$

$$s = -\frac{1}{2} + \frac{\sqrt{3}}{2} i \quad \text{(where } i \text{ designates 'imaginary')} \tag{4.48}$$

$$p_1 = \frac{cd + 3be}{3ad} - \frac{(2bd + 4ae)^2}{3(3ad)^2} \tag{4.49}$$

$$q_1 = \frac{2(2bd + 4ae)^3}{27(3ad)^3} - \frac{(2be + 4ae)(cd + 3be)}{3(3ad)^2} + \frac{2ce}{3ad} \tag{4.50}$$

$$a = \left[\frac{k\pi}{p}\left(\frac{k\pi}{p} + 2\right)\left(\frac{B_g}{B_{\max}}\right)^2 + 2\frac{B_g}{B_{\max}} - 1\right] \tag{4.51}$$

$$b = -\left[2\left(\frac{k\pi}{p} + 1 - 2\frac{h_0}{D_o}\right)\left(\frac{B_g}{B_{max}}\right) + 4\frac{h_0}{D_o}\right] \tag{4.52}$$

$$c = 1 - 4\left(\frac{h_t}{D_o}\right)^2 \tag{4.53}$$

where:

$$k = \frac{1}{3} \qquad \text{for a non-overlapping winding} \tag{4.54a}$$

$$d = \frac{\pi^2 D_o}{4N_s}\left[\frac{1}{2} + \left(1 - \frac{\pi}{2N_s}\right)\frac{B_g}{B_{\max}}\right] \qquad \text{for a non-overlapping winding} \tag{4.54b}$$

$$e = \frac{\pi^2 D_o}{4N_s}\left[\frac{1}{2} + \frac{h_0}{D_o}\right] + L_a \qquad \text{for a non-overlapping winding} \tag{4.54c}$$

and

$$k = \frac{1}{2} \qquad \text{for an overlapping winding} \tag{4.55a}$$

$$d = \frac{3\pi^2 D_o}{2N_s}\left[\frac{1}{2} - \frac{3\pi}{2N_s}\frac{B_g}{B_{\max}}\right] \qquad \text{for an overlapping winding} \tag{4.55b}$$

$$e = \frac{3\pi^2 D_o}{2N_s}\left[\frac{1}{2} + \frac{h_0}{D_o}\right] + L_a \qquad \text{for an overlapping winding} \qquad (4.55c)$$

There are three solutions to equation (4.44), a feasible value for the optimal split ratio $\frac{D_s}{D_o}$ being a real value in the range 0~1.

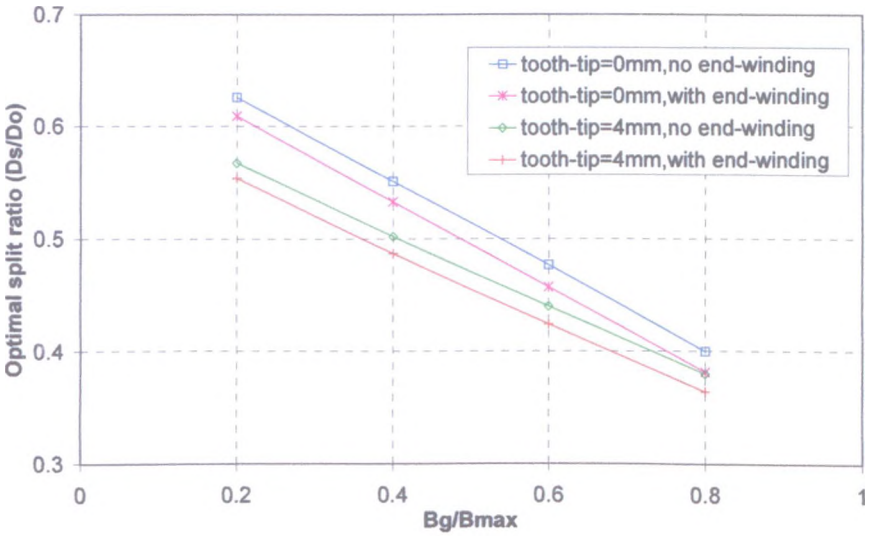

(a) Non-overlapping winding

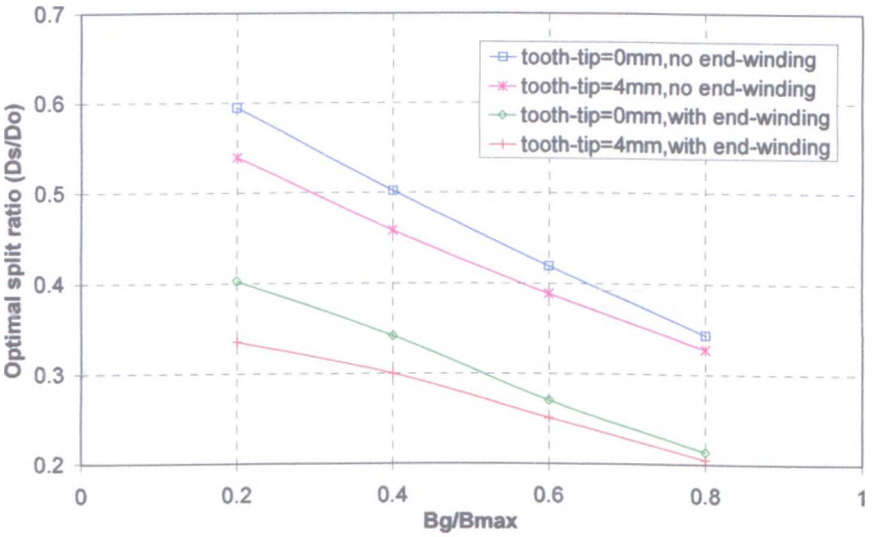

(b) Overlapping winding

Fig. 4.8. Influence of tooth-tip height and end-windings on optimal split ratio

Fig. 4.8 compares the optimal split ratio for machines equipped with a non-overlapping winding and an overlapping winding, both with and without consideration of the end-windings, assuming the same parameters which were cited in Fig. 4.2. As will be seen, when the machine is equipped with a non-overlapping winding, the influence of the end-windings reduces the

optimal split ratio by ~5%, which compares with a reduction of ~25% when the machine is equipped with an overlapping winding, due to the relatively longer end-windings.

4.2.4. Finite element analysis and experimental results

The foregoing analytically derived expressions for the optimal split ratio have been verified by finite element analysis for a 3-phase, 4-pole, 6-slot, permanent magnet brushless machine equipped with a surface-mounted magnet rotor and a fixed outside diameter, and temperature rise at rated load.

Fig. 4.9 shows how the analytically and finite element calculated output torques vary with the split ratio when the machine is equipped with a non-overlapping winding and has the parameters cited in Fig. 4.2, and the full-load copper loss is maintained constant at 50W. It can be seen that, although the maximum torque deduced from finite element analysis is slightly higher than the analytically predicted value, the optimal split ratio is the same as that given by equation (4.43).

In order to comprehensively experimentally validate the predicted dependence of the optimal split ratio on p and $\frac{B_g}{B_{max}}$, a relatively large number of prototype machines would be required for testing, which is not feasible. However a 3-phase, 4-pole, 6-slot, permanent magnet brushless DC machine equipped with a non-overlapping winding and having B_{gm}=0.8T, B_{max}=1.5T, and the optimal split ratio of 0.45 was prototyped, as shown in Fig. 4.10. Its leading design parameters are: outside diameter D_o=90mm, active axial length L_a=50mm, tooth-tips h_0=4mm, slot opening width b_0=4mm, magnet remanence B_r=1.2T, and number of turns per phase N_w=120turns.

To ease manufacture, parallel magnetized magnets rather than radially magnetized magnets, as assumed in the analyses are employed, the open-circuit field distribution being shown in Fig. 4.11.

Fig. 4.12 compares the analytically predicted, finite element calculated, and

measured phase back-emf waveforms at 400 rpm, whilst Fig. 4.13 compare measured and predicted static torque-position and torque-current characteristics when two phases carry a DC current. As will be seen, since the actual back-emf waveform is not rectangular, as assumed in the derivation of the optimal split ratio, and the prototype machine exhibits a significant cogging torque, the torque varies with rotor position. However, Fig. 4.13(b) shows that the analytically derived torque lies between the actual average and peak values.

Overall excellent agreement is achieved between the analytical and finite element predictions and measurements.

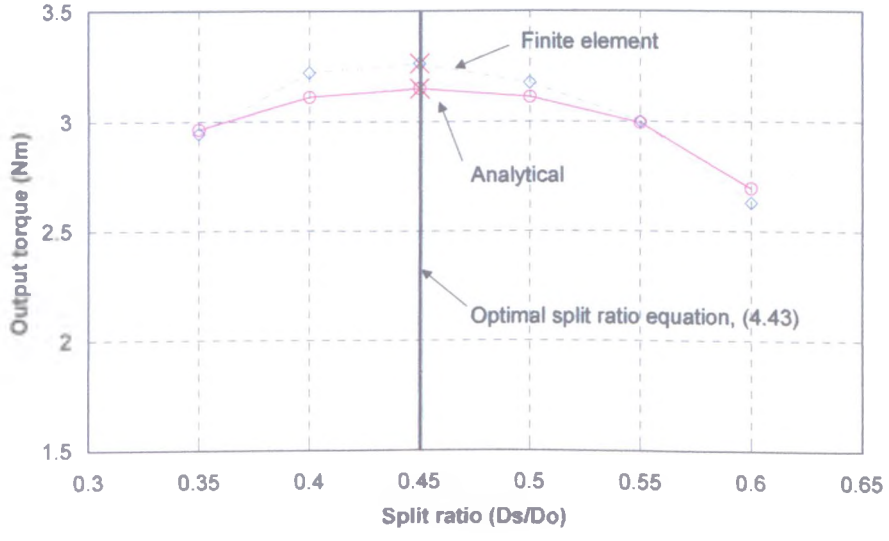

Fig. 4.9. Analytically and finite element predicted variation of torque with split ratio

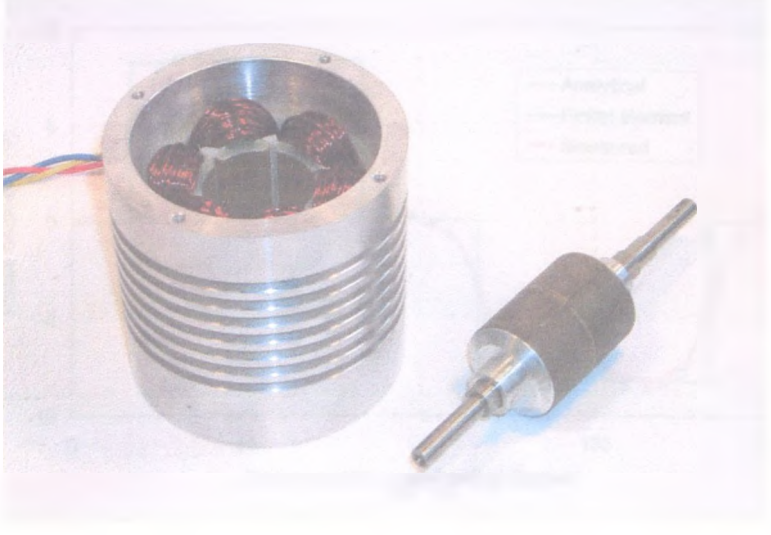

Fig. 4.10. Prototype 4-pole, 6-slot permanent magnet brushless DC machine

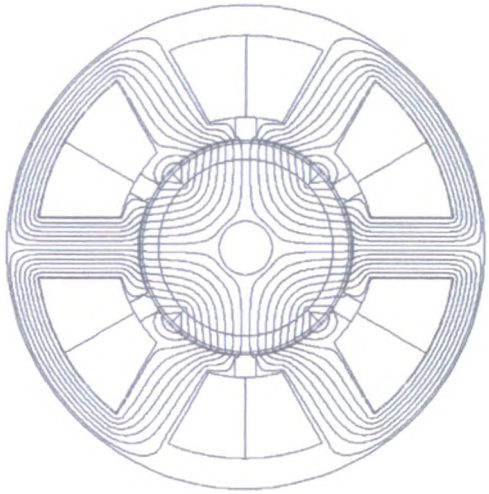

(a) Open-circuit flux distribution

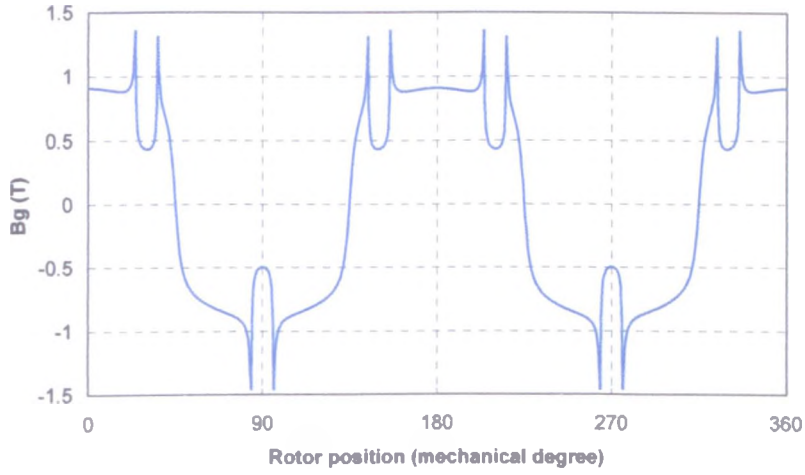

(b) Open-circuit airgap field distribution

Fig. 4.11. Finite element predicted performance of prototype permanent magnet brushless DC machine

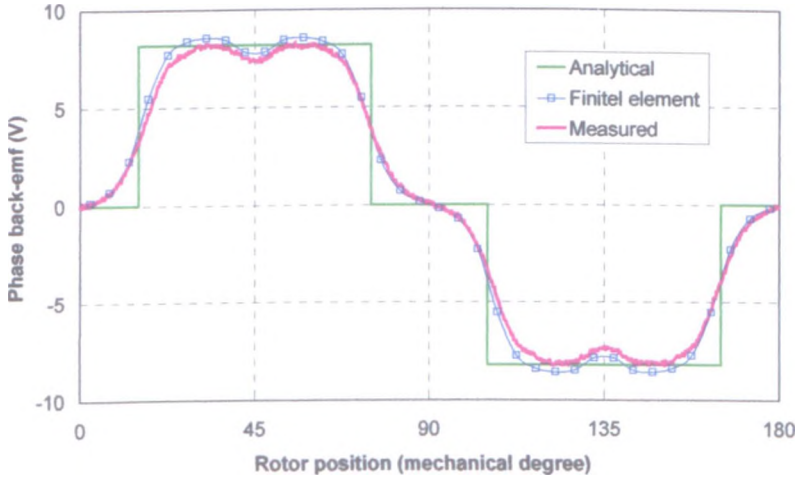

Fig. 4.12. Comparison of predicted and measured phase back-emf waveforms

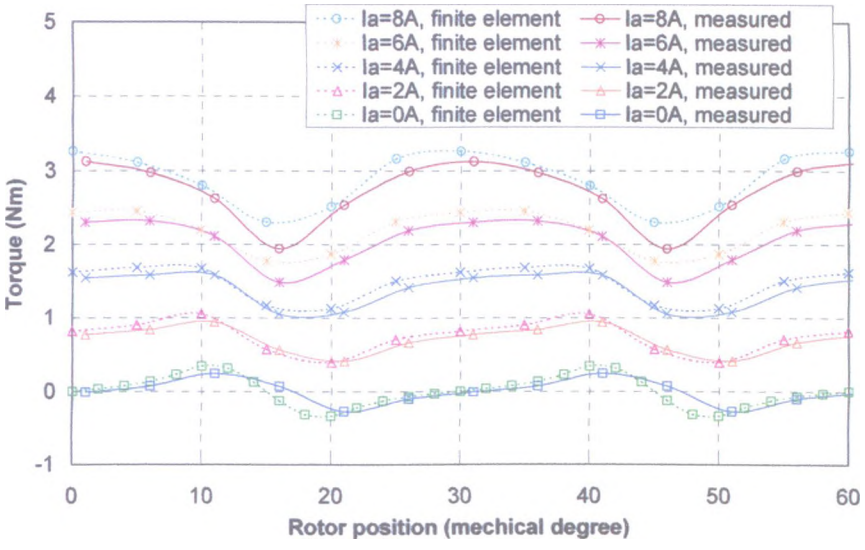

(a) Torque vs. rotor position characteristics

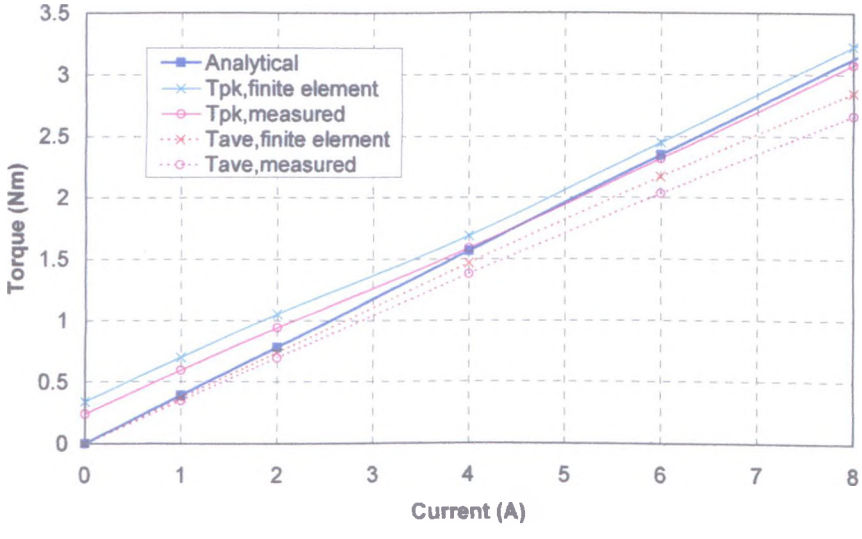

(b) Torque vs. current characteristics

Fig. 4.13. Comparison of predicted and measured torque characteristics of prototype permanent magnet brushless DC machine

4.3. Optimal split ratio of flux-switching PM brushless machines

Similar to conventional PM brushless machines, flux-switching PM machines also have an optimal split ratio for maximum output torque. Therefore, in this section, the optimization of the split ratio is investigated.

The following assumptions are made:

(a) The dq-axis co-ordinate system is employed, since although the airgap field distribution of the flux-switching PM machine is totally different from that of either SPM or IPM machines, both the phase flux-linkage and back-emf waveforms are essentially sinusoidal;

(b) Dq-axis cross-coupling effects are ignored;

(c) The maximum flux density in the stator tooth body is assumed to be as 1.6T;

(d) For the preliminary study, the slot opening width b_0, the magnet thickness b_m, and the stator back-iron thickness h_c are assumed to be the same as the stator tooth width b_t;

(e) Leakage flux is ignored;

(f) The stator and rotor iron losses are neglected.

4.3.1. Analytical equations

The cross-section of the flux-switching PM machine is shown in Fig. 4.14(a), one segment of the stator being shown in Fig. 4.14(b). Details of the flux-switching PM machine under consideration are given in Appendix I.

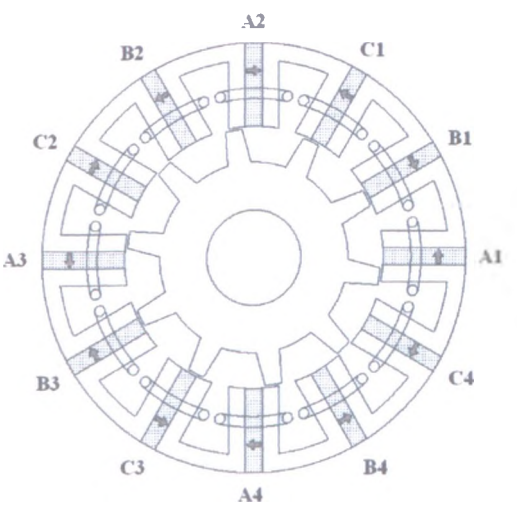

(a) Cross-section of flux-switching PM machine

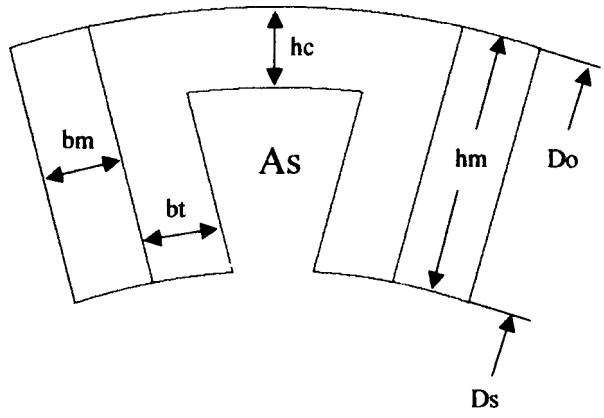

(b) One segment of stator

Fig. 4.14. Flux-switching PM machine

Based on the above assumptions, the basic dimensions of the flux-switching PM machine can be given as:

$$b_t = \frac{\pi D_s}{4N_s} \tag{4.56}$$

$$h_c = b_m = b_t \tag{4.57}$$

where b_t is the stator tooth width, D_s is the stator bore diameter, N_s is the stator slot number, h_c is the stator back-iron thickness, and b_m is the stator magnet thickness.

Assuming the flux density in the stator tooth body is constant, B_{max}, the maximum phase flux-linkage can be obtained as:

$$\psi_m = B_{max} b_t L_a N_w \tag{4.58}$$

where L_a is the stator axial length, and N_w is the number of phase winding turns.

Since the phase flux-linkage of the flux-switching PM machine is essentially sinusoidal, the maximum phase flux-linkage will be exactly the same as the d-axis PM flux-linkage in dq-axis co-ordinates. Hence, the output torque can simply be given by

$$T = \frac{3}{2} p \psi_m I_q = \frac{3}{2} p B_{max} b_t L_a N_w \sqrt{2} I_a \tag{4.59}$$

where p is the electrical pole-pair number, for flux-switching PM machine the electrical pole-pair number is equal to the mechanical pole number, I_q is the q-axis current and I_a is the rms value of the phase current.

The copper loss is given by:

$$P_{Cu} = 3I_a{}^2 R_a = 3I_a^2 \rho_{Cu} \frac{2N_w L_a}{A_{cond}} = 36N_w^2 I_a^2 \rho_{Cu} \frac{L_a}{A_s K_s N_s} \tag{4.60}$$

where the cross-sectional area of the conductors is:

$$A_{cond} = \frac{\frac{A_s}{2} K_s}{\frac{3N_w}{N_s}} \tag{4.61}$$

in which A_s is the slot area; A_{cond} is the conductor area; I_a is the rms phase current; ρ_{Cu} is the resistivity of copper; K_s is the slot packing factor; and N_s is the number of slots.

If the copper loss is fixed, so that the temperature rise within a given stator frame diameter is also fixed, (4.61) can be rewritten as $I_a = f(P_{Cu})$:

$$I_a = \sqrt{\frac{P_{Cu} A_s K_s N_s}{36N_w^2 \rho_{Cu} L_a}} \tag{4.62}$$

Substituting (4.17) into (4.15), the electromagnetic torque per machine volume can be derived as:

$$T = \frac{3}{2} p \psi_m I_q = \frac{3}{2} p B_{max} b_t L_a N_w \sqrt{2} I_a \tag{4.63}$$

$$\frac{T}{V_m} = \frac{\frac{3}{2} p B_{max} b_t L_a N_w \sqrt{2} I_a}{\pi \left(\frac{D_o}{2}\right)^2} = \frac{\frac{3}{2} p B_{max} \frac{\pi}{4N_s} L_a N_w \sqrt{2}}{\frac{\pi D_o}{4}} \sqrt{\frac{P_{cu} K_s N_s}{36N_w^2 \rho_{Cu} L_a}} \sqrt{\left(\frac{D_s}{D_o}\right)^2 A_s} \tag{4.64}$$

$$\frac{T}{V_m} \propto \sqrt{\left(\frac{D_s}{D_o}\right)^2 A_s} \tag{4.65}$$

It can be seen from (4.65) that, similar to a conventional PM brushless machine, the torque capability of a flux-switching PM machine also depends only on the stator slot area A_s, which is determined mainly by the stator tooth width, the stator magnet thickness and the stator back-iron thickness.

Since the basic dimensions of the flux-switching PM machine are given by (4.56) and (4.57), the slot area can be expressed as:

$$A_s = \frac{1}{N_s}\left[\pi\left(\frac{D_o}{2}-b_t\right)^2 - \pi\left(\frac{D_i}{2}\right)^2\right] - 3b_t\left(\frac{D_o}{2}-\frac{D_i}{2}-b_t\right) \tag{4.66}$$

$$A_s = \frac{\pi D_o^2}{4N_s}\left\{\left(\frac{D_s}{D_o}\right)^2\left[\frac{\pi^2}{4N_s^2}+\frac{3\pi}{4N_s}+\frac{1}{2}\right] - \left(\frac{D_s}{D_o}\right)\left(\frac{\pi}{N_s}+\frac{3}{2}\right)+1\right\} \tag{4.67}$$

Substituting (4.67) into (4.65), the relationship between $\frac{T}{V_m}$ and $\frac{D_o}{D_s}$ can be obtained, and the optimal split ratio for maximum torque per machine volume can be obtained by differentiating $\frac{T}{V_m}$ with respect to $\frac{D_o}{D_s}$, and equating to zero. The optimal ratio of $\frac{D_o}{D_s}$ is given by:

$$\left(\frac{D_s}{D_o}\right) = \frac{-b-\sqrt{b^2-4a}}{2a} \tag{4.68}$$

where

$$a = 2\left(\frac{\pi^2}{4N_s^2}+\frac{3\pi}{4N_s}+\frac{1}{2}\right) \tag{4.69}$$

$$b = -\frac{3}{2}\left(\frac{\pi}{N_s}+\frac{3}{2}\right) \tag{4.70}$$

The optimal split ratio of a flux-switching PM machine having a stator outer diameter D_o=90mm, a stator axial length L_a=25mm and a stator slot number N_s=12 is shown in Fig. 4.15. It can be seen that the optimal split ratio is 0.53. With an increase of the stator slot number, the optimal split ratio is increased slightly, because additional slot area is

available due to the reduction in the stator back-iron thickness. In contrast, a reduction in the stator slot number requires thicker stator back-iron, so that less slot area is available. As a consequence, the optimal split ratio is reduced.

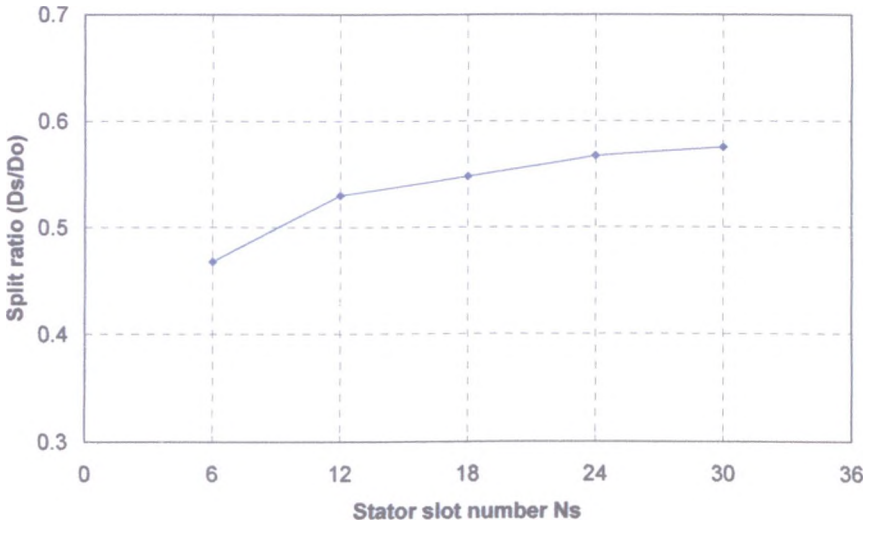

Fig. 4.15. Optimal split ratio of flux-switching PM machine

4.3.2. Influence of end-windings

In flux-switching PM machines, only concentrated non-overlapping windings are employed and the teeth generally do not have tooth-tips. Hence, only the influence of the end-windings is investigated.

Similar to conventional PM brushless machines, the length of the end-windings of the flux-switching PM machine can be given as:

$$L_e = d\frac{D_s}{D_o} + e \tag{4.71}$$

where

$$d = \frac{\pi^2 D_o}{8N_s}\left(\frac{5}{2} - \frac{\pi}{2N_s}\right) \tag{4.72}$$

$$e = \frac{\pi^2 D_o}{8N_s} \tag{4.73}$$

The electromagnetic torque per volume for a given copper loss, equation (4.65), then can be re-written as:

$$\frac{T}{V_m} \propto \sqrt{\left(\frac{D_s}{D_o}\right)^2 \frac{A_s}{L_a + L_e}} = \sqrt{\frac{a\left(\frac{D_s}{D_o}\right)^4 + b\left(\frac{D_s}{D_o}\right)^3 + c\left(\frac{D_s}{D_o}\right)^2}{d\left(\frac{D_s}{D_o}\right) + e + L_a}} \tag{4.74}$$

Therefore, the optimal split ratio for a fixed copper loss can be derived as:

$$\left(\frac{D_s}{D_o}\right) = y_j - \frac{2bd + 4ae}{9ad}, \text{ where } j=1, 2, 3 \tag{4.75}$$

$$y_1 = \sqrt[3]{-\frac{q_1}{2} + \sqrt{\left(\frac{q_1}{2}\right)^2 + \left(\frac{p_1}{3}\right)^3}} + \sqrt[3]{-\frac{q_1}{2} - \sqrt{\left(\frac{q_1}{2}\right)^2 + \left(\frac{p_1}{3}\right)^3}} \tag{4.76}$$

$$y_2 = s \cdot \sqrt[3]{-\frac{q_1}{2} + \sqrt{\left(\frac{q_1}{2}\right)^2 + \left(\frac{p_1}{3}\right)^3}} + s^2 \cdot \sqrt[3]{-\frac{q_1}{2} - \sqrt{\left(\frac{q_1}{2}\right)^2 + \left(\frac{p_1}{3}\right)^3}} \tag{4.77}$$

$$y_3 = s^2 \cdot \sqrt[3]{-\frac{q_1}{2} + \sqrt{\left(\frac{q_1}{2}\right)^2 + \left(\frac{p_1}{3}\right)^3}} + s \cdot \sqrt[3]{-\frac{q_1}{2} - \sqrt{\left(\frac{q_1}{2}\right)^2 + \left(\frac{p_1}{3}\right)^3}} \tag{4.78}$$

$$s = -\frac{1}{2} + \frac{\sqrt{3}}{2} i \quad \text{(where } i \text{ designates 'imaginary')} \tag{4.79}$$

$$p_1 = \frac{cd + 3be}{3ad} - \frac{(2bd + 4ae)^2}{3(3ad)^2} \tag{4.80}$$

$$q_1 = \frac{2(2bd + 4ae)^3}{27(3ad)^3} - \frac{(2be + 4ae)(cd + 3be)}{3(3ad)^2} + \frac{2ce}{3ad} \tag{4.81}$$

$$a = \left(\frac{\pi^2}{4N_s^2} + \frac{3\pi}{4N_s} + \frac{1}{2}\right) \tag{4.82}$$

$$b = -\left(\frac{\pi}{N_s} + \frac{3}{2}\right) \tag{4.83}$$

$$c = 1 \tag{4.84}$$

$$d = \frac{\pi^2 D_o}{8N_s}\left(\frac{5}{2} - \frac{\pi}{2N_s}\right) \tag{4.85}$$

$$e = \frac{\pi^2 D_o}{8N_s} + L_a \tag{4.86}$$

There are three solutions to equation (4.73), a feasible value for the optimal split ratio $\frac{D_s}{D_o}$ being a real value in the range of $0 < \frac{D_s}{D_o} < 1$.

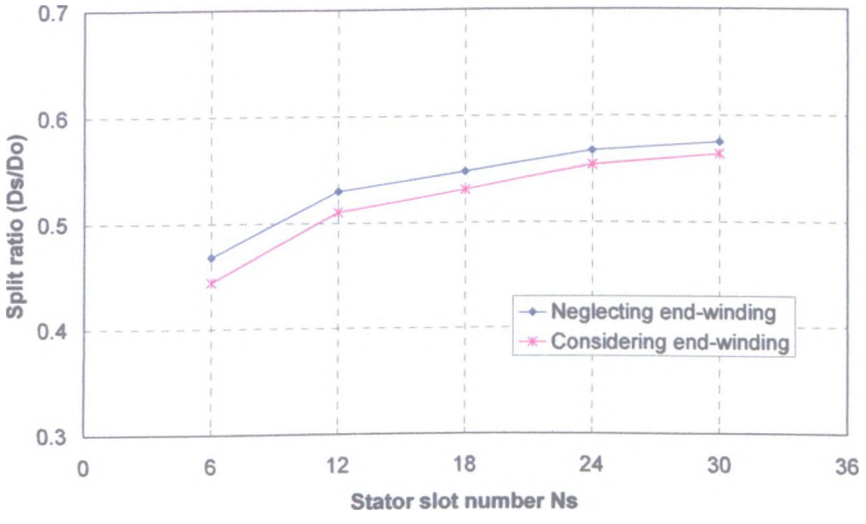

Fig. 4.16. Influence of end-winding on optimal split ratio

The influence of the end-winding on the optimal split ratio of the flux-switching PM machine is shown in Fig. 4.16. It can be seen that, by using the concentrated non-overlapping winding disposition, the influence of the end-winding on the optimal split ratio is very limited, e.g. when N_s=12, the reduction in the optimal split ratio due to the end-winding is less than 4%, although the stator axial length is much smaller than the stator outer diameter. The influence of the end-winding on the optimal split ratio of flux-switching PM machines diminishes when the stator slot number is increased, due to the reduction in the length of the end-windings.

4.3.3. Influence of magnetic loading

In conventional PM brushless machines, the airgap flux density can be varied by changing the thickness of the magnets, while in flux-switching PM machines in which $b_m = b_t$ as illustrated in Fig. 4.14, when the split ratio is specified, the dimensions of the magnet are determined. For example, the thickness of the magnets is:

$$b_m = b_t = \frac{\pi D_s}{4N_s} \tag{4.87}$$

and the width of the magnets will be:

$$h_m = \frac{D_o - D_s}{2} \tag{4.88}$$

As a result, although the flux density in the stator tooth body is assumed to be constant, in practice if the dimensions of the magnets are determined by (4.87) and (4.88), the flux density in the stator body will vary with the split ratio, as shown in Fig. 4.17.

It can be seen that when the magnet remanence B_r=1.2T, the maximum flux density in the stator tooth occurs at a split ratio=~0.65. When the magnet remanence is reduced to B_r=0.4T, the maximum flux density in the stator tooth occurs at a split ratio=~0.55. Hence, the optimal split ratio of the flux-switching PM machine obtained from the foregoing analytical calculation needs to be corrected, considering the variation of the flux density in the stator tooth.

Fig. 4.18 shows that for a flux-switching PM machine with a magnet remanence B_r=1.2T, the optimal split ratio predicted from the analytical equation (4.75) is ~0.5-0.55; while considering the variation of the flux density in the stator tooth, the optimal split ratio is ~0.55-0.6. For a flux-switching PM machine with a magnet remanence B_r=0.4T, the optimal split ratio predicted from the analytical equation (4.75) is still ~0.5-0.55; whilst considering the variation of the flux density in the stator tooth, the optimal split ratio is ~0.55.

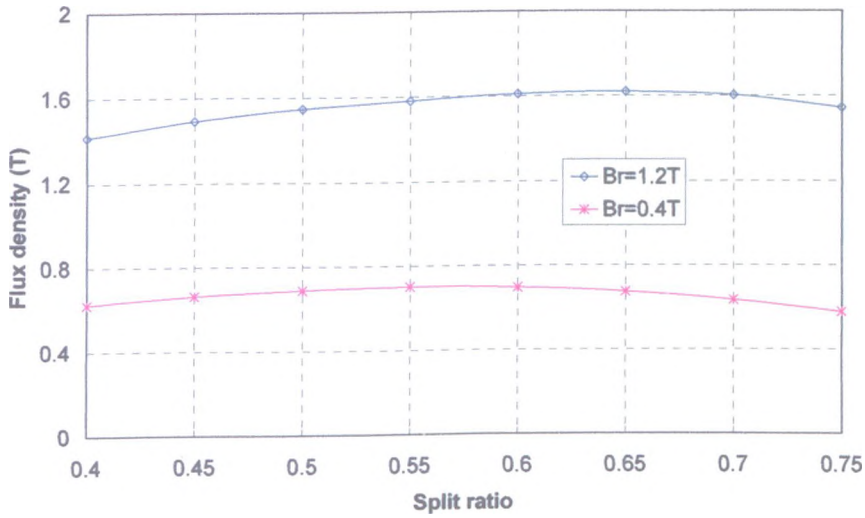

Fig. 4.17. Flux density in stator tooth of flux-switching PM machine

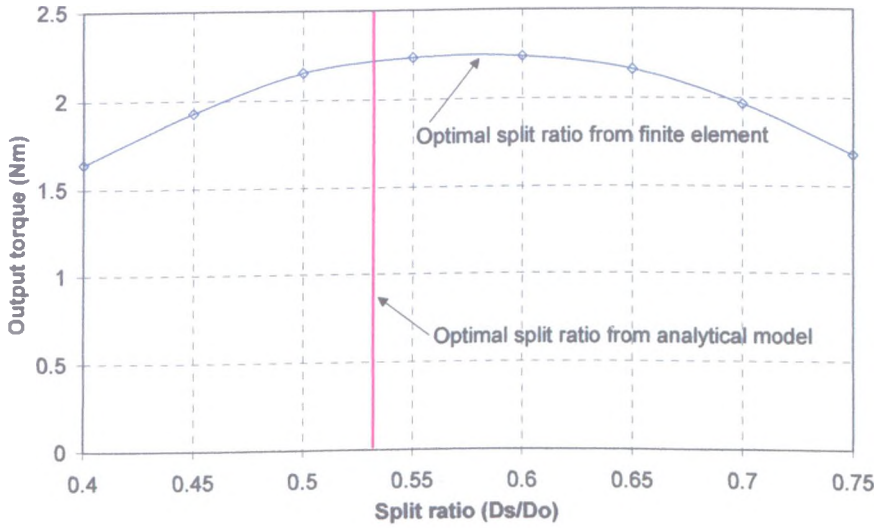

(a) B_r=1.2T

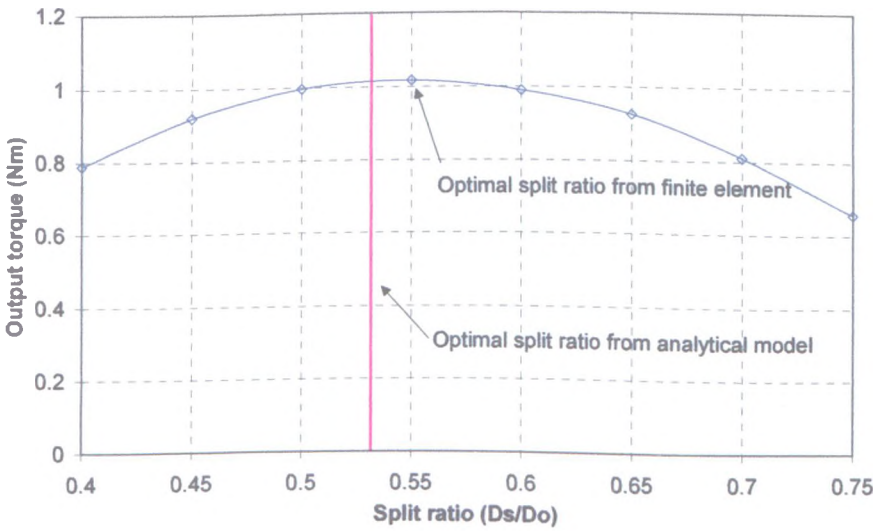

(b) B_r=0.4T

Fig.4.18. Optimal split ratio of flux-switching PM machine

4.3.4. Influence of electric loading

In the previous section, the influence of the magnetic loading on the optimal split ratio of a flux-switching PM machine was investigated, while the influence of the electric loading on the optimal split ratio was ignored. Hence, it will be studied in this section.

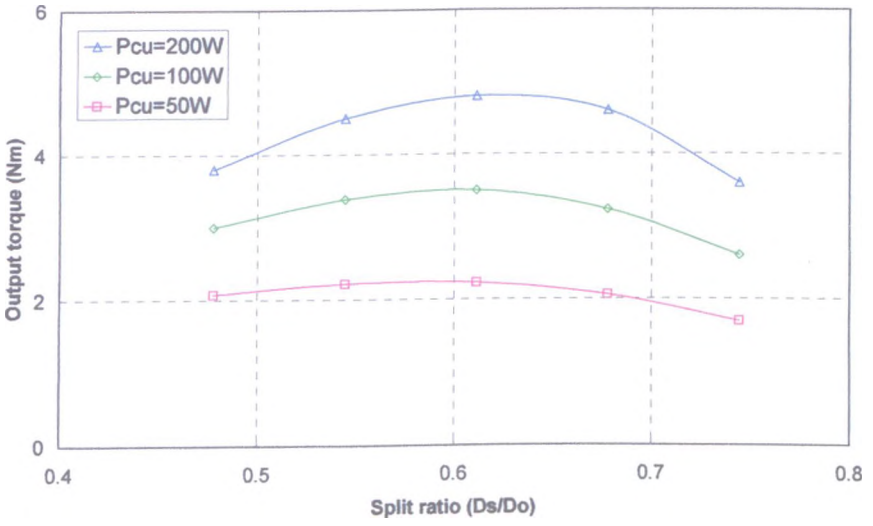

(a) Optimal split ratio

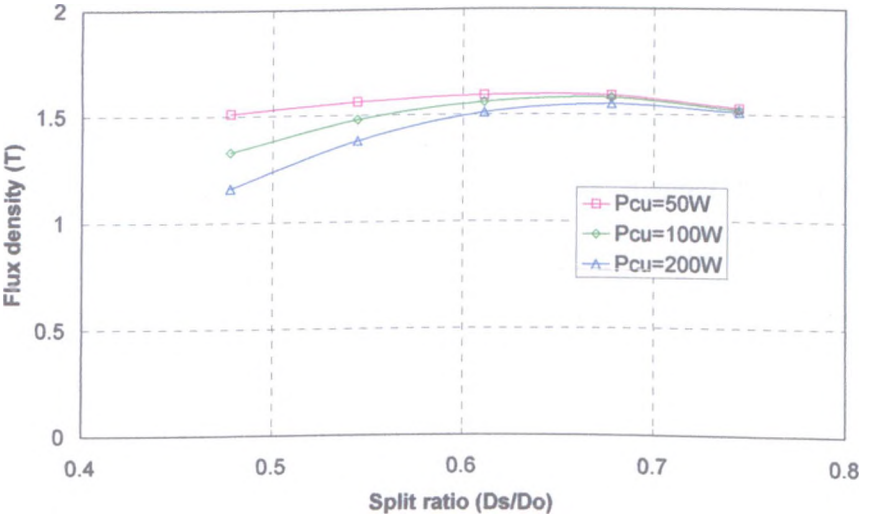

(b) Effective stator tooth flux density

Fig.4.19. Optimal split ratio of flux-switching PM machine (B_r=1.2T)

Fig. 4.19 shows results predicted from finite element analysis, from which it can be seen that the optimal split ratio, based on a fixed copper loss P_{Cu}=50W, is ~0.55-0.6. With an

increase in the copper loss, the optimal split ratio increases, e.g. when the copper loss P_{Cu}=200W, the optimal split ratio increases from ~0.6-0.65. The reason for this can be explained with reference to Fig. 4.19(b). With an increase in the copper loss, the phase current increases, whilst the d-axis PM flux-linkage reduces due to cross-coupling between the d-axis and q-axis magnetic circuits. Consequently, the effective flux density in the stator teeth due to the d-axis PM flux-linkage is reduced, and the smaller the split ratio, the greater the reduction in the effective flux density.

4.4. Summary

Optimal split ratios for maximum output torque of alternative PM brushless machine topologies have been systematically investigated in this chapter.

The analytical equation for the optimal split ratio of conventional PM brushless machines has been derived, and different winding dispositions, different airgap field distributions and different operational modes have been considered, and the influence of the tooth-tip height and the end-windings have also been considered. The equations for the optimal split ratio have been verified by both finite element analysis and measurements on a 3-phase, 4-pole, 6-slot, permanent magnet brushless machines equipped with surface-mounted magnet rotors and having the same outside diameter and temperature rise at rated load. Overall, excellent agreement is achieved between the analytical and finite element predictions and measurements.

The analytical equation for the optimal split ratio of a flux-switching PM brushless machine has been derived, taking account of the end-windings. The influence of the magnetic and electric loadings have also been discussed. The optimal split ratio has been implemented in a prototype flux-switching PM brushless machine, and again, excellent agreement is achieved between finite element predictions and measurements.

Chapter 5 Losses in Flux-switching Permanent Magnet Machines

5.1. Introduction

As shown in previous chapters, the flux-switching permanent magnet brushless machine topology is similar to that of a doubly-salient permanent magnet brushless machine [LIA95]. However, unlike the doubly-salient PM machine, in which the phase flux-linkage waveform is unipolar, the phase flux-linkage waveform of a flux-switching PM machine is bipolar. Hence, its back-emf constant and the specific torque capability are significantly higher than those of a doubly-salient PM machine. Nevertheless, in both machines, a significant leakage flux exists external to the stator core, which not only varies as the rotor rotates, but also changes with the load. Thus, it will result in an eddy current loss being induced in the non-magnetic frame, which will generally be an aluminium casting, into which the stator is either shrunk fit or dove-tailed. However, to date, this issue has not been addressed in the literature. Further, since the frequency of the flux variation in the stator of a flux-switching PM machine is twice the fundamental operating frequency, the stator iron loss may be high, and, therefore, also needs to be investigated. Although the stator coil excitation and the permanent magnet excitation are in parallel, and, hence, theoretically the magnet working point should not be influenced by the armature reaction, in practice due to the flux-switching action, it is found that there is a significant variation of the magnet working point, and, hence, a potentially significant eddy current loss in the magnets, which is another subject, is investigated in this chapter.

The flux-switching PM machine under consideration is designed to operate in both constant torque and constant power modes. Below the base-speed (~1400rpm), I_q=max. and $I_d \approx 0$ control is employed in order to maximize the torque per ampere, and above the base-speed, I_q is gradually reduced while I_d is simultaneously increased negatively to facilitate flux-weakening. The operational profiles of the maximum torque-speed

characteristic and the corresponding d-axis and q-axis currents are shown in Fig. 5.1. Their influence on the loss calculation is considered.

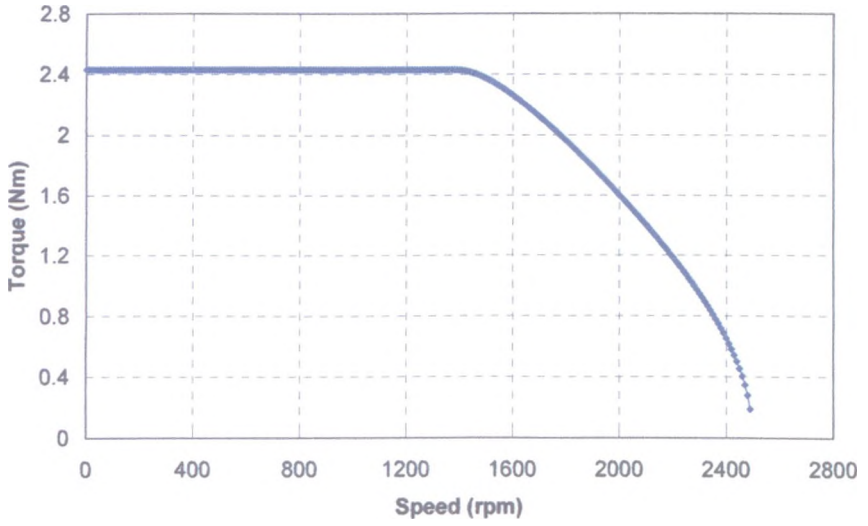

(a) Torque-speed curve

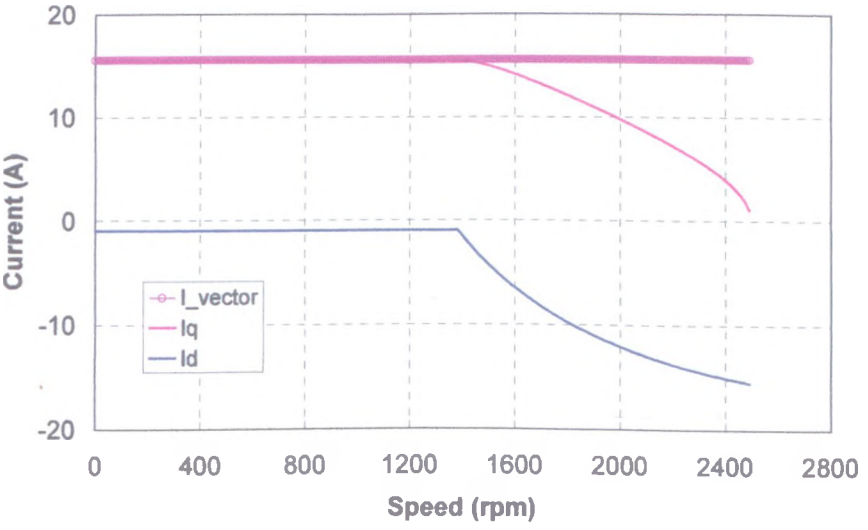

(b) Current-speed curves

Fig. 5.1. Torque and current control profiles of flux-switching PM machine

In this chapter, the losses which occur in the flux-switching PM machine, which will be investigated systematically, include:

1. Copper loss: which will be calculated by assuming a simple shape for the end-windings.

2. Eddy current loss in the aluminium frame: the leakage flux and resultant eddy current loss being investigated by 2-D finite element analysis and validated experimentally. The influence of the rotational speed and the load on the eddy current loss will also be taken into account, as well as the effectiveness of introducing slots into the frame in reducing the loss.

3. Eddy current loss in the permanent magnets: the permanent magnets will be modelled by an equivalent current sheet using the MEGA finite element software, and the eddy current loss will be studied for both constant torque and flux-weakening modes of operation.

4. Iron loss: the stator and rotor iron loss will be investigated, with due account for the complex flux waveforms.

5.2. Copper loss

For prototype flux-switching PM machine, since its maximum speed is only 2400rpm, according to equation (5.3), the skin depth is ~3mm, which is much larger than the actual copper wire diameter 0.93mm. As a result, the phase resistance increase due to the skin effect will be insignificant. Therefore, only the DC copper loss contributed from DC resistance is considered in this thesis.

$$R = \rho_{Cu} \frac{L}{\pi\left(\frac{D}{2}\right)^2} \qquad \text{DC resistance} \qquad (5.1)$$

$$R = \rho_{Cu} \frac{L}{\pi\delta_{Cu}\left(D - \delta_{Cu}\right)} \qquad \text{AC resistance, if } D > \delta_{Cu} \qquad (5.2)$$

$$\delta_{Cu} = \sqrt{\frac{\rho_{Cu}}{\pi f \mu_{Cu}}} \qquad (5.3)$$

where, ρ_{Cu} is the resistivity of copper, D is the diameter of copper, L is the length of copper, δ_{Cu} is the skin depth, f is the frequency, μ_{Cu} is the permeability of copper.

While for some high speed and low voltage applications, since the bigger cross-section of copper is required, larger size of copper wire or high number of copper wire in parallel have to be utilized, the AC copper loss due to skin effect and proximity effect cannot be neglected, which is under investigation in the EMD group at the University of Sheffield [IWA08].

Without considering the AC resistance, the equation of copper loss can be given as:

$$P_{Cu} = mI_a^2 R_a \tag{5.4}$$

$$R_a = \rho_{Cu} \frac{L_w}{A_{cond}} \tag{5.5}$$

where m is the number of phases, I_a is the rms phase current, R_a is the phase resistance, ρ_{Cu} is the resistivity of copper, L_w is the length of the phase winding, and A_{cond} is the cross-sectional area of the conductors.

The resistivity of copper is given by:

$$\rho_{Cu} = \rho_{Cu15°C}\left[1 + \alpha_T (T - 15)\right] \tag{5.6}$$

where

$$\rho_{Cu15°C} = 0.0175 \times 10^{-6} \quad (\Omega m) \tag{5.7}$$

and

$$\alpha_T = 0.004 \tag{5.8}$$

where $\rho_{Cu15°C}$ is the resistivity of copper at 15°C, α_T is the temperature coefficient of resistance of copper, and T is the temperature of the copper.

The cross-sectional area of each conductor is given by:

$$A_{cond} = \frac{A_{slot} \cdot K_s \cdot N_s}{m \cdot 2N_w} \tag{5.9}$$

where A_{slot} is the area of a slot, K_s is the slot packing factor, N_s is the number of slots, m is the number of phases, and N_w is the number of turns per phase.

The shape of the coils also needs to be determined so that the total length of a phase winding can be calculated, with due account for the influence of the end-windings.

A. Simplified coil shape

If the shape of the coils is simplified, with the end-turns assumed to be semi-circular, as in Fig. 5.2, the radius from the centre of the shaft to the centre of the coil is given by:

$$R_1 = \frac{(R_{so} - h_c + R_{si})}{2} \tag{5.10}$$

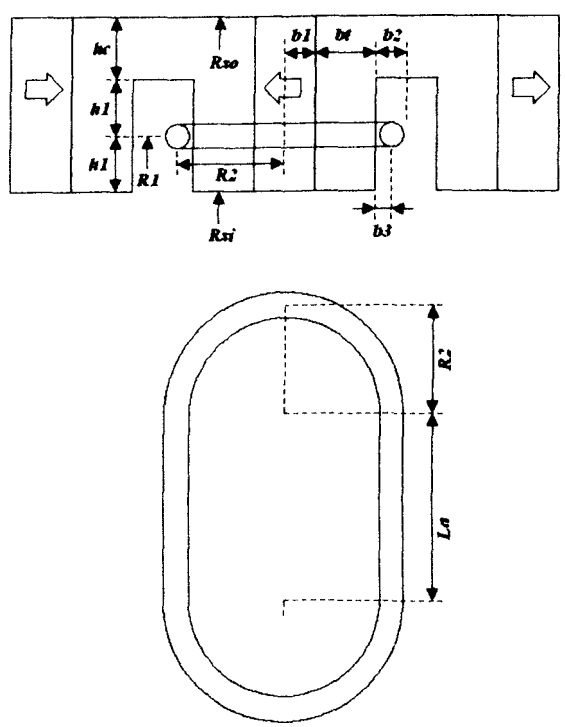

Fig. 5.2. Shape of winding coil

The radius of the end-windings can then be derived as:

$$b_3 = \frac{\frac{2\pi R_1}{2N_s} - b_t - \frac{b_m}{2}}{2} \tag{5.11}$$

$$R_2 = b_m + b_t + b_3 = \frac{\frac{2\pi R_1}{N_s} + 2b_t + b_m}{4} \tag{5.12}$$

where R_{so} is the outer radius of the stator, R_{si} is the inner radius of the stator, h_c is the thickness of the stator back-iron, N_s is the number of slots, b_t is the width of a stator tooth, and b_m is the thickness of the permanent magnets.

Hence, the total length of conductor per phase is given as:

$$L_w = N_w(2L_a + 2\pi R_2) \tag{5.13}$$

The copper loss of the prototype flux-switching PM machine is calculated assuming that m=3, N_s=12, R_{so}=45mm, R_{si}=27.5mm, L_a=25mm, N_w=72turns, and K_s=0.4, and the area of one slot is calculated as:

$$A_{slot} = 0.1009 \times 10^{-3} m^2 \tag{5.14}$$

Then, the copper winding size can be calculated as:

$$D_{coil} = 1.19mm \tag{5.15}$$

In practice, the copper wire with $D_{coil} = 0.93mm$ has been chosen for prototype flux-switching PM machine.

The total length of conductor per coil is calculated as:

$$L_w = N_w(2L_a + 2\pi R_2) = 72 \times (2 \times 25mm + 2 \times 22.6mm) = 6861.6mm \tag{5.16}$$

Hence, the phase resistance is obtained as:

$R_a = 0.176\ \Omega$ if the temperature of the copper is assumed as 15°C

$R_a = 0.218\ \Omega$ if the temperature of the copper is assumed as 75°C

During the prototype motor construction, both ends of each phase winding were brought out so that the actual phase resistance could be measured. The phase resistances have

been measured by using multimeter as shown in Table 5.1. The measured values are slightly higher than prediction due to the extra connection wires.

Table 5.1. Phase resistance of prototype flux-switching PM machine

Predicted (Ω) @ 15°C	Measured A (Ω) @ 15°C	Measured B (Ω) @ 15°C	Measured C (Ω) @ 15°C
0.176	0.179	0.179	0.178

In the prototype flux-switching PM machine having the flux-weakening performance shown in Fig. 5.1, although the dq-axis currents will vary as the degree of flux-weakening is varied, the maximum value of the phase current vector remains unchanged, as shown in Fig. 5.1(b). As a result, the copper loss will be constant during the flux-weakening mode of operation.

The output power, as shown in Fig. 5.3(a), increases with the speed before it reaches a maximum value, at a speed of ~1600rpm. At higher speeds, the output power decreases. Consequently, without considering other losses, the efficiency of the machine rapidly increases with the speed when the speed is relatively low, reaches a maximum value at ~1600rpm, after which the efficiency decreases, as shown in Fig. 5.3(b).

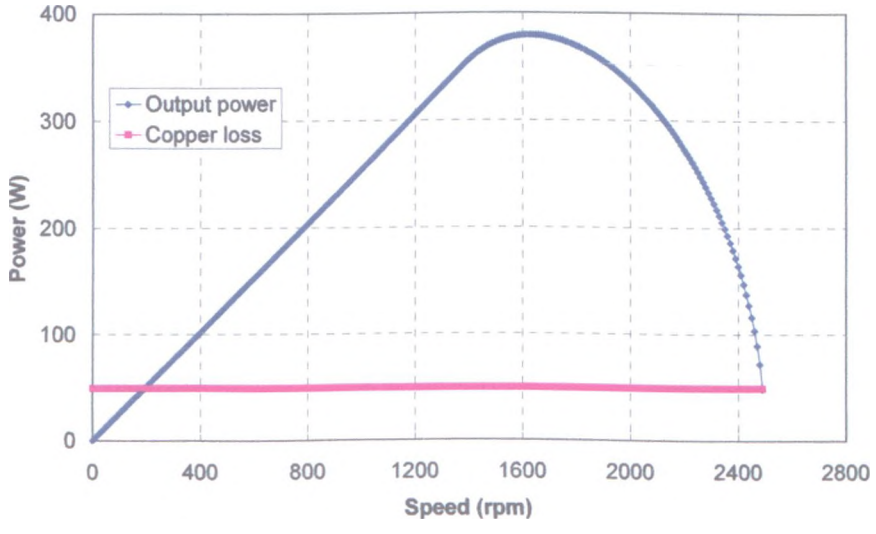

(a) Power

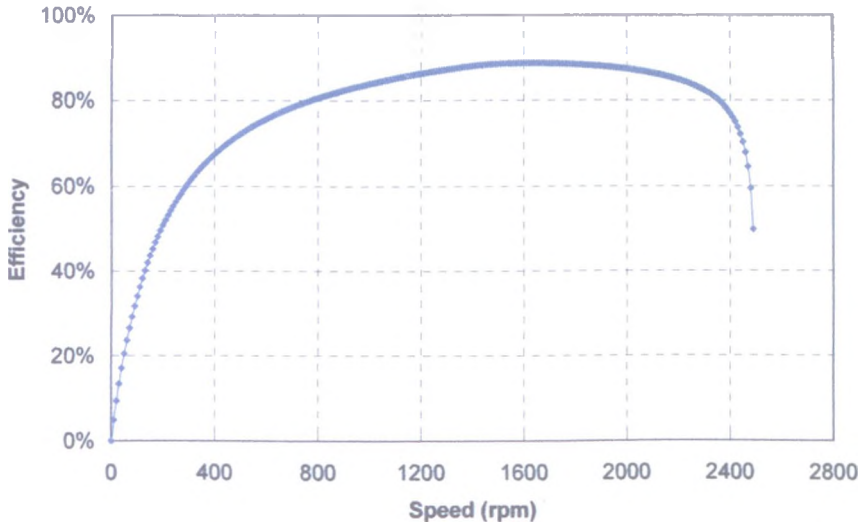

(b) Efficiency

Fig. 5.3. Flux-weakening performance of prototype flux-switching PM machine

5.3. Eddy current loss in aluminium frame

A schematic of the 3-phase, 10-rotor tooth, 12-stator slot, flux-switching PM machine is shown in Fig. 5.4.

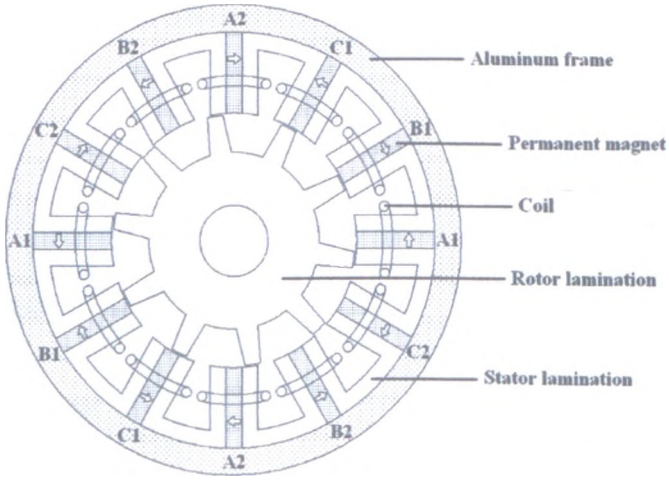

Fig. 5.4. Schematic of 3-phase, 10-rotor tooth, 12-stator slot flux-switching PM machine

The machine has an aluminium frame, and its electrical conductivity is $3.76676\times10^{+7}$ $\Omega^{-1}m^{-1}$. The rated power, torque and phase current are 100W, 2.4Nm and 11A, respectively. The base-speed is ~1400rpm, while the maximum speed is ~2400rpm. The remanence of the sintered NdFeB magnets is 1.2T. The outer and bore diameters of the

stator are 90mm and 55mm respectively, the machine axial length is 25mm, while the aluminium frame thickness is 5mm. In order to simplify the analysis, only the eddy currents which are induced in the frame are considered, i.e. the electrical conductivity of the stator and rotor laminations and the permanent magnets is assumed to be zero.

5.3.1. External leakage flux distribution

Fig. 5.5 shows open-circuit field distributions of the flux-switching PM machine both with and without aluminium frame when the machine is rotating at the maximum speed of 2400rpm. Clearly, the leakage flux varies as the rotor rotates, the frequency of the time-variation being 400Hz. However, the flux variation diminishes rapidly with distance from the outer surface of the stator, as will be evident in Fig. 5.6. As can be seen, the maximum leakage flux density is ~0.7T at the stator surface and the 400Hz variation is ~0.1T. Fig. 5.6 also shows that since the reaction field created by the eddy currents is relatively much smaller than that from the permanent magnets, the influence of the eddy current on the leakage flux distribution is very limited, as will also be confirmed in the discussion in Section 5.3.4.

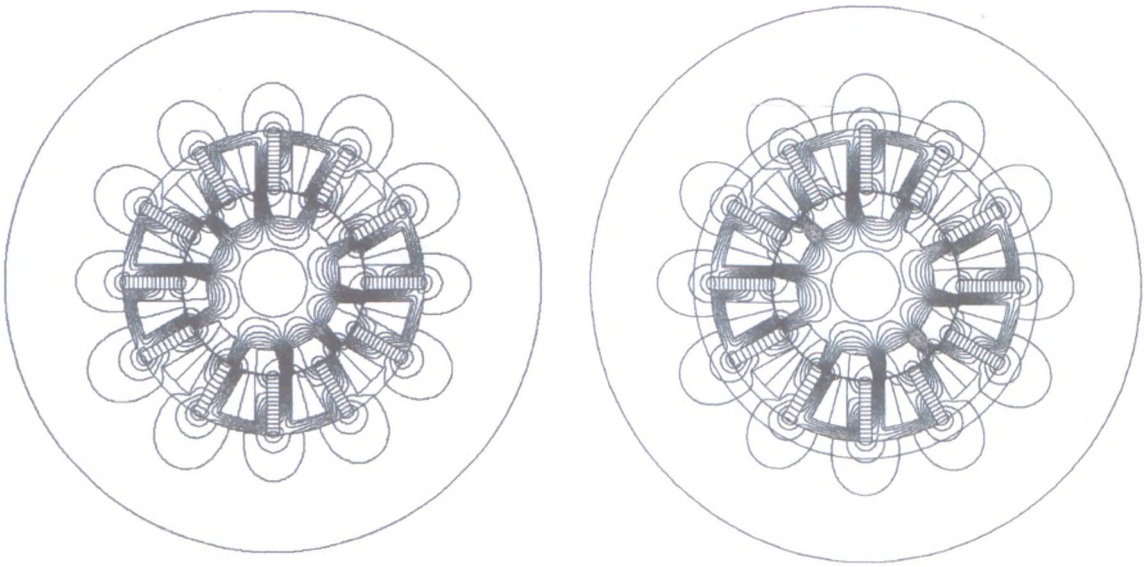

(a) Without aluminium frame (b) With aluminium frame

Fig. 5.5. Open-circuit field distributions of flux-switching PM machine @ 2400rpm

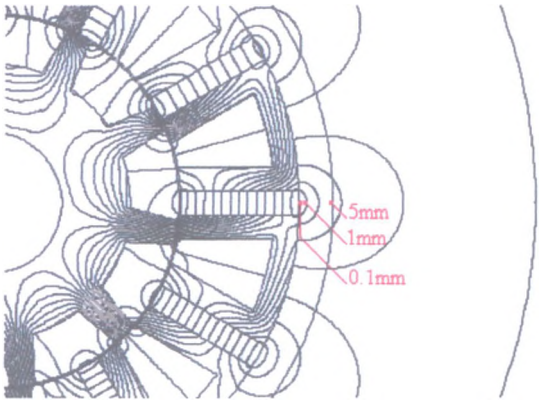

(a) Leakage flux distribution

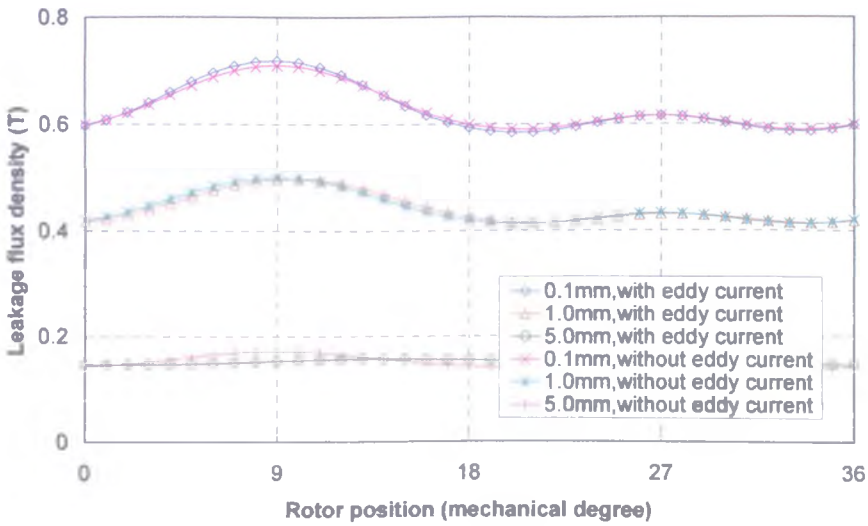

(b) Leakage flux variation

Fig. 5.6. Leakage flux of flux-switching PM machine@ 2400rpm

5.3.2. 2-D finite element prediction

Two critical dimensions need to be determined before undertaking further finite element calculations, one being the location of the outer boundary, so that it does not unduly affect the leakage flux distribution; the other being the size of the finite elements, so that skin effect can be accurately accounted for.

A. Influence of external boundary

The influence of the location of the external boundary has been briefly discussed in the previous chapter, albeit with the aluminium frame neglected. It was observed that although the influence of the boundary on the phase flux-linkage was very small, its influence on the leakage flux distribution was very significant, as shown in Fig. 5.9. Hence, the external boundary for the finite element model was located at twice the stator outer radius, i.e. R_{bound}=2*R_{so}.

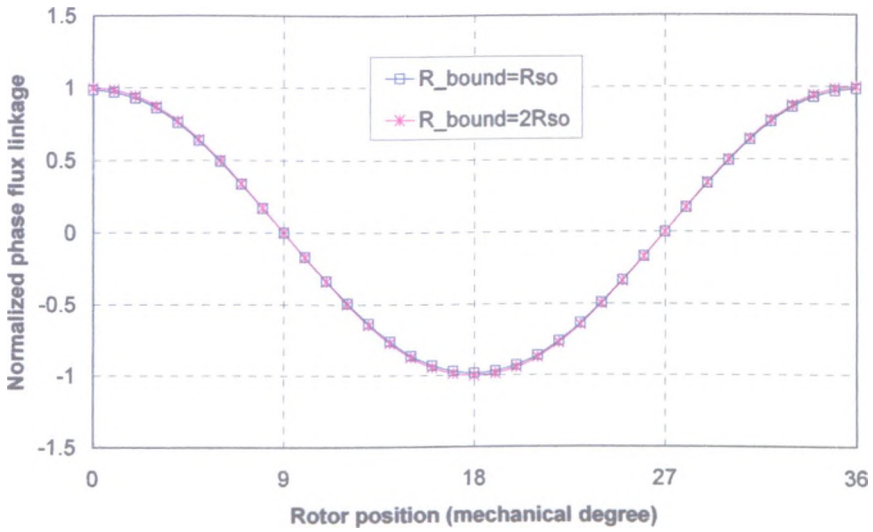

(a) Influence of outer boundary on phase flux-linkage

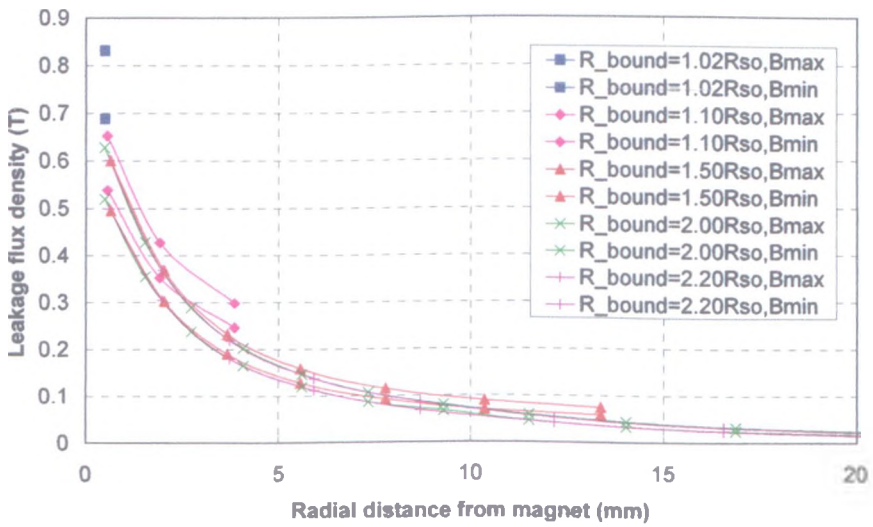

(b) Influence of outer boundary on leakage flux distribution

Fig. 5.7. Influence of outer boundary on flux-switching PM machine

(R_{bound} = radius of external boundary, R_{so} = stator outer radius)

B. Skin effect

The skin depth is calculated from:

$$\delta_{Al} = \frac{1}{\sqrt{\pi f \mu_{Al} \sigma_{Al}}} \tag{5.17}$$

where f is the electrical frequency (Hz), μ_{Al} is the permeability of the aluminium frame (H/m), and σ_{Al} is the electrical conductivity of the aluminium frame (1/Ωm). For aluminium $\mu_{Al}=\mu_0=4\pi\times10^{-7}$ (H/m), and $\sigma_{Al}=3.76676\times10^{7}$ (1/Ωm). Fig. 5.8 shows the variation of the skin depth with the rotational speed, 2400rpm corresponding to a leakage flux variation of 400 Hz. It can be seen that when the machine is running at 2400rpm, the skin depth is ~4mm, while when the maximum speed is doubled to 4800rpm, the skin depth reduces to ~3mm. Therefore, the maximum size of finite elements in the aluminium frame was chosen to be 0.45mm, in order to accurately determine the eddy current loss.

It will also be noticed that at 2400rpm, the skin depth in the aluminium frame, viz. ~4mm, which is similar to the radial thickness of the frame, viz. 5mm. As a result, the eddy currents are essentially resistance-limited, which is also evidenced by the fact that the finite element predicted field distributions both with and without the frame are virtually identical, Fig. 5.5.

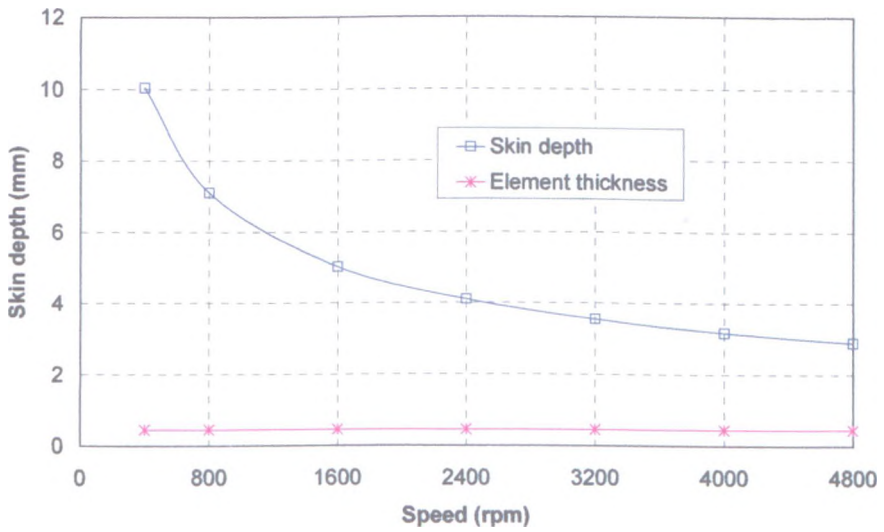

Fig. 5.8. Skin depth in aluminium frame of flux-switching PM machine

C. Eddy current loss

After carefully discreting and defining the electrical parameters of the aluminium frame, the eddy current and eddy current loss were predicted using the MEGA finite element software. The software first calculates the induced eddy current in each element of aluminium frame due to the variation of the leakage flux density, then, since the frame has been defined as conductive region, the resultant eddy current loss can be obtained. It can be seen from Fig. 5.9 that the induced eddy currents and the resultant eddy current loss are concentrated in very localized regions of the frame, adjacent to the ends of the permanent magnets.

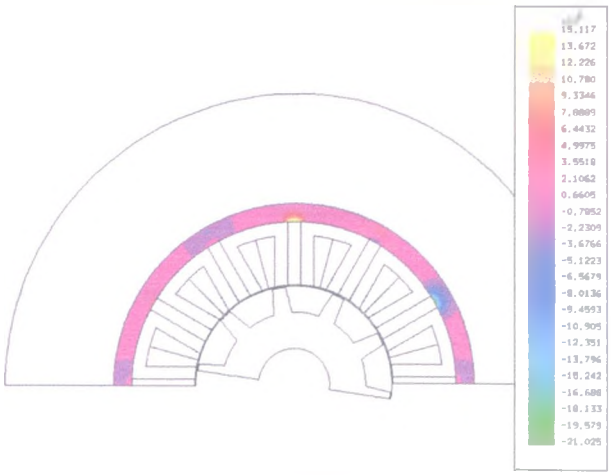

(a) Eddy current distribution (A/m^2)

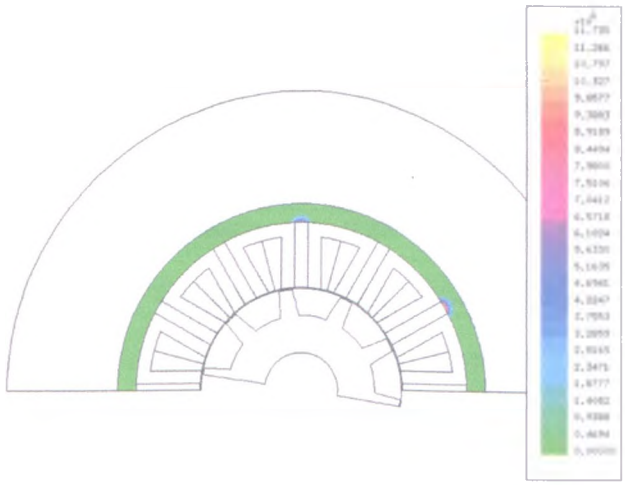

(b) Eddy current loss distribution ($W/m^2/m$)

Fig. 5.9. Eddy current and eddy current loss distribution in aluminium frame of flux-switching PM machine @ 2400rpm (open-circuit)

The variation of the open-circuit eddy current loss with speed is shown in Fig. 5.10. As can be seen, the loss increases approximately linearly with speed, although the eddy current loss density increases in proportion to the square of the frequency and the skin depth reduces inversely with the square root of the frequency.

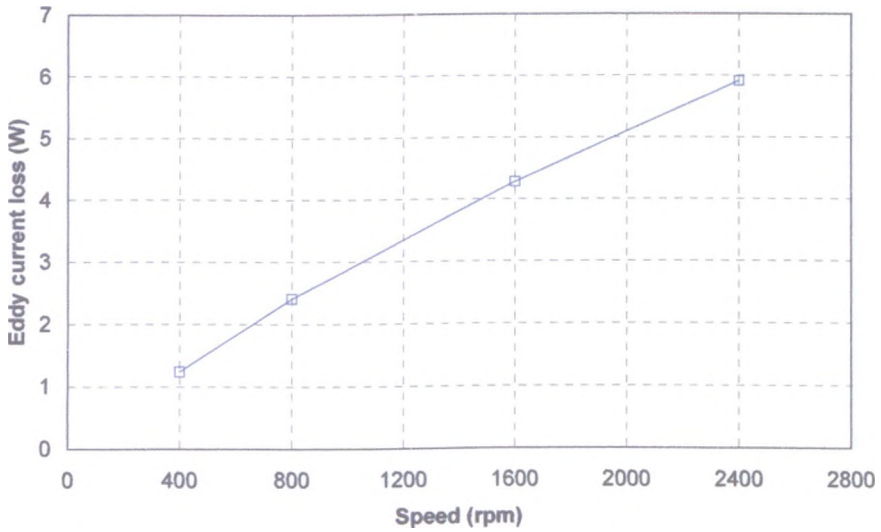

Fig. 5.10. Eddy current loss of flux-switching PM machine (open-circuit)

5.3.3. Comparison of predicted and measured loss

Fig. 5.11 compares finite element predicted and measured leakage flux density waveforms and the open-circuit eddy current loss in the aluminum frame. The external leakage flux density waveforms were measured directly at a specified position by using a flux density sensor when the aluminium frame was removed. Two machine frames were made, aluminium one and plastic one. The open-circuit eddy current loss in the frame was derived from the difference of the losses when the flux-switching PM machine was equipped with aluminium frame and plastic frame, respectively, when it was driven by another machine.

As will be seen, although the measured external leakage flux densities are always lower than the predicted values, due to primarily to 3-D end-effects. It has to be noticed that since the prototype flux-switching PM machine is very small, it is relatively difficult to obtain the accurate test results, while both predicted and measured results in Fig. 5.11(b)

show that the eddy current loss in aluminium frame is ~1W when the speed is ~400rpm and ~7W when the speed is ~2400rpm.

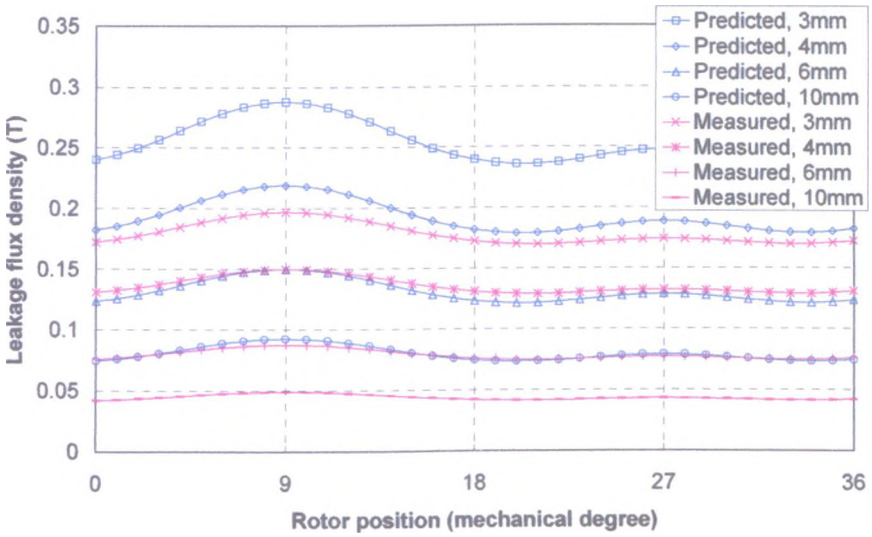

(a) External leakage flux density distributions (without frame)

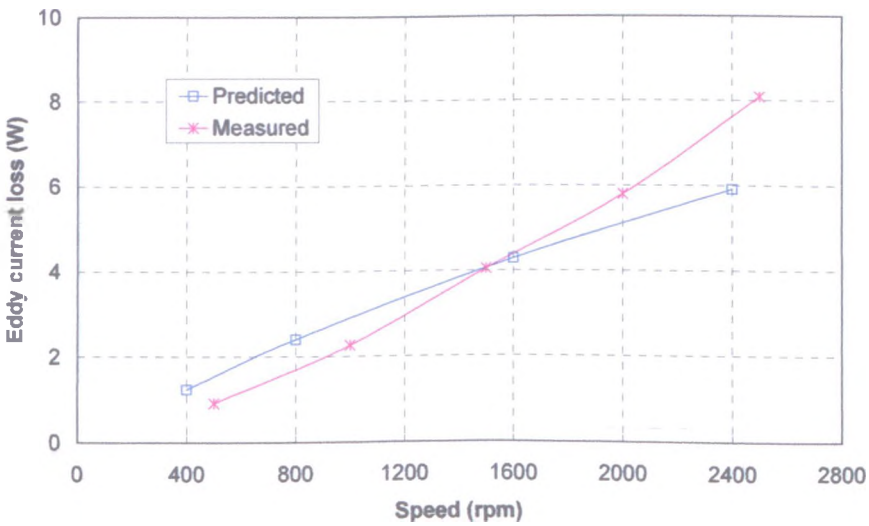

(b) Eddy current loss

Fig. 5.11. Comparison of predicted and measured external leakage flux density waveforms and eddy current loss in aluminium frame

5.3.4. Influence of eddy current loss on machine performance

The previous section has shown that the maximum open-circuit eddy current loss in the aluminium frame of the prototype flux-switching PM machine will be ~6W at the maximum rotational speed of 2400rpm. The influence of the eddy currents on the

performance of the machine has also been investigated, finite element predicted results being shown in Fig. 5.12. However, similar to the influence of the eddy current on the external leakage flux distribution, it can be seen that, the influence on both the phase flux-linkage and the torque is also negligible.

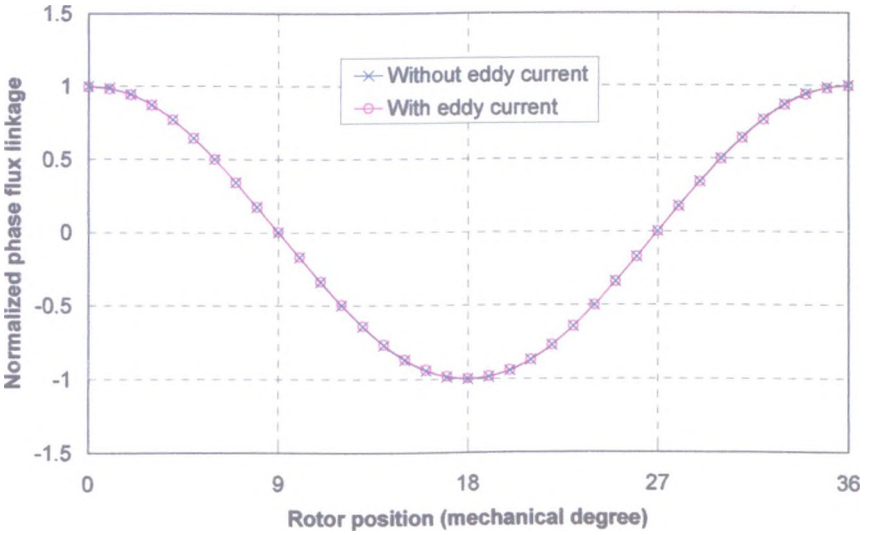

(a) Phase flux-linkage

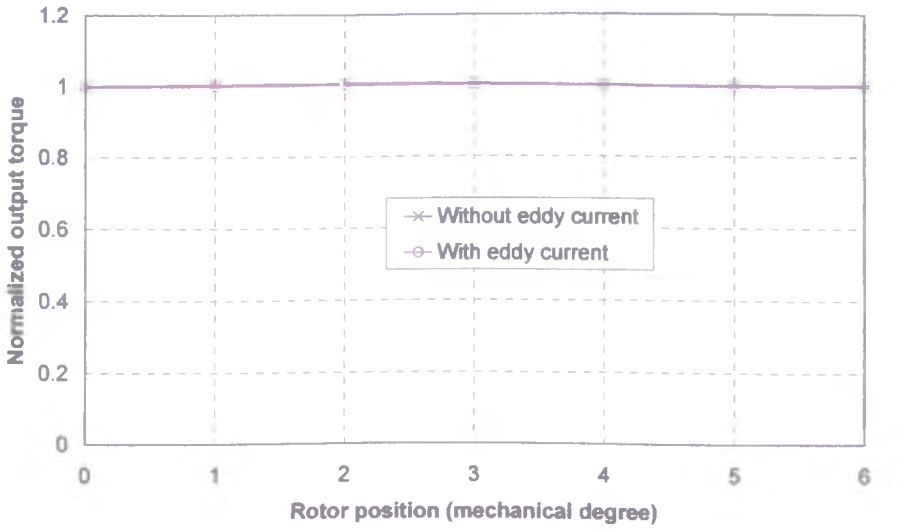

(b) Output torque

Fig. 5.12. Influence of eddy current loss on performance of flux-switching PM machine

5.3.5. Influence of flux-weakening operation

The influence of the different operating modes on the eddy current loss in the

aluminium frame has also been studied by finite element analysis, when the flux-switching PM machine follows the torque-speed curve as shown in Fig. 5.1(a), and the d/q-axis currents vary as shown in Fig. 5.1(b).

Fig. 5.13 shows the eddy current loss variation during the different operational regions. As can be seen, in the constant torque region, i.e. I_q=max. and I_d≈0, the eddy current loss in the aluminium frame is increased slightly, compared to that which results when the machine is on open-circuit. In the flux-weakening operation region, since the d-axis PM flux-linkage is weakened by the negative d-axis current, the eddy current loss in the aluminium frame remains almost unchanged when running above the base speed.

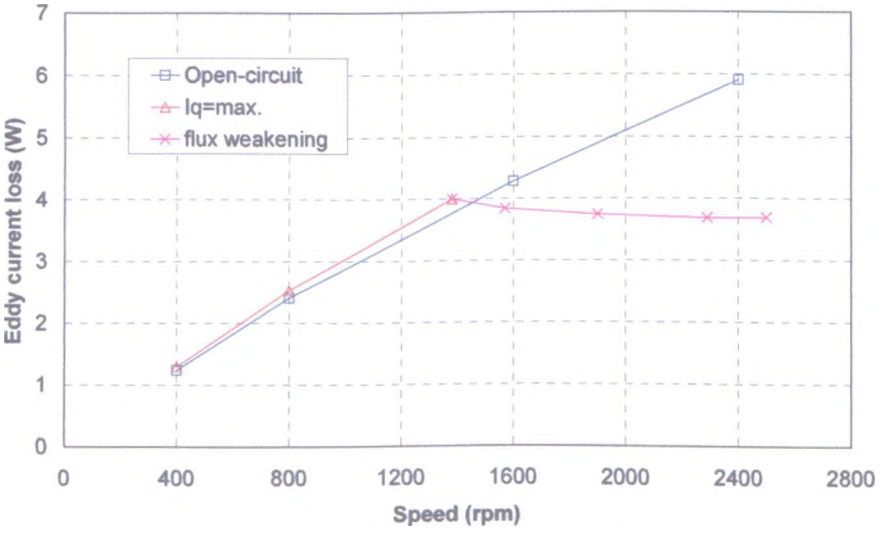

Fig. 5.13. Eddy current loss in aluminium frame of flux-switching PM machine

5.3.6. Influence of magnet bridges

As has been stated earlier, by incorporating bridges at the outer ends of the permanent magnets, as illustrated in Fig. 5.14(a), the manufacture of flux-switching PM machines might be simplified.

The open-circuit eddy current loss distribution which results in the aluminium frame when the flux-switching PM machine is equipped with such bridges is shown in Fig. 5.14(b). It shows that compared with Fig. 5.9, although the maximum eddy current loss density is reduced, due to the fact that the bridges are highly saturated, the eddy current

loss is re-distributed, and as a result, the total eddy current loss remains almost unchanged for bridges up to a thickness of 2mm, while other performance factors, e.g. the phase flux-linkage, decreased significantly, Fig. 5.15. However, when the thickness of the bridges is increased further, the eddy current loss in the aluminium frame reduces.

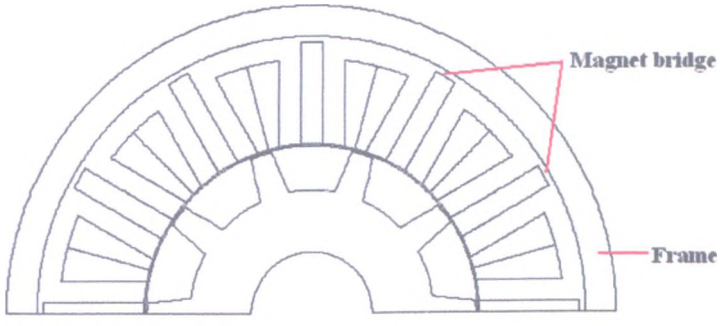

(a) Magnet bridge

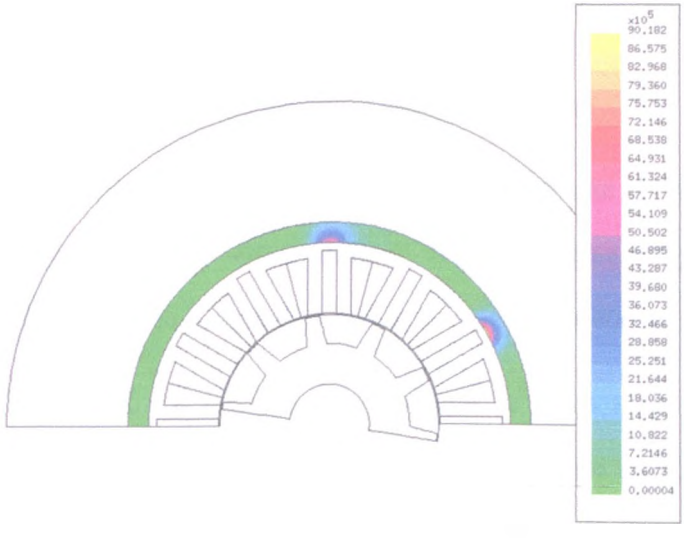

(b) Eddy current loss distribution at 2400rpm ($W/m^2/m$), magnet bridge=2mm

Fig. 5.14. Flux-switching PM machine with magnet bridge

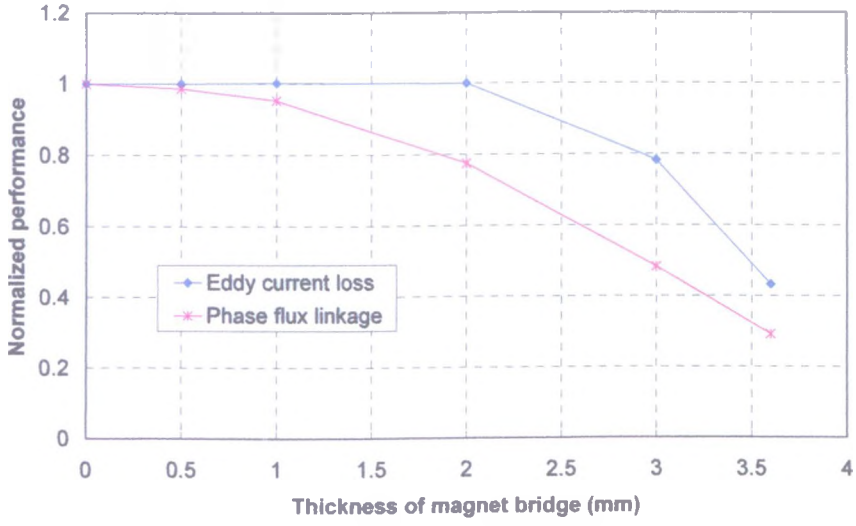

Fig. 5.15. Influence of magnet bridge on eddy current loss in aluminium frame of flux-switching PM machine

5.3.7. Reduction of eddy current loss in aluminium frame

Fig. 5.9 shows that the eddy current loss in the aluminium frame is concentrated in very localised regions adjacent to the outer ends of the permanent magnets. Hence, one means of reducing the loss is to introduce slots in the frame, as shown in Fig. 5.16.

Similar to the influence of the bridges, the addition of such slots changes the eddy current loss distribution, as shown in Fig. 5.16(b). However, the finite element results in Fig. 5.17 show that the total eddy current loss can only be reduced significantly by employing slots having appropriate dimensions.

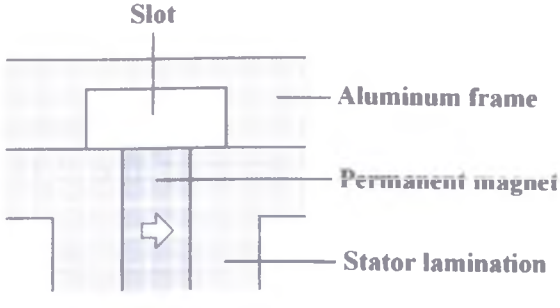

(a) Slot in aluminium frame

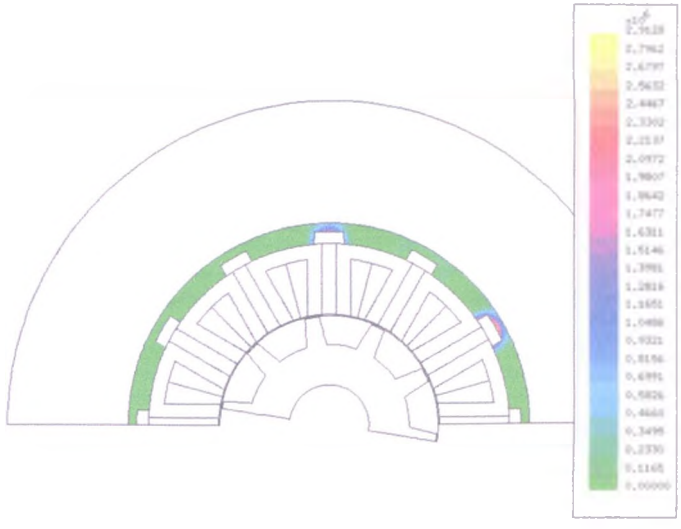

(b) Eddy current loss distribution at 2400rpm ($W/m^2/m$), slot=7.2mm*3mm

Fig. 5.16. Flux-switching PM machine with slot in aluminium frame

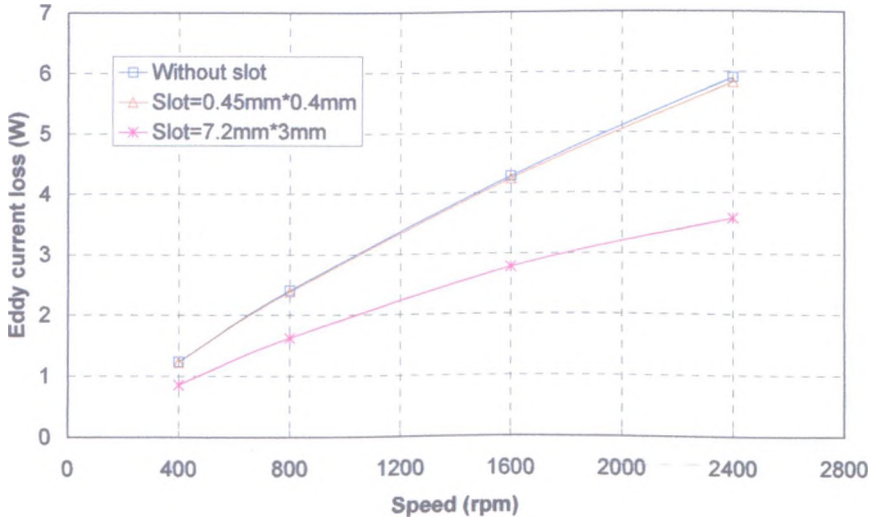

Fig. 5.17. Reduction of eddy current loss in aluminium frame of flux-switching PM machine

5.4. Eddy current loss in permanent magnets

The eddy current loss in the permanent magnets of PM brushless machines has been investigated extensively [MIL94][ATA00][ZHU04], especially for machines equipped with NdFeB magnets, which have a relatively high electrical conductivity, and are relatively sensitive to the working temperature, compared with other permanent magnet

materials, e.g. ferrite, SmCo, etc.

In this section, the eddy current loss in the permanent magnets of the flux-switching PM machine is studied by using finite element analysis. The influence of the eddy current loss on the machine performance, and the influence of flux-weakening operation on the eddy current loss, are investigated, and methods of reducing the loss are discussed.

5.4.1. Eddy current loss calculation in permanent magnets

The MEGA™ finite element software has been used for the eddy current loss calculation in the aluminium frame. However, the eddy current loss in the permanent magnets cannot be calculated by this software directly. Instead, the permanent magnets have to be modelled as an equivalent current sheet, as illustrated in Fig. 5.18.

(a) Permanent magnet (b) Current sheet model

Fig. 5.18. Current sheet model of permanent magnet

Since the permanent magnets which are used in the flux-switching PM machine are parallel magnetized, if the thickness of the current sheet is b_c, the density of the current sheet can be simply derived as:

$$J_c = \frac{H_c}{b_c} \qquad (\mathrm{A/m^2}) \qquad (5.18)$$

where

$$H_c = \frac{B_r}{\mu_r \mu_0} \qquad (5.19)$$

and B_r is the remanence of the permanent magnets, μ_r is the relative recoil permeability and μ_0 is the permeability of air. For sintered NdFeB, B_r=1.2T, μ_r=1.05, $\mu_0=4\pi\times10^{-7}$ (H/m), and the electrical conductivity $\sigma_m=6.25\times10^{+5}$ (1/Ωm).

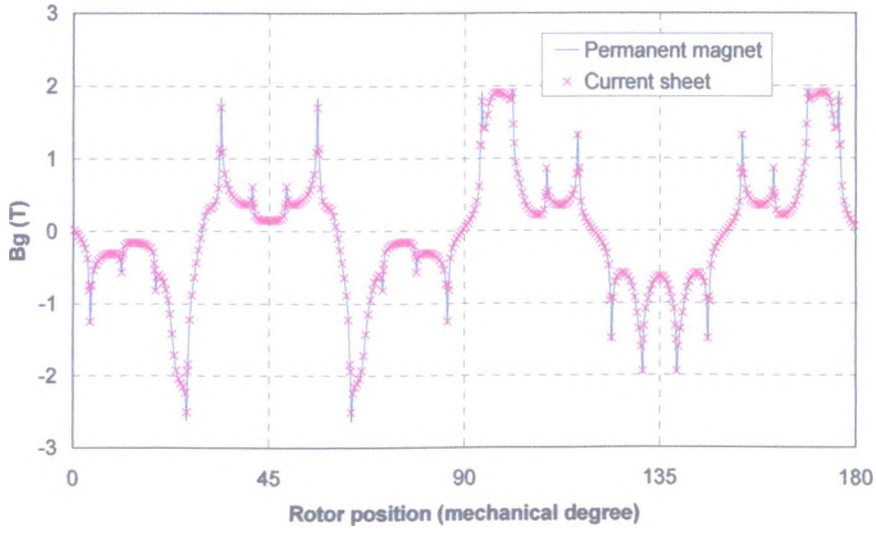

Fig. 5.19. Airgap field distribution of flux-switching PM machine

Fig. 5.19 shows that if the thickness of the current sheet is sufficiently small, viz. 0.05mm, the difference in the predicted performance of the flux-switching PM machine when equipped with the actual permanent magnets and with equivalent current sheets is negligible.

5.4.2. Open-circuit flux waveform in magnets

The open-circuit flux density variation which results at different locations in the permanent magnets is shown in Fig. 5.21, in which, the flux density is resolved into two components, viz. circumferential component B_{theta} and radial component B_{radial}. It can be seen that the variation is relatively small, and, hence, the eddy current loss in the magnets is also expected to be relatively small.

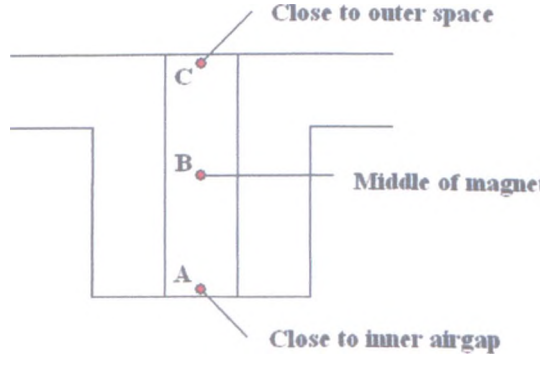

Fig. 5.20. Locations of flux waveform sampling point

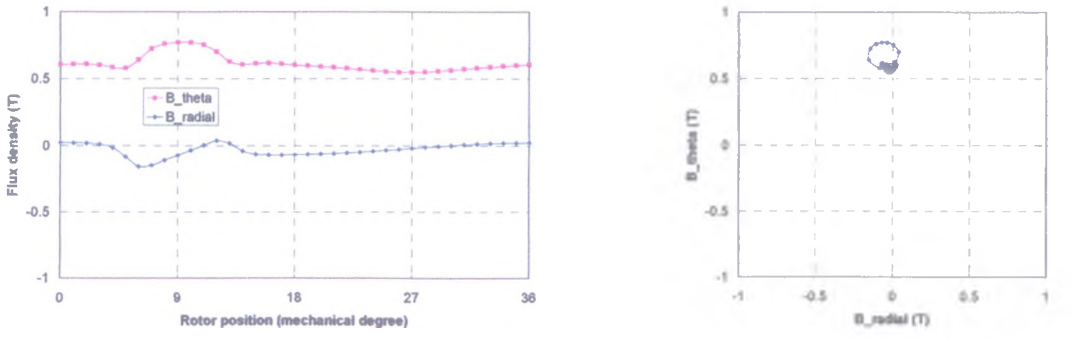

(a) Magnet flux waveform at A

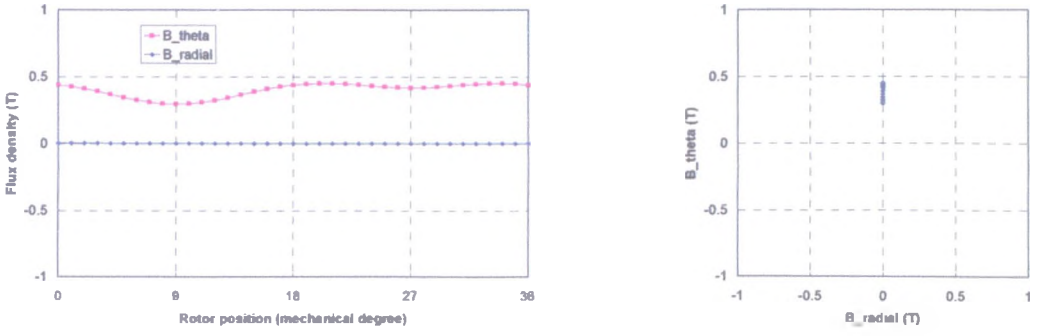

(b) Magnet flux waveform at B

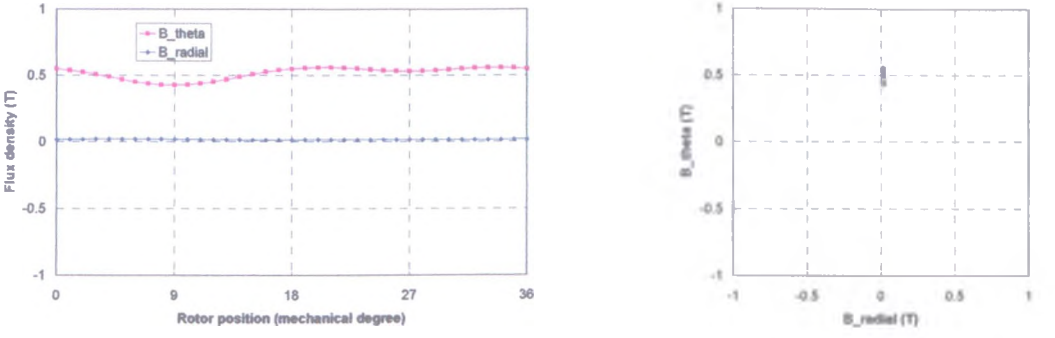

(c) Magnet flux waveform at C

Fig. 5.21. Open-circuit magnet flux waveforms in magnet

5.4.3. 2-D finite element predicted open-circuit eddy current loss

The finite element calculated eddy current and eddy current loss distribution in the permanent magnets when the flux-switching PM machine is on open-circuit are shown

in Fig. 5.22. It can be seen that the eddy current and the associated loss are concentrated at the ends of the magnets, particularly at the inner radius. Fig. 5.23(a) shows the variation of the eddy current loss with rotor position, while Fig. 5.23(b) shows that the eddy current loss increases with the square of the rotational speed. At the maximum speed of 2400rpm, the open-circuit eddy current loss in the permanent magnets is ~10W.

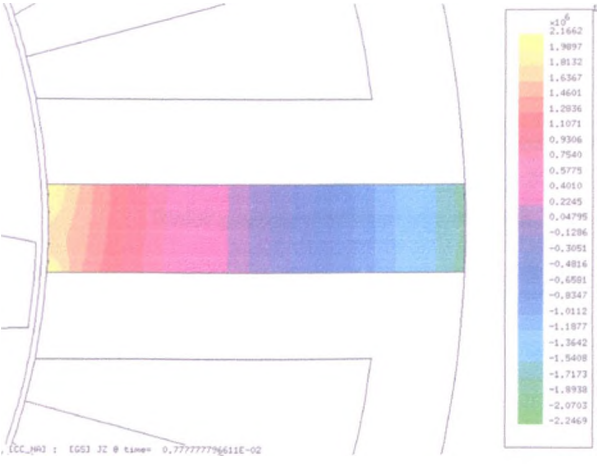

(a) Eddy current distribution (A/m^2)

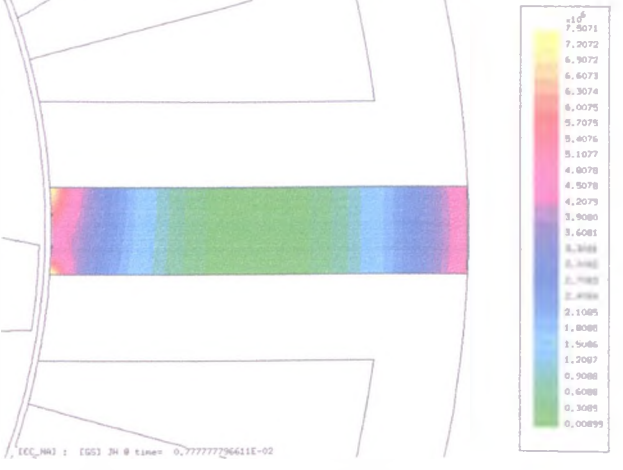

(b) Eddy current loss distribution ($W/m^2/m$)

Fig. 5.22. Eddy current and eddy current loss distribution in permanent magnet of flux-switching PM machine (open-circuit, at 2400rpm, rotor tooth=4°)

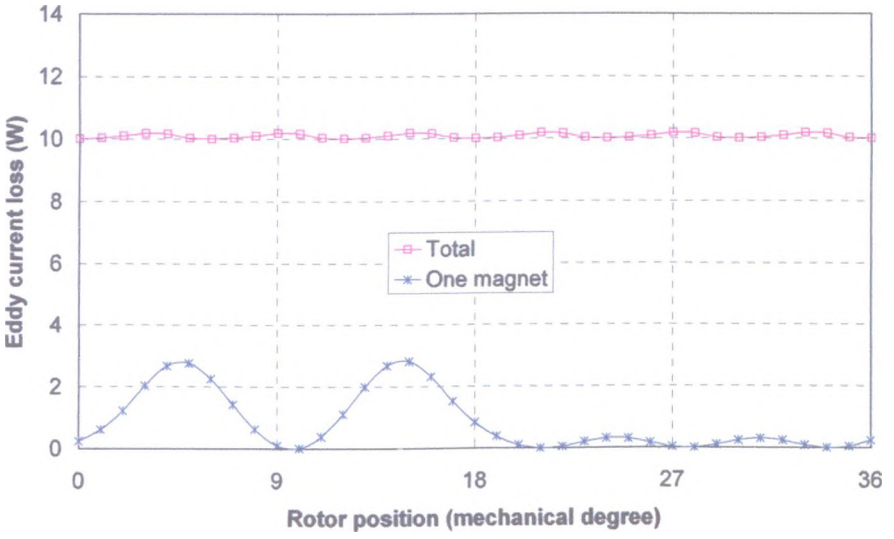

(a) Eddy current loss waveform

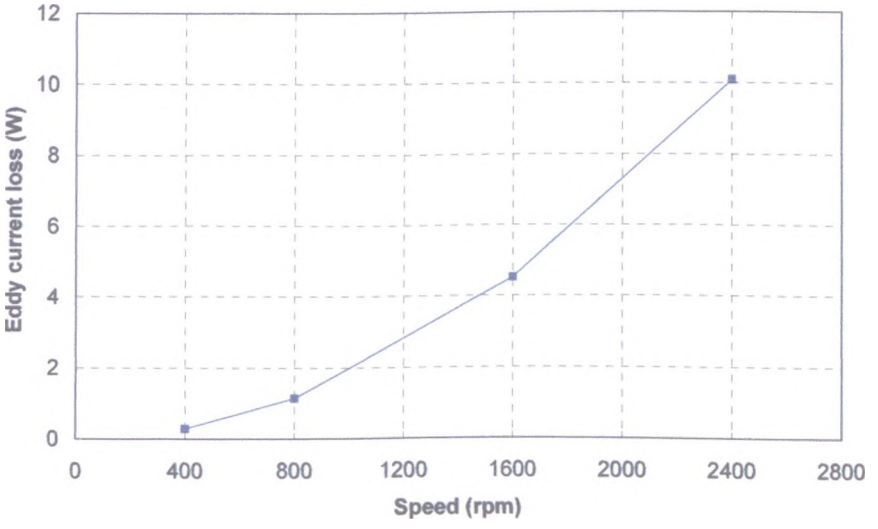

(b) Eddy current loss

Fig. 5.23. Eddy current loss in permanent magnets of prototype flux-switching PM machine (open-circuit)

5.4.4. Influence of eddy current loss on machine performance

The influence of the open-circuit eddy current loss in the permanent magnets on the performance of the flux-switching PM machine is shown in Fig. 5.24. As will be seen, the influence on the phase flux-linkage is negligible, and the output torque is only very slightly reduced.

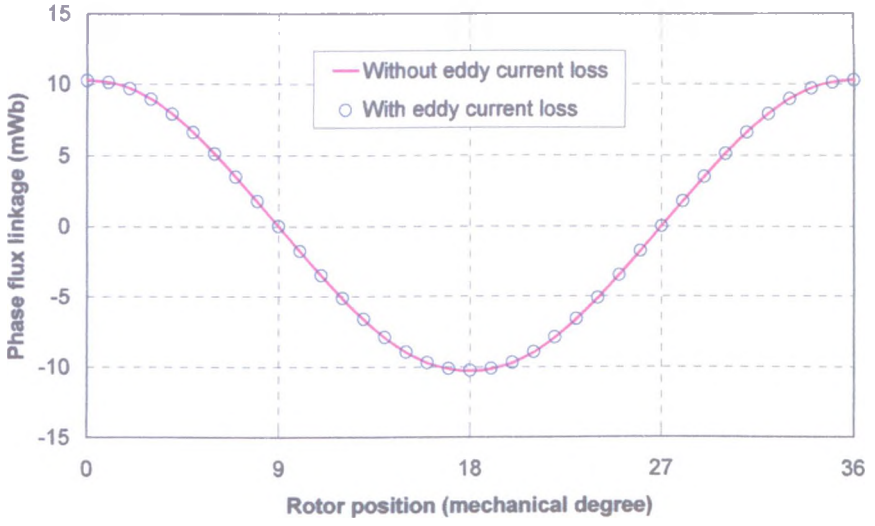

(a) Phase flux-linkage

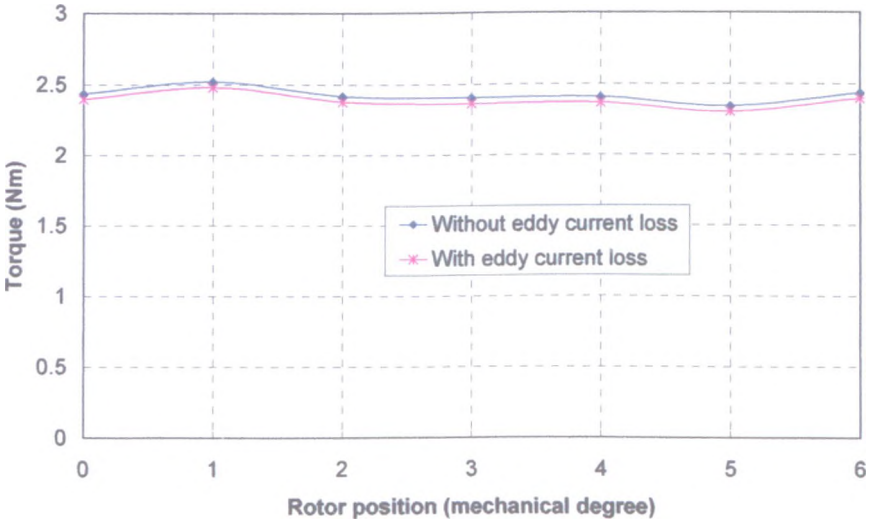

(b) Output torque

Fig. 5.24. Influence of eddy current loss on performance of flux-switching PM machine

5.4.5. Influence of flux-weakening operation

Fig. 5.25 shows that compared with the open-circuit loss, the eddy current loss is increased slightly when maximum q-axis current flows, while the eddy current loss which results in the flux-weakening mode decreases, since the flux variation in the permanent magnets reduces.

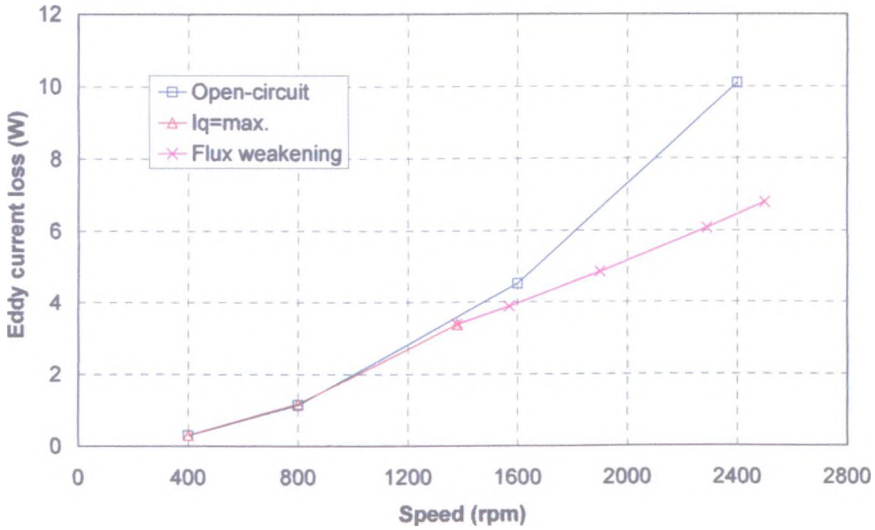

Fig. 5.25. Eddy current loss in permanent magnet of flux-switching PM machine

Unlike the eddy current loss in the aluminium frame which remained almost constant, when the flux-switching PM machine was operated in the flux-weakening region, the eddy current loss in the permanent magnets increases with the speed but no longer follows a square relationship with the speed. At the maximum speed of 2400rpm, the eddy current loss in the permanent magnets is ~30% less than that which results when the machine runs at the same speed on open-circuit, due to the influence of flux-weakening.

5.4.6. Reduction of eddy current loss in permanent magnets

The eddy current and eddy current loss distributions in the permanent magnets in Fig. 5.22 show that both are concentrated at the ends of the magnets. However, since the stator teeth are relatively highly saturated, it is possible to reduce the eddy current loss in the magnets by slightly reducing their radial length as will be seen from Fig. 5.26. Whilst a useful reduction in the eddy current loss can be achieved in this way, the phase flux-linkage is only slightly reduced, since the stator teeth still remain relatively highly saturated. For example, reducing the radial length of the magnets by 1mm at the inner end reduces the eddy current loss in the magnets by ~18%, and the phase flux-linkage only decreases by ~4%; while reducing the length of the magnets by 1mm at both ends

reduces the eddy current loss by ~25%, and the phase flux-linkage only decreases by ~4%.

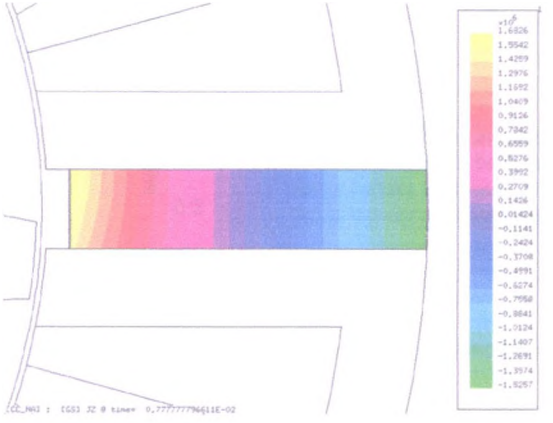

(a1) Eddy current (A/m^2)

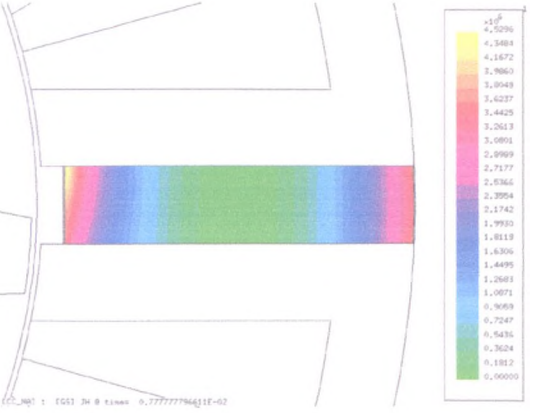

(a2) Eddy current loss ($W/m^2/m$)

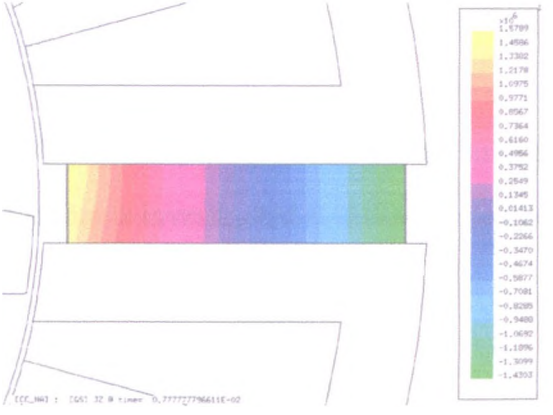

(b1) Eddy current (A/m^2)

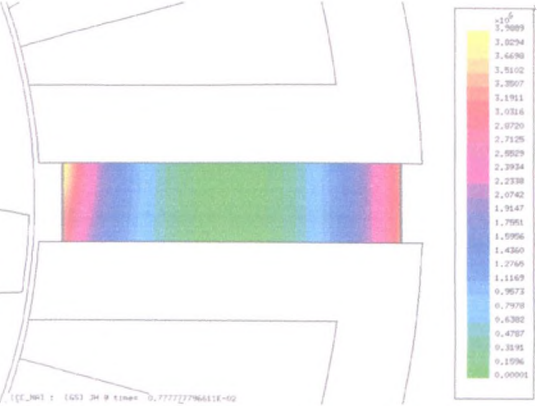

(b2) Eddy current loss ($W/m^2/m$)

Fig. 5.26. Eddy current and eddy current loss distributions in permanent magnets of flux-switching PM machine (2mm, 2400rpm, rotor tooth=4°)

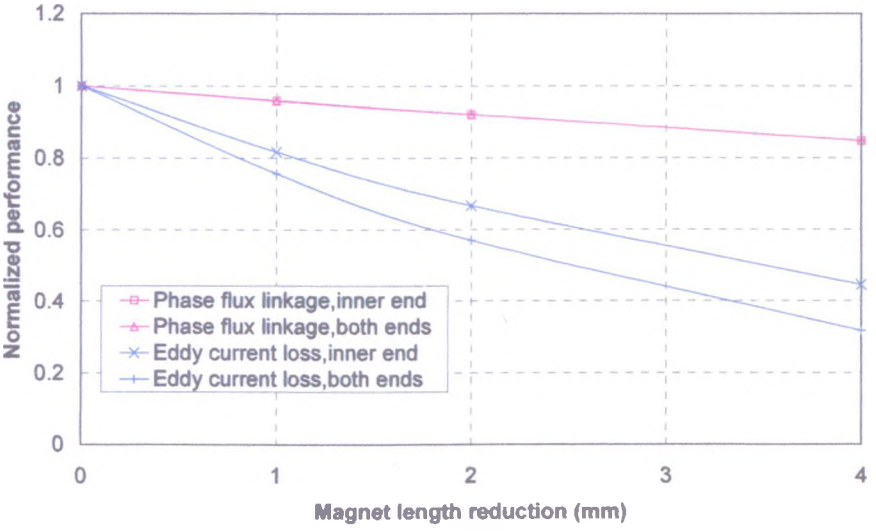

Fig. 5.27. Eddy current loss and phase flux-linkage reduction

5.5. Iron loss

In this section, the iron loss in the laminated stator and rotor of the flux-switching PM machine is investigated at different rotational speeds and load conditions.

5.5.1. Iron loss calculation

Generally, the iron loss in ferromagnetic materials can be separated into three components, viz. the hysteresis loss, the classical eddy current loss and the excess loss associated with localized eddy currents due to domain wall movements.

A. Hysteresis loss

The hysteresis loss is the result of irreversible "jumps" within the material domain structure as the material is exposed to a varying magnetic field.

For a steady-state flux density waveform, in which each cycle comprises only one minimum and one maximum, the hysteresis loss per cycle is only dependent on the magnitude of the peak flux density. For example, if the flux density waveform is sinusoidal, the hysteresis loss is given by (5.17), typically using three material specific

constants.

$$P_{hyst} = k_h f B_{max}^{a_h + b_h B_{max}} \tag{5.20}$$

where P_{hyst} Hysteresis loss (W/kg);

k_h Hysteresis coefficient, deduced experimentally;

a_h Hysteresis coefficient, deduced experimentally;

b_h Hysteresis coefficient, deduced experimentally;

f Frequency (Hz);

B_{max} Amplitude of flux density variation (T).

However, the flux density waveform may contain more than one minimum and maximum within each electrical cycle, as illustrated in Fig. 5.28 for the flux-switching PM machine. These so-called "minor loops" will generate additional hysteresis loss.

The minor loop hysteresis loss has been studied extensively, and several mathematical models have been proposed [CAL01][HAY95][LAV78]. The model proposed in [CAL01] will be adopted in this section.

The method is based on the relationship between the minor loop of magnitude ΔB traversing about zero and a loop of similar magnitude traversing about some non-zero flux density, as illustrated in Fig.5.29.

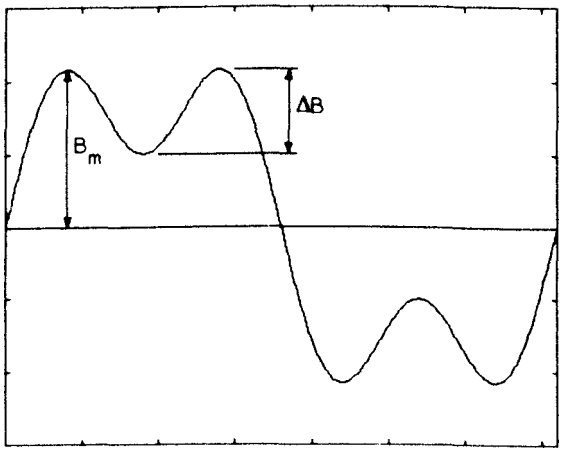

Fig. 5.28. Flux density waveform with one minor loop

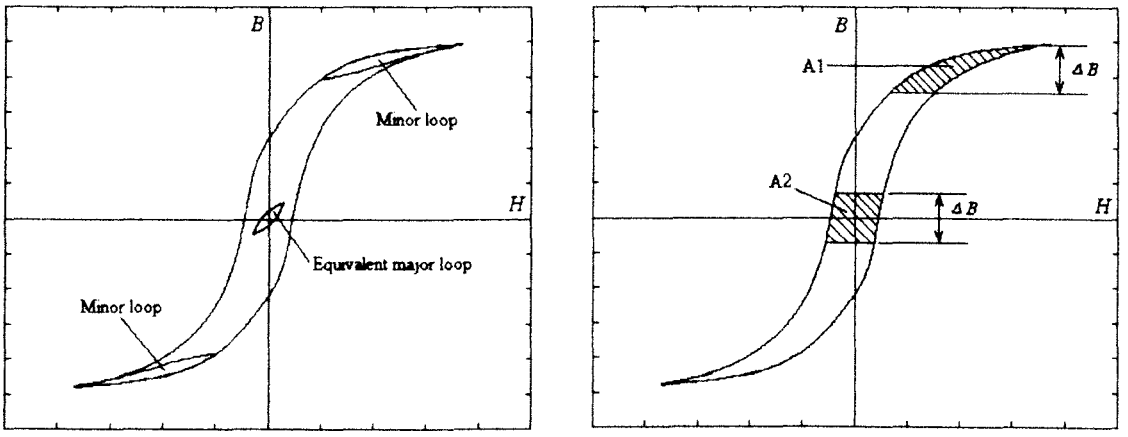

(a) Real loops (b) Schematic loops

Fig. 5.29. Major loop with minor loop

The shaded areas in Fig. 5.29(b) can be used for pre-setting the real minor loop areas shown in Fig. 5.29(a). The minor loop hysteresis loss can be determined from:

$$P_{hyst\ minor}\Big|_{B_m-\Delta B}^{B_m} = Q_{minor} P_{hyst}\Big|_{-\Delta B/2}^{\Delta B/2} \tag{5.21}$$

where

$$Q_{minor} = \frac{A_1}{A_2} \times \left(1 - e^{-k_c \Delta B/2}\right)\left(1 + e^{-k_c \Delta B}\right) \tag{5.22}$$

and k_c is a coefficient which is deduced from measurements

B. Classical eddy current loss

The classical eddy current loss represents the power loss component due to Joule effect heating caused by the induced eddy currents within the electrically conducting laminations, and can be expressed as:

$$P_{class} = \frac{d_{iron}^2}{12 m_v \rho_{iron}} \frac{1}{T_{cycle}} \int_0^{T_{cycle}} \left(\frac{dB}{dt}\right)^2 dt \tag{5.23}$$

where P_{class} Classical eddy current loss (W/kg);

d_{iron} Thickness of lamination (m);

m_v Mass density of lamination (kg/m^3);

ρ_{iron} Resistivity of lamination (Ωm);

T_{cycle} Cycle time of flux density variation (s);

B Flux density variation (T).

If the flux density variation is sinusoidal, the equation can be simplified to:

$$P_{class} = \frac{d_{iron}^2 \pi^2}{6 m_v \rho_{iron}} f^2 B_{max}^2 \tag{5.24}$$

where B_{max} Peak flux density (T);

f Frequency (Hz);

C. Excess loss

The mechanism of excess loss can be explained by the fact that, in practical lamination materials, the magnetic domains are separated by so-called Bloch walls (groups of which are termed "magnetic objects") which interact with themselves and other similar walls, which creates an "internal correlation" field between magnetic domains. These correlation fields, coupled with coercive and eddy current effects, act as a damping field, opposing any changes in the external magnetizing field. Hence, the excess loss is produced [BER87].

The excess loss can be determined from:

$$P_{excess} = \frac{k_e}{T_{cycle}} \int_0^{T_{cycle}} \left| \frac{dB}{dt} \right|^{1.5} dt \tag{5.25}$$

where P_{excess} Excess loss (W/kg);

k_e Coefficient, deduced experimental measurements;

T_{cycle} Cycle time of flux density variation (s);

B Flux density variation (T).

If the flux density variation is sinusoidal, the equation can be simplified as:

$$P_{excess} = 8.67 k_e f^{1.5} B_{max}^{1.5} \quad (5.26)$$

where B_{max} Peak flux density (T);

f Frequency (Hz).

5.5.2. Flux waveforms in stator and rotor

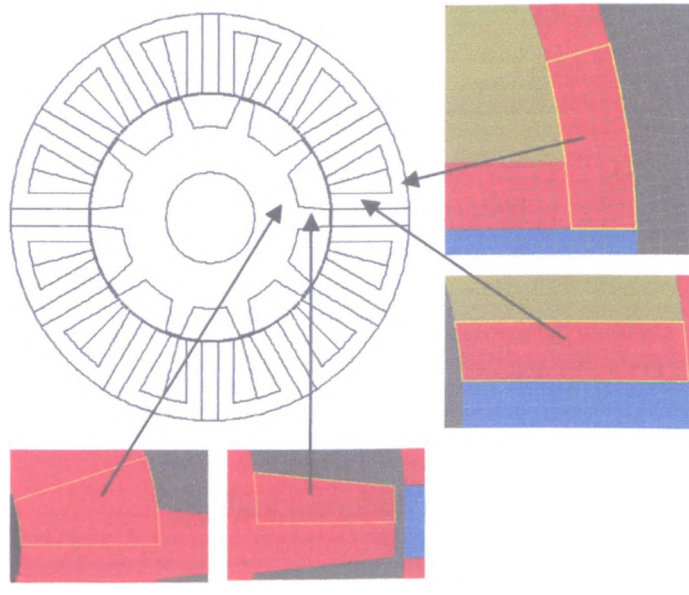

Fig. 5.30. Main ferromagnetic regions of flux-switching PM machine

Flux waveforms in the stator and rotor of the flux-switching PM machine have been obtained by finite element analysis, the flux waveforms in four main regions, viz. the centre of a stator tooth, the middle of the stator back-iron, the centre of a rotor tooth, and the middle of the rotor back-iron being shown in Fig. 5.31. Each flux waveform can be resolved into a radial component (B_{radial}) and a circumferential component (B_{theta}).

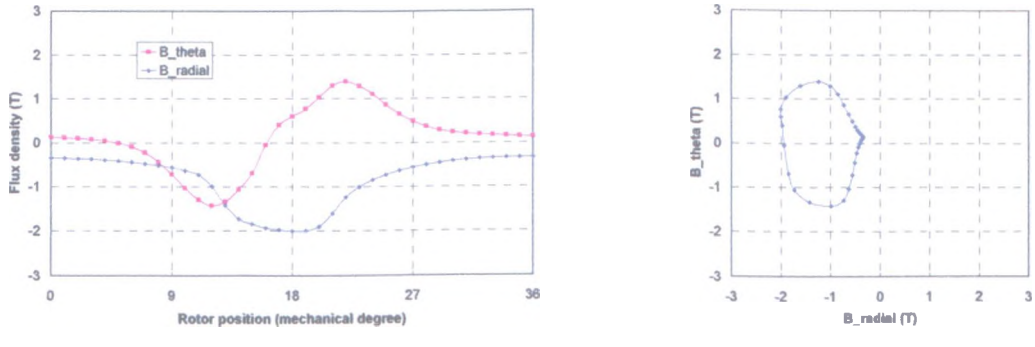

(a) Flux waveform in stator tooth

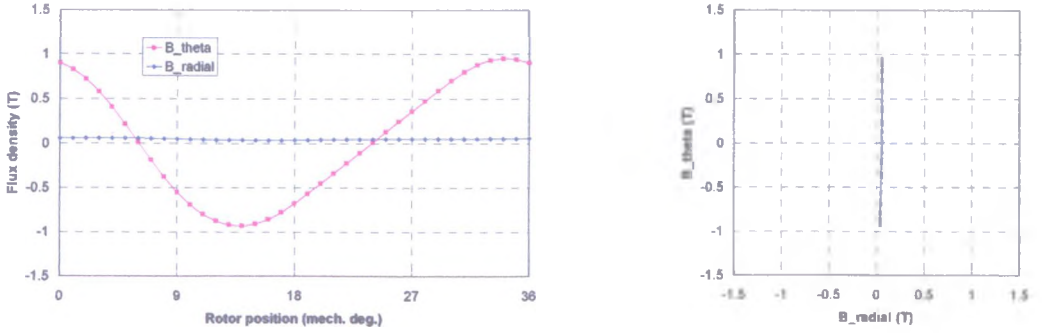

(b) Flux waveform in stator back-iron

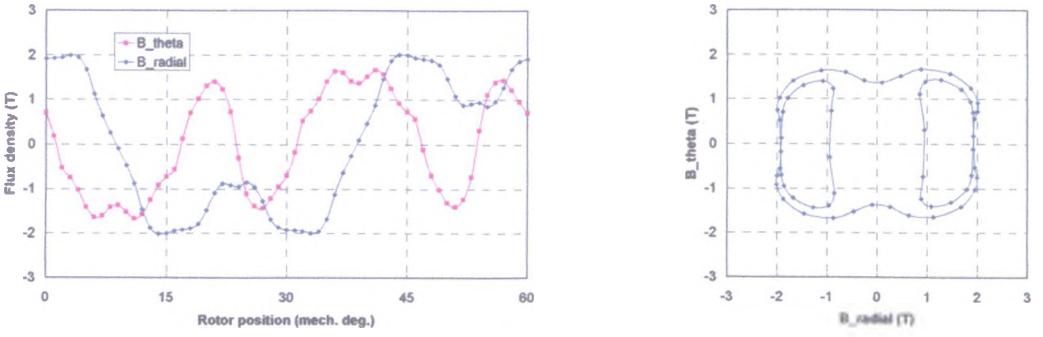

(c) Flux waveform in rotor tooth

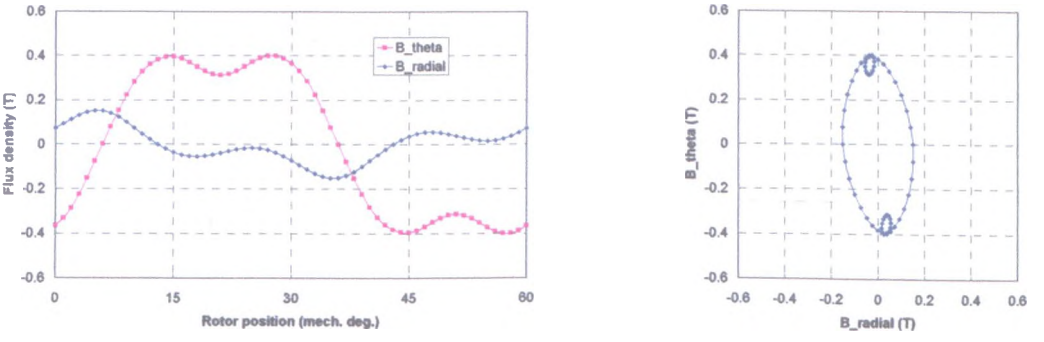

(d) Flux waveform in rotor back-iron

Fig. 5.31. Flux waveforms in stator and rotor of flux-switching PM machine

5.5.3. Finite element calculation of iron loss

Since the magnetic circuit of the flux-switching PM machine is relatively highly saturated, it is impossible to accurately calculate the flux waveform in different parts of

the machine by using an analytical method. Thus, it is necessary to employ finite element analysis, in which the flux waveform in each element is calculated, and the iron loss is subsequently calculated by using the iron loss equations which are given in Section 5.5.1.

The constants for the lamination material which is used in the prototype flux-switching PM machine were measured by employing a single-sheet tester, and are given in Table 5.2. The variation of the calculated iron loss with speed is shown in Fig. 5.32. Clearly, the iron loss increases with an increase in the speed, the stator and rotor iron losses accounting for ~55% and ~45% of the total iron loss, respectively.

Table 5.2. Material constants for V300 lamination material used in prototype flux-switching PM machine

k_{hyst}	17.9e-3	d_{iron}	0.35E-3 (m)
a_h	0.841	ρ_{iron}	45E-8 (Ωm)
b_h	1.023	m_v	7.65E+3 (kg/m^3)
k_c	2.61	k_e	2.0e-4

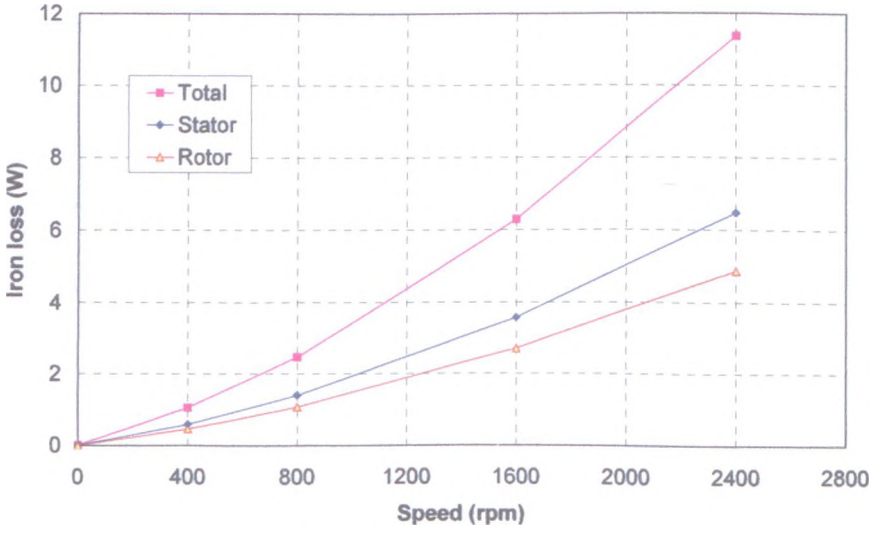

Fig. 5.32. Iron loss in flux-switching PM machine

5.5.4. Comparison of predicted and measured loss

Two search coils were wound on the stator tooth and back-iron as shown in Fig. 5.33.

By driving the prototype flux-switching PM machine, the emf waveforms in the search coils can be measured, and the flux-linkage waveform can be calculated, then the flux density waveforms can be obtained. Fig. 5.34 compares predicted and measured open-circuit flux density waveforms in the stator tooth and the stator back-iron of the prototype flux-switching PM machine. As will be seen, the measured maximum flux densities in both the stator tooth and the stator back-iron are slightly smaller than those predicted from the finite element analysis.

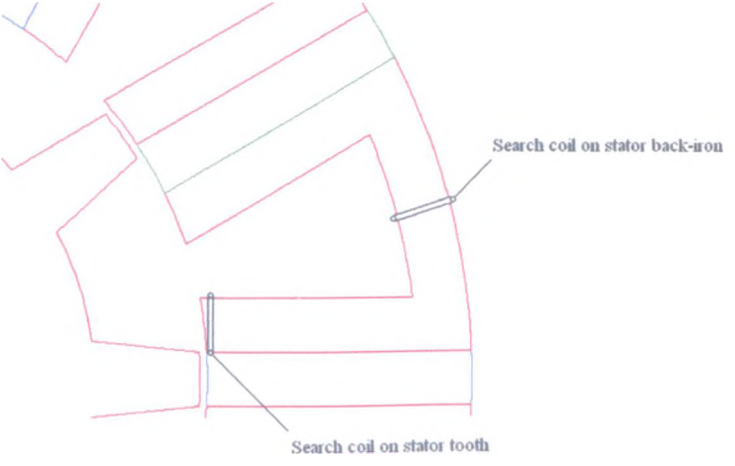

Fig. 5.33. Search coils on stator tooth and back-iron

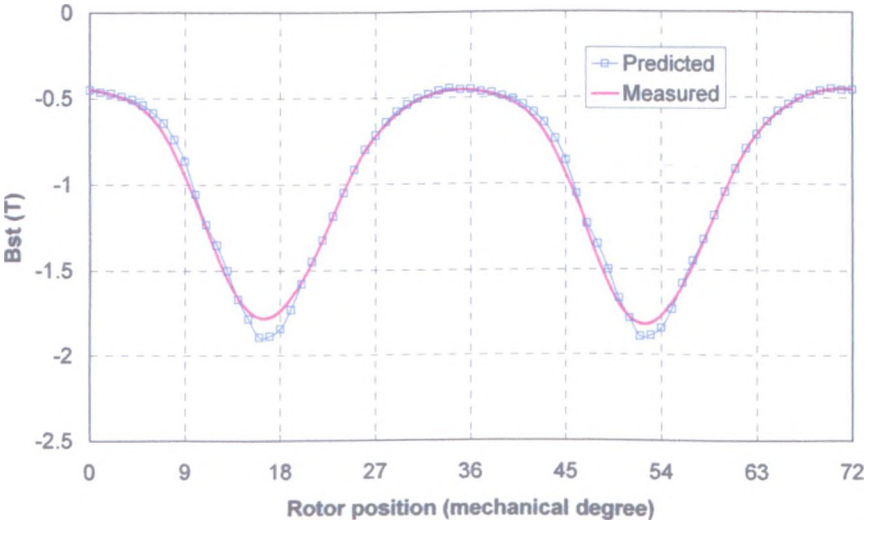

(a) Flux density in stator tooth

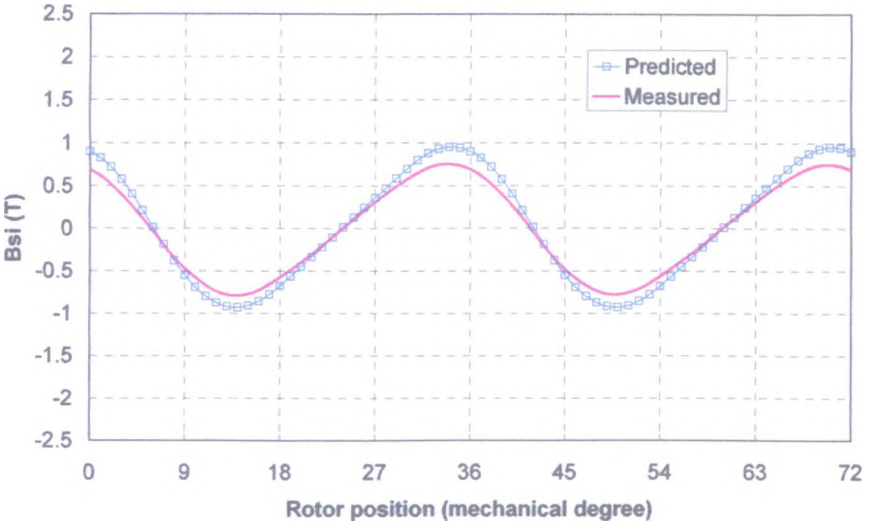

(b) Flux density in stator back-iron

Fig. 5.34. Open-circuit stator flux density waveform in flux-switching PM machine

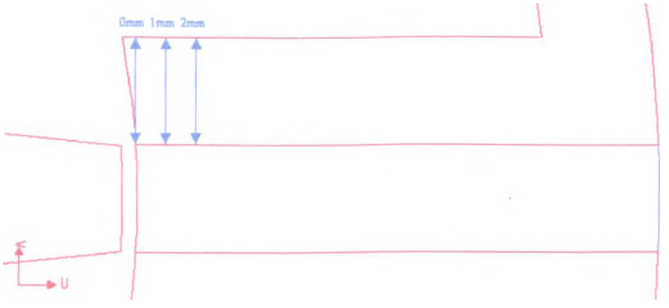

Fig. 5.35. Search coils on stator tooth in finite element model

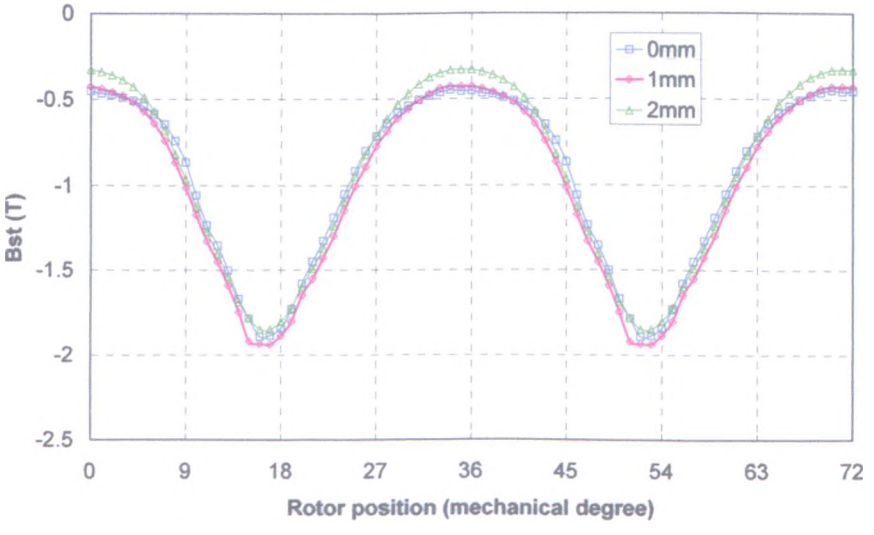

Fig. 5.36. Open-circuit stator tooth flux density waveform

However, it is important to recognise that the search coil is located in an area of

relatively high field gradient. In order to assess the sensitivity of the measured flux-linkage to actual search coil position, the finite element predicted flux-linkage was predicted for 3 search coil positions as shown in Fig. 5.35. As will be apparent in Fig. 5.36, although there is some difference, the likely contribution of coil position tolerance to the observed discrepancy between measured and predicted will be relatively small.

Foregoing investigation shows that by swapping the aluminium frame with a plastic frame, the eddy current loss in the aluminium frame can be measured. By replacing the rotor with a plastic dummy rotor, the mechanical losses, e.g. friction loss and aerodynamic loss, can also be measured. However, it is impractical to separate the loss in the permanent magnets and the iron loss. Thus, Fig. 5.37 shows the predicted open-circuit stator and rotor losses and the measured losses, which were obtained by subtracting the mechanical loss and the eddy current loss in the frame from the total loss. Overall, a relatively good agreement is achieved between the measured and predicted values.

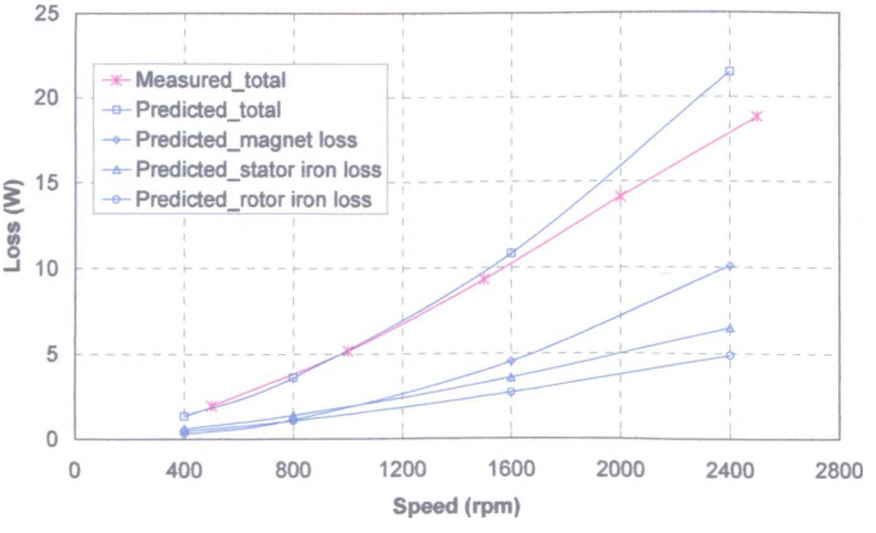

Fig. 5.37. Open-circuit stator and rotor losses in flux-switching PM machine

5.5.5. Influence of flux-weakening operation

The influence of the different operating modes on the iron loss in the flux-switching PM machine has been investigated, the resultant iron loss being shown in Fig. 5.38. Due to

the influence of the q-axis current in the constant torque region, the total iron loss increases by ~10%, compared with the iron loss on open-circuit. In the flux-weakening region the total iron loss remains almost the same as the value which results at the base-speed. As a result, when the machine reaches its maximum speed of 2400rpm, the iron loss under flux-weakening operation is only ~60% of that on open-circuit.

The iron loss has been determined separately for the stator and rotor by finite element analyses. It can be seen that, without flux-weakening, the iron loss in the stator is about 20% higher than that in the rotor. However, with flux-weakening, the flux in the stator is reduced significantly while the flux change in the rotor is relatively small. As a result, the iron loss in the stator reduces with an increase in speed, while the iron loss in the rotor gradually increases speed. Overall, when the flux-switching PM machine enters the flux-weakening operation region, the total iron loss increases only slightly, compared with the loss at base-speed.

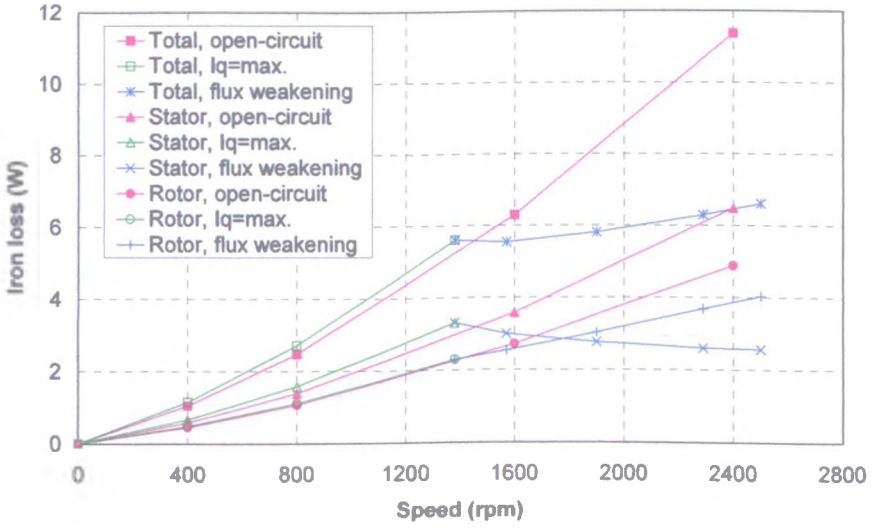

Fig. 5.38. Iron loss of flux-switching PM machine

5.6. Summary

In this chapter, the losses which occur in a flux-switching PM machine, i.e. the copper loss, the eddy current loss in the frame and permanent magnets, and the iron loss in the stator and rotor cores, have been investigated, with due account of the operating mode.

1. Only the DC copper loss is considered in this thesis; while for some high speed and low voltage application, extra AC copper loss due to skin effect and proximity effect may not be neglected. The simple coil shape has been adopted and the winding temperature factor has been considered. Since the rms current remains constant throughout the speed range, including the flux-weakening region, the copper loss does not change with the speed.

2. The eddy current loss in the aluminium frame increases with the speed during the constant torque region, and is almost constant in the flux-weakening region. Since the eddy current loss is concentrated in a small region close to the ends of the permanent magnets, by removing aluminium material in this area, the eddy current loss can be reduced.

3. In the flux-weakening region, unlike the eddy current loss in the frame, which is almost constant, the eddy current loss in the permanent magnets gradually increases with the speed, and is significantly lower than that which results on open-circuit. Since the eddy current loss is concentrated at the inner ends of the permanent magnets, it can be reduced by removing magnet material in this area, although a compromise has to be made between the reduction in the eddy current loss and the reduction in performance.

4. The iron loss in a flux-switching machine is fairly complex since the flux loci not only have a major loop, but may also have minor loops. In the flux-switching machine under consideration, ~55% of the open-circuit iron loss is in the stator, and ~45% is in the rotor. In the flux-weakening mode, the rotor iron loss increases with speed, while the stator iron loss reduces. As a result, the total iron loss only increases slightly with the speed, and is significantly lower than that which results on open-circuit.

5. Overall, in the flux-switching PM machine under consideration, the major loss component is the copper loss, which remains constant over the whole operating speed range if the rms current remains constant, while the other loss components

increase with speed, as shown in Fig. 5.39(a).

In terms of efficiency, as shown in Fig. 5.39(b), an efficiency >80% can be obtained over a wide operating speed range, from ~800rpm to ~2300rpm. The maximum efficiency of 85% occurs at ~1600rpm.

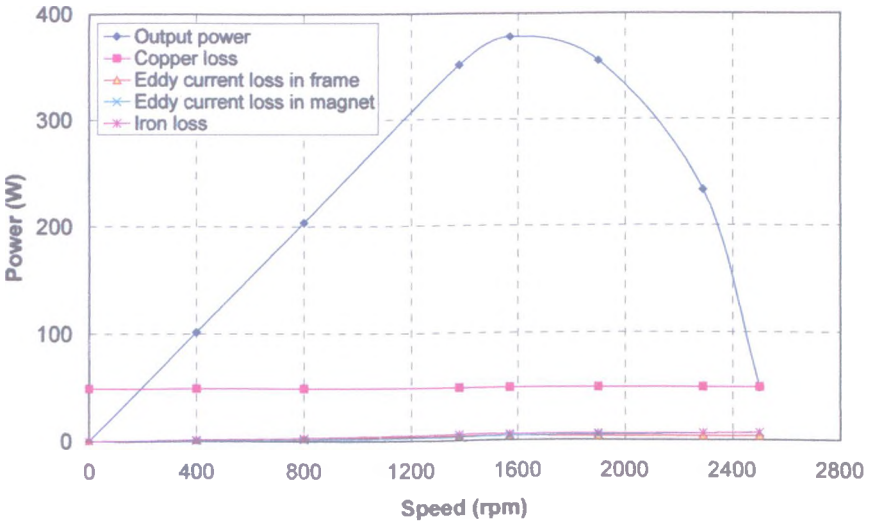

(a) Output power and losses

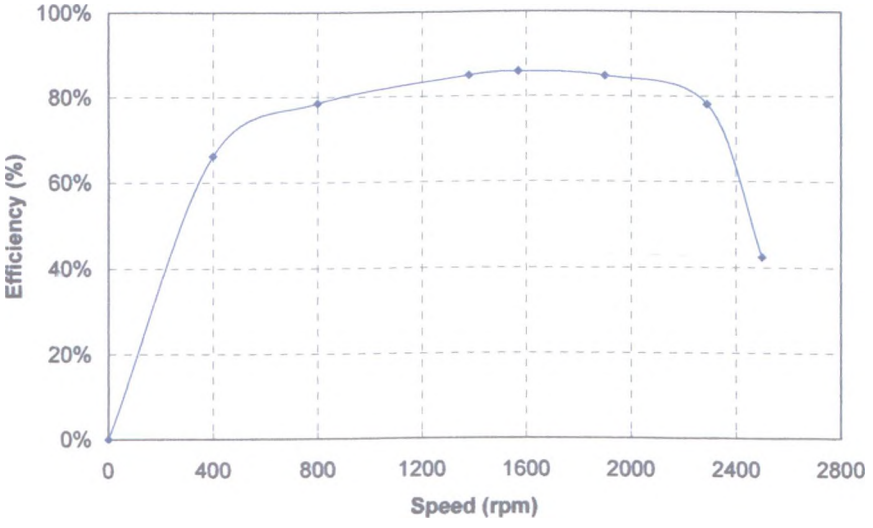

(b) Efficiency

Fig. 5.39. Performance of flux-switching PM machine

Chapter 6 General Conclusions

Compared with conventional PM brushless machines, the advantages and disadvantages of flux-switching PM machines can be summarized as follows:

Advantages:

1. Without permanent magnets in the rotor, the rotor of a flux-switching PM machine is simple and robust, similar to that of a switched reluctance machine.

2. Since the permanent magnets are located in the stator, they are in an environment in which there is greater scope to manage their thermal environment, since more precise and higher heat flux cooling methods can be applied to the stator than the rotor and the influence of heat-soak from other components can be similarly more readily managed.

3. Although the airgap field distribution in a flux-switching PM machine is far from sinusoidal, due to the unusual combination of rotor pole number and stator slot number (viz. 10:12), the phase flux-linkage and phase back-emf waveforms are essentially sinusoidal, which makes flux-switching PM machines good candidates for brushless AC drives.

Disadvantages:

1. The original flux-switching PM machine, which was used as a reference machine for the investigation which has been described, had circumferentially magnetized permanent magnets sandwiched between 'U'-shaped laminated stator segments. Although lamination bridges could be added at the outer ends of the magnets so that the stator core could be assembled from single laminations, the manufacture of flux-switching PM machine is likely to be challenging.

2. Since the permanent magnets are sandwiched between 'U'-shaped stator segments, there is significant leakage flux from the outer ends of the magnets. The variation of this leakage flux with rotor position results in an eddy current loss in the aluminium

frame.

3. The flux-switching PM machine exploits the principle of flux-switching and flux-concentration. Consequently, magnetic saturation in the stator laminations, especially the stator teeth, is usually relatively high, compared with conventional PM brushless machines, which has implications on the volume of permanent magnet material which is required.

4. Since the permanent magnets are located in the stator, the slot area is reduced significantly, compared with that in conventional PM brushless machines.

In this thesis, the design and operation of flux-switching PM machines has been studied systematically, the following investigations being carried out.

Design of Flux-switching Permanent Magnet Machine

Since only 3-phase flux-switching PM machines can offer essentially sinusoidal phase flux-linkage and phase back-emf waveforms, which are desirable for brushless AC drives, only 3-phase machines have been investigated in this thesis. Further, since the magnetic circuit of flux-switching PM machines is relatively highly saturated, the design optimization has been studied primarily by using finite element analysis. It has been shown that:

1. The original shape of the permanent magnets, i.e. rectangular cross-section, is better than tapered or stepped permanent magnets in terms of the phase flux-linkage, and therefore, the torque density.

2. Since the stator back-iron of the original flux-switching PM machine was not as saturated as the stator teeth, the output torque could be increased by ~5% when the thickness of the stator back-iron is reduced by ~30%, due to the increase of the available slot area.

3. In order to simplify manufacture of the stator, bridges could be added to connect two

'U'-shaped stator segments. However, the thickness of the bridges is a compromise between mechanical strength and electromagnetic performance considerations.

4. As long as the rotor poles provide sufficient saliency, their shape does not appear to have much influence on the torque.

The dimensional scaling of flux-switching PM machines has been studied and it has been shown that if the influence of cross-coupling from the q-axis current is neglected, the effect of scaling can be predicted by using analytical equations, e.g. if all the dimensions are scaled up by a factor of 2.62, the torque density is increased by 2.62; while when the influence of cross-coupling is taken into account, the increase in the torque density is significantly lower.

The investigation has also shown that due to 3-D end-effects, the average airgap flux density may be reduced significantly.

The output torque capabilities of flux-switching PM machines and conventional interior PM machines have been investigated in [PAN07]. The analytical results are listed in Table 6.1. It can be seen that by using optimal rotor tooth-arc, i.e. increasing rotor tooth-arc from 7.5° to 10.5°, the torque density of flux-switching PM machine can be improved by ~9%. Compared with the conventional interior PM machine, which has the same space envelope and thermal condition, Fig. 6.1, the original flux-switching PM machine has similar torque density. Hence, the flux-switching PM machine with optimized rotor tooth-arc has a higher torque density.

Table 6.1. Analytical comparison of flux-switching and interior PM machines

	FSPM 1	FSPM 2	IPM 1	IPM2
Rotor tooth/pole number	10-tooth	10-tooth	8-pole	12-pole
Stator slot number	12	12	12	18
Stator outer radius (mm)	45	45	45	45
Stator inner diameter (mm)	27.5	27.5	27.5	25.5
Stator tooth thickness (mm)	3.6	3.6	8	5
Total slot areas (mm^2)	1207	1207	1621	2140

Rotor tooth-arc (mech. deg.)	7.5°	10.5°	-	-
Max. airgap flux density (T)	-	-	0.8	0.8
Max. iron flux density (T)	1.6	1.6	1.5	1.5
Copper loss (W)	50	50	50	50
Current density (Arms/mm^2)	10	10	8.8	8.4
Output torque (Nm)	2.46	2.65	2.34	2.71
Torque density (kN/m^2)	15.4	16.6	14.7	17.0

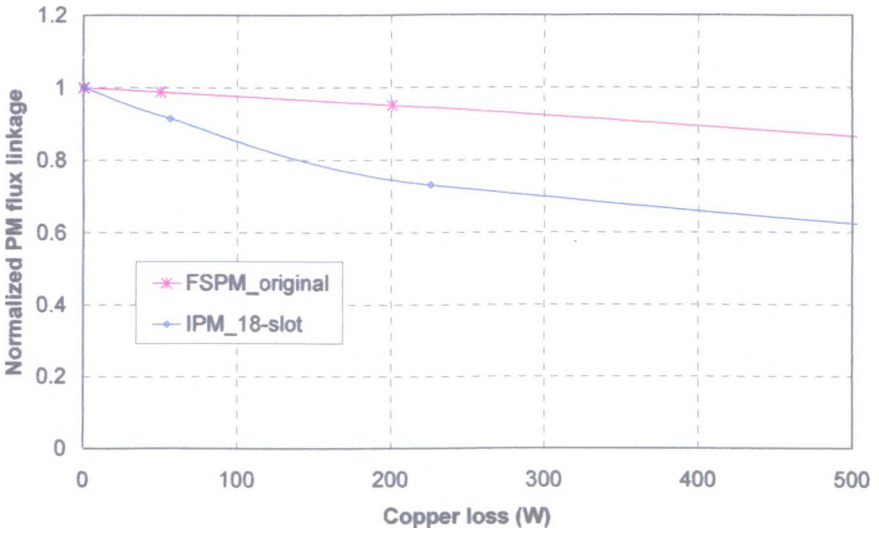

(a) Normalized PM flux linkage

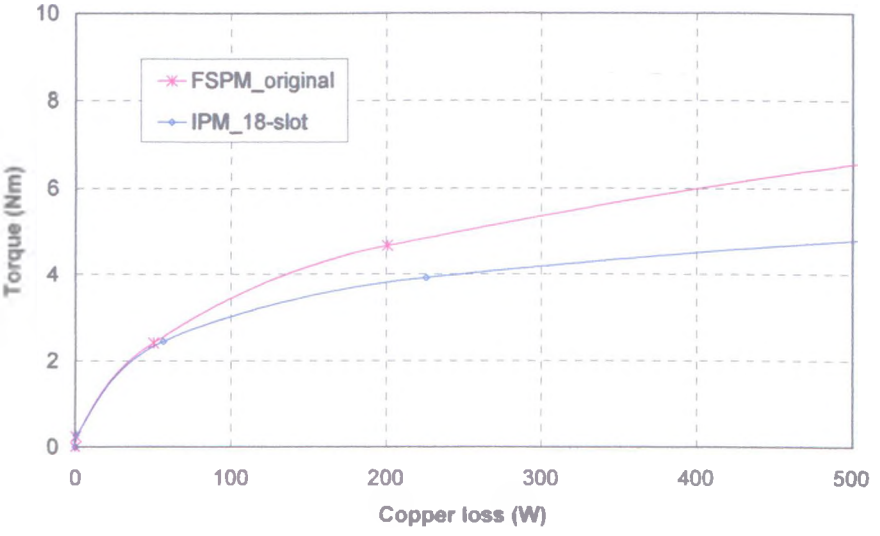

(b) Output torque

Fig. 6.1. Finite element comparison of flux-switching and interior PM machines

Non-Linear Adaptive Lumped Parameter Magnetic Circuit Model

A non-linear adaptive lumped parameter magnetic circuit model of the flux-switching PM machine has been established in order to enable the performance to be predicted quickly.

By using the model the influence of magnetic saturation, the remanence of the permanent magnets, flux leakage external to the stator core, and end-leakage flux, etc. on the electromagnetic performance can been assessed. It has been shown that:

1. Since flux-switching PM machines utilize flux concentration, the higher the magnet remanence, the better the machine performance. Of course, the volume of magnet material and the magnetic circuit design have to be carefully matched.
2. Although leakage flux external to the stator core results in an eddy current loss in the aluminium frame, its influence on the phase flux-linkage and torque is negligible.
3. Due to the relatively small ratio of axial length to stator diameter of the machine which has been considered in this thesis, i.e. axial length=25mm, outer stator diameter=90mm, 3-D end-effects were significant.

The non-linear adaptive lumped parameter magnetic circuit model which has been established has also been used for design optimization, to determine optimum dimensions, such as the stator tooth width, the rotor pole width and the split ratio.

Split Ratio of Permanent Magnet Brushless Machines

The optimal split ratio for maximum specific torque of alternative PM brushless machines topologies, i.e. conventional SPM/IPM machines and flux-switching PM machines, has been investigated.

An analytical equation for the optimal split ratio has been derived for conventional PM brushless machines, and it has been shown that:

1. For both SPM and IPM machines, the determination of the optimal split ratio depends on the nature of the airgap field distribution, irrespective of the rotor topology.
2. Both trapezoidal and sinusoidal airgap field distributions have been considered, similar equations can be used for both types of airgap field distribution.
3. Both brushless DC and AC machine machines can be considered using the same analytical equation, for the optimal split ratio for maximum torque capability.
4. Both non-overlapping and overlapping stator winding dispositions have been considered, based on appropriate winding coefficients.
5. When the end-windings are considered, the optimal split ratio is reduced, since the phase resistance will be increased.

An analytical equation for the optimal split ratio has also been derived for flux-switching PM machines, and it has been shown that:

1. The optimal split ratio increases with an increase in the slot number, due to the reduction in stator back-iron thickness and the increase in the stator slot area.
2. Similar to conventional PM brushless machines, the optimal split ratio reduces when the end-windings are considered.
3. Since the magnetic circuit of a flux-switching PM machine is generally relatively highly saturated, the optimal split ratio needs to be established by using finite element analysis, so that the influence of the magnetic and electric loadings can be considered.

Losses in Flux-switching Permanent Magnet Machine

The losses which occur in a flux-switching PM machine have been investigated systematically.

1. The copper loss is calculated with due account for the shape and the size of the stator coils, and remains constant throughout the operating speed range, including the flux-weakening mode, if the rms current remains unchanged.

2. The eddy current loss in the aluminium frame increases with the speed in the constant torque region, but in the flux-weakening region, the loss remains almost constant. Since the loss is concentrated in localized regions close to the outer ends of the magnets, the eddy current loss can be reduced by introducing slots in the frame.

3. Similarly, the eddy current loss in the permanent magnets increases with speed in the constant torque region, but reduces in the flux-weakening region, although it gradually increases with the speed. Since the loss is concentrated at the inner ends of the magnets, the eddy current loss can be reduced by shortening the magnets. However, a compromise needs to be made between the eddy current loss in permanent magnet and the performance of the flux-switching PM machine.

4. The stator iron loss increases significantly with the speed in the constant torque region, but reduces significantly when the machine is operated in the flux-weakening mode. However, the iron loss in the rotor laminations increases with the speed. As a result, the total iron loss is increased slightly.

Future Work:

Due to time constraints, the investigation which is reported in this thesis has been restricted to the electromagnetic performance of 3-phase, radial-field, flux-switching PM machines. It has not been possible to cover all the important issues related to such flux-switching PM machines, such as mechanical stress analysis - in order to highlight the advantage of the simple rotor structure, thermal analysis - in order to demonstrate the advantage of having the magnets on the stator; single-phase flux-switching machines for low cost applications, flux-switching generators, hybrid excited machine designs, and alternative machine topologies, etc. However, some of these issues are currently

being addressed by members of the Electrical Machines and Drives Group at the University of Sheffield.

REFERENCES

[AKE00] D. A. Akemakou, "Rotary electric machine, especially an alternator for a motor vehicle," US patent 6051904, April 18 2000.

[AKE01] D. A. Akemakou, "Brushless polyphased machine, in particular motor vehicle alternator," US patent 6242834, June 5 2001.

[AMA03] Y. Amara, E. Hoang, M. Gabsi, M. Lecrivain, and S. Allano, "Design and comparison of different flux-switch synchronous machines for an aircraft oil breather application," Proceedings of 2nd IEEE International Conference on Signals, Systems, Decision and Information Technology, March 26-28 2003.

[ATA00] K. Atallah, D. Howe, P. H. Mellor, and D. A. Stone, "Rotor loss in Permanent-Magnet Brushless AC Machines," IEEE Transactions on Industry Applications, Vol.36, No.6, pp.1612-1618, November/December 2000.

[ATA98] K. Atallah, and D. Howe, "The application of Halbach cylinders to brushless AC servo motors," IEEE Transactions on Magnetics, Vol.34, No.4, pp.2060-2062, July 1998.

[AYD01] M. Aydin, S. R. Huang, and T. A. Lipo, "Torque quality and comparison of internal and external rotor axial flux surface-magnet disc machines," 27th Annual Conference of the IEEE Industrial Electronics Society. Conference Publication pp.1428-1434, 2001.

[BER87] G. Bertotti, "Principles of characterization and classification of power losses on soft metallic ferromagnetic materials," Proceedings of the International Symposium on Physics of Magnetic Materials, pp.422, Sendai 1987.

[BIA02] N. Bianchi, and A. Canova, "FEM analysis and optimization design of an

IPM synchronous motor," Power Electronics, Machines and Drives, April 2002, Conference Publication No. 487, pp.49-54, 2002.

[BIN93] K. J. Binns, F. B. Chaaban, and A. A. K. Hameed, "Major design parameters of a solid canned permanent magnet motor with skewed magnets," IEE Proceedings-B, Vol.140, No.3, pp.161-165, May 1993.

[BIN96] K. J. Binns, and D. W. Shimmin, Relationship between rated torque and size of permanent magnet machines," IEE Proceedings on Electrical Power Applications, Vol.143, No.6, pp.417-422, November 1996.

[BOL90] H. R. Bolton, and Y. Shakweh, "Performance prediction of Laws's relay actuator," IEE Proceedings, Vol.137, Pt. B, No.1, pp.1-13, January 1990.

[CAL01] S. D. Calverley, "Design of a High Speed Switched Reluctance Machine for Automotive Turbo-Generator Applications," Ph.D Thesis, the University of Sheffield, 2001.

[CAV02] A. Cavagnino, M. Lazzari, F. Profumo, and A. Tenconi, "A comparison between the axial flux and the radial flux structures for PM synchronous motors," IEEE Transactions on Industry Applications, Vol.38, No.6, pp.1517-1524, November/December 2002.

[CHA00] F. B. Chaaban, and A. EL-HAJJ, "A cost-effective design approach for permanent magnet brushless machines," Electric Machines and Power Systems, 28, 2000, pp.893-900.

[CHA94] F. B. Chaaban, "Determination of the optimum rotor/stator diameter ratio of permanent magnet machines," Electric Machines and Power Systems, 22, pp.521-531, 1994.

[CHA98] B. J. Chalmers, R. Akmese, and L. Musaba, "Design and field-weakening performance of permanent-magnet/reluctance motor with two-part rotor," IEE Proceedings of Electrical Power Applications, Vol.145, No.2, pp.133-139, March 1998.

[CHA99] B. J. Chalmers, and R. Akmese, "Synchronous machines with inset surface NdFeB magnets," Journal of Magnetism and Magnetic Materials, Vol.196-197, pp.277-279, 1999.

[CHE00] M. Cheng, K. T. Chau, C. C. Chan, E. Zhou, and X. Huang, "Nonlinear varying-network magnetic circuit analysis for doubly salient permanent-magnet machines," IEEE Transactions on Magnetics, Vol.36, No.1, pp.339-348, 2000.

[CHE01] M. Cheng, K. T. Chau, and C. C. Chan, "Static characteristics of a new doubly saliency permanent magnet machine," IEEE Transaction on Energy Conversion, Vol.16, No.1, pp.20-25, 2001.

[CHE05] Y. Cheng, C. Pollock, and H. Pollock, "A permanent magnet flux switching motor for low energy axial fans," Proc. IEEE Ind. Appl. Soc. Annual Meeting, Vol. 3, pp. 2168-2175, 2005.

[CHE06] Y. Chen, Z. Q. Zhu, D. Howe, and Y. Y. Ye, "Starting torque of single-phase flux-switching Permanent magnet motors," IEEE Transactions on Magnetics, Vol.42, No.10, pp.3416-3418, October 2006.

[CRO02] J. Cros, and P. Viarouge, "Synthesis of high performance PM motors with concentrated windings," IEEE Transactions on Energy Conversion, Vol.17, No.2, pp.248-253, June 2002.

[CRO98] J. Cros, P. Viarouge, and C. Gelinas, "Design of PM brushless motors using iron-resin composites for automotive applications," 33rd Industry Applications Conference Annual Meeting, October 1998, Vol.1, pp.5-11, 1998.

[DEO96] R. P. Deodhar, S. Adnersson, I. Boldea, and T. J. E. Miller, "The flux-reversal machines: anew brushless doubly-salient permanent-magnet machine," 31st Industry Application Society Annual Meeting, October 1996, V ol.2, pp.786-793, 1996.

[DEO97] R. P. Deodhar, S. Andersson, I. Boldea, and T. J. E. Miller, "The flux-reversal machine: a new brushless doubly-salient permanent-magnet machine," IEEE Transactions on Industry Applications, Vol.33, No.4, pp.925-934, 1997.

[EDE01] J. D. Ede, Z. Q. Zhu, and D. Howe, "Optimal split ratio for high-speed permanent magnet brushless DC motors," Proceeding of International Conference on Electrical Machines and Systems, Shenyang, China, pp.909-912, 2001.

[EL04] A. M. El-Refaie, and T. M. Jahns, "Optimal flux weakening in surface PM machines using concentrated windings," 39th Industry Application Conference Annual Meeting, Conference, October 2004 Publication Vol.2, pp.1038-1047, 2004.

[FIT92] A. E. Fitzgerald, C. Kingsley, and Jr, S. D. Umans, "Electric Machinery," McGraw-Hill Book Company, 1992.

[FUR97] E. P. Furlani, and M. A. Knewtson, "A three-dimensional field solution for permanent-magnet axial-field motors," IEEE Transactions on magnetics, Vol.33, No.3, pp.2322-2325, May 1997.

[HAL80] K. Halbach, "Design of permanent multipole magnets with oriented rare earth cobalt material. Nuclear Instruments and Methods," Vol.168, pp.1-10, 1980.

[HEC74] C. Heck, "Magnetic materials and their applications," Butterworths, London, 1974.

[HEN94] G. Henneberger, S. Domack, and J. Berndt, "Comparison of the utilization of brushless DC servomotors with different rotor length by 3D-finite element analysis," IEEE Transactions on Magnetics, Vol.30, No.5, pp.3675-3678, September 1994.

[HEN94] G. Henneberger, J. R. Hadji-Minaglou, and R. C. Ciorba, "Design and tests of a permanent magnet synchronous motor with auxiliary excitation winding for electric vehicle application," European Power Electronics Chapter Symposium, Electric Drive Design and Applications, pp.645-649, 1994.

[HES87] D. E. Hesmondhalgh, D. Tipping, and M. Amrani, "Design and construction of a high-speed high-performance direct-drive handpiece," IEE Proceedings, Pt.B, 134(6), pp.286-296, 1987.

[HOA00] E. Hoang, M. Gabsi, M. Lecrivain, and B. Multon, "Influence of magnetic losses on maximum power limits of synchronous permanent magnet drives in flux-weakening mode," Proceedings of IEEE Industry Applications Society Annual Conference. Vol.1, pp.299-303, 2000.

[HOA97] E. Hoang, A. H. Ben-Ahmed, and J. Lucidarme, "Switching flux permanent magnet polyphased synchronous machines," 7th European Conference on Power Electronics and Applications, Vol.3, pp.903-908, 1997.

[HON87] V. B. Honsinger, "Sizing equations for electrical machinery" IEEE Transactions on Energy Conversion, Vol.EC-2, No.1, pp.116-121, March 1987.

[HUA05] W. Hua, Z.Q. Zhu, M. Cheng, Y. Pang, and D. Howe, "Comparison of flux-switching and doubly-salient permanent magnet brushless machines," Proc. Eighth International Conference on Electrical Machines and Systems – September 27 ~ 29, 2005, Nanjing, China, pp.165-170, 2005.

[HUA07] W. Hua, "Analysis, design and control of a novel flux-switching permanent magnet machine," PhD thesis, School of Electrical Engineering, Southeast University, China. January 19, 2007.

[HUA98] S. Huang, J. Luo, F. Feonardi, and T. A. Lipo, "A general approach to sizing and power density equations for comparison of electrical machines," IEEE Transactions on Industry Applications, Vol.34, No.1, pp.92-97, January/February 1998.

[HUA99] S. Huang, J. Luo, F. Leonardi, and T. A. Lipo, "A comparison of power density for axial flux machines based on general purpose sizing equations," IEEE Transactions on Energy Conversion, Vol.14, No.2, pp.185-192, June 1999.

[ISH04] D. Ishak, Z. Q. Zhu, and D. Howe, "High torque density permanent magnet brushless machines with similar slot and pole numbers," Journal of Magnetism and Magnetic Materials, Vol.272-276, pp.1767-1769, 2004.

[ISH05] D. Ishak, Z.Q. Zhu, and D. Howe, "Permanent magnet brushless machines with unequal tooth widths and similar slot and pole numbers," IEEE Transactions of Industry Applications, Vol.41, No.2, pp.584-590, March/April 2005.

[JAH01] T. M. Jahns, and V. Blasko, "Recent advances in power electronics technology for industrial and traction machine drives," Proceeding of the IEEE, Vol. 89, No.6, pp.963-975, June 2001.

[JAH86] T. M. Jahns, G. B. Kliman, and T. W. Neumann, "Interior permanent-magnet synchronous motors for adjustable-speed drives," IEEE Transactions on Industry Applications, Vol.22, No.4, pp.738-747, July/August 1986.

[JAH87] T. M. Jahns, "Flux-Weakening Regime Operation of an Interior Permanent-Magnet Synchronous Motor Drive," IEEE Transactions on Industry Applications, Vol.IA-23, No.4, pp.681-689, July/August 1987.

[JAH94] T. M. Jahns, "Motion control with permanent-magnet AC machines," Proceedings of the IEEE, Vol.82, No.8, pp.1241-1252, August 1994.

[JAH96] T. M. Jahns, and W. L. Soong, "Pulsating torque minimization techniques for permanent magnet AC motor drives – a review," IEEE Transactions on Industry Applications, Vol.43, No.2, pp.321-330, April 1996.

[JAM03] J. Jamali, "End effect in linear induction and rotating electrical machines," IEEE Transactions on Energy Conversion, Vol.18, No.3, pp.440-447, September 2003.

[KAM05] M. Kamiya, "Development of Traction Drive Motors for the Toyota Hybrid System," Toyota-cho, Toyota, Aichi, 471-8571 Japan.

[KEN85] T. Kenjo, "Electric motors and their controls: an introduction," Oxford University Press, 1985.

[KIM04] T. H. Kim, and J. Lee, "A study of the design for the flux reversal machine," IEEE Transactions on Magnetics, Vol.40, No.4, pp.2053-2055, July 2004.

[KIM05] T. H. Kim, K. B. Jang, Y. D. Chun, and J. Lee, "Comparison of the caracteristics of a flux reversal mchine under the different driving methods," IEEE Transactions on Magnetics, Vol.41, No.5, pp.1916-1919, May 2005.

[LEO96] F. Leonardi, T. Matsuo, Y. Li, T. A. Lipo, and P. McCleer, "Design considerations and test results for a doubly salient PM motor with flux control," Proceedings of IEEE Industry Applications Society Annual Meeting 1996, Vol.1, pp.458-463, 1996.

[LI03] Y. Li, J. B. Zou, and Y. P. Lu, "Optimum design of magnet shape in permanent-magnet synchronous motors," IEEE Transactions on Magnetics, Vol.39, No.6, pp.3523-3526, November 2003.

[LI95] Y. Li, and T. A. Lipo, "A doubly salient Permanent magnet motor capable of field weakening," Proceedings of IEEE Power Electronics Specialists

Conference, Vol.1, pp.565-571, 1995.

[LI96] Y. Li, J.D. Lloyd, and G.E. Horst, "Switched reluctance motor with dc assisted excitation," Proceedings of IEEE Industry Applications Society Annual Meeting 1996, Vol.2, pp.801-807, 1996.

[LIA92] Y. F. Liao, F. Liang, and T. A. Lipo, "A novel permanent magnet motor with doubly salient structure," Industry Application Society Annual Meeting, October 1992, Vol.1, pp.308-314, 1992.

[LIA94] F. Liang, Y. Liao, and T.A. Lipo, "A new variable reluctance motor utilizing an auxiliary commutation winding," IEEE Transactions on Industry Applications, Vol.30, No.2 pp.423-432, 1994.

[LIA95] Y. Liao, F. Liang, and T. A. Lipo, "A novel permanent magnet machine with doubly saliency structure," IEEE Transactions on Industry Applications, Vol.3, No.5, pp.1069-1078, 1995.

[LIN98] J. Lindstrom, J. Luomi, and J. Hellsing. "Permanent magnet motor for a hybrid electric vehicle," 1998 IEEE Nordic Workshop on Power and Industrial Electronics, Espoo Finland, pp. 200-205, August 1998.

[LOV02] E. C. Lovelance, T. M. Jahns, and J. H. Lang, "A saturating lumped-parameter model for an interior PM synchronous machine,". IEEE Transactions on Industry Applications, Vol. 38, No.3, pp.645-650, 2002.

[LOV98] E. C. Lovelace, T. M. Jahns, J. L. Kirtley Jr., and J. H. Lang, "An Interior PM Starter/Alternator for Automotive Applications," ICEM 1998, pp.1802-1808, 1998.

[LOW97] T. S. Low, M. A. Jabbar, and T. S. Tan, "Slotless PM motor design for hard disk drives," IEEE Industry Applications Magazine, pp.43-51, November/December 1997.

[MAR92] M. Marinescu, and N. Marinescu, "New concept of permanent magnet excitation for electrical machines," Analytical and numerical computation. IEEE Transactions on Magnetics, Vol.28, No.2, pp.1390-1393, March 1992.

[MEC96] B. C. Mecrow, A. G. Jack, J. A. Haylock, and J. Coles, "Fault-tolerant permanent magnet machine drives," IEE Proceedings of Electrical Power Applications, Vol.143, No.5, pp.437-442, November 1996.

[MIL91] T. J. E. Miller, A. Hutton, C. Cossar, and D. A. Staton, "Design of a synchronous reluctance motor drive," IEEE Transactions on Industry Applications, Vol.27, No.4, pp.741-749, July/August 1991.

[MIL94] T. J. E. Miller, and R. Rabinovici, "Back-EMF waveforms and core losses in brushless DC motors," IEE Proceedings of Electric Power Applications, Vol.141, No.3, pp.144-154, May 1994.

[MIW04] M. Miwa, D. Dibben, T. Yamada, „High accuracy torque calculation for a rotating machine using adaptive meshing," IEEE Transactions on Magnetics, Vol.40, No.2, pp.1001-1004, March 2004.

[MOR90A] S. Morimoto, Y. Takeda, and T. Hirasa, "Current phase control methods for permanent magnet synchronous motors," IEEE Transactions on Power Electronics, Vol.5, No.2, pp.133-139, April 1990.

[MOR90B] S. Morimoto, Y. Takeda, T. Hirasa, and K. Taniguchi, "Expansion of operating limits for permanent magnet motor by current vector control considering inverter capacity," IEEE Transactions on Industry Applications, Vol.26, No.5, pp.866-871, September/October 1990.

[MUR01] H. Murakami, H. Kataoka, Y. Honda, S. Morimoto, and Y. Takeda, "Highly efficient brushless motor design for an air conditioner of the next generation 42V vehicle," IEEE Industry Applications Society Annual Meeting, pp.461-466, 2001.

[MUR99] H. Murakami, Y. Honda, H. Kiriyama, S. Morimoto, and Y. Takeda, "The Performance Comparison of SPMSM, IPMSM and SynRM in Use as Air-conditioning Compressor," 34th IAS 1999, Vol.2, pp.840-845, 1999.

[NG96] K. Ng, Z. Q. Zhu, and D. Howe, "Open-circuit field distribution in a brushless motor with diametrically magnetized PM rotor, accounting for slotting and eddy current effects," IEEE Transactions on Magnetics, Vol.32, No.5, pp.5070-5072, September 1996.

[PAN07] Y. Pang, Z. Q. Zhu, D. Howe, S. Iwasaki, R. Deodhar, A. Pride, "Comparative Study of Flux-Switching and Interior Permanent Magnet Machines," International Conference on Electrical Machines and Systems, South Korea, 2007.

[PAR01] A. Parviainen, J. Pyrhonen, and M. Niemela, "Axial flux interior permanent magnet synchronous motor with sinusoidally shaped magnets," 10th International Symposium on Electromagnetic Fields in Electrical Engineering, pp.1-10, September 2001.

[PLA89] D. Platt, "Permanent magnet synchronous motor with axial flux geometry," IEEE Transactions on Magnetics, Vol.25, No.4, pp.3076-3079, July 1989.

[POL99] C. Pollock, and M. Wallace, "The flux-switching motor, a DC motor without magnets or brushes," Proceedings of IEEE Industry Applications Society Annual Meeting 1999, pp.1980-1987, 1999.

[RAU55] S. E. Rauch, and L. J. Johnson, "Design principles of flux-switching alternators," AIEE Transactions Vol.74 No.3, pp.1261-1268, 1955.

[RIC85] E. Richter, T. J. E. Miller, T. W. Neumann, and T. L. Hudson, "The ferrite permanent magnet AC motor – a technical and economical assessment," IEEE Transactions on Industry Applications, Vol.IA-21, No.4, pp.644-650, May/June 1985.

[SAG84] M. Sagawa, S. Fugimura, N. Togawa, H. Yamamoto, and Y. Maysuura, "New magerial for permanent magnets on a base of Nd and Fe," Journal of Applied Physics., Vol.55, No.6, pp.2083-2087, 1984.

[SAR94] B. Sarlioglu, Y. F. Zhao, and T. A. Lipo, "A novel doubly salient single phase permanent magnet generator," Industry Application Society Annual Meeting, October 1994, Vol.1, pp.9-15, 1994.

[SLE94] G. R. Slemon, "Electrical machines for variable-frequency drives," Proceedings of the IEEE, Vol.82, No.8, pp.1123-1139, August 1994.

[SNE85] B. Sneyers, D. W. Novotny, and T. A. Lipo, "Field Weakening in Buried Permanent Magnet AC Motor Drives," IEEE Transactions on Industry Applications, Vol.IA-21, No.2, pp.398-407, March/April 1985.

[SOO94] W. L. Soong, and T. J. E. Miller, "Field-weakening performance of brushless synchronous AC motor drives," IEE Proceedings of Electrical Power Applications, Vol.141, No.6, pp.331-340, November 1994.

[SPO92] E. Spooner, and B. J. Chalmers, "'TORUS': a slotless, toroidal-stator, permanent-magnet generator," IEE Proceedings-B, Vol.139, No.6, pp.497-506, November 1992.

[SPO96] E. Spooner, and A. C. Williamson, "Direct coupled, permanent magnet generators for wind turbine applications" IEE Proceedings of Electrical Power Applications, Vol.143, No.1, pp.1-8, January 1996.

[STR99] R. J. Strahan, and D. B. Watson, "Effects of Airgap and Magnet Shapes on Permanent Magnet Reluctance Torque," IEEE Transactions on Magnetics, Vol.35, No.1, pp.536-542, January 1999.

[THE98] P. Thelin, and H. P. Nee, "Analytical calculation of the airgap flux density of PM motors with buried magnets," International Conference on Electric Machine, Istanbul Turkey, Conference Publication Vol.2, pp.1166-1171,

September 1998.

[VAG96] A. Vagati, A. Fratta, G. Franceschini, and P. Rosso, "AC motors for high-performance drives: a design-based comparison," IEEE Transactions on Industry Applications, Vol.32, No.5, pp.1211-1219, September/ October 1996.

[WAN02] Y. Wang, K. T. Chau, C. C. Chan, and J. Z. Jiang, "Transient analysis of a new outer-rotor permanent-magnet brushless DC drive using circuit-field-torque coupled time-stepping finite-element method. IEEE Transactions on Magnets, Vol.38, No.2, pp.1297-1300, March 2002.

[WAN99] C. Wang, S. A. Nasar, and I. Boldea, "Three-phase flux reversal machine (FRM)," IEE Proceedings of Electrical Power Applications, Vol.146, No.2, pp.139-146, March 1999.

[XIA04] Z. P. Xia, Z. Q. Zhu, and D. Howe, "Analytical magnetic field analysis of Halbach magnetized permanent magnet machines" IEEE Transactions on Magnetics, Vol.40, No.4, pp.1864-1872, July 2004.

[YAN00] Y. P. Yang, and T. C. Chiao, "Multiobjective optimal design of a high speed brushless DC motor," Electric Machines and Power Systems, Vol.28, pp.13-20, 2000.

[ZHU00] Z. Q. Zhu, Z. P. Xia, K. Atallah, G. W. Jewell, and D. Howe, "Powder alignment system for anisotropic bonded NdFeB Halbach cylinders," IEEE Transactions on Magnetics, Vol.36, No.5, pp.3349-3352, September 2000.

[ZHU01] Z. Q. Zhu, and D. Howe, "Halbach permanent magnet machines and applications: a review," IEE Proceedings of Electric Power Applications, Vol.148, No.4, pp.299-308, July 2001.

[ZHU02A] Z. Q. Zhu, D. Howe, and C. C. Chan, "Improved analytical model for predicting the magnetic field distribution in brushless permanent-magnet

machines," IEEE Transactions on Magnetics, Vol.38, No.1, pp.229-238, January 2002.

[ZHU02B] Z. Q. Zhu, Y. S. Chen, and D. Howe, "Iron loss in permanent-magnet brushless AC machines under maximum torque per ampere and flux weakening control," IEEE Transactions on Magnetics, Vol.38, No.5, pp.3285-3287, September 2002.

[ZHU02C] Z. Q. Zhu, Z. P. Xia, and D. Howe, "Comparison of Halbach magnetized brushless machines having discrete magnet segments or single ring magnet," IEEE Transactions on Magnetics, Vol.38, pp.2997-2999, 2002.

[ZHU04] Z. Q. Zhu, K. Ng, N. Schofield, and D. Howe, "Improved analytical modeling of rotor eddy current loss in brushless machines equipped with surface-mounted permanent magnets," IEE Proceedings of Electric Power Applications, Vo.151, No.6, pp.641-650, November 2004.

[ZHU05] Z. Q. Zhu, Y. Pang, D. Howe, S. Iwasaki, R. Deodhar, and A. Pride, "Analysis of electromagnetic performance of flux-switching permanent magnet machines by non-linear adaptive lumped parameter magnetic circuit model," IEEE Transaction on Magnetics, Vol.41, No.11, pp.4277-4287, 2005.

[IWA08] S. Iwasaki, R. Deodhar, Z.Q. Zhu, D. Howe, "Influence of PWM on the Proximity Loss in Permanent Magnet Brushless AC Machines", IAS 2008 to be published.

[ZHU97] Z. Q. Zhu, K. Ng, and D. Howe, "Design and analysis of high-speed brushless permanent magnet motors," Proceeding of International Conference on Electrical Machines and Drives, Cambridge, UK, pp.381-385, 1997.

PUBLICATIONS

Journal papers:

1. Y. Pang, Z. Q. Zhu, and D. Howe, "Self-shielding magnetized vs. shaped parallel-magnetized PM brushless AC motors," Korea International Transactions on Electrical Machinery and Energy Conversion Systems, Vol.5-B, No.1, pp.13-19, 2005.

2. Y. Pang, Z. Q. Zhu, and D. Howe, "Analytical determination of optimal split ratio for permanent magnet brushless motors," IEE Proceeding on Electric Power Applications, Vo.153, No.1, pp.7-13, January 2006.

3. Z. Q. Zhu, Y. Pang, D. Howe, S. Iwasaki, R. Deodhar, and A. Pride, "Analysis of electromagnetic performance of flux-switching permanent magnet machines by non-linear adaptive lumped parameter magnetic circuit model," IEEE Transactions on Magnetics, Vol.41, No.11, pp.4277-4287, November 2005.

4. Y. Pang, Z. Q. Zhu, D. Howe, S. Iwasaki, R. Deodhar, and A. Pride, "Eddy current loss in the frame of a flux-switching permanent magnet machine," IEEE Transactions on Magnetics, Vol.42, No.10, pp.3413-3415, October 2006.

5. Z.Q. Zhu, Y. Pang, W. Hua, M. Cheng, and D. Howe, "Investigation of end-effect in PM brushless machines having magnets in the stator," J. Applied Physics, Vol.99, No.8, 08R319, 1-3, April 2006.

Conference papers:

1. Y. Pang, Z. Q. Zhu, and D. Howe, "Optimal split ratio for permanent magnet brushless motors," International Conference on Electrical Machines and Systems, China, Vol.1, pp.128-131, 2003.

2. Y. Pang, Z. Q. Zhu, D. Howe, and S. Ruangsinchaiwanich, "Comparison of Halbach

magnetized PM motor and conventional surface-mounted PM motor with magnet shaping," Proc. 18th Int. workshop on high performance magnets and their applications, 29 August – 2 September 2004, Annecy, France, pp.400-407.

3. Y. Pang, Z. Q. Zhu, and D. Howe, "Halbach magnetised vs shaped parallel magnetised PM brushless ac motors," Int. Conf. on Electrical Machines and Systems, 2-5 November 2004, Korea. Paper No. ON-05 (421-M06-020), Digest Book: p.340, CDROM, Full paper: 4 pages. (Best paper award, recommended for journal publication)
4. W. Hua, Z.Q. Zhu, M. Cheng, Y. Pang, and D. Howe, "Comparison of flux-switching and doubly-salient permanent magnet brushless machines," Proc. Eighth International Conference on Electrical Machines and Systems – September 27 ~ 29, 2005, Nanjing, China, pp.165-170.
5. Z. Q. Zhu, Y. Pang, W. Hua, M., Cheng, D. and Howe, "Investigation of end-effect in PM brushless machines having magnets in the stator," Proc. 50th Annual Conf. on Magnetism and magnetic Materials, San Jose, CA, USA, 30 Oct.- 3 Nov. 2005, paper GW-08.
6. Y. Pang, Z. Q. Zhu, D. Howe, S. Iwasaki, R. Deodhar, A. Pride, "Eddy current loss in the frame of a flux-switching permanent magnet machine," Proc. Intermag2006, 8-12 May 2006, San Diego, California, USA, paper no: CS-01.
7. Y. Pang, Z. Q. Zhu, D. Howe, S. Iwasaki, R. Deodhar, A. Pride, "Comparative Study of Flux-Switching and Interior Permanent Magnet Machines," International Conference on Electrical Machines and Systems, South Korea, 2007.
8. Z. Q. Zhu, J. T. Chen, Y. Pang, D. Howe, S. Iwasaki, R. Deodhar, "Modelling of End-Effect in Flux-Switching Permanent Magnet Machine," International Conference on Electrical Machines and Systems, South Korea, 2007.

The Best Paper Award

The Board of Directors of Technical Program Committee

recognizes

Y.Pang, Z. Q. Zhu, D. Howe (Univ. of Sheffield., UK)

"Halbach magnetized vs Shaped Parallel Magnetized PM Brushless AC Motors"

as the best paper

presented at the International Conference on Electrical Machines and Systems 2004 (ICEMS 2004)

November, 3, 2004

Prof. Soo-Hyun Baek

General Chairman

ICEMS 2004, Jeju, Korea, October 31- November 3, 2004

APPENDIX I FLUX-SWITCHING PM BRUSHLESS MACHINE

Table A.I. Design data and specification of flux-switching PM brushless machine

Number of phases	m	3
Number of rotor poles	p	10
Number of stator slots	N_s	12
Angle of rotor pole	θ_p	7.5° for motor 1 10.5° for motor 2
Outer radius of stator	R_{so}	45mm
Inner radius of stator	R_{si}	27.5mm
Airgap length	g	0.5mm
Active axial length	L_a	25mm
Number of turns per phase	N_w	72
Diameter of coil	D_{coil}	1.19mm
Slot packing factor	K_s	0.4
Magnet remanence	B_r	1.2T
Magnet relative permeability	μ_r	1.05
Magnet coercivity	H_c	-909.46kA/m
DC voltage	V_{DC}	36V
Phase current (rms)	I_a	11A
Rated torque	T_N	2.2Nm for motor 1 2.4Nm for motor 2
Rated speed	n_N	400rpm
Stator and rotor lamination material		TRANSIL315
Lamination thickness	b_{iron}	0.35mm

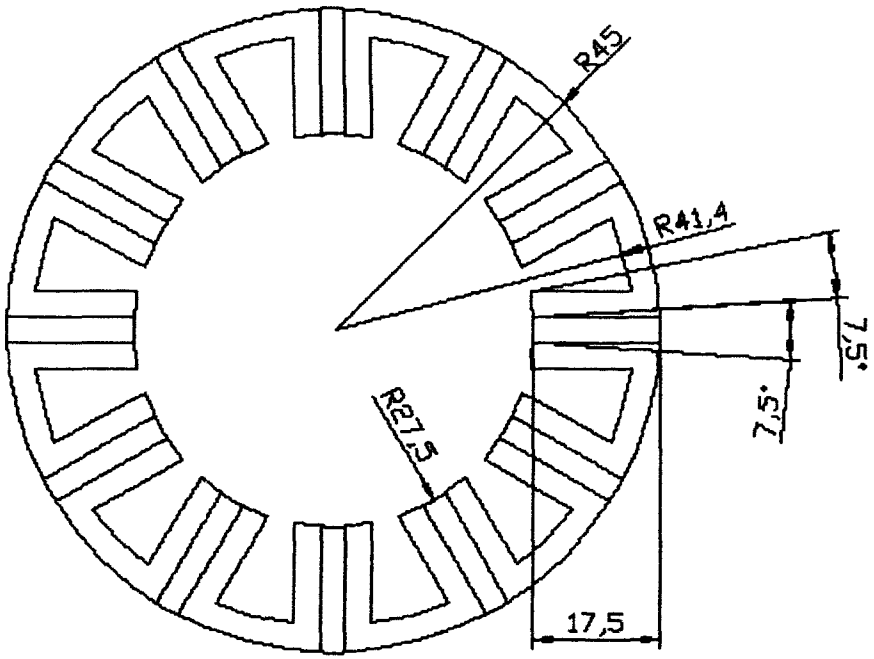

Axial length = 25mm
Number of turns per coil = 18
Number of coils per phase = 4
Conductor diameter = 1.1931mm

Magnet

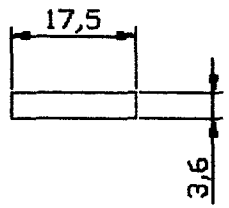

Number of magnet = 12
Br=1.2T

Stator_1
IMRA
By: Yong Pang
June 2004

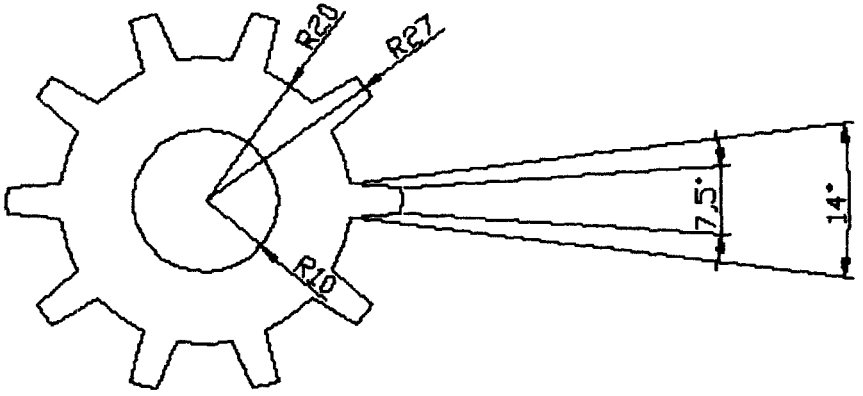

Axial length = 25mm

Rotor_1
IMRA
By: Yong Pang
June 2004

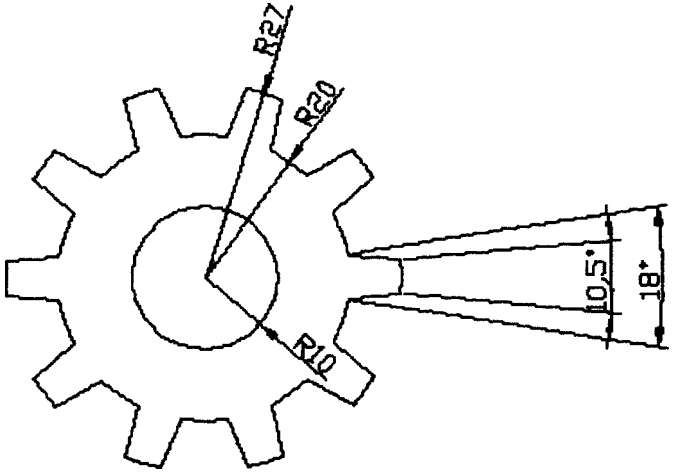

Axial length = 25mm

Rotor_2
IMRA motor
By: Yong Pang
June 2004

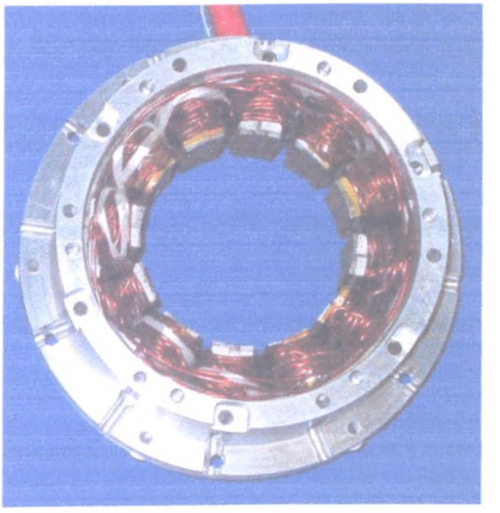

(a) Wound stator

(b) Rotor with pole=7.5°

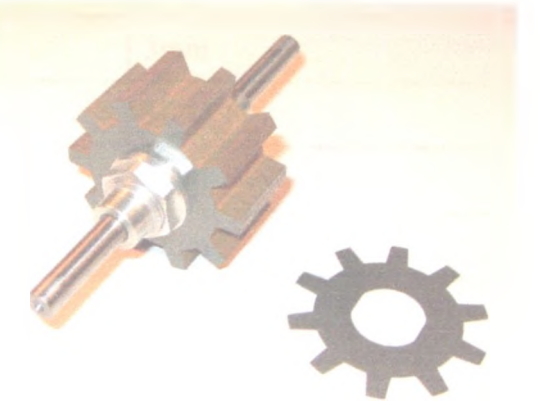

(b) Rotor with pole=10.5°

Fig. A.I. Flux-switching PM brushless machine

APPENDIX II SPM BRUSHLESS MACHINE WITH OPTIMAL SPLIT RATIO

Table A.II. Design data and specification of SPM brushless machine

Number of phases	m	3
Number of rotor pole-pairs	p	2
Number of stator slots	N_s	6
Outer radius of stator	R_{so}	45mm
Inner radius of stator	R_{si}	20.25mm
Airgap length	g	0.8mm
Thickness of permanent magnet	h_m	3mm
Outer radius of rotor	R_{ro}	16.45
Active axial length	L_a	50mm
Slot opening	b_0	4mm
Tooth tip height	h_0	4mm
Number of turns per phase	N_w	120
Diameter of coil	D_{coil}	1.2mm
Slot packing factor	K_s	0.4
Magnet remanence	B_r	1.2T
Magnet relative permeability	μ_r	1.05
Magnet coercivity	H_c	-909.46kA/m
DC voltage	V_{DC}	36V
Phase current (rms)	I_a	5.7A
Rated torque	T_N	3.2Nm
Rated speed	n_N	400rpm

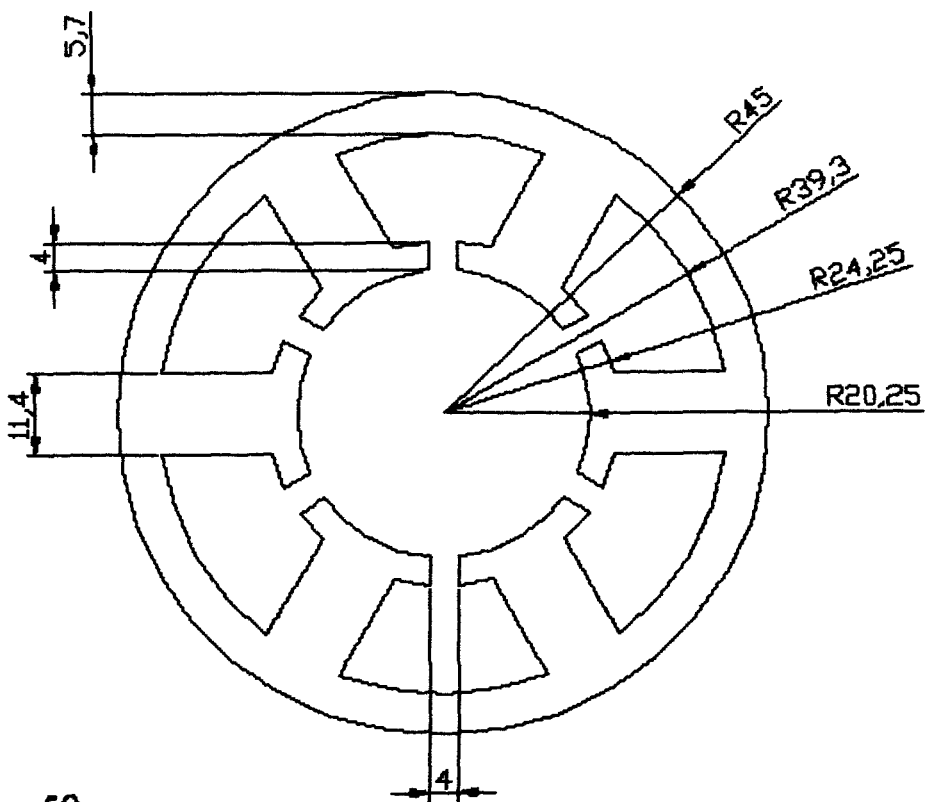

La = 50mm
Nw/coil=60turn
D_coil=1.1869mm

Stator
SPM motor (split=0.45)
By: Yong Pang
October 2004

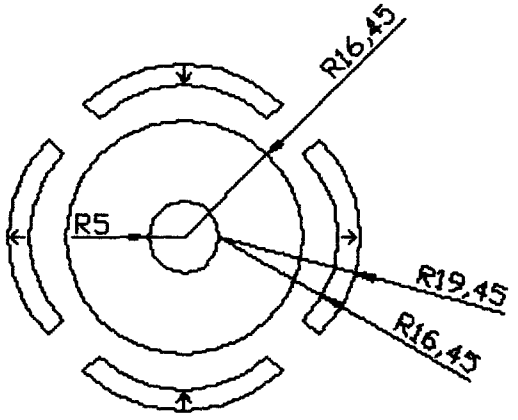

La = 50mm
Br=1.2T, radial magnetization

Rotor
SPM motor (split=0.45)
By: Yong Pang
October 2004

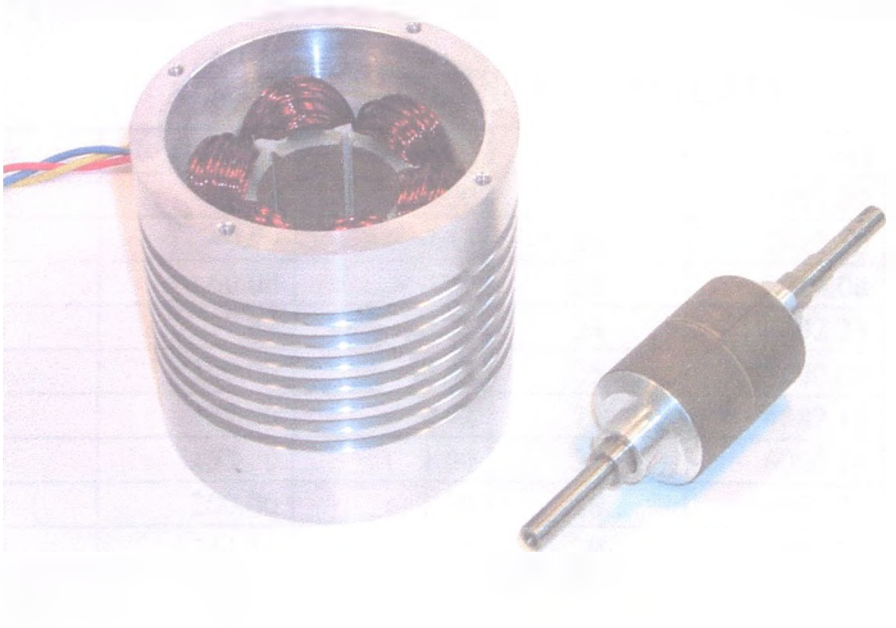

Fig. A.II. SPM brushless machine with optimal split ratio

APPENDIX III B-H CURVE OF STATOR AND ROTOR LAMINATIONS (TRANSIL315)

No.	H (A/m)	B (T)	No.	H (A/m)	B (T)
1	0.00	0.00	21	1991.09	1.53
2	40.00	0.43	22	2425.50	1.56
3	60.00	0.61	23	2914.08	1.58
4	77.83	0.73	24	3492.23	1.61
5	100.00	0.83	25	4000.00	1.63
6	127.26	0.92	26	4882.18	1.66
7	153.70	1.00	27	6006.14	1.69
8	200.00	1.10	28	6963.26	1.72
9	244.34	1.16	29	8000.00	1.74
10	300.00	1.23	30	9997.11	1.78
11	347.10	1.27	31	12130.73	1.81
12	400.00	1.31	32	14255.09	1.84
13	448.56	1.33	33	17061.12	1.88
14	508.99	1.36	34	20000.00	1.91
15	600.00	1.39	35	24660.76	1.96
16	723.55	1.41	36	30974.31	2.00
17	883.56	1.44	37	36703.28	2.04
18	1037.35	1.45	38	40000.00	2.05
19	1290.87	1.48			
20	1569.53	1.50			

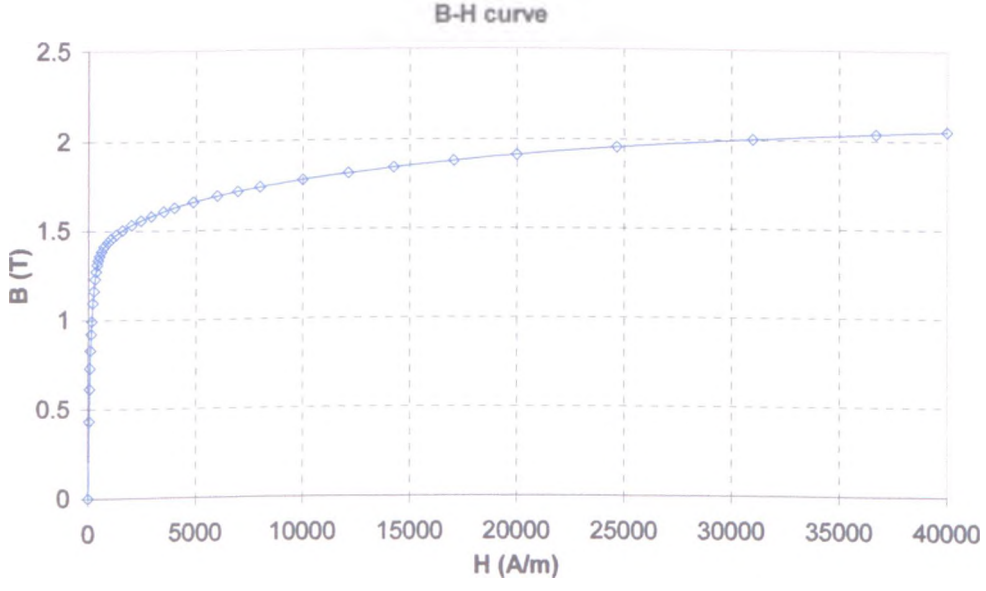

Fig. A.III. B-H curve

APPENDIX IV CONTROL STRATEGY OF PM BRUSHLESS AC MOTOR

A. Dq-axis model

According to the Park transformation, 3-phase sinusoidal time-variable voltage in abc coordination can be transferred to 2-phase time-constant voltage in dq coordination, as described in (A.IV.1)-(A.IV.4)

$$\begin{bmatrix} U_d \\ U_q \\ U_0 \end{bmatrix} = \frac{2}{3} \begin{bmatrix} cos(\theta) & cos(\theta - 120^o) & cos(\theta + 120^o) \\ -sin(\theta) & -sin(\theta - 120^o) & -sin(\theta + 120^o) \\ \frac{1}{2} & \frac{1}{2} & \frac{1}{2} \end{bmatrix} \begin{bmatrix} U_a \\ U_b \\ U_c \end{bmatrix} \tag{A.IV.1}$$

where

$$\begin{bmatrix} U_a \\ U_b \\ U_c \end{bmatrix} = \begin{bmatrix} R_a i_a + \frac{d\psi_a}{dt} \\ R_a i_b + \frac{d\psi_b}{dt} \\ R_a i_c + \frac{d\psi_c}{dt} \end{bmatrix} \tag{A.IV.2}$$

U_d, U_q d- and q-axis voltages;

U_0 zero-order voltage, which can be neglected in 3-phase system;

U_a, U_b, U_c phase-a, -b, -c voltages;

R_a phase resistance;

i_a, i_b, i_c phase-a, -b, -c currents;

ψ_a, ψ_b, ψ_c phase-a, -b, -c flux-linkages;

θ electrical angle between rotor d-axis and stator phase-a axis.

Correspondingly, the current and flux linkage can also be transferred from abc coordination to dq coordination as follows:

$$\begin{bmatrix} I_d \\ I_q \\ I_0 \end{bmatrix} = \frac{2}{3}\begin{bmatrix} cos(\theta) & cos(\theta-120^o) & cos(\theta+120^o) \\ -sin(\theta) & -sin(\theta-120^o) & -sin(\theta+120^o) \\ \frac{1}{2} & \frac{1}{2} & \frac{1}{2} \end{bmatrix}\begin{bmatrix} i_a \\ i_b \\ i_c \end{bmatrix} \quad \text{(A.IV.3)}$$

$$\begin{bmatrix} \psi_d \\ \psi_q \\ \psi_0 \end{bmatrix} = \frac{2}{3}\begin{bmatrix} cos(\theta) & cos(\theta-120^o) & cos(\theta+120^o) \\ -sin(\theta) & -sin(\theta-120^o) & -sin(\theta+120^o) \\ \frac{1}{2} & \frac{1}{2} & \frac{1}{2} \end{bmatrix}\begin{bmatrix} \psi_a \\ \psi_b \\ \psi_c \end{bmatrix} \quad \text{(A.IV.4)}$$

where

I_d, I_q d- and q-axis currents;

I_0 zero-order current, which can be neglected in 3-phase system;

ψ_d, ψ_q d- and q-axis flux-linkages;

ψ_0 zero-order flux-linkage, which can be neglected in 3-phase system.

Combine equations (A.IV.1), (A.IV.3) and (A.IV.4), U_d and U_q can be simplified as:

$$\begin{bmatrix} U_d \\ U_q \end{bmatrix} = \begin{bmatrix} R_a I_d + \frac{d\psi_d}{dt} - \omega\psi_q \\ R_a I_q + \frac{d\psi_q}{dt} + \omega\psi_d \end{bmatrix} \quad \text{(A.IV.5)}$$

where

$\omega = \frac{d\theta}{dt}$ electrical angular velocity.

Considering the iron saturation, the d- and q-axis inductances can be defined as follows:

$$L_{di} = \frac{d\psi_d}{dI_d} \quad \text{(A.IV.6)}$$

$$L_{qi} = \frac{d\psi_q}{dI_q} \quad \text{(A.IV.7)}$$

$$L_{da} = \frac{\psi_d - \psi_m}{I_d} \quad \text{(A.IV.8)}$$

$$L_{qa} = \frac{\psi_q}{I_q} \tag{A.IV.9}$$

where

L_{di}, L_{qi} d- and q-axis incremental inductances;

L_{da}, L_{qa} d- and q-axis apparent inductances;

ψ_m d-axis PM flux-linkage.

Then,

$$\begin{bmatrix} \psi_d \\ \psi_q \end{bmatrix} = \begin{bmatrix} L_{da} I_d + \psi_m \\ L_{qa} I_q \end{bmatrix} \tag{A.IV.10}$$

$$\begin{bmatrix} U_d \\ U_q \end{bmatrix} = \begin{bmatrix} R_a I_d + L_{di} \dfrac{dI_d}{dt} - \omega L_{qa} I_q \\ R_a I_q + L_{qi} \dfrac{dI_q}{dt} + \omega\left(L_{da} I_d + \psi_m\right) \end{bmatrix} \tag{A.IV.11}$$

Under steady-state operation, both I_d and I_q are constant, therefore, $\frac{dI_d}{dt} = 0$ and $\frac{dI_q}{dt} = 0$. Hence, the above equations can be re-written as:

$$\begin{bmatrix} U_d \\ U_q \end{bmatrix} = \begin{bmatrix} R_a I_d - \omega L_q I_q \\ R_a I_q + \omega\left(L_d I_d + \psi_m\right) \end{bmatrix} \tag{A.IV.12}$$

$$\begin{bmatrix} \psi_d \\ \psi_q \end{bmatrix} = \begin{bmatrix} L_d I_d + \psi_m \\ L_q I_q \end{bmatrix} \tag{A.IV.13}$$

$$\begin{bmatrix} L_d \\ L_q \end{bmatrix} = \begin{bmatrix} \dfrac{\psi_d - \psi_m}{I_d} \\ \dfrac{\psi_q}{I_q} \end{bmatrix} \tag{A.IV.14}$$

and the output torque, then, can be described as:

$$T = \frac{2}{3} p\left[\psi_m I_q - \left(L_q - L_d\right) I_d I_q\right] \tag{A.IV.15}$$

where p is the number of pole-pairs.

B. Vector control

In the modern motion control of PM motor, the desirable torque-speed performance is shown in Fig. A.IV [SNE85][JAH87][MOR90A]. When the speed is lower than the base speed, the constant torque is desired. Normally, in this operation region the maximum torque per ampere control can be employed so that the output torque can be maximized at the fixed level of current or the current can be minimized for the fixed output torque. When the speed is higher than the base speed, the output power reaches the maximum capability. Therefore, in this operation region the output power will be fixed at a constant value. In order to operate the motor at higher speed, the PM flux needs to be weakened.

It is Mr. Morimoto in [MOR90B] in 1990, who first summarized the three operation regions of PM motor, being:

(1) Constant torque region ($I_{apk}=I_{max}$, $U_{apk}<U_{max}$);

(2) Flux weakening region I ($I_{apk}=I_{max}$, $U_{apk}=U_{max}$);

(3) Flux weakening region II ($I_{apk}<I_{max}$, $U_{apk}=U_{max}$), respectively.

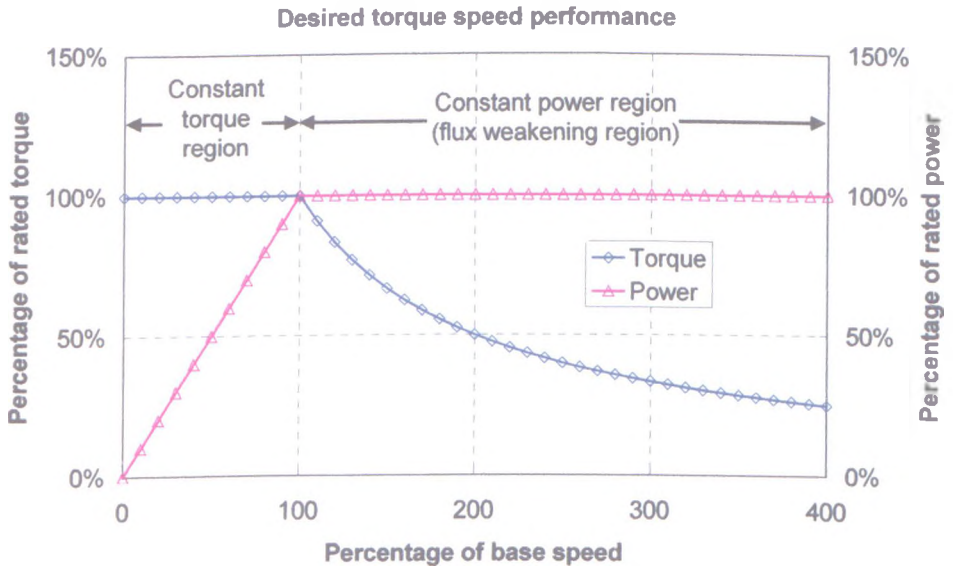

Fig. A.IV.1. Desired torque speed performance

a. Constant torque region ($I_{apk}=I_{max}$, $U_{apk}<U_{max}$)

The output torque and d-/q-axis currents can be given as:

$$T=\frac{2}{3}p\left[\psi_m I_q-\left(L_q-L_d\right)I_d I_q\right] \tag{A.IV.16}$$

$$I_d=-I_{apk}\sin\beta \tag{A.IV.17}$$

$$I_q=I_{apk}\cos\beta \tag{A.IV.18}$$

In this region, the constrains from inverter are $I_{apk}=I_{max}$, $U_{apk}<U_{max}$, where, I_{apk} and U_{apk} are the peak values of phase current and phase voltage, I_{max} and U_{max} are the maximum phase current and maximum phase voltage inverter can supply, respectively.

In order to achieve the maximum torque per ampere current, the optimal current phase angle β can be derived from $\frac{\partial T}{\partial\beta}=0$:

$$\beta=0 \qquad \text{for } L_d=L_q \tag{A.IV.19a}$$

$$\beta=arcsin\left[-\frac{\psi_m}{4\left(L_q-L_d\right)I_{apk}}+\sqrt{\frac{\psi_m^2}{16\left(L_q-L_d\right)^2I_{apk}^2}+\frac{1}{2}}\right] \qquad \text{for } L_d<L_q \tag{A.IV.19b}$$

$$\beta=arcsin\left[-\frac{\psi_m}{4\left(L_q-L_d\right)I_{apk}}-\sqrt{\frac{\psi_m^2}{16\left(L_q-L_d\right)^2I_{apk}^2}+\frac{1}{2}}\right] \qquad \text{for } L_d>L_q \tag{A.IV.19c}$$

Hence, I_d can be given as:

$$I_d=0 \qquad \text{for } L_d=L_q \tag{A.IV.20a}$$

$$I_d=-I_{apk}\sin\beta=\frac{\psi_m}{4\left(L_q-L_d\right)I_{apk}}-\sqrt{\frac{\psi_m^2}{16\left(L_q-L_d\right)^2I_{apk}^2}+\frac{1}{2}} \qquad \text{for } L_d<L_q \tag{A.IV.20b}$$

$$I_d=I_{apk}\sin\beta=-\frac{\psi_m}{4\left(L_q-L_d\right)I_{apk}}+\sqrt{\frac{\psi_m^2}{16\left(L_q-L_d\right)^2I_{apk}^2}+\frac{1}{2}} \qquad \text{for } L_d>L_q \tag{A.IV.20c}$$

I_q can be calculated from $I_d^2+I_q^2=I_{apk}^2$.

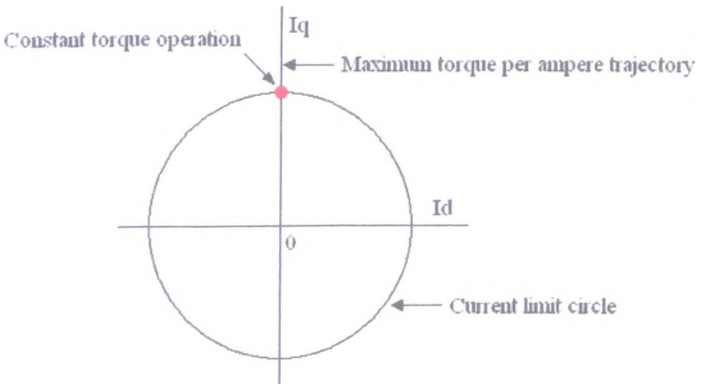

(a) $L_d=L_q$

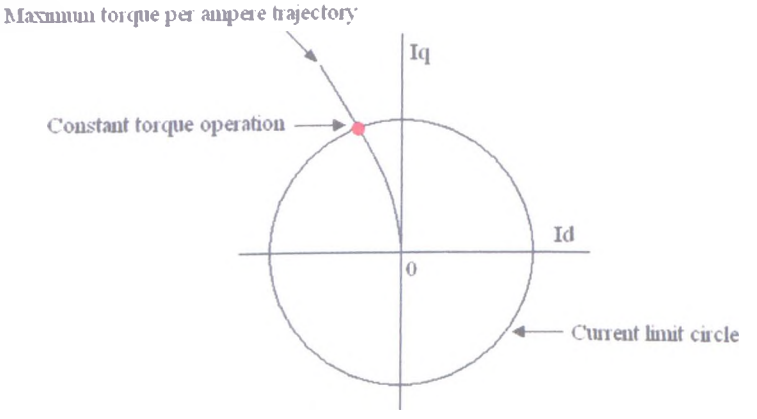

(b) $L_d<L_q$

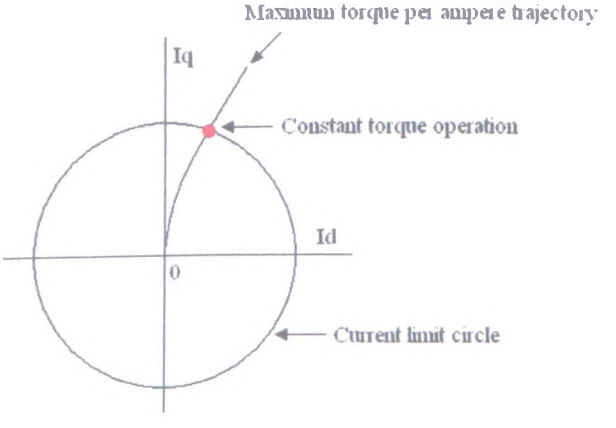

(c) $L_d>L_q$

Fig. A.IV.2. Constant torque region

b. Flux weakening region I ($I_{apk}=I_{max}$, $U_{apk}=U_{max}$)

When the motor speed is beyond the base speed, the phase voltage will be limited by the

inverter. Therefore, the voltage constrain has to be accounted in the current vector calculation.

$$U_d = RI_d - \omega L_q I_q \tag{A.IV.21}$$

$$U_q = RI_q + \omega L_d I_d + \omega \psi_m \tag{A.IV.22}$$

If the phase resistance R_a can be neglected, then:

$$\sqrt{(\omega L_q I_q)^2 + (\omega L_d I_d + \omega \psi_m)^2} = U_{apk} \tag{A.IV.23}$$

$$I_d^2 + I_q^2 = I_{apk}^2 \tag{A.IV.24}$$

D-axis current can be derived as:

$$I_d = \frac{L_d \psi_m - L_q \sqrt{\psi_m^2 + (L_q^2 - L_d^2)\left(I_{apk}^2 - \frac{U_{apk}^2}{\omega^2 L_q^2}\right)}}{L_q^2 - L_d^2} \quad \text{for } L_d \neq L_q \tag{A.IV.25a}$$

$$I_d = -\frac{\psi_m^2 + L_q^2 I_{apk}^2 - \frac{U_{apk}^2}{\omega^2}}{2 L_d \psi_m} \quad \text{for } L_d = L_q \tag{A.IV.25b}$$

I_q could be calculated from $I_d^2 + I_q^2 = I_{apk}^2$.

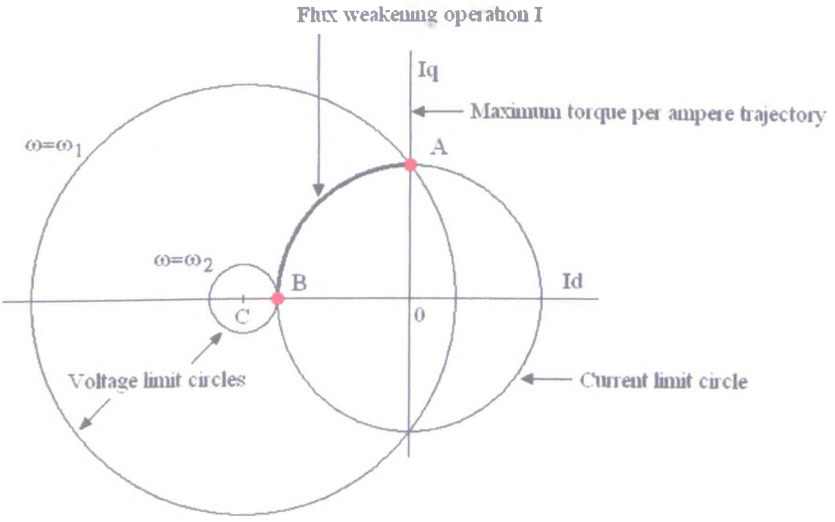

(a) L_d=L_q

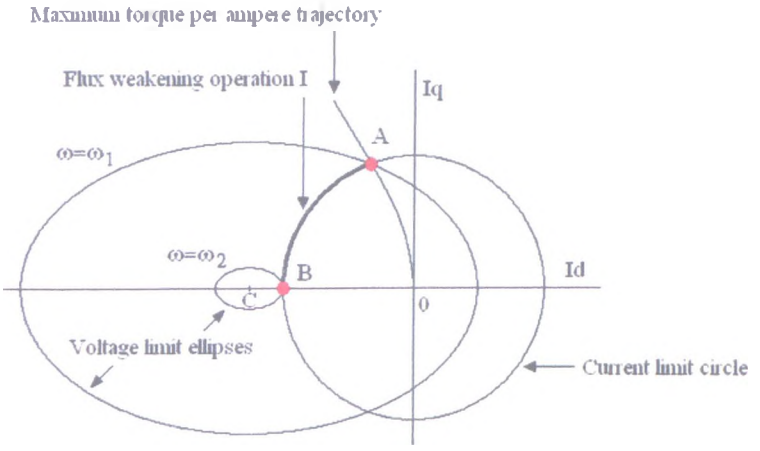

(b) $L_d<L_q$

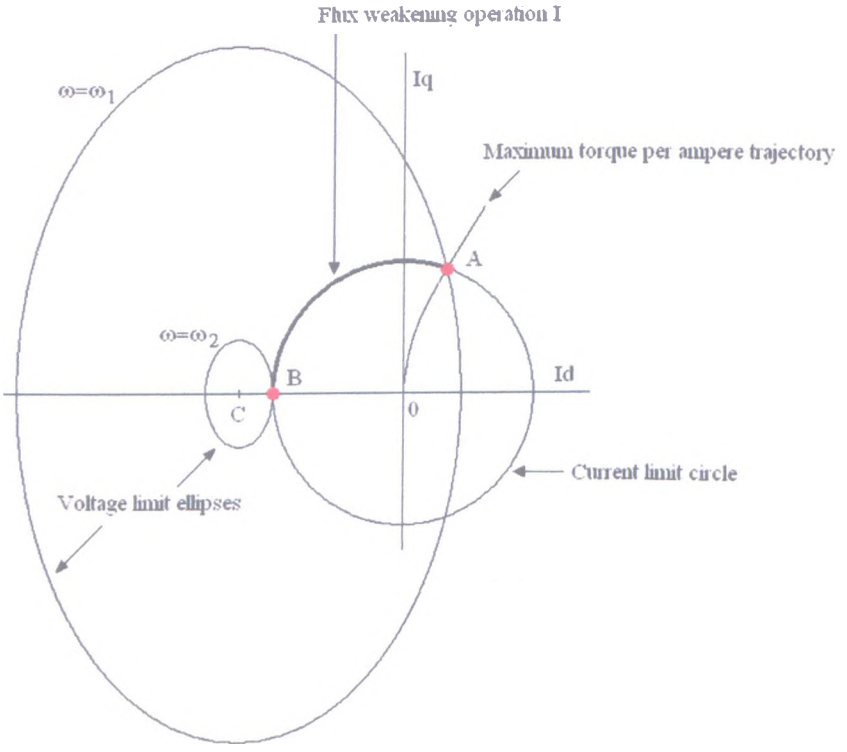

(c) $L_d>L_q$

Fig. A.IV.3. Flux weakening region I

c. Flux weakening region II ($I_{apk}<I_{max}$, $U_{apk}=U_{max}$)

If $\frac{L_d I_{max}}{\psi_m} > 1$, the infinite speed capability can be achieved. In this case, the motor could be operated in flux weakening region II, where $I_{apk}<I_{max}$ and $U_{apk}=U_{max}$. Combining voltage constrain (A.IV.27) into torque equation (A.IV.26):

$$T = \frac{2}{3} p\left[\psi_m I_q - \left(L_q - L_d\right) I_d I_q\right] \tag{A.IV.26}$$

$$\sqrt{\left(\omega L_q I_q\right)^2 + \left(\omega L_d I_d + \omega \psi_m\right)^2} = U_{apk} \tag{A.IV.27}$$

D/q-axis currents can be derived from $\frac{\partial T}{\partial U_{apk}} = 0$:

$$I_d = -\frac{\psi_m}{L_d} - \Delta I_d \tag{A.IV.28}$$

$$I_q = \frac{\sqrt{\frac{U_{apk}^2}{\omega^2} - \left(L_d \Delta I_d\right)^2}}{L_q} \tag{A.IV.29}$$

where

$$\Delta I_d = 0 \qquad \text{for } L_d = L_q \tag{A.IV.30}$$

$$\Delta I_d = \frac{-\psi_m L_q + \sqrt{\psi_m^2 L_q^2 + 8\left(L_q - L_d\right)^2 \frac{U_{apk}^2}{\omega^2}}}{4 L_d \left(L_q - L_d\right)} \qquad \text{for } L_d \neq L_q \tag{A.IV.31}$$

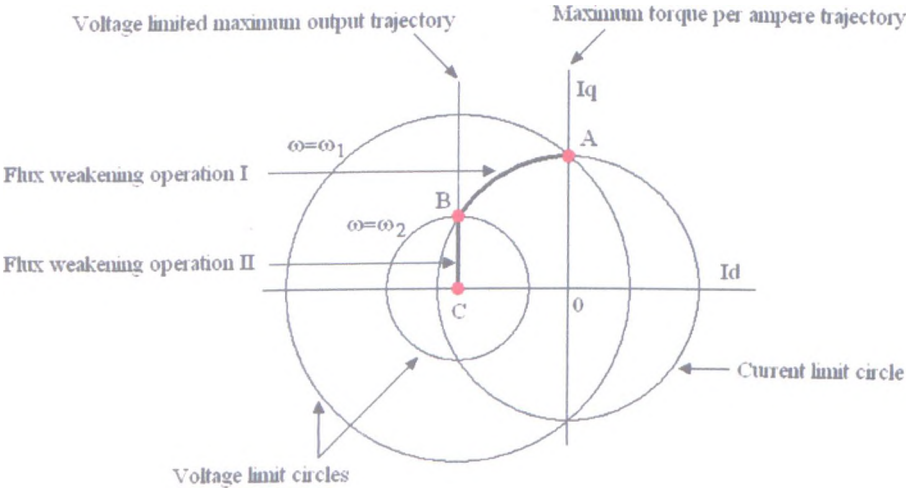

(a) L_d=L_q

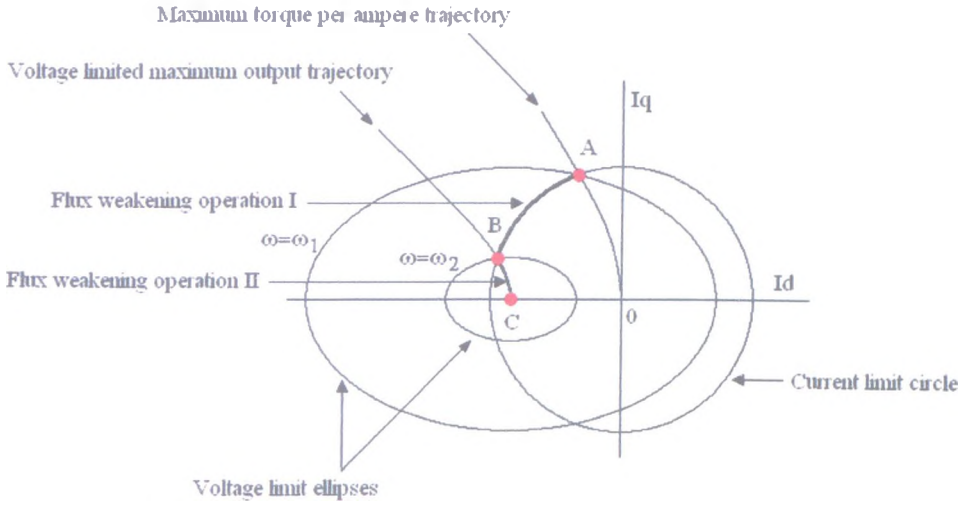

(b) $L_d<L_q$

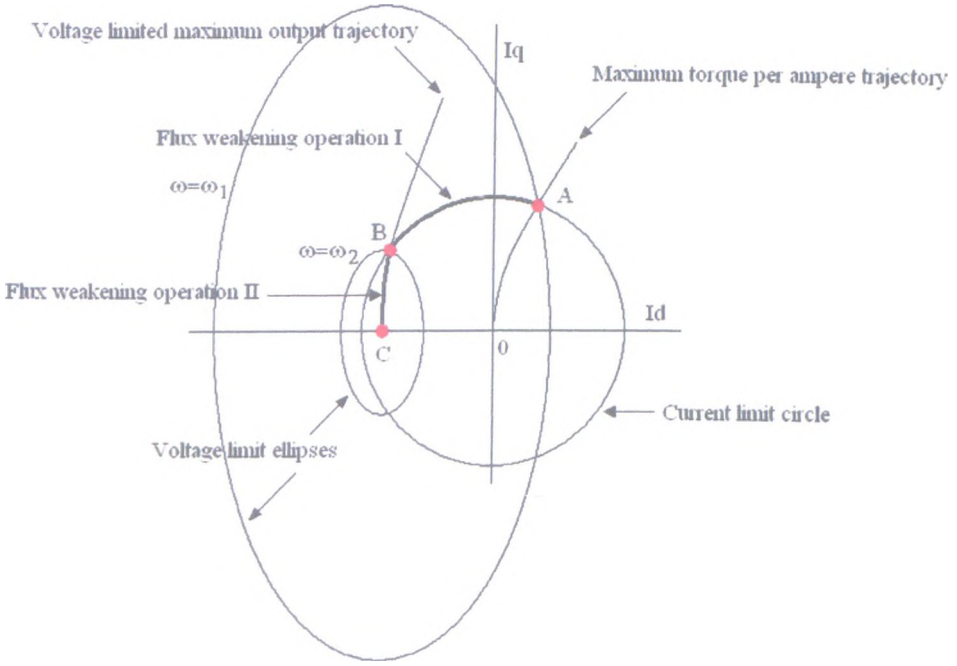

(c) $L_d>L_q$

Fig. A.IV.4. Flux weakening region II